Dynamics and Control of Satellite Relative Motion in Elliptic Orbits using Lyapunov-Floquet Theory

by

Ryan Edward Sherrill

A dissertation submitted to the Graduate Faculty of
Auburn University
in partial fulfillment of the
requirements for the Degree of
Doctor of Philosophy

Auburn, Alabama
May 4, 2013

Approved by

Andrew J. Sinclair, Chair, Associate Professor of Aerospace Engineering
John E. Cochran Jr., Professor and Head of Aerospace Engineering
David A. Cicci, Professor of Aerospace Engineering
Subhash C. Sinha, Professor of Mechanical Engineering
T. Alan Lovell, Research Aerospace Engineer, Air Force Research Laboratory
George Flowers, Dean of the Graduate School

Abstract

Rendezvous and proximity operations involving satellites operating near each other have been performed since the Gemini missions. A better understanding of the dynamics of satellites in close proximity could be helpful for both mission planners and operators as well as for algorithm development. With this increased understanding, future satellite missions may involve an impromptu fly-around of another satellite and a greater focus on satellite autonomy.

In satellite proximity operations, it is desirable to express the relative motion of a deputy satellite with respect to the chief satellite. For satellites in elliptic orbits, this relative motion can be described by the time-varying Linearized Equations of Relative Motion. Making an assumption that the chief satellite is in a circular orbit results in the linear time-invariant Hill-Clohessy-Wiltshire equations. These equations allow the relative-motion solution to be intuitively visualized. Due to the abundance of algorithms in the literature based on the Hill-Clohessy-Wiltshire equations, the focus of this dissertation is to explore the relationship between relative motion in elliptic orbits and the Hill-Clohessy-Wiltshire equations.

The major contributions of this work are twofold. First, three time-varying coordinate transformations are derived which relate the Hill-Clohessy-Wiltshire equations to the Linearized Equations of Relative Motion. These transformations show that the Hill-Clohessy-Wiltshire equations are able to exactly capture the time-varying dynamics. Second, the literature does not contain infinite-horizon continuous-thrust control for satellites in elliptic orbits. A time-varying gain matrix was constructed using the time-varying coordinate transformations, optimal-control theory, and a control method from the literature. This control is able to drive the deputy's position toward rendezvous with an elliptic chief.

Acknowledgments

The author is forever indebted to Dr. Andrew J. Sinclair for the guidance, patience, and encouragement shown during his graduate education, and for the help given while completing this dissertation. Our many conversations have lead to a deeper understanding of dynamics and established the foundation for my future career. The author also thanks the following members of his committee for their time, suggestions, and criticisms of this dissertation: Dr. John E. Cochran Jr., Dr. David A. Cicci, Dr. Subhash C. Sinha, Dr. T. Alan Lovell, and Dr. John Y. Hung.

In addition, the author thanks Dr. R. Steven Gross for a decade of helpful advisement and the opportunity to teach. The author also acknowledges the financial support offered by the Department of Aerospace Engineering. Three summers of research experience at the Air Force Research Laboratory, Space Vehicles Directorate were provided by the American Society for Engineering Education's Summer Faculty Fellowship Program and the Air Force Research Laboratory's Space Scholars Program.

Finally, the author thanks his beautiful fiancee Judith Ann Bailey for her constant support, love, and encouragement.

When I Heard the Learn'd Astronomer

When I heard the learn'd astronomer,
When the proofs, the figures, were ranged in columns before me,
When I was shown the charts and the diagrams,
    to add, divide, and measure them,
When I, sitting, heard the astronomer,
    where he lectured with much applause in the lecture-room,
How soon, unaccountable, I became tired and sick,
Till rising and gliding out, I wanderd off by myself,
In the mystical moist night-air, and from time to time,
Lookd up in perfect silence at the stars.

-Walt Whitman

Table of Contents

List of Figures

List of Tables

Chapter 1

Introduction

Missions involving satellites operating in close proximity to each other are commonly referred to as rendezvous and proximity operations. Rendezvous and proximity operations are not a recent development; the Gemini and Apollo missions, as well as over forty percent of all Space Shuttle missions, involved on-orbit docking. However, missions currently being planned may involve an impromptu fly-around of a satellite and a greater focus on satellite autonomy. For these types of missions, thoroughly understanding the dynamics is helpful for both mission planners and operators, as well as for engineers designing the computer algorithms used onboard the satellite.

In satellite proximity operations, it is often desirable to describe the motion of a "deputy" satellite relative to a "chief" satellite. Several models exist to predict these motions. One choice is the Hill-Clohessy-Wiltshire equations, which are a set of linearized time-invariant ordinary differential equations, derived by assuming a circular chief orbit. Deriving linearized equations of motion without assuming a circular chief orbit results in time-varying differential equations. The relative motion can also be predicted by propagating the orbit of each satellite relative to the Earth. Among these approaches, the Hill-Clohessy-Wiltshire equations offer an advantage in the ability to understand and intuitively visualize the geometry of the relative-motion solutions. The solutions obtained via linearized time-varying equations or by differencing the nonlinear orbit propagations of the chief and deputy are more accurate in describing elliptic orbits, but can be difficult to visualize conceptually.

The focus of this dissertation is to explore the relationship between relative motion in elliptic orbits and the Hill-Clohessy-Wiltshire equations. This exploration is driven by the abundance of algorithms in the literature based on the Hill-Clohessy-Wiltshire equations and

the intuitive understanding these equations provide. By using Lyapunov-Floquet theory, several time-varying transformations are presented that relate the linearized time-varying equations of motion to the Hill-Clohessy-Wiltshire equations. These transformations show that the Hill-Clohessy-Wiltshire equations can be generalized to describe relative motion in elliptic orbits. Since the Hill-Clohessy-Wiltshire equations are able to capture the exact time-varying dynamics, existing methods for describing circular relative motion could be utilized for elliptic orbits. One application shown in this dissertation is continuous-thrust maneuvering in elliptic orbits based on infinite-horizon optimal control.

The following chapter presents a review of orbital mechanics including basic formulations and several relative-motion equations. Next, preliminary investigations into the generalization of the Hill-Clohessy-Wiltshire equations are discussed. Lyapunov-Floquet theory is then introduced, including an existing transformation from the literature and the author's Lyapunov-Floquet generalization of the Hill-Clohessy-Wiltshire equations. The subsequent chapter presents three time-varying coordinate transformations which are able to relate the linearized time-varying equations to the Hill-Clohessy-Wiltshire equations. This chapter also includes using the coordinate transformations to select initial conditions to approximate the motion using the Hill-Clohessy-Wiltshire equations. Finally, control algorithms and continuous-thrust maneuvering are discussed.

The chapters in this dissertation are organized with background material and novel contributions conjointly presented. The specific contributions of the author to the field of satellite relative motion can be found in the following sections: Chapter 3, the Virtual-Chief and Virtual-Time methods; Section 4.5, Lyapunov-Floquet Generalization of the Hill-Clohessy-Wiltshire Equations in the f-Domain; Chapter 5, Time-Varying Coordinate Transformations of the linear equations of relative motion; Section 6.3.2, Discussion of the Lyapunov-Floquet Based Control Method; and Section 6.4, Continuous-Thrust Control of Satellites in Elliptic Orbits.

Chapter 2

Orbital Mechanics

Classically, what is now called orbital mechanics was once referred to as celestial mechanics, or the study of the motion of heavenly bodies. A few of the well-known classical philosophers and astronomers included: Hipparchus who cataloged over 1000 stars by brightness and expanded the theory of epicycles; Claudius Ptolemy who's *Almagest* was a complete exposition of astronomy known to the Greeks and became the definitive work on astronomy for over 1000 years; and Copernicus who proposed the heliocentric model of the universe.[1,2,3]

Since the beginning of the 'Space Age' following the launch of Sputnik in 1957, the methods originally used to describe the motion of the planets have been adapted to artificial satellites. The first half of this chapter focuses on the basic laws of orbital mechanics which describe the motion of a satellite relative to the Earth developed by two seventeenth century mathematicians: Johannes Kepler and Isaac Newton. After discussing the motion of one body orbiting another, the later parts of the chapter will apply these principles to the problem of relative motion between objects in neighboring orbits.

2.1 Orbital Motion of a Spacecraft

2.1.1 Kepler's Laws of Planetary Motion

The Danish astronomer Tycho Brahe collected accurate measurements of the movement of the planets, and willed his observations to Johannes Kepler upon his death in 1601. Kepler was able to formulate his three comprehensive laws of planetary motion through intensive study of Brahe's empirical data. In 1609, Kepler published *Astronomia nova* containing his first two laws of planetary motion. His third law was published in 1619 in *Harmonices Mundi*. Kepler's three laws of planetary motion are stated below.[4]

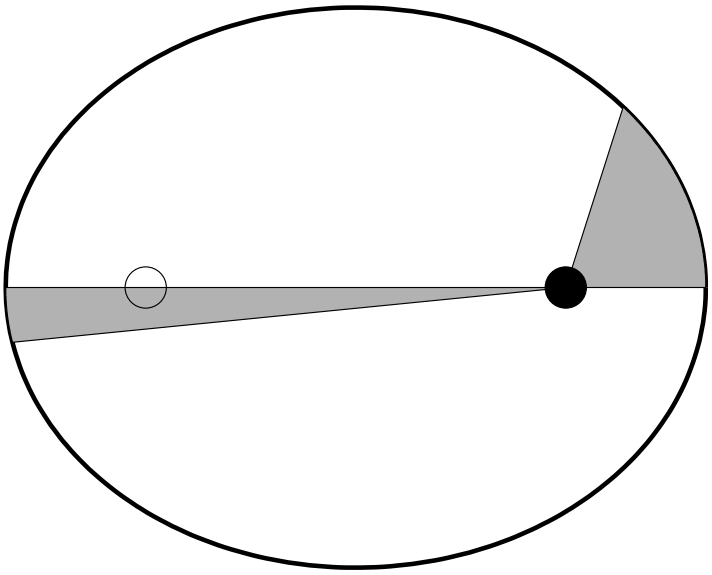

Figure 2.1: Kepler's First and Second Laws.

1. The orbit of each planet is an ellipse with the sun at one focus.

2. The line from the sun to a planet sweeps out equal areas inside the ellipse in equal lengths of time.

3. The squares of the orbital periods of the planets are proportional to the cubes of their mean distance from the Sun.

Kepler's first law describes the shape of a planet's orbit. As depicted in Figure 2.1, the planets's orbit is an ellipse in the orbital plane. The Sun occupies one focus while the other focus of the ellipse remains empty. As a planet travels in its orbit, its velocity changes with its position. The shaded regions in Figure 2.1 were traced out in equal amounts of time, demonstrating Kepler's second law. While Kepler's first two laws describes a planet's orbit and how it traverses that orbit, the third law is a mathematical relationship describing how the motion of different planets are related as they revolve around the Sun. It should be

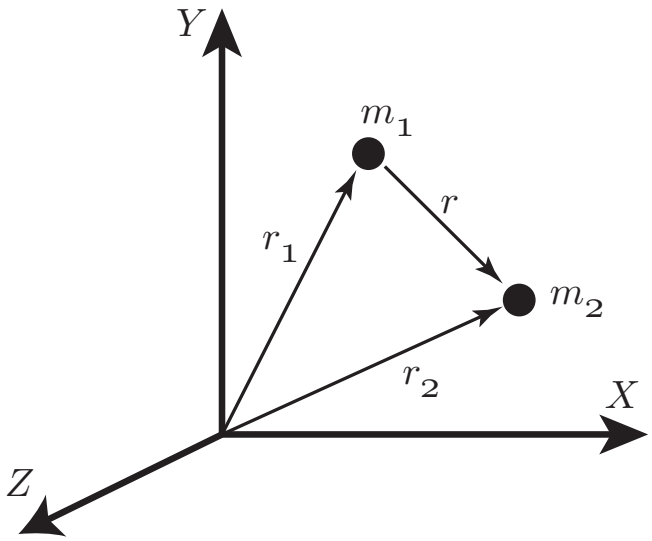

Figure 2.2: Inertial coordinate frame.

noted that Kepler's laws apply to any body in orbit of another. Therefore, the same forces apply to a comet orbiting the Sun, or the Space Shuttle orbiting the Earth.

2.1.2 The Two-Body Problem

In the *Philosophiae Naturalis Principia Mathematica*, Isaac Newton introduced the three fundamental laws of classical mechanics. The development of the two-body problem, which can describe the motion of a satellite with respect to the Earth, begins with a mathematical representation of Newton's Second Law.

$$\sum \boldsymbol{F} = m\boldsymbol{a} \tag{2.1}$$

Here, $\boldsymbol{F}$ represents the forces acting on an object, m is the mass of the object, and $\boldsymbol{a}$ represents the acceleration of the object. Consider the motion of two point masses in an inertial coordinate system shown in Figure 2.2. The point masses are attracted to each other with a magnitude given by Newton's Law of Universal Gravitation $F = \dfrac{Gm_1m_2}{r^2}$ where G is the gravitational constant, m_1 and m_2 are the masses of the bodies and r is the distance between the center of the masses. Equations of motion for each mass can be written in vector

form.

$$m_1\ddot{\boldsymbol{r}}_1 = \frac{Gm_1m_2}{r^3}\boldsymbol{r} \tag{2.2}$$

$$m_2\ddot{\boldsymbol{r}}_2 = \frac{-Gm_1m_2}{r^3}\boldsymbol{r} \tag{2.3}$$

Here, $\boldsymbol{r}$ represents the relative motion of the bodies given by $\boldsymbol{r} = \boldsymbol{r}_2 - \boldsymbol{r}_1$, and an overdot ($\dot{}$) represents a derivative with respect to time. Differentiating this equation twice gives the relative acceleration of the bodies.

$$\ddot{\boldsymbol{r}} = \ddot{\boldsymbol{r}}_2 - \ddot{\boldsymbol{r}}_1 = -\frac{G\left(m_1 + m_2\right)}{r^3}\boldsymbol{r} \tag{2.4}$$

Define the gravitational parameter μ such that $\mu = G\left(m_1 + m_2\right)$. Often when calculating the gravitational parameter, the mass of one of the bodies will be negligible such as the case of a satellite compared to the Earth. The relative equation of motion can be written in the familiar form.

$$\ddot{\boldsymbol{r}} = -\frac{\mu}{r^3}\boldsymbol{r} \tag{2.5}$$

2.1.3 The Orbit in Space

In order to describe the position of a satellite in orbit, a coordinate system must be chosen. One choice is a Cartesian system shown in Figure 2.3. In this system, the origin is located at the center of the Earth where the X axis points toward the first point of Aries, symbolized by Υ, the Z axis goes through the geographic North Pole, and the Y axis lies in the equatorial plane and completes the orthogonal triad. Using a Cartesian coordinate system, a satellite's state can be completely described by six independent parameters: position (x, y, z) and velocity $(\dot{x}, \dot{y}, \dot{z})$.

A disadvantage of selecting a Cartesian coordinate system is that, with the exception of a few select cases, visualizing a satellite's orbit is difficult. Therefore, it is often advantageous to select another set of coordinates called orbital elements. When using orbital elements, five of the six parameters needed to describe a satellite's state are constant and represent the

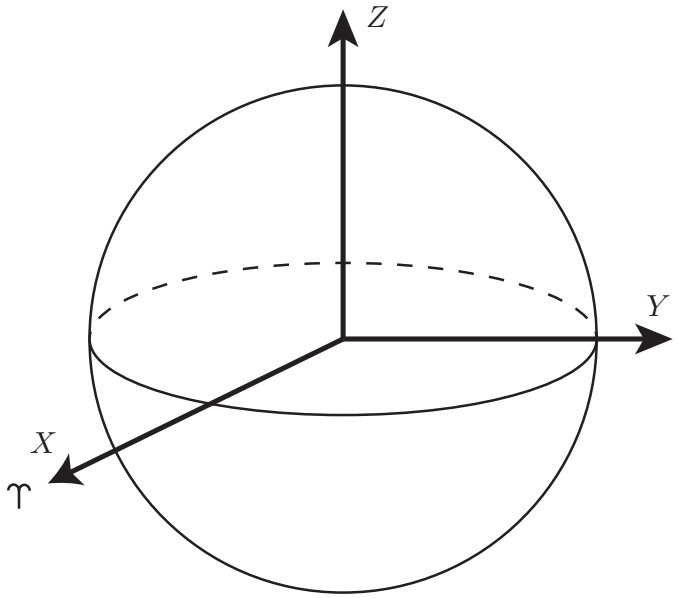

Figure 2.3: The Earth centered inertial (ECI) coordinate frame.

size, shape, and orientation of the orbit. The sixth parameter represents the motion along that orbit. The six orbital elements, shown Figure 2.4, are stated below.

a: The *semi-major axis* describes the size of the ellipse.

e: The *eccentricity* of the orbit which describes the shape of the ellipse.

i: The *inclination*, or angle, of the orbital plane from the equator.

Ω: The *right ascension of the ascending node*, is the angle from the vernal equinox to the point on the equator where the satellite makes its south to north crossing.

ω: The *argument of perigee* is the angle from the ascending node to perigee.

f: The *true anomaly* represents the angle between the satellite's current position in the orbit and perigee.

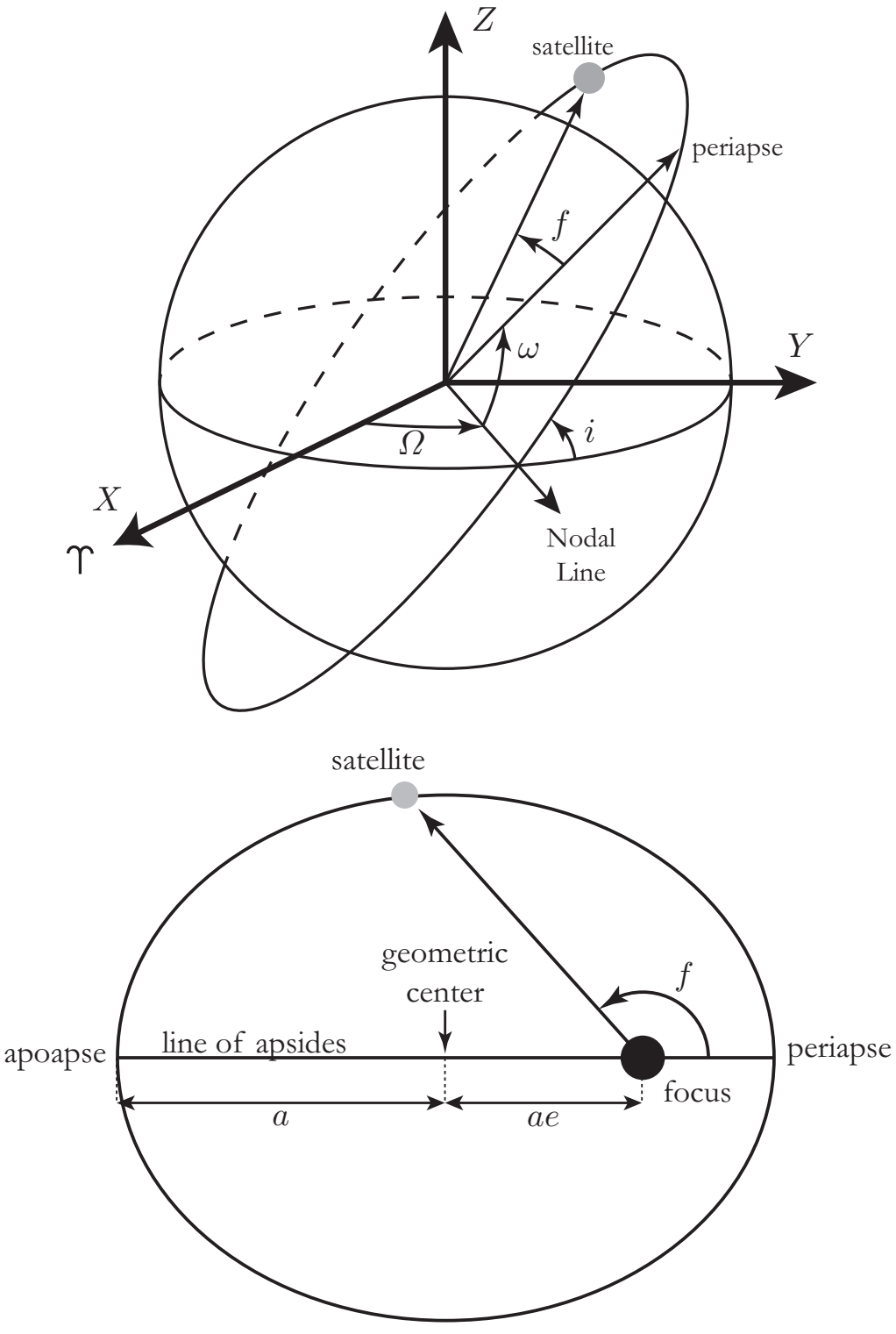

Figure 2.4: Orbital Elements.

As can be seen in Figure 2.4, the closest point on the ellipse to the focus is called periapse while apoapse is defined as the point on the ellipse furthest from the focus. The line of apsides passes through both periapse and apoapse. The focus is located a distance ae along the apse line from the geometric center of the ellipse. Note that the true anomaly is measured from periapse, i.e. the closest point on the ellipse to the focus occurs at $f = 0$.

2.1.4 Orbital Integrals of Motion

In a polar coordinate frame $(\hat{\boldsymbol{i}}_r \quad \hat{\boldsymbol{i}}_\theta \quad \hat{\boldsymbol{i}}_z)$ centered at m_1, the position of the satellite is given by $\boldsymbol{r} = r\hat{\boldsymbol{i}}_r$, and the velocity is given $\boldsymbol{v} = \dot{\boldsymbol{r}} = \dot{r}\hat{\boldsymbol{i}}_r + r\dot{f}\hat{\boldsymbol{i}}_\theta$. The massless angular momentum can be determined by taking the cross product of these vectors.

$$\boldsymbol{h} = \boldsymbol{r} \times \boldsymbol{v} = r^2 \dot{f} \hat{\boldsymbol{i}}_z \tag{2.6}$$

It is easy to see that $\boldsymbol{h}$ is a constant, and that the orbital motion lies in a plane perpendicular to $\boldsymbol{h}$. Multiply both sides of Equation (2.5) by $\boldsymbol{h}$ (note that $\ddot{\boldsymbol{r}}$ is written as $\frac{\mathrm{d}\boldsymbol{v}}{\mathrm{d}t}$).

$$\begin{aligned} \frac{\mathrm{d}\boldsymbol{v}}{\mathrm{d}t} \times \boldsymbol{h} &= -\frac{\mu}{r^3}\boldsymbol{r} \times \boldsymbol{h} \\ \frac{\mathrm{d}}{\mathrm{d}t}(\boldsymbol{v} \times \boldsymbol{h}) &= \mu \frac{\mathrm{d}f}{\mathrm{d}t}\hat{\boldsymbol{i}}_\theta \end{aligned} \tag{2.7}$$

Integrating both sides of Equation (2.7) and simplifying gives the following.

$$\boldsymbol{v} \times \boldsymbol{h} = \frac{\mu}{r}\boldsymbol{r} + \mu \boldsymbol{e} \tag{2.8}$$

Here, $\mu\boldsymbol{e}$ is the constant of integration and $\boldsymbol{e}$ is the eccentricity vector. The eccentricity vector points toward periapse. The magnitude of the eccentricity vector is given by the following.

$$e^2 = \boldsymbol{e} \cdot \boldsymbol{e} = \frac{1}{\mu^2}(\boldsymbol{v} \times \boldsymbol{h}) \cdot (\boldsymbol{v} \times \boldsymbol{h}) - \frac{2}{\mu r}\boldsymbol{r} \cdot \boldsymbol{v} \times \boldsymbol{h} + 1 \tag{2.9}$$

Using the properties of cross products, $(\boldsymbol{v} \times \boldsymbol{h}) = vh$ and $\boldsymbol{r} \cdot \boldsymbol{v} \times \boldsymbol{h} = \boldsymbol{r} \times \boldsymbol{v} \cdot \boldsymbol{h}$, Equation (2.9) can be written as shown below.

$$\begin{aligned} e^2 &= \frac{1}{\mu^2} h^2 v^2 - \frac{2}{\mu r} h^2 + 1 \\ e^2 - 1 &= \frac{h^2}{\mu} \left(\frac{v^2}{\mu} - \frac{2}{r} \right) \\ 1 - e^2 &= \frac{h^2}{\mu} \left(\frac{2}{r} - \frac{v^2}{\mu} \right) \end{aligned} \tag{2.10}$$

Define $p = \dfrac{h^2}{\mu}$ and $a = \left(\dfrac{2}{r} - \dfrac{v^2}{\mu} \right)^{-1}$ where p is called the parameter. From Equation (2.10), the parameter is related to a and e by the following.

$$p = \frac{h^2}{\mu} = a \left(1 - e^2 \right) \tag{2.11}$$

The total energy of the system is related to a by the following.

$$\frac{v^2}{2} - \frac{\mu}{r} = -\frac{u}{2a} \tag{2.12}$$

Where the kinetic energy is given by $\dfrac{v^2}{2}$, potential energy by $-\dfrac{\mu}{r}$, and $-\dfrac{\mu}{2a}$ is the energy constant. The above expression can be rewritten as the energy integral or the vis-viva equation (latin for "live force").

$$v^2 = \mu \left(\frac{2}{r} - \frac{1}{a} \right) \tag{2.13}$$

Solving Equation (2.8) for $\boldsymbol{e}$ and taking the dot product with position vector gives the following.

$$\begin{aligned} \boldsymbol{e} \cdot \boldsymbol{r} &= \frac{1}{\mu} \left(\boldsymbol{v} \times \boldsymbol{h} - \mu \frac{\boldsymbol{r}}{r} \right) \cdot \boldsymbol{r} \\ er \cos f &= \frac{1}{\mu} \left(\boldsymbol{r} \times \boldsymbol{v} \cdot \boldsymbol{h} - \mu r \right) \\ er \cos f &= \frac{h^2}{\mu} - r \end{aligned} \tag{2.14}$$

Solving Equation (2.14) for r and substituting for p gives the equation of an orbit.

$$r = \frac{p}{1 + e\cos f} \tag{2.15}$$

2.1.5 Kepler's Equation

Substituting the square of Equation (2.15) into Equation (2.6) gives the following expression.

$$\begin{aligned} h &= \frac{p^2}{(1 + e\cos f)^2}\frac{\mathrm{d}f}{\mathrm{d}t} \\ \sqrt{\mu p} &= \frac{p^2}{(1 + e\cos f)^2}\frac{\mathrm{d}f}{\mathrm{d}t} \\ \sqrt{\frac{\mu}{p^3}}\mathrm{d}t &= \frac{\mathrm{d}f}{(1 + e\cos f)^2} \end{aligned} \tag{2.16}$$

Integrating Equation (2.16) provides the relationship between time and true anomaly.

$$\sqrt{\frac{\mu}{p^3}}\,(t - t_p) = \int_0^f \frac{\mathrm{d}f}{(1 + e\cos f)^2} \tag{2.17}$$

Here, the constant of integration is given by t_p, and is the time when $f = 0$. For $e = 0$, Equation (2.17) can be easily integrated.

$$\sqrt{\frac{\mu}{p^3}}\,(t - t_p) = f \tag{2.18}$$

For $e = 0$, $p = a$, which allows Equation (2.18) to be written as the following.

$$f = \sqrt{\frac{\mu}{a^3}}\,(t - t_p) \tag{2.19}$$

Define the mean motion $n = \sqrt{\frac{\mu}{a^3}}$. The mean motion is an average value of how fast a satellite progresses in its orbit. The period of an orbit P, is related to the mean motion

by $P = \dfrac{2\pi}{n}$. For circular orbits, the mean motion equals the satellite's angular velocity. Equation (2.19) can be written in the following form which gives the relationship between time and true anomaly for circular orbits.

$$f = n\,(t - t_p) \tag{2.20}$$

Analogous to Equation (2.20), a relationship between time and true anomaly for elliptic orbits will now be developed. Evaluating the right hand side of Equation (2.17) for $e \neq 0$ results in the following.[5]

$$\int_0^f \frac{\mathrm{d}f}{(1 + e\cos f)^2} = \frac{1}{(1-e^2)^{\frac{3}{2}}}\left(2\tan^{-1}\sqrt{\frac{1-e}{1+e}}\tan\frac{f}{2} - \frac{e\sqrt{1-e^2}\sin f}{1+e\cos f}\right) \tag{2.21}$$

Define the mean anomaly, M, as the following.

$$M = 2\tan^{-1}\sqrt{\frac{1-e}{1+e}}\tan\frac{f}{2} - \frac{e\sqrt{1-e^2}\sin f}{1+e\cos f} \tag{2.22}$$

Substituting the result of Equation (2.21) and (2.22) into Equation (2.17) gives the following relationship.

$$\sqrt{\frac{\mu}{p^3}}\,(t - t_p) = \frac{1}{(1-e^2)^{\frac{3}{2}}}M \tag{2.23}$$

Solving Equation (2.23) for M, and substituting $p = a(1 - e^2)$ and $n = \sqrt{\dfrac{\mu}{a^3}}$ gives the relationship between time and mean anomaly.

$$M = n\,(t - t_p) \tag{2.24}$$

Note that for elliptic orbits, the mean motion does not equal the angular velocity, but does provide an average value of the satellite's progression. The expression for mean anomaly given by Equation (2.22) can be simplified by introducing an auxiliary angle, E, called the

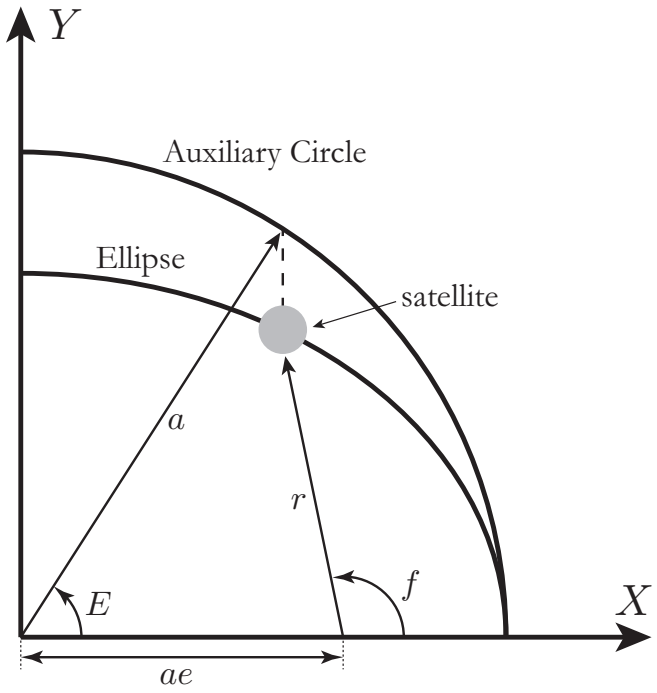

Figure 2.5: The circumscribed auxiliary circle and eccentric anomaly.

eccentric anomaly shown in Figure 2.5. Since the eccentric anomaly is measured from the geometric center, the satellite's position on the ellipse can expressed in parametric form by $x = a\cos E$, and $y = b\sin E = a\sqrt{1-e^2}\sin E$. In terms of the true anomaly, these expressions are given by $x = ae + r\cos f$ and $y = r\sin f$. By equating the x components, the following expression is developed.

$$a\cos E = ae + r\cos f \tag{2.25}$$

Using Equation (2.15) to substitute for r in Equation (2.25) and simplifying gives the following.

$$\cos E = \frac{e + \cos f}{1 + e\cos f} \tag{2.26}$$

The above expression for $\cos E$ is not ideal because for a given value of $\cos E$, there are two corresponding values of E. To eliminate this ambiguity, the trigonometric identity

$\tan^2 \dfrac{E}{2} = \dfrac{\sin^2 \dfrac{E}{2}}{\cos^2 \dfrac{E}{2}} = \dfrac{1 - \cos E}{1 + \cos E}$ is used. Here, $1 - \cos E = \dfrac{(1-e)(1-\cos f)}{1 + e\cos f}$ and $1 + \cos E = \dfrac{(1+e)(1+\cos f)}{1 + e\cos f}$. Upon simplification, the following relationship between true anomaly and eccentric anomaly can be determined.

$$\tan \frac{E}{2} = \sqrt{\frac{1-e}{1+e}} \tan \frac{f}{2} \tag{2.27}$$

Solving this expression for E gives the following.

$$E = 2 \tan^{-1} \left(\sqrt{\frac{1-e}{1+e}} \tan \frac{f}{2} \right) \tag{2.28}$$

Recall that in terms of the mean anomaly the deputy's y position is given by $y = a\sqrt{1-e^2} \sin E$, while in terms of the true anomaly the position is given by $y = r \sin f$. Equating these expressions, solving for $\sin E$, and using Equation (2.15) gives the following.

$$\sin E = \frac{\sqrt{1-e^2} \sin f}{1 + e \cos f} \tag{2.29}$$

Using Equations (2.28) and (2.29), it is clear that Equation (2.22) can be simplified.

$$M = n(t - t_p) = E - e \sin E \tag{2.30}$$

Equation (2.30) is known as Kepler's Equation which relates time to eccentric anomaly, which can be related to true anomaly through Equation (2.27). This relationship is considerably more complicated than the expression for circular orbits, and requires an iterative technique to transform time to true anomaly.

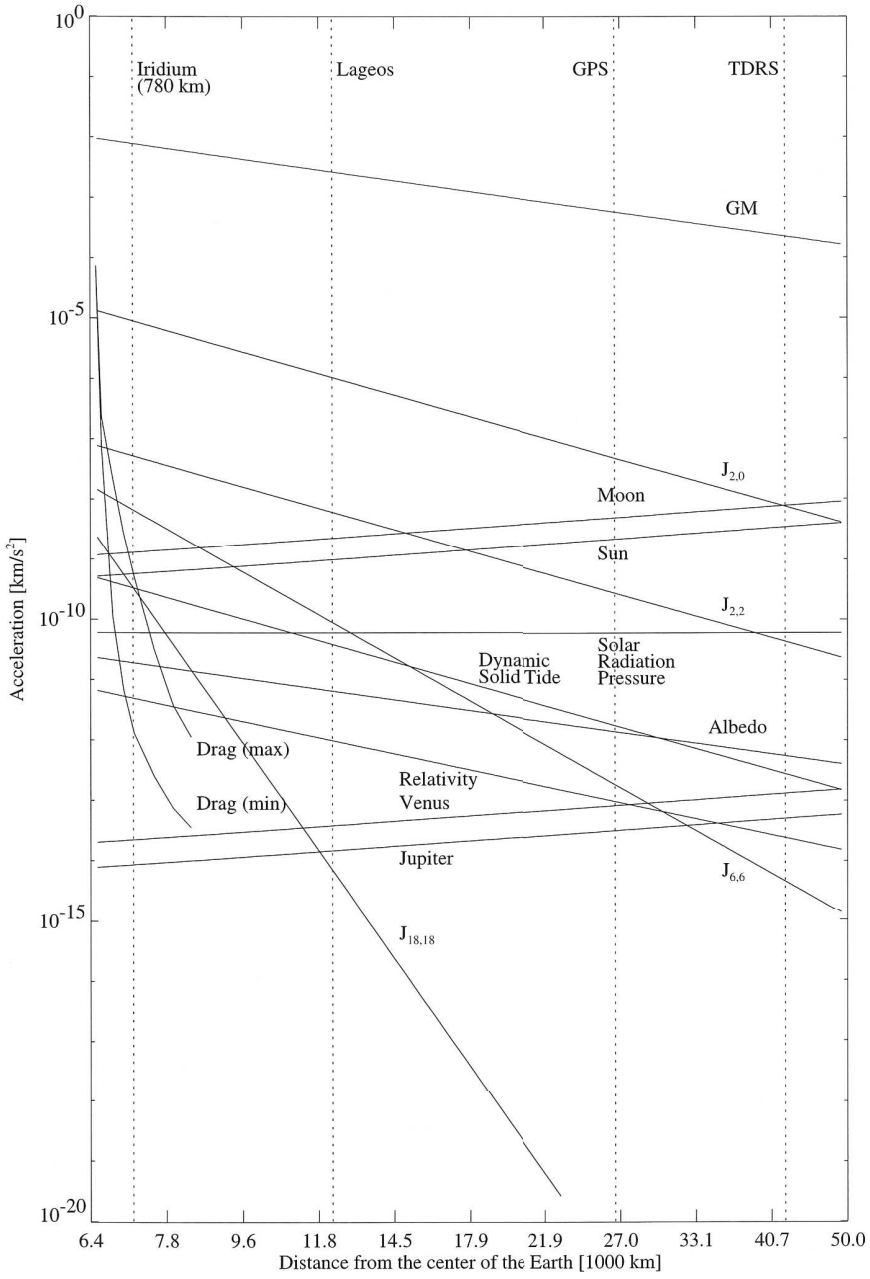

Figure 2.6: Magnitude of orbital perturbations vs satellite radius. (Reproduced from Reference 6)

2.1.6 Perturbations

The discussion presented in this chapter has only considered gravitational attraction of a point masses. While this basic model has allowed the development of Keplerian orbits, it is only an approximation of true satellite motion. The Earth, in fact, is not a point mass.

Due to the Earth's rotation, the equatorial radius is approximately twenty kilometers greater than the polar radius. In addition, the mass of the Earth is not centered at a point, but distributed unequally under the surface. Models with increasing complexity up to seventy terms exist to model the zonal, tesseral, and sectorial harmonics. The mass distribution is also time-varying due to tidal effects. In addition to gravity, atmospheric effects such as drag perturb satellites in low Earth orbit. The motion of the solar system also effects a satellite due to the presence and movement of the Moon, Venus, and Jupiter. The Sun's gravity effects a satellite as well as causing solar radiation pressure and solar wind. Figure 2.6, reproduced from Montenbruck and Gill, shows the relative magnitude of the acceleration caused by these forces as a function of orbital radius.[6]

While these perturbations will disturb a satellite from its orbit, these forces will not be considered in this dissertation. The idealization of point masses allows analytical solutions of the motion (and relative motion) to be constructed. These solutions provide geometrical interpretations of the orbit, and allow for intuitive understanding of the orbit geometry. In addition, the idealized problem provides a foundation for the future study of more complicated and realistic motion.

2.2 Relative Motion of Two Spacecraft

In the previous section, equations of motion for an object in an inverse-squared gravity field were developed. While this expression is useful for describing the motion of a satellite around a central body, it can not directly describe the relative motion of two satellites in neighboring orbits. This section will develop three sets equations which directly describe the relative motion between two satellites.

2.2.1 Nonlinear Equations of Relative Motion

Recall the nomenclature used to distinguish the satellites: one is often called the chief, and the other is referred to as the deputy. Note that the chief satellite is not necessarily

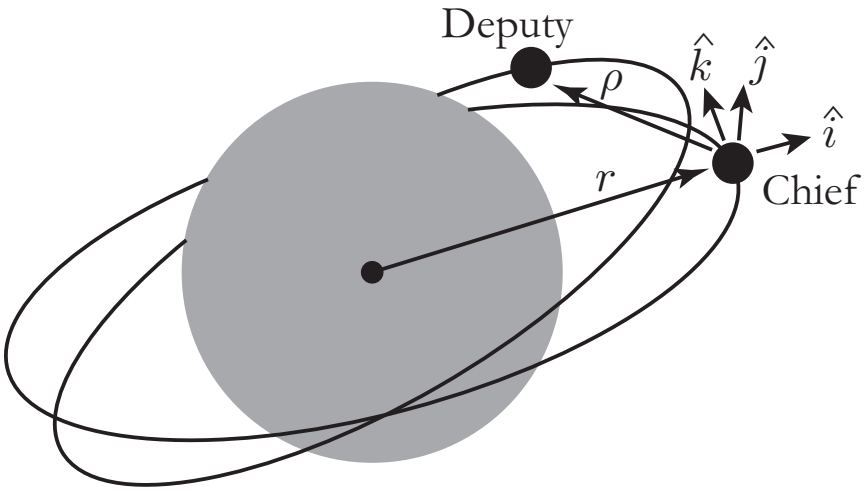

Figure 2.7: Local-vertical local-horizonal (LVLH) coordinate frame

a physical object; in the case of a satellite formation it could be a useful reference point to describe the relative motion. The relative motion equations developed in this section utilize a Cartesian local-vertical, local-horizontal (LVLH) frame attached to the chief satellite, as shown in Figure 2.7. This coordinate frame rotates with the chief's radius vector and is a convenient reference frame to describe the relative motion.[4] This reference frame is also sometimes referred to as the Hill frame or the CW frame. In this coordinate frame, x lies in the chief's radial direction, z lies in the direction of the chief's orbital angular momentum, and y completes the right-handed orthogonal triad. Note that the x and y directions correspond to the in-plane motion, and z corresponds to the out-of-plane motion.

In the chief's LVLH frame, the position of the deputy satellite is given by the following.

$$\boldsymbol{r}_d = \boldsymbol{r}_c + \boldsymbol{\rho} = (r_c + x)\,\hat{\boldsymbol{i}} + y\hat{\boldsymbol{j}} + z\hat{\boldsymbol{k}} \tag{2.31}$$

The angular velocity and acceleration of the LVLH frame are given by $\boldsymbol{\omega} = \dot{f}_c\hat{\boldsymbol{k}} = \dfrac{h}{r_c^2}\hat{\boldsymbol{k}}$ and $\boldsymbol{\alpha} = \ddot{f}_c\hat{\boldsymbol{k}} = -\dfrac{2\dot{r}_c\dot{f}_c}{r_c}\hat{\boldsymbol{k}}$ respectively. In the subsequent discussion, the subscript c will be omitted from r and f. From kinematics, the equation of motion for the deputy in the chief's

frame is given by the following.

$$\ddot{\boldsymbol{r}}_d = \ddot{\boldsymbol{r}} + \boldsymbol{\alpha} \times \boldsymbol{\rho} + \boldsymbol{\omega} \times (\boldsymbol{\omega} \times \boldsymbol{\rho}) + 2\boldsymbol{\omega} \times \dot{\boldsymbol{\rho}} + \ddot{\boldsymbol{\rho}} \tag{2.32}$$

Substitution and collecting terms in Equation (2.32) gives the following.

$$\begin{aligned}
\ddot{\boldsymbol{r}}_d &= \ddot{r}\hat{\boldsymbol{i}} + \ddot{f}\hat{\boldsymbol{k}} \times \left(x\hat{\boldsymbol{i}} + y\hat{\boldsymbol{j}} + z\hat{\boldsymbol{k}}\right) + \dot{f}\hat{\boldsymbol{k}} \times \left(\dot{f}\hat{\boldsymbol{k}} \times \left(x\hat{\boldsymbol{i}} + y\hat{\boldsymbol{j}} + z\hat{\boldsymbol{k}}\right)\right) \\
&\qquad + 2\dot{f}\hat{\boldsymbol{k}} \times \left(\dot{x}\hat{\boldsymbol{i}} + \dot{y}\hat{\boldsymbol{j}} + \dot{z}\hat{\boldsymbol{k}}\right) + \left(\ddot{x}\hat{\boldsymbol{i}} + \ddot{y}\hat{\boldsymbol{j}} + \ddot{z}\hat{\boldsymbol{k}}\right) \\
&= \ddot{r}\hat{\boldsymbol{i}} + \ddot{f}x\hat{\boldsymbol{j}} - \ddot{f}y\hat{\boldsymbol{i}} - \dot{f}^2x\hat{\boldsymbol{i}} - \dot{f}^2y\hat{\boldsymbol{j}} + 2\dot{x}\dot{f}\hat{\boldsymbol{j}} - 2\dot{y}\dot{f}\hat{\boldsymbol{i}} + \ddot{x}\hat{\boldsymbol{i}} + \ddot{y}\hat{\boldsymbol{j}} + \ddot{z}\hat{\boldsymbol{k}} \\
&= \left(\ddot{r} - \ddot{f}y - \dot{f}^2x - 2\dot{y}\dot{f} + \ddot{x}\right)\hat{\boldsymbol{i}} + \left(\ddot{f}x - \dot{f}^2y + 2\dot{x}\dot{f} + \ddot{y}\right)\hat{\boldsymbol{j}} + \ddot{z}\hat{\boldsymbol{k}}
\end{aligned} \tag{2.33}$$

Recall that the chief's position in the LVLH frame is given by $\boldsymbol{r} = r\hat{\boldsymbol{i}}$. Substitution into Equation (2.5) allows the chief's acceleration to be written as the following.

$$\ddot{r} = -\frac{\mu}{r^2} \tag{2.34}$$

Substituting Equation (2.34) into Equation (2.33) gives the following.

$$\ddot{\boldsymbol{r}}_d = \left(-\frac{\mu}{r^2} - \ddot{f}y - \dot{f}^2x - 2\dot{y}\dot{f} + \ddot{x}\right)\hat{\boldsymbol{i}} + \left(\ddot{f}x - \dot{f}^2y + 2\dot{x}\dot{f} + \ddot{y}\right)\hat{\boldsymbol{j}} + \ddot{z}\hat{\boldsymbol{k}} \tag{2.35}$$

From Equation (2.5), the acceleration of the deputy is given by $\ddot{\boldsymbol{r}}_d = \dfrac{-\mu}{r_d^3}\boldsymbol{r}_d$ where $\boldsymbol{r}_d = [(r+x) \;\; y \;\; z]^{\mathsf{T}}$. Equating coefficients in Equation (2.35) gives the full nonlinear equations of relative motion (NERM).

$$\begin{aligned}
\ddot{x} - 2\dot{f}\dot{y} - \ddot{f}y - \dot{f}^2x - \frac{\mu}{r^2} &= \frac{-\mu}{r_d^3}(r+x) \\
\ddot{y} + 2\dot{f}\dot{x} + \ddot{f}x - \dot{f}^2y &= \frac{-\mu}{r_d^3}y \\
\ddot{z} &= \frac{-\mu}{r_d^3}z
\end{aligned} \tag{2.36}$$

The only assumption made in deriving Equation (2.36) was that both satellites obeyed Keplerian motion, i.e. the only force acting on each satellite was gravity.

2.2.2 Linear Equations of Relative Motion

The nonlinear equations of motion presented in the previous section can be linearized for small separations between the chief and deputy. The deputy's radius can be linearized as follows by neglecting higher order terms.

$$\begin{aligned} r_d &= \sqrt{(r+x)^2 + y^2 + z^2} \\ &= r\sqrt{1 + \frac{2x}{r} + \frac{x^2+y^2+z^2}{r^2}} \\ &\approx r\sqrt{1 + \frac{2x}{r}} \end{aligned} \tag{2.37}$$

Using the binomial theorem, the term $\frac{\mu}{r_d^3}$ can be expanded in terms of r. Retaining only first order terms gives the following.

$$\begin{aligned} \frac{\mu}{r_d^3} &\approx \frac{\mu}{\left(r\sqrt{1+\frac{2x}{r}}\right)^3} \\ &\approx \frac{\mu}{r^3}\left(1 + \frac{2x}{r}\right)^{-\frac{3}{2}} \\ &\approx \frac{\mu}{r^3}\left(1 - \frac{3x}{r}\right) \end{aligned} \tag{2.38}$$

Equation (2.38) is used to approximate the right hand side of the deputy's acceleration given by Equation (2.5).

$$-\frac{\mu}{r_d^3}\boldsymbol{r}_d = -\frac{\mu}{r_d^3}\begin{bmatrix} r+x \\ y \\ z \end{bmatrix} \approx -\frac{\mu}{r^3}\left(1 - \frac{3x}{r}\right)\begin{bmatrix} r+x \\ y \\ z \end{bmatrix} \approx -\frac{\mu}{r^3}\begin{bmatrix} r-2x \\ y \\ z \end{bmatrix} \tag{2.39}$$

Using Equation (2.39), Equation (2.36) can be linearized for small separations between the chief and deputy. These equations are here called the linearized equations of relative motion (LERM).

$$\begin{aligned} \ddot{x} - 2\dot{f}\dot{y} - \left(\dot{f}^2 + 2\frac{\mu}{r^3}\right) x - \ddot{f}y = 0 \\ \ddot{y} + 2\dot{f}\dot{x} + \ddot{f}x - \left(\dot{f}^2 - \frac{\mu}{r^3}\right) y = 0 \\ \ddot{z} + \frac{\mu}{r^3} z = 0 \end{aligned} \tag{2.40}$$

The system can be described by the state vector $\boldsymbol{x} = [x\ y\ z\ \dot{x}\ \dot{y}\ \dot{z}]^\mathsf{T}$. In state-space form, the LERM are given by the following.

$$\dot{\boldsymbol{x}} = \mathbf{A}(t)\boldsymbol{x} = \begin{bmatrix} 0 & 0 & 0 & 1 & 0 & 0 \\ 0 & 0 & 0 & 0 & 1 & 0 \\ 0 & 0 & 0 & 0 & 0 & 1 \\ \left(\dot{f}^2 + 2\frac{\mu}{r^3}\right) & \ddot{f} & 0 & 0 & 2\dot{f} & 0 \\ -\ddot{f} & \left(\dot{f}^2 - \frac{\mu}{r^3}\right) & 0 & -2\dot{f} & 0 & 0 \\ 0 & 0 & -\frac{\mu}{r^3} & 0 & 0 & 0 \end{bmatrix} \boldsymbol{x} \tag{2.41}$$

The state matrix $\boldsymbol{A}(t)$ is time varying, as r, $\dot{f}$, and $\ddot{f}$ vary with time. Significantly, for elliptic orbits these quantities are all time-periodic with the orbital period, $T = P = \dfrac{2\pi}{n}$.

2.2.3 Tschauner-Hempel Equations

Solutions to Equation (2.40) can be found by first applying a coordinate scaling and a change of independent variable from time to true anomaly. The new state vector is $\tilde{\boldsymbol{x}} = [\tilde{x}\ \tilde{y}\ \tilde{z}\ \tilde{x}'\ \tilde{y}'\ \tilde{z}']^\mathsf{T}$, where primes indicate derivatives with respect to true anomaly. The coordinate scaling is given by $\tilde{x} = (1 + e\cos f)\, x$. Taking one derivative with respect to true anomaly gives $\tilde{x}' = -e\sin f x + (1 + e\cos f)\, x'$, where $x' = \dfrac{\dot{x}}{\dot{f}} = \dfrac{\dot{x}r^2}{h} = \dfrac{p^2}{h\,(1 + e\cos f)}$. Generalizing this transformation for $\tilde{y}$, $\tilde{z}$, $\tilde{y}'$, and $\tilde{z}'$ allows a transformation matrix between

$\boldsymbol{x}$ and $\tilde{\boldsymbol{x}}$ to be constructed as shown below.

$$\tilde{\boldsymbol{x}} = \boldsymbol{T}(f)\,\boldsymbol{x} \tag{2.42}$$

$$\boldsymbol{T}(f) = \begin{bmatrix} (1+e\cos f)\,\boldsymbol{I} & \boldsymbol{0} \\ -e\sin f\,\boldsymbol{I} & \frac{p^2}{h(1+e\cos f)}\boldsymbol{I} \end{bmatrix} \qquad \boldsymbol{T}^{-1}(f) = \begin{bmatrix} \frac{1}{1+e\cos f}\boldsymbol{I} & \boldsymbol{0} \\ \frac{he}{p^2}\sin f\,\boldsymbol{I} & \frac{h}{p^2}(1+e\cos f)\,\boldsymbol{I} \end{bmatrix} \tag{2.43}$$

Here, $\boldsymbol{I}$ is a three-by-three identity matrix, and $\boldsymbol{0}$ is a three-by-three null matrix. Applying the transformation given by Equation (2.42) to Equation (2.41) results in the Tschauner-Hempel (TH) equations.[7] The TH equations were first presented for relative motion by DeVries, who published an approximate solution in 1963.[8] In fact, the inplane components of these equations were known and solved by Lawden in 1954.[9] Lawden was not attempting to formulate equations for relative satellite motion, instead he was attempting to describe the primer vector for optimal spacecraft trajectory design.

$$\begin{aligned} \tilde{x}'' - 2\tilde{y}' - \frac{3}{1+e\cos f}\tilde{x} &= 0 \\ \tilde{y}'' + 2\tilde{x}' &= 0 \\ \tilde{z}'' + \tilde{z} &= 0 \end{aligned} \tag{2.44}$$

In state-space form, the TH equations are given by the following.

$$\tilde{\boldsymbol{x}}' = \mathbf{B}(f)\tilde{\boldsymbol{x}} = \begin{bmatrix} 0 & 0 & 0 & 1 & 0 & 0 \\ 0 & 0 & 0 & 0 & 1 & 0 \\ 0 & 0 & 0 & 0 & 0 & 1 \\ \frac{3}{1+e\cos f} & 0 & 0 & 0 & 2 & 0 \\ 0 & 0 & 0 & -2 & 0 & 0 \\ 0 & 0 & -1 & 0 & 0 & 0 \end{bmatrix} \boldsymbol{x} \tag{2.45}$$

Because the TH equations use true anomaly as an independent variable, it is important to note that the true anomaly is not modulo 2π (in elliptic cases) but increases monotonically with time.

The solution for the inplane states in TH equations reduces to solving a second-order, linear, nonhomogeneous, non-autonomous differential equation. The solution of this type of equation requires two homogeneous solutions and a particular solution, which were first presented by Tschauner and Hempel in 1965.[7] This solution loses its independence at $e = 0$ and is undefined for $e = 1$. Yamanaka and Ankersen presented an alternative solution and showed how a recombination of terms eliminates the singularity at $e = 0$.[10] Carter used the method of order reduction to eliminate both the singularities at $e = 0$ and $e = 1$, but this formulation is less compact than other solutions.[11] A detailed review of the solutions to the TH equations can be found in Reference [12]. The specific form below consists of six fundamental solutions. For elliptic orbits, the fundamental solutions can be arranged in a matrix $\boldsymbol{\Psi}$, and the vector of constants $\boldsymbol{k} = [k_1 \; k_2 \; k_3 \; k_4 \; k_5 \; k_6]^\mathsf{T}$ is defined.

$$\tilde{\boldsymbol{x}} = \boldsymbol{\Psi}(f)\,\boldsymbol{k} \qquad\qquad \boldsymbol{\Psi}(f) = \begin{bmatrix} \boldsymbol{\psi}_1 & \boldsymbol{\psi}_2 & \boldsymbol{\psi}_3 & \boldsymbol{\psi}_4 & \boldsymbol{\psi}_5 & \boldsymbol{\psi}_6 \end{bmatrix} \tag{2.46}$$

$$\boldsymbol{\psi}_1 = \begin{bmatrix} \sin f\,(1 + e\cos f) \\ 2\cos f - e\sin^2 f \\ 0 \\ \cos f + e\cos 2f \\ -2\sin f\,(1 + e\cos f) \\ 0 \end{bmatrix} \qquad \boldsymbol{\psi}_2 = \begin{bmatrix} \cos f\,(1 + e\cos f) \\ -2\sin f - e\sin f\cos f \\ 0 \\ -\sin f - e\sin 2f \\ e - 2\cos f\,(1 + e\cos f) \\ 0 \end{bmatrix} \tag{2.47}$$

$$\boldsymbol{\psi}_3 = \begin{bmatrix} 1 - \frac{3e}{2} K \sin f \left(1 + e \cos f\right) \\ -\frac{3}{2} K \left(1 + e \cos f\right)^2 \\ 0 \\ -\frac{3e}{2} K \left(\cos f + e \cos 2f\right) - \frac{3e \sin f}{2(1+e\cos f)} \\ 3eK \sin f \left(1 + e \cos f\right) - \frac{3}{2} \\ 0 \end{bmatrix} \qquad \boldsymbol{\psi}_4 = \begin{bmatrix} 0 \\ 1 \\ 0 \\ 0 \\ 0 \\ 0 \end{bmatrix} \tag{2.48}$$

$$\boldsymbol{\psi}_5 = \begin{bmatrix} 0 \\ 0 \\ \sin f \\ 0 \\ 0 \\ \cos f \end{bmatrix} \qquad \boldsymbol{\psi}_6 = \begin{bmatrix} 0 \\ 0 \\ \cos f \\ 0 \\ 0 \\ -\sin f \end{bmatrix} \tag{2.49}$$

For elliptic orbits, K is related to the mean anomaly through the relationship $K = M/(1 - e^2)^{3/2}$. The fundamental solutions correspond to four solutions for the in-plane motion and two solutions for the out-of-plane motion. General relative motions are composed of linear combinations of these six fundamental solutions in proportion to the constants $\boldsymbol{k}$. These constants have units of length and are geometrically related to the size of the relative-motion contributions. The constants can also be considered integrals of Equation (2.40) and can be used to describe relative motion and plan maneuvers.[13] By using Equation (2.43) and defining $\boldsymbol{x}(t_0) = \boldsymbol{x}_0$, the state-transition matrix for the original states, $\boldsymbol{x}$, can be constructed as follows.

$$\boldsymbol{k} = \boldsymbol{\Psi}^{-1}(f)\boldsymbol{T}(f)\boldsymbol{x}(t) \tag{2.50}$$

$$\boldsymbol{x}\left(t\right) = \boldsymbol{T}^{-1}\left(f\right)\boldsymbol{\Psi}\left(f\right)\boldsymbol{\Psi}^{-1}\left(f_0\right)\boldsymbol{T}\left(f_0\right)\boldsymbol{x}_0 = \boldsymbol{\Phi}_{LERM}(f, f_0)\boldsymbol{x}_0 \tag{2.51}$$

Note that time is the independent variable of the LERM, but the Tschauner-Hempel solution was used to construct the state transition matrix. Therefore, it is convenient to write the state transition matrix of the LERM, $\boldsymbol{\Phi}_{LERM}(f, f_0)$, in terms of true anomaly.

2.2.4 Hill-Clohessy-Wiltshire Equations

Clohessy and Wiltshire published one of the most frequently used equations for relative satellite motion in 1960 when studying satellite rendezvous.[14] These equations are frequently called the Hill-Clohessy-Wiltshire (HCW) equations, as Hill in 1878 was the first to linearize a set of equations to describe the motion of the moon relative to the Earth.[15] Following the traditional derivation, assuming chief eccentricity equal to zero in Equation (2.40) results in the HCW equations.

$$\begin{aligned} \ddot{x} - 2n\dot{y} - 3n^2 x &= 0 \\ \ddot{y} + 2n\dot{x} &= 0 \\ \ddot{z} + n^2 z &= 0 \end{aligned} \tag{2.52}$$

Recall, n represents the mean motion. The HCW equations in state-space form are given by the following.

$$\dot{\boldsymbol{x}} = \boldsymbol{C}\boldsymbol{x} = \begin{bmatrix} 0 & 0 & 0 & 1 & 0 & 0 \\ 0 & 0 & 0 & 0 & 1 & 0 \\ 0 & 0 & 0 & 0 & 0 & 1 \\ 3n^2 & 0 & 0 & 0 & 2n & 0 \\ 0 & 0 & 0 & -2n & 0 & 0 \\ 0 & 0 & -n^2 & 0 & 0 & 0 \end{bmatrix} \boldsymbol{x} \tag{2.53}$$

The state matrix in this case is clearly time-independent. The state matrix has two eigenvalues equal to zero that share a single independent eigenvector, and two pairs of imaginary eigenvalues both equal to $\pm in$ which have four independent eigenvectors. The state matrix

can be decomposed as shown below.

$$\boldsymbol{C} = \boldsymbol{M}\boldsymbol{J}\boldsymbol{M}^{-1} \tag{2.54}$$

$$\boldsymbol{J} = \begin{bmatrix} 0 & 1 & 0 & 0 & 0 & 0 \\ 0 & 0 & 0 & 0 & 0 & 0 \\ 0 & 0 & 0 & -n & 0 & 0 \\ 0 & 0 & n & 0 & 0 & 0 \\ 0 & 0 & 0 & 0 & 0 & -n \\ 0 & 0 & 0 & 0 & n & 0 \end{bmatrix} \quad ; \quad \boldsymbol{M} = \begin{bmatrix} 0 & -\frac{2}{n} & 0 & 2 & 0 & 0 \\ 3 & 3 & 4 & 0 & 0 & 0 \\ 0 & 0 & 0 & 0 & -1 & 0 \\ 0 & 0 & 2n & 0 & 0 & 0 \\ 0 & 3 & 0 & -4n & 0 & 0 \\ 0 & 0 & 0 & 0 & 0 & n \end{bmatrix} \tag{2.55}$$

This decomposition is similar to the Jordan canonical form but instead of having the imaginary eigenvalues on the diagonal in $\boldsymbol{J}$, the imaginary magnitudes are placed in blocks on the diagonal. Associated with this, the imaginary and real parts of the eigenvectors appear separately in $\boldsymbol{M}$. Note that the magnitude of each of the eigenvectors that make up $\boldsymbol{M}$ is arbitrary. However, the particular values chosen for $\boldsymbol{M}$ in Equation (2.55) will become important in later sections.

Using this decomposition, a canonical form of the HCW equations is given by the following.

$$\boldsymbol{w} = \boldsymbol{M}^{-1}\boldsymbol{x} \quad ; \qquad \dot{\boldsymbol{w}} = \boldsymbol{J}\boldsymbol{w} \tag{2.56}$$

This canonical form decomposes the system into three independent second-order subsystems. These subsystems are clearly related to a drifting in-plane (x and y directions) motion, a periodic in-plane motion, and a periodic out-of-plane (z direction) motion.

Given an initial condition $\boldsymbol{x}_0$ at time t_0, the HCW solution at time t can be expressed as $\boldsymbol{x}(t) = e^{\boldsymbol{C}(t-t_0)}\boldsymbol{x}_0 = \boldsymbol{\Phi}_{HCW}(t, t_0)\boldsymbol{x}_0$. The solution of Equation (2.52) is given by the following.[16]

$$\mathbf{\Phi}_{HCW}(t,t_0) = \begin{bmatrix} 4-3\cos\left(n(t-t_0)\right) & 0 & 0 \\ 6\left(\sin\left(n(t-t_0)\right)-n(t-t_0)\right) & 1 & 0 \\ 0 & 0 & \cos\left(n(t-t_0)\right) \\ 3n\sin\left(n(t-t_0)\right) & 0 & 0 \\ 6n\left(\cos\left(n(t-t_0)\right)-1\right) & 0 & 0 \\ 0 & 0 & -n\sin\left(n(t-t_0)\right) \end{bmatrix}$$

$$\begin{bmatrix} \frac{1}{n}\sin\left(n(t-t_0)\right) & \frac{2}{n}\left(1-\cos\left(n(t-t_0)\right)\right) & 0 \\ \frac{2}{n}\left(\cos\left(n(t-t_0)\right)-1\right) & \frac{1}{n}\left(4\sin\left(n(t-t_0)\right)-3n(t-t_0)\right) & 0 \\ 0 & 0 & \frac{1}{n}\sin\left(n(t-t_0)\right) \\ \cos\left(n(t-t_0)\right) & 2\sin\left(n(t-t_0)\right) & 0 \\ -2\sin\left(n(t-t_0)\right) & 4\cos\left(n(t-t_0)\right)-3 & 0 \\ 0 & 0 & \cos\left(n(t-t_0)\right) \end{bmatrix} \tag{2.57}$$

Approaches exist in the literature using the HCW equations as the basis for maneuver planning, see e.g. References [4, 17, 18, 19, 20, 21]. London extended the HCW equations for larger separation between the chief and deputy satellites in 1963.[22] Like the HCW equations, London's equations still assume a circular orbit, but the relative distance terms are retained to the second order. The solution of these equations is found through the method of successive approximations and includes secular and mixed-secular terms.

2.2.5 Geometric Parameterization of the HCW Equations

An advantage of the HCW equations is the geometric insight into the solutions. Lovell and Tragesser found a geometric parametrization of the HCW equations called relative-orbit elements (ROEs).[18] The ROEs allow relative motion described by the HCW equations to be described by geometric parameters similar to the concept of orbital elements for Keplerian

motion, which were discussed in Section 2.2.5. Lovell et al. have investigated using ROEs to extend the HCW equations to elliptic orbits and also for continuous-thrust maneuvering.[23,24,25] The transformations between ROEs and Cartesian coordinates are given by the following.

$$
\begin{aligned}
a_e &= 2\sqrt{\left(\frac{\dot{x}}{n}\right)^2 + \left(3x + 2\frac{\dot{y}}{n}\right)^2} & x &= -\frac{a_e}{2}\cos\beta + x_d \\
x_d &= 4x + 2\frac{\dot{y}}{n} & y &= a_e \sin\beta + y_d \\
y_d &= y - 2\frac{\dot{x}}{n} & z &= z_{\max}\sin\psi \\
\beta &= \tan^{-1}\left(\frac{\dot{x}}{3nx + 2\dot{y}}\right) & \dot{x} &= \frac{a_e}{2} n \sin\beta \\
z_{\max} &= \sqrt{\left(\frac{\dot{z}}{n}\right)^2 + z^2} & \dot{y} &= a_e n\cos\beta - \frac{3}{2} n x_d \\
\psi &= \tan^{-1}\left(\frac{nz}{\dot{z}}\right) & \dot{z} &= z_{\max} n \cos\psi
\end{aligned}
\tag{2.58}
$$

Here, the inverse tangent function is assumed to return a value between zero and 2π. An advantage of the ROEs is their simple behavior with respect to time. This behavior can be seen by substituting Equation (2.57) into Equation (2.58).

$$
\begin{aligned}
a_e &= a_{e0} \\
x_d &= x_{d0} \\
y_d &= y_{d0} - \frac{3}{2} n x_d t \\
\beta &= \beta_0 + nt \pmod{2\pi} \\
z_{\max} &= z_{\max 0} \\
\psi &= \psi_0 + nt \pmod{2\pi}
\end{aligned}
\tag{2.59}
$$

Combined, Equations (2.58) and (2.59) describe both the inplane and out-of-plane relative motion. As shown in Figure 2.8, the inplane motion traces an ellipse that has a semimajor axis a_e in the y direction, a semiminor axis $a_e/2$ in the x direction, centered at (x_d, y_d), and

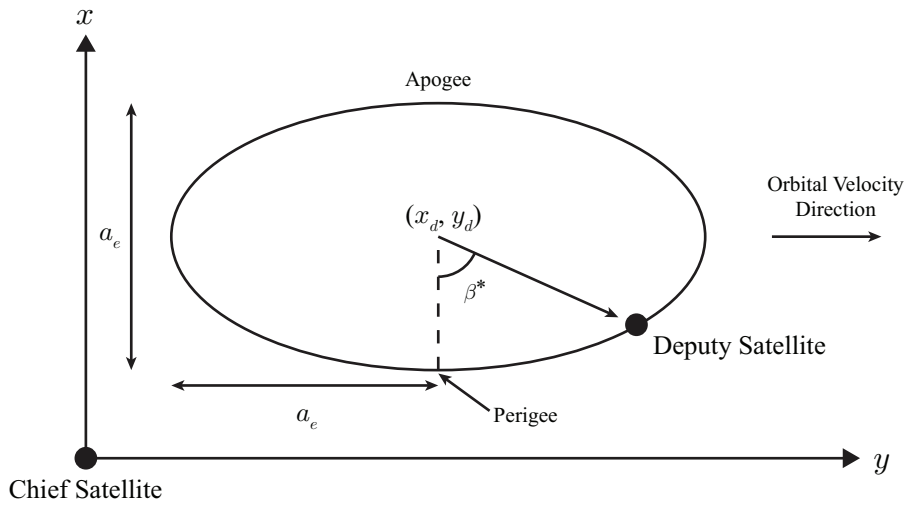

Figure 2.8: In-plane relative-orbit elements.

possibly drifts in the y direction. The out-of-plane motion oscillates about $z = 0$ with an amplitude $z_{\max}$. Note that β^* shown in Figure 2.8 is related to β through $\tan(\beta) = 2\tan(\beta^*)$, and both angles are always in the same quadrant. In fact, β is equal to the deputy's mean anomaly.

2.2.6 Summary of Cartesian Linearized Relative-Motion Representations

The previous sections presented three linearized descriptions of relative motion: the LERM, the TH equations, and the HCW equations. To summarize, the LERM are linear time-varying equations of motion which can describe the motion of a deputy satellite relative to a chief of any eccentricity. The assumptions used to derive the LERM was a chief and deputy satellite in close proximity, and both satellites obeying Keplerian motion. If an assumption is made that the chief is circular, the LERM reduce to the linear time-invariant HCW equations. Due to their simplicity, many solutions in the literature utilize the HCW equations. Applying a scaling and change of independent variable to the LERM results in the TH equations. The TH equations allow a state transition matrix of the LERM to be constructed.

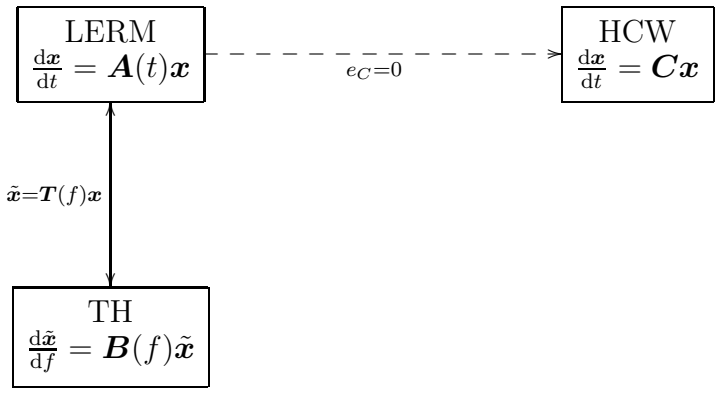

Figure 2.9: Different Representations of Relative Motion Equations

The relationships between the LERM, TH equations, and HCW equations are shown in Figure 2.9. Starting with the LERM, the assumption that the chief satellite is in a circular orbit is shown by a dashed line. One goal of this dissertation is to replace this assumption with a coordinate transformation. Note that the LERM and HCW equations share the same state vector. From the LERM, the transformation leading to the TH equations is shown by a solid line. Although an exact transformation exists, the state vector is now $\tilde{\boldsymbol{x}}$. The following chapter discusses two approximate methods for applying the HCW equations to elliptic orbits. These methods result in time-varying equations of motion, but as will be seen, are lower fidelity than the LERM.

2.2.7 Additional Relative-Motion Representations

The relative motion models presented above are not exclusive. A linearized set of equations similar to the TH equations was developed by Brumberg and later expanded on by Kelly.[26,27] The Brumberg-Kelly equations differ from the TH equations in that the independent variable is not transformed from time to true anomaly and that non-orthogonal coordinate axes are used. Kelly provides a state transition matrix in terms of time and eccentric anomaly, which reduces to a form similar to the HCW equations for circular orbits. However, these equations are not as compact as the TH equations and suffer from singularity issues. Representations for relative motion can also be performed with respect to various

parameter sets which are associated with an orbit. An element set defined using inclination and eccentricity vectors are attractive for defining the orbit of geostationary satellites and insuring safe collocation.[28] Jones used this element set to describe rendezvous in circular orbits, while D'Amico and Montenbruck also used these vectors to describe relative motion and presented a case study for the TerraSAR-X/TanDEM-X formation.[29,30] The relative motion can also be described through orbit element differences. In this method, the difference between any two complete sets of orbit elements can be determined. Using orbit element differences, the parameterization of the relative motion at any instant of time can be determined by solving Kepler's equation instead of a differential equation.[31,32]

2.2.8 Calculation of Initial Conditions

Propagation of any of the equations of motion discussed in this section requires a set of initial conditions for the relative motion. The position and velocity of the deputy relative to the chief are related to the inertial position and velocity of each satellite through the following kinematic relationships.

$$\begin{aligned} [\boldsymbol{\rho}]_C &= [\boldsymbol{R}]\left([\boldsymbol{r}_D]_I - [\boldsymbol{r}_C]_I\right) \\ [\dot{\boldsymbol{\rho}}]_C &= [\boldsymbol{R}]\left([\boldsymbol{v}_D]_I - [\boldsymbol{v}_C]_I\right) - [\boldsymbol{\Omega}]_C\,[\boldsymbol{\rho}]_C \end{aligned} \tag{2.60}$$

Here, inertial position vectors of the chief and deputy satellites are given by $\boldsymbol{r}_C$ and $\boldsymbol{r}_D$ respectively. The inertial velocities of the chief and deputy with respect an inertial frame are $\boldsymbol{v}_C$ and $\boldsymbol{v}_D$. The skew-symmetric matrix of the angular velocity of the chief's LVLH frame is given by $[\boldsymbol{\Omega}]$, and the rotation matrix from inertial into the chief's LVLH frame is given by $[\boldsymbol{R}]$. The matrix operator $[\,]_I$ indicates coordinatization in an inertial frame, and $[\,]_C$ indicates coordinatization in the chief's LVLH frame. In this dissertation, initial conditions for the chief and deputy will be specified using orbital elements. Orbital elements can be transformed into inertial position and velocity vectors (see, e.g. Reference [31] §9.6.2), and using Equation (2.60), the relative position and velocity are calculated. As an example,

consider a chief satellite orbiting the Earth with the following orbital elements: $a_C = 8000$ km, $e_C = 0.1$, and $i_C = \Omega_C = \omega_C = f_C = 0$. Additionally, a deputy satellite is specified in close proximity with the orbital elements: $a_D = 8000$ km, $e_D = 0.10001$, and $i_D = \Omega_D = \omega_D = f_D = 0$. For this case, $\boldsymbol{\rho} = [-0.080000\ 0\ 0]^{\mathsf{T}}$ km and $\dot{\boldsymbol{\rho}} = [0\ 0.0001655329\ 0]^{\mathsf{T}}$ km/s.

The concept of calculating initial conditions will be revisited later in this dissertation. Specifically, Section 3.1 develops a virtual-chief method which propagates the motion in a coordinate frame which is more consistent with the assumptions of the HCW equations. Later, Section 5.1.3 compares the LERM to the HCW equations showing how the computed Lyapunov-Floquet transformations completely capture the dynamics, while in Section 5.3.2, the Lyapunov-Floquet transformations are used to select initial conditions which allows the underlying HCW equations to approximate the LERM solution.

Chapter 3

Preliminary Investigations*

The assumptions made in deriving the HCW equations were a chief satellite in a circular orbit, a deputy satellite in close proximity to the chief, and both satellites obeying Keplerian motion. The assumption of a chief satellite with zero eccentricity is rarely achieved in practice. As the chief's eccentricity increases, the HCW equations become less accurate. Alternative models exist in the literature, such as the LERM and TH equations discussed in the previous chapter, which are valid for arbitrary values of chief eccentricity. However, the analytical solutions of these alternative equations can be less intuitive to understand than the solutions of the HCW equations.

This chapter presents two investigations into applying the HCW equations to elliptic chiefs. The Virtual-Chief (VC) model propagates the relative motion in a frame more consistent with the assumptions of the HCW equations. The Virtual-Time (VT) method evaluates the HCW equations at a virtual time to account for the time-varying effects of eccentric orbital motion. Both of these methods define (somewhat ad hoc) transformations to the HCW solutions, and essentially construct approximate linear time-varying models for the relative motion. A comparison of both methods is presented in Section 3.3.

*Material in this chapter taken from the following papers:

[33] R. E. Sherrill, A. J. Sinclair, T. A. Lovell, K. W. Johnson, and D. D. Decker, "The Virtual-Chief Method for Modeling Relative Motion of Noncircular Satellites," *AAS 11-214*, presented at the 21st AAS/AIAA Space Flight Mechanics Meeting, New Orleans, Louisiana, 2011.

[34] R. E. Sherrill, A. J. Sinclair, and T. A. Lovell, "A Virtual-Time Method for Modeling Relative Motion of Noncircular Satellites," *AAS 11-208*, presented at the 21st AAS/AIAA Space Flight Mechanics Meeting, New Orleans, Louisiana, 2011.

3.1 Virtual-Chief Method

In the virtual-chief (VC) method, a fictional satellite with zero eccentricity is used as the chief satellite for the HCW equations, with both the actual chief and deputy satellites treated as deputies. This virtual chief satellite is a circularized version of the actual chief satellite, and is defined by setting its eccentricity to zero, and all other orbital element values equal to those of the chief.[23]

$$\begin{aligned} a_{VC} &= a_C \\ e_{VC} &= 0 \\ i_{VC} &= i_C \\ \Omega_{VC} &= \Omega_C \\ \omega_{VC} &= \omega_C \\ f_{VC} &= M_{VC} = M_C \end{aligned} \tag{3.1}$$

Here, a subscript VC refers to the virtual chief satellite. The above definitions for ω_{VC} and f_{VC} are somewhat arbitrary, because the virtual chief's orbit is circular. Note that the virtual chief's LVLH frame has constant angular velocity, unlike the chief's LVLH frame. The three satellites are illustrated in Figure 3.1a.

The VC method can also be called a dual-deputy approach, as both the real chief and deputy satellites are treated as deputies to the virtual chief. Because the circular orbit of the virtual chief has been defined, the motion of both the chief and deputy relative to the virtual chief can be described using the HCW equations without violating the circularity assumption. The motion of the deputy relative to the real chief is the difference of these solutions.

However, the HCW equations do not need to be propagated twice in order to use the VC method. Since the HCW equations are linear, the difference of two solutions is also a solution to the equations. The state vector for the VC method is defined by $\boldsymbol{u} = [\,[\boldsymbol{\rho}]_{VC}^{\mathsf{T}}\ [\mathring{\boldsymbol{\rho}}]_{VC}^{\mathsf{T}}\,]^{\mathsf{T}}$, where $[\,]_{VC}$ indicates coordinatization in the virtual chief's frame, and $(\mathring{})$ indicates vector differentiation with respect to the virtual chief's frame. The VC solution is propagated using

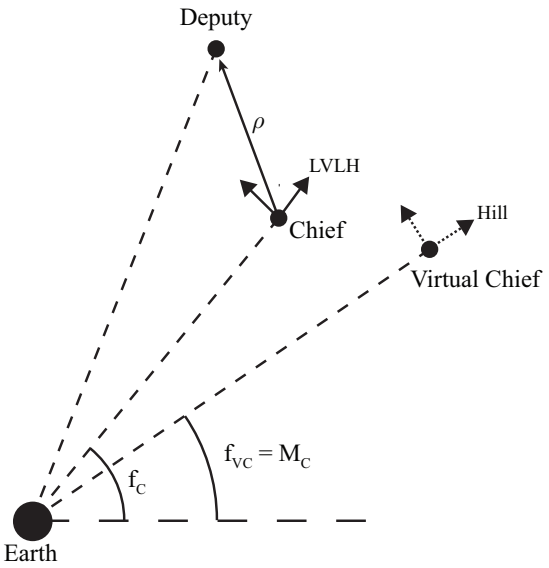

(a) Coordinate transformation between virtual-chief and chief frames.

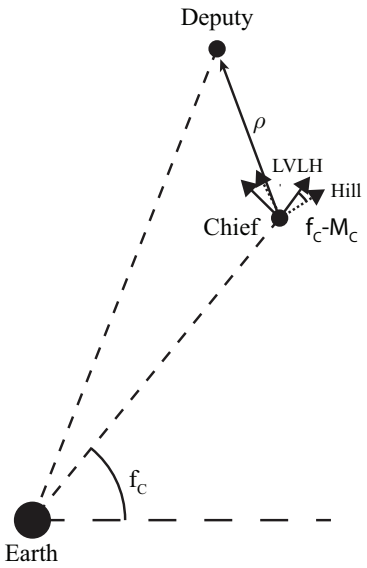

(b) Virtual-chief, chief, and deputy satellites.

Figure 3.1: Virtual-Chief Method

the HCW equations.

$$\boldsymbol{u}(t) = e^{\boldsymbol{C}t}\boldsymbol{u}_0 \tag{3.2}$$

Since the relative motion is propagated in the virtual chief's frame, a coordinate transformation is necessary to convert the solution into the actual chief's frame. For the position components, this coordinate transformation is a rotation in the chief's orbital plane by the difference between the chief's mean anomaly and the chief's true anomaly, $f_C - M_C$. Notice that only the in-plane motion is transformed since the chief and virtual chief are coplanar. For the velocity components, the angular velocity of the virtual chief's frame relative to the chief's frame is given by $\omega_1 = \omega_2 = 0$, and $\omega_3 = n - \dot{f}_C$ (components are identical in the chief's and virtual chief's frame). Given an initial condition, the VC solution $\boldsymbol{x}_{VC} = \boldsymbol{P}_{VC}\boldsymbol{u}$

is given by the following.

$$\boldsymbol{R}(t) = \begin{bmatrix} \cos(f_C - M_C) & \sin(f_C - M_C) & 0 \\ -\sin(f_C - M_C) & \cos(f_C - M_C) & 0 \\ 0 & 0 & 1 \end{bmatrix} \quad ; \quad \boldsymbol{\Omega}_{VC/C}(t) = \begin{bmatrix} 0 & \dot{f}_C - n & 0 \\ n - \dot{f}_C & 0 & 0 \\ 0 & 0 & 0 \end{bmatrix} \tag{3.3}$$

$$\boldsymbol{P}_{VC}^{-1}(t) = \begin{bmatrix} \boldsymbol{R}(t)^{\mathsf{T}} & \boldsymbol{0} \\ -\boldsymbol{\Omega}_{VC/C}(t)\boldsymbol{R}(t)^{\mathsf{T}} & \boldsymbol{R}(t)^{\mathsf{T}} \end{bmatrix} \tag{3.4}$$

$$\boldsymbol{x}_{VC} = \boldsymbol{P}_{VC}(t) e^{\boldsymbol{C}(t-t_0)} \boldsymbol{P}_{VC}^{-1}(t_0) \boldsymbol{x}_0 \tag{3.5}$$

Note that evaluating the VC solution does not require propagating the virtual chief's position, and only requires knowledge of the orientation of the virtual chief's frame. This suggests an alternative perspective for the VC method. The VC method can be thought of as propagating the relative motion in a constant-angular-velocity frame attached to the chief, labeled in Figure 3.1b as the Hill frame, which is more consistent with the HCW assumptions.

In Reference 23, a set of governing equations for the VC method were presented. These equations are linear time-periodic differential equations. Equations (3.2-3.5) are a solution of those equations by Lyapunov-Floquet transformation (see e.g. References 35 and 36). The VC method applies a time-varying coordinate transformation to the solution of time-invariant ordinary differential equations. As will be seen, however, the VC equations are lower fidelity than the LERM. The next section describes the virtual-time method, which is another method for extending the HCW equations to eccentric chiefs.

3.2 Virtual-Time Method

Consider a chief and deputy satellite orbiting the Earth, sharing the following orbital elements of $a = 11,000$ km and $i = \Omega = \omega = 0$. Both satellites are initially at perigee. Figure 3.2 shows the NERM trajectory for a range of chief eccentricities, but in each case,

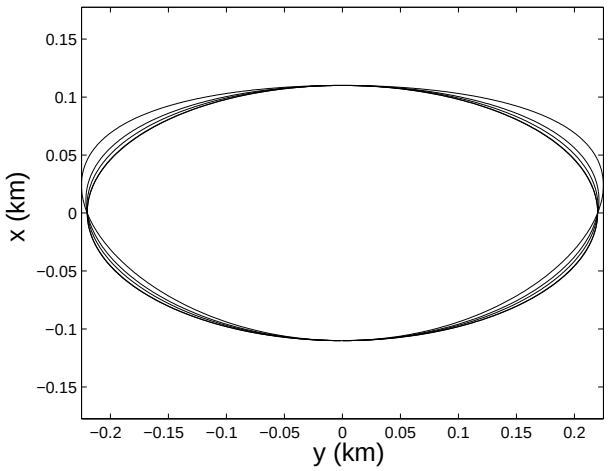

Figure 3.2: NERM trajectories for chief eccentricities of 0, 0.01, 0.1, 0.2, and 0.4.

the chief and deputy eccentricities are related by $e_D = e_C + 10^{-5}$. In these cases, the trajectory shapes display only minor displacement from a 2×1 ellipse.

In the above example it was seen that even for moderate chief eccentricity, the shape of the relative-motion trajectory is similar to the trajectory shape predicted by the HCW equations. This suggests that in some cases the error in applying the HCW equations to noncircular chiefs has largely to do with the motion along the trajectory, instead of the shape of the trajectory. This motivates an approach to describe the relative-motion state at time t, by evaluating the HCW solution at some virtual time τ. Define a state vector $\boldsymbol{w} = [\,[\boldsymbol{\rho}]_C^{\mathsf{T}}\ \boldsymbol{\nu}^{\mathsf{T}}\,]^{\mathsf{T}}$ consisting of the virtual-time (VT) solution for the relative position, $\boldsymbol{\rho}$, and a set of velocity-like variables, $\boldsymbol{\nu}$.

$$\boldsymbol{w}(t) = e^{\boldsymbol{C}(\tau(t)-t_0)}\boldsymbol{x}_0 \tag{3.6}$$

This solution can be evaluated at t_0, and $\boldsymbol{x}_0$ can be eliminated.

$$\boldsymbol{w}(t) = e^{\boldsymbol{C}(\tau(t)-\tau(t_0))}\boldsymbol{w}_0 \tag{3.7}$$

This VT solution for $\boldsymbol{w}$ passes through the same points in state space as the HCW solution for $\boldsymbol{x}$, and the trajectory shape for the VT solution is identical to the HCW solution. However, in the VT approach, each point along the trajectory is reached at a different time than in the HCW solution.

Solving for the virtual time $\tau(t)$ as a function of the true time can be posed as an optimization problem over an interval $0 < t < T$. The error in the virtual-time solution is defined as the difference from the NERM solution.

$$\begin{aligned} J &= \int_0^T \left(\boldsymbol{\rho}_V(t) - \boldsymbol{\rho}_N(t)\right)^{\mathsf{T}} \left(\boldsymbol{\rho}_V(t) - \boldsymbol{\rho}_N(t)\right) \mathrm{d}t \\ &= \int_0^T \left(\boldsymbol{\rho}_H(\tau(t)) - \boldsymbol{\rho}_N(t)\right)^{\mathsf{T}} \left(\boldsymbol{\rho}_H(\tau(t)) - \boldsymbol{\rho}_N(t)\right) \mathrm{d}t \end{aligned} \tag{3.8}$$

Here, the chosen objective function focuses on the relative positions from the virtual-time solution, $\boldsymbol{\rho}_V$, and the NERM solution, $\boldsymbol{\rho}_N$. The value of $\tau(t)$ that minimizes Equation (3.8) is the optimal virtual time and will be denoted τ^*.

This optimization problem can be solved numerically by an exhaustive search comparing the NERM and HCW solution at discrete time steps. Returning to the example motions shown in Figure 3.2, the optimal solution for the virtual time in each case is shown in Figure 3.3, with a time step of 15 seconds. For small chief eccentricities, τ^* is approximately equal to t; but as the chief eccentricity increases, τ^* begins to depart significantly from t.

In each plot of Figure 3.3, two heuristic values of the virtual time are also shown. In these examples, the optimal virtual time is larger than the true time as the chief travels from periapse to apoapse, and the optimal virtual time is smaller than the true time as the chief travels from apoapse to periapse. This is the same behavior that eccentric anomaly and true anomaly exhibit relative to the mean anomaly. This motivates two heuristic values for the virtual time, τ_E and τ_f, that are related to the eccentric anomaly and true anomaly, respectively.

$$n\left(t + t_p\right) = n\tau_E - e_C \sin n\tau_E \tag{3.9}$$

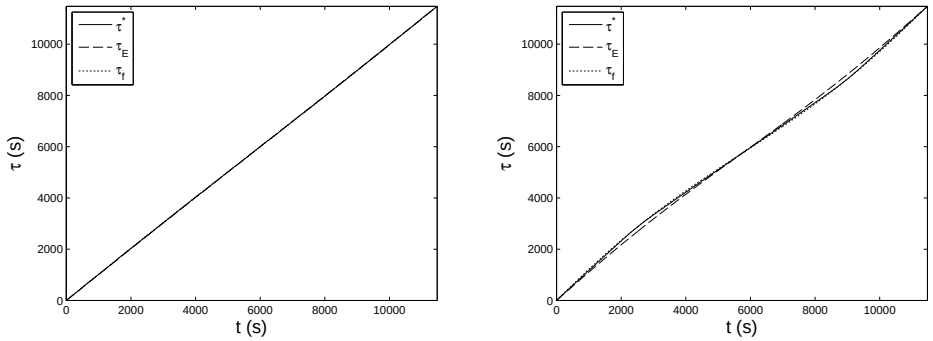

(a) $e_C = 0.01$ (b) $e_C = 0.1$

(c) $e_C = 0.2$ (d) $e_C = 0.4$

Figure 3.3: Solutions for the virtual time for several chief eccentricities.

$$\tan\frac{n\tau_f}{2} = \sqrt{\frac{1+e_C}{1-e_C}}\tan\frac{n\tau_E}{2} \tag{3.10}$$

Here, t_p is the amount of time at $t = 0$ since the chief's last periapse passage. If $t = 0$ occurs at the chief's periapse, then at $t = 0$ all three solutions for the virtual time equal zero: $\tau(0) = 0$. But this is not true for general initial locations, and in general $\boldsymbol{w}_0 \neq \boldsymbol{x}_0$. Solving for τ_E (or τ_f) at a particular instant t requires numerical solution of Equation (3.9). For completeness, the derivatives of τ_E and τ_f can be also be calculated.

$$\dot{\tau}_E = \frac{1}{1 - e_C\cos n\tau_E} \tag{3.11}$$

The derivative of τ_f is calculated by analogy with the true anomaly.[37]

$$\dot{\tau}_f = \frac{(1 + e_C\cos f)^2}{(1-e_C)^{3/2}} \tag{3.12}$$

For the examples shown in Figure 3.3, τ_f is a good approximation of the optimal virtual time, particularly at low chief eccentricities, and will be used to approximate the virtual time in the following subsection.

It is possible to investigate a set of governing equations that admit the VT solution, by differentiating Equation (3.7) with respect to time.

$$\dot{\boldsymbol{w}} = \boldsymbol{C}\dot{\tau}e^{\boldsymbol{C}(\tau(t)-\tau(0))}\boldsymbol{w}_0 = \dot{\tau}\boldsymbol{C}\boldsymbol{w} \tag{3.13}$$

The first three of these equations relate the velocity-like variables $\boldsymbol{\nu}$ to the VT solution for the relative velocity.

$$[\dot{\boldsymbol{\rho}}]_C = \dot{\tau}\boldsymbol{\nu} \tag{3.14}$$

These equations are a linear time-varying system where the state matrix varies with respect to time in a very specific manner: the time-varying state matrix is equal to a time-invariant matrix multiplied by a time-varying scalar. These equations can be compared to higher-fidelity linearized time-varying models where the state matrix varies with respect to time in more complicated manners, see References 10 and 38.

The kinematics in Equation (3.14) can be further analyzed.

$$\boldsymbol{\nu} = \frac{1}{\dot{\tau}}[\dot{\boldsymbol{\rho}}]_C \qquad\qquad \dot{\boldsymbol{\nu}} = \frac{1}{\dot{\tau}}[\ddot{\boldsymbol{\rho}}]_C - \frac{\ddot{\tau}}{\dot{\tau}^2}[\dot{\boldsymbol{\rho}}]_C \tag{3.15}$$

Substituting these relations into Equation (3.13) gives the virtual-time equations in second order form.

$$\begin{aligned} \ddot{x} - \frac{\ddot{\tau}}{\dot{\tau}}\dot{x} - 2n\dot{\tau}\dot{y} - 3n^2\dot{\tau}^2 x = 0 \\ \ddot{y} + 2n\dot{\tau}\dot{x} - \frac{\ddot{\tau}}{\dot{\tau}}\dot{y} = 0 \\ \ddot{z} - \frac{\ddot{\tau}}{\dot{\tau}}\dot{z} + n^2\dot{\tau}^2 z = 0 \end{aligned} \tag{3.16}$$

Finally, the scalar form of the VT solution for the relative position can be written by evaluating Equation (2.57) at the virtual time and taking into account Equation (3.15). For compactness, $\tau_{t-0} \equiv \tau(t) - \tau(0)$ and $\dot{\tau}_0 \equiv \dot{\tau}(0)$ are defined.

$$
\begin{aligned}
x(t) &= (4 - 3\cos n\tau_{t-0})\, x_0 + \frac{\sin n\tau_{t-0}}{n\dot{\tau}_0}\dot{x}_0 + \frac{2}{n\dot{\tau}_0}(1 - \cos n\tau_{t-0})\, \dot{y}_0 \\
y(t) &= 6(\sin n\tau_{t-0} - n\tau_{t-0})\, x_0 + y_0 + \frac{2}{n\dot{\tau}_0}(\cos n\tau_{t-0} - 1)\, \dot{x}_0 + \frac{1}{n\dot{\tau}_0}(4\sin n\tau_{t-0} - 3n\tau_{t-0})\, \dot{y}_0 \\
z(t) &= \cos n\tau_{t-0}\ z_0 + \frac{\sin n\tau_{t-0}}{n\dot{\tau}_0}\dot{z}_0
\end{aligned}
\tag{3.17}
$$

Equation (3.17) shows that by construction, the solutions of the linear time-varying system in Equation (3.16) have the same shapes as the linear time-invariant HCW equations but pass through these points at different times.

3.3 Results and Discussion

To evaluate the performance of the virtual-chief and the virtual-time approaches relative to the HCW equations and the LERM, the motion of each method can be compared to the NERM. Here, initial conditions for the chief and deputy will be specified in terms of orbital elements. These orbital elements are transformed into the true initial conditions, $\boldsymbol{x}_0$, using Equation (2.60). These initial conditions were used for the NERM, the LERM, and the HCW equations. Recall that the VC method applies a coordinate transformation to the initial conditions before propagating the motion with the HCW equations: $\boldsymbol{u}_0 = \boldsymbol{P}_{VC}^{-1}(t_0)\boldsymbol{x}_0$. Here, the VT method will be evaluated using the same initial conditions: $\boldsymbol{w}_0 = e^{\boldsymbol{C}(\tau(t_0)-t_0)}\boldsymbol{P}_{VC}^{-1}(t_0)\boldsymbol{x}_0$

For each solution, the motion is propagated for one complete revolution of the chief's orbit and at each time step, the position-error magnitude is computed. The root-mean-square

Case	a_C (km)	e_C	a_D (km)	e_D	ω_D (rad)
1	11,000	0.1	11,000	0.10001	0
2	11,000	0.4	11,000	0.40001	0
3	11,000	0.1	11,000.2	0.10001	0
4	11,000	0.4	11,000.2	0.40001	0
5	11,000	0.1	11,000	0.10001	2×10^{-5}
6	11,000	0.4	11,000	0.40001	2×10^{-5}

Table 3.1: Initial conditions for inplane test cases.

(RMS) of these errors, ϵ, is given by the following.

$$\epsilon_{RMS} = \sqrt{\frac{1}{m}\sum_{l=1}^{m}(\boldsymbol{\rho}_l - \boldsymbol{\rho}_{N,l})^T(\boldsymbol{\rho}_l - \boldsymbol{\rho}_{N,l})} \tag{3.18}$$

Here, $\boldsymbol{\rho}_l$ indicates the position vector at the lth time step obtained by propagating the LERM, HCW, VC, or VT method, $\boldsymbol{\rho}_{N,l}$ indicates the position vector at the lth time step obtained by propagating the NERM, and m represents the total number of time-steps in each solution.

Six cases in particular were chosen to compare the performance of the LERM, HCW, VC, and VT methods. Table 3.1 gives the chief and deputy orbital elements for each case. Orbital elements not listed are set to zero. The RMS error was calculated for each case and is presented in Table 3.2. The RMS error indicates that both the VC and VT methods had considerably less error that the HCW solution for every case. For every case except cases 3 and 4, the VT method has less error than the VC method, although the improvement was not as significant as VC compared to HCW. For all cases, the LERM offered four orders of magnitude or more greater accuracy.

The methods in this chapter selected transformations the the HCW equations which defined new approximate linear time-varying models. Whereas these models provide some accuracy improvement to the HCW equations, they are still lower fidelity than the LERM.

Case	HCW Error (km)	VC Error (km)	VT Error (km)	LERM Error (km)
1	0.4714	0.1625	0.1581	1.0460×10^{-5}
2	3.2406	1.1377	1.0906	4.2539×10^{-5}
3	0.4409	0.2559	0.2588	8.5585×10^{-5}
4	0.8417	0.6887	0.6959	1.2905×10^{-4}
5	0.4893	0.1294	0.1270	5.8095×10^{-5}
6	3.3216	0.9411	0.8679	7.7002×10^{-5}

Table 3.2: RMS error distances for inplane test cases.

Therefore, Chapter 5 will investigate the opposite approach. Instead of defining a linear time-varying model by selecting a transformation, the transformation will be directly calculated by choosing the desired linear time-varying model.

Chapter 4

Lyapunov-Floquet Theory

In 1883, Floquet published a theory on the solutions of linear systems with periodic coefficients.[39] Floquet theory showed that once a fundamental solution to a linear periodic system over the principal period T has been found, it can be extended to all time. Additionally, the solution at some time $T + t$ is given by the product of the solution at time T and the solution at time t. In 1949, Lyapunov extended Floquet's work by developing a transformation that converts a linear periodic system to a time-invariant form.

4.1 Floquet Theorem

Consider a linear time-periodic system of the form, $\dot{\boldsymbol{x}} = \boldsymbol{A}(t)\boldsymbol{x}$, where $\boldsymbol{A}(t)$ is T periodic such that $\boldsymbol{A}(t+T) = \boldsymbol{A}(t)$. Let $\boldsymbol{\Phi}(t, t_0)$ be the state-transition matrix for the system. Because of the time periodicity of the system, clearly $\boldsymbol{\Phi}(t, t_0) = \boldsymbol{\Phi}(t+T, t_0+T)$. Additionally, if one considers the mapping from t_0 to some time $t+T$, the state-transition matrix can be broken up arbitrarily.

$$\boldsymbol{\Phi}\left(t+T, t_0\right) = \boldsymbol{\Phi}\left(t+T, t_0+T\right)\boldsymbol{\Phi}\left(t_0+T, t_0\right) = \boldsymbol{\Phi}\left(t, t_0\right)\boldsymbol{\Phi}\left(t_0+T, t_0\right) \tag{4.1}$$

The constant matrix $\boldsymbol{\Phi}(t_0 + T, t_0)$ is often referred to as the discrete transition matrix, monodromy matrix, or the Floquet transition matrix. It is convenient to write this matrix as follows.

$$\boldsymbol{\Phi}(t_0 + T, t_0) = \boldsymbol{P}_0 e^{\boldsymbol{\Lambda} T}\boldsymbol{P}_0^{-1} \tag{4.2}$$

Here, $\boldsymbol{\Lambda}$ is a constant matrix, and $\boldsymbol{P}_0$ is also a constant, nonsingular matrix. Equation (4.1) can now be rewritten using Equation (4.2).

$$\boldsymbol{\Phi}\left(t+T,t_0\right)=\boldsymbol{\Phi}\left(t,t_0\right)\boldsymbol{P}_0 e^{\boldsymbol{\Lambda}T}\boldsymbol{P}_0^{-1} \tag{4.3}$$

Next, define $\boldsymbol{P}(t)$ as follows.

$$\boldsymbol{P}(t)=\boldsymbol{\Phi}(t,t_0)\boldsymbol{P}_0 e^{-\boldsymbol{\Lambda}(t-t_0)} \tag{4.4}$$

Evaluating Equation (4.4) at t_0 gives $\boldsymbol{P}(t_0)=\boldsymbol{P}_0$. Using Eqs. (4.1) and (4.2), $\boldsymbol{P}(t)$ is seen to be T periodic.

$$\begin{aligned}\boldsymbol{P}(t+T)&=\boldsymbol{\Phi}(t+T,t_0)\boldsymbol{P}_0 e^{-\boldsymbol{\Lambda}(t+T-t_0)}\\&=\boldsymbol{\Phi}(t,t_0)\boldsymbol{P}_0 e^{\boldsymbol{\Lambda}T}\boldsymbol{P}_0^{-1}\boldsymbol{P}_0 e^{-\boldsymbol{\Lambda}T}e^{-\boldsymbol{\Lambda}(t-t_0)}\\&=\boldsymbol{\Phi}(t,t_0)\boldsymbol{P}_0 e^{-\boldsymbol{\Lambda}(t-t_0)}\\&=\boldsymbol{P}(t)\end{aligned} \tag{4.5}$$

Since $\boldsymbol{\Phi}(t,t_0)$ is nonsingular by definition, $\boldsymbol{P}(t)$ is also nonsingular.[40] Therefore, inverting Equation (4.4) leads to a formal definition of Floquet Theory.

If $\boldsymbol{A}(t)$ is a continuous, T-periodic matrix, then for all t $\in \mathbb{R}$ the state-transition matrix for $\dot{\boldsymbol{x}}=\boldsymbol{A}(t)\boldsymbol{x}$ can be written in the form

$$\boldsymbol{\Phi}(t,t_0)=\boldsymbol{P}(t)e^{\boldsymbol{\Lambda}(t-t_0)}\boldsymbol{P}^{-1}(t_0) \tag{4.6}$$

where $\boldsymbol{P}(t)$ is a nonsingular, differentiable, T-periodic matrix and $\boldsymbol{\Lambda}$ is a constant matrix.[41]

4.1.1 Discussion of Floquet Theorem

Note that Floquet Theory only guarantees the existence of $\boldsymbol{P}(t)$ and $\boldsymbol{\Lambda}$. In general, there is no easy way to calculate $\boldsymbol{\Phi}(t, t_0)$ for an arbitrary time-periodic system. Generally, a numeric algorithm is used to integrate the state equation over the principal period. See the work of Sinha et al. (e.g. References 42, 43, 44, 45, 46, 47, 48 and the references contained within) for more information on numerical methods.

The previous paragraphs focused on evaluating the state transition matrix at the end of one period, T, and in general, both $\boldsymbol{P}(t)$ and $\boldsymbol{\Lambda}$ will be complex. It is possible to instead evaluate the state transition matrix at the end of two periods, $2T$. The resulting matrices, $\boldsymbol{L}(t)$ and $\boldsymbol{\Sigma}$ (analogous to $\boldsymbol{P}(t)$ and $\boldsymbol{\Lambda}$ respectively) will now be real.

4.1.2 System Stability

The characteristic exponents, λ_i, are defined as the eigenvalues of $\boldsymbol{\Lambda}$. The characteristic exponents can also be referred to as Floquet exponents. The characteristic exponents are related to the characteristic multipliers, ρ_i, by $\lambda_i = \frac{1}{T} \ln |\rho_i|$. Note that the characteristic multipliers are the eigenvalues of $\boldsymbol{\Phi}(t_0 + T, t_0)$.[36] System stability can be determined by examining the characteristic exponents or the multipliers. A necessary condition for the existence of T-periodic solutions is that one or more of the characteristic exponents are purely imaginary (multiplier has modulus 1). A necessary and sufficient condition for asymptotic stability is that all of the exponents have negative real parts (multipliers have modulus less than one).[49]

4.2 Lyapunov-Floquet Theory

Lyapunov extended Floquet Theory by introducing a change of coordinates that reduces the linear time-periodic system to a system of constant coefficients. Under the following periodic change of coordinates.

$$\boldsymbol{x} = \boldsymbol{P}(t)\boldsymbol{z} \tag{4.7}$$

The system is reduced to the linear time-invariant form.

$$\dot{\boldsymbol{z}} = \boldsymbol{\Lambda} \boldsymbol{z} \tag{4.8}$$

This decomposition implies that the solution for $\boldsymbol{x}$ is a time-periodic coordinate transformation of the solution to an underlying linear time-invariant system. The implication of this transformation is that the study of a time-periodic system can be reduced to the study of a much simpler time-invariant system.

4.3 Determining a Lyapunov-Floquet Transformation

While Lyapunov-Floquet theory is a powerful tool in studying linear time-periodic equations, it does not provide a framework for calculating $\boldsymbol{P}(t)$ and $\boldsymbol{\Lambda}$. This section will discuss two methods for calculating a Lyapunov-Floquet transformation for commutative and non-commutative systems.

4.3.1 Commutative System

For a certain class of systems called commutative systems, the state-transition matrix and the Lyapunov-Floquet matrices can easily be found in closed form.[50] A periodic system matrix $\boldsymbol{A}(t)$ is called commutative if there exists a matrix $\boldsymbol{B}(t)$, where $\boldsymbol{A}(t)$ and $\boldsymbol{B}(t)$ have the following relationship.

$$\frac{\mathrm{d}\boldsymbol{B}(t)}{\mathrm{d}t} = \boldsymbol{A}(t) \tag{4.9}$$

The matrix $\boldsymbol{B}(t)$ must satisfy the following properties.

$$\begin{aligned} \boldsymbol{A}(t)\boldsymbol{B}(t) &= \boldsymbol{B}(t)\boldsymbol{A}(t) \\ \boldsymbol{B}(T)\boldsymbol{B}(0) &= \boldsymbol{B}(0)\boldsymbol{B}(T) \end{aligned} \tag{4.10}$$

Here, $\boldsymbol{B}(t)$ is called the commutating antiderivative of $\boldsymbol{A}(t)$. The state-transition matrix is found through the matrix exponential.

$$\boldsymbol{\Phi}(t, t_0) = e^{\boldsymbol{B}(t)} e^{-\boldsymbol{B}(t_0)} \tag{4.11}$$

The term $e^{\boldsymbol{B}(t)}$ from Equation (4.11) can be factored by defining another matrix $\boldsymbol{B}_P(t)$.

$$e^{\boldsymbol{B}(t)} = e^{\boldsymbol{B}_P(t)} e^{t\boldsymbol{\Lambda}} \tag{4.12}$$

The constant matrix $\boldsymbol{\Lambda}$ is found by evaluating $\boldsymbol{B}(t)$ at two points.

$$\boldsymbol{\Lambda} = \frac{1}{T} \int_{t_0}^{t_0+T} \boldsymbol{A}(\tau) \mathrm{d}\tau = \frac{1}{T} \left(\boldsymbol{B}(T + t_0) - \boldsymbol{B}(t_0) \right) \tag{4.13}$$

From Equation (4.12), the matrix $\boldsymbol{B}_P(t)$ can be determined by the following.

$$\boldsymbol{B}_P(t) = \boldsymbol{B}(t) - t\boldsymbol{\Lambda} \tag{4.14}$$

The T-periodic transformation matrix $\boldsymbol{P}(t)$ is found through the matrix exponential of Equation (4.14).

$$\boldsymbol{P}(t) = e^{\boldsymbol{B}_P(t)} \tag{4.15}$$

Equations (4.13) and (4.15) allow the state-transition matrix given by Equation (4.11) to be written as $\boldsymbol{\Phi}(t, t_0) = \boldsymbol{P}(t) e^{\boldsymbol{\Lambda}(t-t_0)} \boldsymbol{P}^{-1}(t_0)$.

As an example, consider the periodic state matrix $\boldsymbol{A}(t)$ shown below.

$$\boldsymbol{A}(t) = \begin{bmatrix} 0 & \sin t & 1 \\ \sin t & 1 & \sin t \\ 1 & \sin t & 0 \end{bmatrix} \tag{4.16}$$

Here, $T = 2\pi$. The commutating antiderivative matrix $\boldsymbol{B}(t)$ can be determined which satisfies the conditions given by Equation (4.10).

$$\boldsymbol{B}(t) = \begin{bmatrix} 0 & -\cos t & t \\ -\cos t & t & -\cos t \\ t & -\cos t & 0 \end{bmatrix} \tag{4.17}$$

Using Equation (4.17), the state-transition matrix for Equation (4.16) can be calculated from Equation (4.11).

$$\boldsymbol{\Phi}(t, t_0) = \begin{bmatrix} \frac{1}{2}\cosh(t-t_0)(1+a_1) + \frac{1}{2}\sinh(t-t_0)(a_1-1) & -\frac{a_2}{\sqrt{2}}e^{t-t_0} \\ -\frac{a_2}{\sqrt{2}}e^{t-t_0} & e^{t-t0}a_1 \\ \frac{1}{2}\cosh(t-t_0)(a_1-1) + \frac{1}{2}\sinh(t-t_0)(1+a_1) & -\frac{a_2}{\sqrt{2}}e^{t-t_0} \end{bmatrix}$$

$$\begin{bmatrix} \frac{1}{2}\cosh(t-t_0)(a_1-1) + \frac{1}{2}\sinh(t-t_0)(1+a_1) \\ -\frac{a_2}{\sqrt{2}}e^{t-t_0} \\ \frac{1}{2}\cosh(t-t_0)(1+a_1) + \frac{1}{2}\sinh(t-t_0)(a_1-1) \end{bmatrix} \tag{4.18}$$

Here, $a_1 = \cosh\left(\sqrt{2}\left(\cos t - \cos t_0\right)\right)$ and $a_2 = \sinh\left(\sqrt{2}\left(\cos t - \cos t_0\right)\right)$. The matrices $\boldsymbol{\Lambda}$ and $\boldsymbol{B}_P(t)$ can be determined from Equations (4.13) and (4.14) respectively.

$$\boldsymbol{\Lambda} = \frac{1}{2\pi}\left(\boldsymbol{B}(2\pi) - \boldsymbol{B}(0)\right) = \begin{bmatrix} 0 & 0 & 1 \\ 0 & 1 & 0 \\ 1 & 0 & 0 \end{bmatrix} \tag{4.19}$$

$$\boldsymbol{B}_P(t) = \boldsymbol{B} - t\boldsymbol{\Lambda} = \begin{bmatrix} 0 & -\cos t & 0 \\ -\cos t & 0 & -\cos t \\ 0 & -\cos t & 0 \end{bmatrix} \tag{4.20}$$

Using Equation (4.20), the periodic transformation matrix $\boldsymbol{P}(t)$ can be found through Equation (4.15).

$$\boldsymbol{P}(t) = e^{\boldsymbol{B}_P(t)} = \begin{bmatrix} \cosh\left(\frac{\cos t}{\sqrt{2}}\right)^2 & -\frac{\sinh\left(\sqrt{2}\cos t\right)}{\sqrt{2}} & \sinh\left(\frac{\cos t}{\sqrt{2}}\right)^2 \\ -\frac{\sinh\left(\sqrt{2}\cos t\right)}{\sqrt{2}} & \cosh\left(\sqrt{2}\cos t\right) & -\frac{\sinh\left(\sqrt{2}\cos t\right)}{\sqrt{2}} \\ \sinh\left(\frac{\cos t}{\sqrt{2}}\right)^2 & -\frac{\sinh\left(\sqrt{2}\cos t\right)}{\sqrt{2}} & \cosh\left(\frac{\cos t}{\sqrt{2}}\right)^2 \end{bmatrix} \tag{4.21}$$

4.3.2 Non-commutative System

For non-commutative systems, a Lyapunov-Floquet transformation can be determined from the state-transition matrix of a time-periodic system as discussed in Section 4.1. It is commonly assumed that $\boldsymbol{P}(t_0) = \boldsymbol{I}$. Using this assumption, the constant matrix $\boldsymbol{\Lambda}$ can be found from the monodromy matrix given by Equation (4.2).

$$\boldsymbol{\Lambda} = \frac{1}{2\pi} \ln\left(\boldsymbol{\Phi}(t_0 + T, t_0)\right) \tag{4.22}$$

Once $\boldsymbol{\Lambda}$ has been determined, $\boldsymbol{P}(t)$ is determined from Equation (4.4).

Consider the previous example where the state matrix was given by Equation (4.16) and the state-transition matrix for this system was given by Equation (4.18). Evaluating the state-transition matrix over one period gives the following.

$$\boldsymbol{\Phi}(2\pi, 0) = \begin{bmatrix} \cosh 2\pi & 0 & \sinh 2\pi \\ 0 & e^{2\pi} & 0 \\ \sinh 2\pi & 0 & \cosh 2\pi \end{bmatrix} = \begin{bmatrix} \frac{1}{2}\left(e^{-2\pi} + e^{2\pi}\right) & 0 & \frac{1}{2}\left(-e^{-2\pi} + e^{2\pi}\right) \\ 0 & e^{2\pi} & 0 \\ \frac{1}{2}\left(-e^{-2\pi} + e^{2\pi}\right) & 0 & \frac{1}{2}\left(e^{-2\pi} + e^{2\pi}\right) \end{bmatrix} \tag{4.23}$$

The matrix $\boldsymbol{\Phi}(2\pi, 0)$ can be written in canonical form as shown below.

$$\boldsymbol{\Phi}(2\pi, 0) = \boldsymbol{M}\boldsymbol{J}\boldsymbol{M}^{-1}$$

$$\boldsymbol{J} = \begin{bmatrix} e^{2\pi} & 0 & 0 \\ 0 & e^{2\pi} & 0 \\ 0 & 0 & e^{-2\pi} \end{bmatrix} \quad ; \quad \boldsymbol{M} = \begin{bmatrix} 1 & 0 & -1 \\ 0 & 1 & 0 \\ 1 & 0 & 1 \end{bmatrix} \tag{4.24}$$

From Equation (4.22), the matrix $\boldsymbol{\Lambda}$ can be determined.

$$\boldsymbol{\Lambda} = \frac{1}{2\pi} \ln\left(\boldsymbol{\Phi}(t_0 + T, t_0)\right) = \frac{1}{2\pi} \ln\left(\boldsymbol{M}\boldsymbol{J}\boldsymbol{M}^{-1}\right) = \frac{1}{2\pi} \boldsymbol{M} \ln\left(\boldsymbol{J}\right) \boldsymbol{M}^{-1} = \begin{bmatrix} 0 & 0 & 1 \\ 0 & 1 & 0 \\ 1 & 0 & 0 \end{bmatrix} \tag{4.25}$$

From Equation (4.4), $\boldsymbol{P}(t)$ is determined and is shown below.

$$\boldsymbol{P}(t) = \begin{bmatrix} \cosh\left(\frac{\cos t}{\sqrt{2}}\right)^2 & -\frac{\sinh\left(\sqrt{2}\cos t\right)}{\sqrt{2}} & \sinh\left(\frac{\cos t}{\sqrt{2}}\right)^2 \\ -\frac{\sinh\left(\sqrt{2}\cos t\right)}{\sqrt{2}} & \cosh\left(\sqrt{2}\cos t\right) & -\frac{\sinh\left(\sqrt{2}\cos t\right)}{\sqrt{2}} \\ \sinh\left(\frac{\cos t}{\sqrt{2}}\right)^2 & -\frac{\sinh\left(\sqrt{2}\cos t\right)}{\sqrt{2}} & \cosh\left(\frac{\cos t}{\sqrt{2}}\right)^2 \end{bmatrix} \tag{4.26}$$

Note that Equations (4.25) and (4.26) give the same result as Equations (4.19) and (4.21) obtained in the previous subsection.

4.3.3 Discussion

In Chapter 5, two Lyapunov-Floquet transformations will be determined which relate the LERM to the HCW equations. Recall that the time-invariant HCW equations are a special case of the time-varying LERM when the chief satellite is in a circular orbit. In general, choosing a time-invariant special case of a time-varying system as $\boldsymbol{\Lambda}$ does not produce a valid Lyapunov-Floquet transformation. Consider the Mathieu Equation without damping given by $\ddot{x} + (a + \varepsilon \cos 2t)\, x = 0$. In state-space form, the Mathieu Equation is given by the following.

$$\begin{bmatrix} \dot{x} \\ \ddot{x} \end{bmatrix} = \begin{bmatrix} 0 & 1 \\ -(a + \varepsilon \cos 2t) & 0 \end{bmatrix} \begin{bmatrix} x \\ \dot{x} \end{bmatrix} \tag{4.27}$$

The following time-invariant form of Equation (4.27) is found by setting $\varepsilon = 0$.

$$\begin{bmatrix} \dot{\tilde{x}} \\ \ddot{\tilde{x}} \end{bmatrix} = \begin{bmatrix} 0 & 1 \\ -a & 0 \end{bmatrix} \begin{bmatrix} \tilde{x} \\ \dot{\tilde{x}} \end{bmatrix} \tag{4.28}$$

For constructing a Lyapunov-Floquet transformation of the Mathieu equation, the time-invariant system calculated in Equation (4.28) does not correspond with the time-invariant matrix $\mathbf{\Lambda}$ calculated by Sinha et al. through perturbation methods or through expansion by Chebyshev polynomials.[51] This indicates that in general, $\mathbf{\Lambda}$ must be calculated using the time-periodic state matrix. Further, since the Lyapunov-Floquet transformation cannot change stability characteristics (being periodic), Equations (4.27) and (4.28) must have identical stability properties; which is obvious not the case.

4.4 Lyapunov-Floquet Transformation of the TH Equations

A Lyapunov-Floquet (LF) transformation of the TH equations has previously been determined.[7,52,53] The review of LF transformations in the previous sections generically used time for the independent variable. For the TH equations, of course, the independent variable is true anomaly.

$$\tilde{\boldsymbol{x}} = \boldsymbol{P}(f)\boldsymbol{z} \;\; ; \qquad \boldsymbol{z}' = \mathbf{\Lambda}\boldsymbol{z} \tag{4.29}$$

$$\mathbf{\Lambda} = \begin{bmatrix} 0 & 1 & 0 & 0 & 0 & 0 \\ 0 & 0 & 0 & 0 & 0 & 0 \\ 0 & 0 & 0 & 1 & 0 & 0 \\ 0 & 0 & -1 & 0 & 0 & 0 \\ 0 & 0 & 0 & 0 & 0 & 1 \\ 0 & 0 & 0 & 0 & -1 & 0 \end{bmatrix} \tag{4.30}$$

$$\boldsymbol{P}^{-1}(f) = \begin{bmatrix} c & p_1 & \frac{1}{3} & -q_2 & 0 & 0 \\ -2q_1 + e\mu' & -e\mu & 0 & -q_1 & 0 & 0 \\ -\frac{1}{2}e\sin f & -\frac{1}{2}(1+e\cos f) & \frac{1}{2}e\cos f & 0 & 0 & 0 \\ -\frac{1}{2}(3+e\cos f) & 0 & -\frac{1}{2}e\sin f & -\frac{1}{2}(2+e\cos f) & 0 & 0 \\ 0 & 0 & 0 & 0 & 1 & 0 \\ 0 & 0 & 0 & 0 & 0 & 1 \end{bmatrix} \tag{4.31}$$

where

$$c = \frac{1}{e}\left[1 - \left(1+2e^2\right)\sqrt{1-e^2}\right]\sin f - \left(2 + 3e\cos f + e^2\right)\sin^{-1}\lambda$$

$$p_1 = -\frac{1}{6}\left[1 + 3\sqrt{1-e^2}\right] - \frac{1}{3e}\left[1 - \left(1-e^2\right)^{3/2}\right]\cos f + \frac{1}{6}\left[\left(1+2e^2\right)\sqrt{1-e^2} - 1\right]\cos 2f - e\mu\sin^{-1}\lambda$$

$$q_1 = (1 + e\cos f)^2$$

$$q_2 = \frac{1}{3e}\left[\left(2+e^2\right)\sqrt{1-e^2} - 2\right]\sin f + \frac{1}{6}\left[\left(1+2e^2\right)\sqrt{1-e^2} - 1\right]\sin 2f + (1+e\cos f)^2\sin^{-1}\lambda$$

$$\mu = \sin f\,(1 + e\cos f)$$

$$\lambda = \frac{\sin f}{1+e\cos f}\left[e + \left(1 - \sqrt{1-e^2}\right)\cos f\right]$$

For $e = 0$, the elements c, p_1, and q_2 in Equation (4.31) must be calculated using L'Hospital's Rule. For this case, $\boldsymbol{P}^{-1}(f)$ is given by the following.

$$\boldsymbol{P}^{-1}|_{e=0} = \begin{bmatrix} 0 & -\frac{2}{3} & \frac{1}{3} & 0 & 0 & 0 \\ -2 & 0 & 0 & -1 & 0 & 0 \\ 0 & -\frac{1}{2} & 0 & 0 & 0 & 0 \\ -\frac{3}{2} & 0 & 0 & -1 & 0 & 0 \\ 0 & 0 & 0 & 0 & 1 & 0 \\ 0 & 0 & 0 & 0 & 0 & 1 \end{bmatrix} \tag{4.32}$$

Note that when deriving Equations (4.30) and (4.31), the state vector $\boldsymbol{x} = [\tilde{x}\ \tilde{x}'\ \tilde{y}\ \tilde{y}'\ \tilde{z}\ \tilde{z}']^{\mathsf{T}}$ was used. To remain consistent with the state vector used in this dissertation, a transformation matrix $\boldsymbol{F}$ is required.

$$\boldsymbol{F} = \begin{bmatrix} 1 & 0 & 0 & 0 & 0 & 0 \\ 0 & 0 & 0 & 1 & 0 & 0 \\ 0 & 1 & 0 & 0 & 0 & 0 \\ 0 & 0 & 0 & 0 & 1 & 0 \\ 0 & 0 & 1 & 0 & 0 & 0 \\ 0 & 0 & 0 & 0 & 0 & 1 \end{bmatrix} \tag{4.33}$$

Using this LF transformation, the LERM solution at time t can be written as the following.

$$\boldsymbol{x}(t) = \boldsymbol{T}(f)^{-1}\boldsymbol{F}^{-1}\boldsymbol{P}(f)e^{\boldsymbol{\Lambda}(f-f_0)}\boldsymbol{P}(f_0)^{-1}\boldsymbol{F}\boldsymbol{T}(f_0)\boldsymbol{x}(0) \tag{4.34}$$

4.5 Lyapunov-Floquet Generalization of the HCW Equations in the f-Domain*

The constant matrix $\boldsymbol{\Lambda}$ in Equation (4.30) strongly resembles $\boldsymbol{J}$ given in Equation (2.55). Due to this similarity, a transformation between $\boldsymbol{\Lambda}$ and $\boldsymbol{J}$ should exist which would relate the HCW equations to the TH equations (and also the LERM). In order to relate $\boldsymbol{\Lambda}$ and $\boldsymbol{J}$, first define a virtual-time τ such that $\tau = \frac{1}{n}f$ and $\frac{\mathrm{d}}{\mathrm{d}f} = \frac{1}{n}\frac{\mathrm{d}}{\mathrm{d}\tau}$. Therefore, the derivative $\boldsymbol{z}' = \boldsymbol{\Lambda}\boldsymbol{z}$ in Equation (4.29) can be rewritten in terms of τ and is given by $\frac{\mathrm{d}}{\mathrm{d}\tau}(\boldsymbol{z}) = n\boldsymbol{\Lambda}\boldsymbol{z}$.

*Material in this section taken from the following paper:
[54] R. E. Sherrill, A. J. Sinclair, and T. A. Lovell, "A Lyapunov-Floquet Generalization of the Hill-Clohessy-Wiltshire Equations," *AAS 12-103*, presented at the 22nd AAS/AIAA Space Flight Mechanics Meeting, Charleston, SC, 2012.

The matrix $n\boldsymbol{\Lambda}$ can be written in canonical form $n\boldsymbol{\Lambda} = \boldsymbol{S}\boldsymbol{J}\boldsymbol{S}^{-1}$ where $\boldsymbol{S}$ is given by

$$\boldsymbol{S} = \begin{bmatrix} 0 & 1 & 0 & 0 & 0 & 0 \\ \frac{1}{n} & 0 & 0 & 0 & 0 & 0 \\ 0 & 0 & -1 & 0 & 0 & 0 \\ 0 & 0 & 0 & 1 & 0 & 0 \\ 0 & 0 & 0 & 0 & -1 & 0 \\ 0 & 0 & 0 & 0 & 0 & 1 \end{bmatrix} \tag{4.35}$$

Note that the magnitude of the eigenvectors that comprise $\boldsymbol{S}$ is somewhat arbitrary. Solving $n\boldsymbol{\Lambda} = \boldsymbol{S}\boldsymbol{J}\boldsymbol{S}^{-1}$ for $\boldsymbol{J}$ and substituting for $\boldsymbol{J}$ in $\boldsymbol{C} = \boldsymbol{M}\boldsymbol{J}\boldsymbol{M}^{-1}$ motivates another coordinate transformation, $\boldsymbol{R} = \boldsymbol{M}\boldsymbol{S}^{-1}$.

$$\boldsymbol{y} = \boldsymbol{R}\boldsymbol{z} = \begin{bmatrix} 0 & -2 & 0 & 2 & 0 & 0 \\ 3 & 0 & -4 & 0 & 0 & 0 \\ 0 & 0 & 0 & 0 & 1 & 0 \\ 0 & 0 & -2n & 0 & 0 & 0 \\ 0 & 3n & 0 & -4n & 0 & 0 \\ 0 & 0 & 0 & 0 & 0 & n \end{bmatrix} \boldsymbol{z} \tag{4.36}$$

$$\frac{\mathrm{d}}{\mathrm{d}\tau}(\boldsymbol{y}) = \boldsymbol{R}\frac{\mathrm{d}}{\mathrm{d}\tau}(\boldsymbol{z}) = n\boldsymbol{R}\boldsymbol{\Lambda}\boldsymbol{z} = n\boldsymbol{R}\boldsymbol{\Lambda}\boldsymbol{R}^{-1}\boldsymbol{y} = \boldsymbol{M}\boldsymbol{J}\boldsymbol{M}^{-1}\boldsymbol{y} = \boldsymbol{C}\boldsymbol{y} \tag{4.37}$$

The virtual-time can be calculated from the true time through Kepler's Equation.[34]

In order to derive the HCW equations presented earlier, an assumption was made that the chief satellite was in a circular orbit. However, Equation (4.37) shows that the same equations apply to any elliptic orbit through the appropriate coordinate and independent variable transformations. Figure (4.1) shows the different representations of the relative

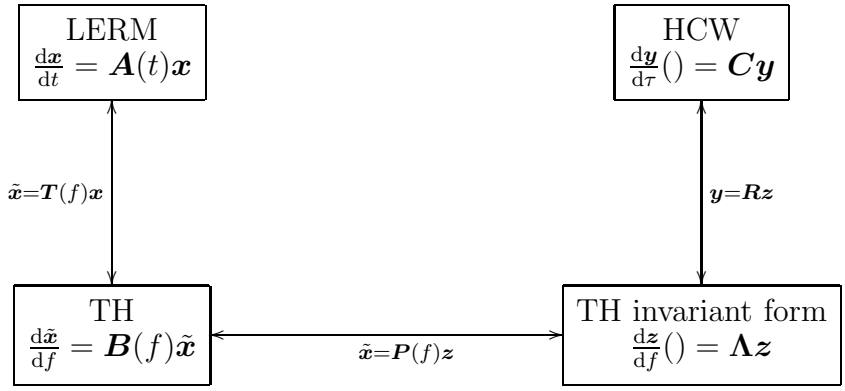

Figure 4.1: Different Representations of Relative Motion Equations

motion equations, and the corresponding state vectors are shown below.

$$\begin{aligned} \boldsymbol{x} &= \boldsymbol{T}^{-1}(f)\tilde{\boldsymbol{x}} \\ &= \boldsymbol{T}^{-1}(f)\boldsymbol{P}(f)\boldsymbol{z} \\ &= \boldsymbol{T}^{-1}(f)\boldsymbol{P}(f)\boldsymbol{R}^{-1}\boldsymbol{y} \end{aligned} \tag{4.38}$$

The chief eccentricity equal to zero is the special case where $t = \tau$ and $\boldsymbol{T}^{-1}\boldsymbol{P}\boldsymbol{R}^{-1} = \boldsymbol{I}$, for the choices of $\boldsymbol{M}$ and $\boldsymbol{S}$ shown in Equation (2.55) and Equation (5.13), respectively.

Using Equation (4.38), the relative motion of two elliptic satellites can be related to an underlying circular relative motion, which can be described by the HCW equations. Given an initial state $\boldsymbol{x}_0$ at t_0, the state $\boldsymbol{x}$ at time t can be determined as follows. The inverse of Equation (4.38) converts the initial condition $\boldsymbol{x}_0$ to $\boldsymbol{y}_0$, and Kepler's Equation is used to convert t and t_0 to τ and τ_0. The solution given by the HCW equations is $\boldsymbol{y}(\tau(t)) = e^{\boldsymbol{C}(\tau-\tau_0)}\boldsymbol{y}_0$. Equation (4.38) is then used to convert $\boldsymbol{y}(\tau(t))$ to $\boldsymbol{x}$.

Chapter 5

Time-Varying Coordinate Transformations of the LERM*

The previous chapter reviewed Lyapunov-Floquet theory and presented a Lyapunov-Floquet generalization of the HCW equations. Whereas this generalization was able to relate the relative motion in elliptic orbits to an underlying circular system, the HCW equations had to be evaluated at a virtual time as opposed to the true time. Lyapunov-Floquet theory clearly states the existence of a periodic coordinate change that relates the LERM to an underlying linear time-invariant system at the true time.

Two Lyapunov-Floquet transformations are presented in this chapter that directly relate the linearized equations of relative motion to the HCW equations with time as the independent variable. One of these transformations approximately matches satellite position at periapse, whereas the other approximately matches satellite position at apoapse. An integral-preserving transformation is also presented, which matches the relative motion in elliptic orbits to the HCW solution that shares certain integral values.

5.1 Lyapunov-Floquet Transformations

5.1.1 Periapse-Matching Transformation

Whereas Lyapunov-Floquet theory guarantees the existence of $\boldsymbol{P}(t)$ and $\boldsymbol{\Lambda}$, it does not provide a mechanism for calculating them. Here, it will be assumed that for the LERM

*Material in this chapter taken from the following papers:
[55] R. E. Sherrill, A. J. Sinclair, S. C. Sinha, and T. A. Lovell, "Lyapunov-Floquet Transformation of Satellite Relative Motion in Elliptic Orbits," *AAS 13-466*, presented at the 23nd AAS/AIAA Space Flight Mechanics Meeting, Kauai, Hawaii, 2013.

[56] R. E. Sherrill, A. J. Sinclair, S. C. Sinha, and T. A. Lovell, "Calibration of Hill-Clohessy-Wiltshire Initial Conditions for Elliptic Relative Motion," submitted to the AAS/AIAA Astrodynamics Specialist Conference, Hilton Head, South Carolina, 2013.

it is possible to choose $\boldsymbol{\Lambda}$ to equal the state matrix of the HCW equations, $\boldsymbol{C}$, given in Equations. (2.53). Based on this assumption it must be determined if a corresponding $\boldsymbol{P}(t)$ can be computed which satisfies Equations. (4.6). This solution for $\boldsymbol{P}(t)$ will provide a coordinate transformation between the LERM solution $\boldsymbol{x}$ and an underlying HCW solution $\boldsymbol{z}$.

Recall that the state-transition matrix of the LERM is written as a function of f while the independent variable of the HCW equations is t. Defining $f = 0$ at $t = 0$ and arbitrarily choosing $t_0 = 0$, Equation (4.6) can be rewritten as shown below.

$$\boldsymbol{\Phi}_{LERM}(f, 0) = \boldsymbol{P}(f)e^{\boldsymbol{C}(t-0)}\boldsymbol{P}^{-1}(0) = \boldsymbol{P}(f)\boldsymbol{\Phi}_{HCW}(t, 0)\boldsymbol{P}^{-1}(0) \tag{5.1}$$

As discussed in the previous section, $\boldsymbol{P}(f)$ must be periodic with the period of the system. Therefore, $\boldsymbol{P}(0) = \boldsymbol{P}(2\pi)$. To determine $\boldsymbol{P}(0)$, the state-transition matrices of both the LERM and the HCW equations, given by Equations. (2.51) and (2.57) respectively, are evaluated at the end of one period.

$$\boldsymbol{\Phi}_{LERM}(2\pi, 0) = \begin{bmatrix} 1 & 0 & 0 & 0 & 0 & 0 \\ \frac{-6\pi(e+1)^3(e+2)}{(1-e^2)^{\frac{5}{2}}} & 1 & 0 & 0 & \frac{-6\pi p^2(e+1)^2}{h(1-e^2)^{\frac{5}{2}}} & 0 \\ 0 & 0 & 1 & 0 & 0 & 0 \\ \frac{-6\pi eh(e+1)^4(e+2)}{p^2(1-e^2)^{\frac{5}{2}}} & 0 & 0 & 1 & \frac{-6\pi e(e+1)^3}{(1-e^2)^{\frac{5}{2}}} & 0 \\ 0 & 0 & 0 & 0 & 1 & 0 \\ 0 & 0 & 0 & 0 & 0 & 1 \end{bmatrix} \tag{5.2}$$

$$\boldsymbol{\Phi}_{HCW}\left(\frac{2\pi}{n},0\right)=\begin{bmatrix}1 & 0 & 0 & 0 & 0 & 0\\ -12\pi & 1 & 0 & 0 & \frac{-6\pi}{n} & 0\\ 0 & 0 & 1 & 0 & 0 & 0\\ 0 & 0 & 0 & 1 & 0 & 0\\ 0 & 0 & 0 & 0 & 1 & 0\\ 0 & 0 & 0 & 0 & 0 & 1\end{bmatrix} \tag{5.3}$$

Note that Equation (5.3) equals Equation (5.2) evaluated at $e = 0$. Equations (5.2) and (5.3) can be written in Jordan canonical form by defining $\boldsymbol{\Phi}_{LERM}(2\pi,0) = \boldsymbol{MJM}^{-1}$ and $\boldsymbol{\Phi}_{HCW}\left(\frac{2\pi}{n},0\right) = \boldsymbol{NJN}^{-1}$.

$$\boldsymbol{M}=\begin{bmatrix}0 & \frac{2(1-e^2)^{\frac{5}{2}}}{(e+1)^3(e+2)} & 0 & -1 & 0 & 0\\ -12\pi & 0 & 2 & 0 & 0 & 0\\ 0 & 0 & 0 & 0 & 1 & 0\\ \frac{-12\pi eh(e+1)}{p^2} & 0 & M_{43} & 0 & 0 & 0\\ 0 & 0 & 0 & \frac{h(e+1)(e+2)}{p^2} & 0 & 0\\ 0 & 0 & 0 & 0 & 0 & 1\end{bmatrix} \tag{5.4}$$

$$M_{43}=\frac{2eh(e+1)}{p^2}+\frac{n^2p^2(e+1)^2}{2h(1-e^2)^{\frac{5}{2}}}$$

$$\boldsymbol{J}=\begin{bmatrix}1 & 1 & 0 & 0 & 0 & 0\\ 0 & 1 & 0 & 0 & 0 & 0\\ 0 & 0 & 1 & 0 & 0 & 0\\ 0 & 0 & 0 & 1 & 0 & 0\\ 0 & 0 & 0 & 0 & 1 & 0\\ 0 & 0 & 0 & 0 & 0 & 1\end{bmatrix} \quad ; \quad \boldsymbol{N}=\begin{bmatrix}0 & 1 & 0 & -1 & 0 & 0\\ -12\pi & 0 & 2 & 0 & 0 & 0\\ 0 & 0 & 0 & 0 & 1 & 0\\ 0 & 0 & \frac{n}{2} & 0 & 0 & 0\\ 0 & 0 & 0 & 2n & 0 & 0\\ 0 & 0 & 0 & 0 & 0 & 1\end{bmatrix} \tag{5.5}$$

Note that the values of $\boldsymbol{M}$ and $\boldsymbol{N}$ are not unique as the magnitude of each of the eigenvectors that comprise $\boldsymbol{M}$ and $\boldsymbol{N}$ are arbitrary. These eigenvectors correspond to three different second-order subsystems contained in $\boldsymbol{J}$, related to a drifting in-plane motion, a periodic in-plane motion (here chosen to represent two different phasings of the motion on a 2×1 ellipse), and a periodic out-of-plane motion. Since $\boldsymbol{\Phi}_{LERM}(2\pi, 0)$ and $\boldsymbol{\Phi}_{HCW}\left(\frac{2\pi}{n}, 0\right)$ have the same canonical form, $\boldsymbol{J}$, a similarity transformation $\boldsymbol{P}_0$ can be determined.

$$\begin{aligned} \boldsymbol{P}_0 &= \boldsymbol{M}\boldsymbol{N}^{-1} \\ \boldsymbol{M}\boldsymbol{J}\boldsymbol{M}^{-1} &= \boldsymbol{P}_0\boldsymbol{N}\boldsymbol{J}\boldsymbol{N}^{-1}\boldsymbol{P}_0^{-1} \\ \boldsymbol{\Phi}_{LERM}(2\pi, 0) &= \boldsymbol{P}_0\boldsymbol{\Phi}_{HCW}\left(\frac{2\pi}{n}, 0\right)\boldsymbol{P}_0^{-1} \end{aligned} \tag{5.6}$$

$$\boldsymbol{P}_0 = \begin{bmatrix} \frac{2(1-e^2)^{\frac{5}{2}}}{(e+1)^3(e+2)} & 0 & 0 & 0 & \frac{(1-e^2)^{\frac{5}{2}}}{n(e+1)^3(e+2)} - \frac{1}{2n} & 0 \\ 0 & 1 & 0 & 0 & 0 & 0 \\ 0 & 0 & 1 & 0 & 0 & 0 \\ 0 & \frac{eh(e+1)}{p^2} & 0 & \frac{np^2(e+1)^2}{h(1-e^2)^{\frac{5}{2}}} & 0 & 0 \\ 0 & 0 & 0 & 0 & \frac{h(e+1)(e+2)}{2np^2} & 0 \\ 0 & 0 & 0 & 0 & 0 & 1 \end{bmatrix} \tag{5.7}$$

Due to the nonuniqueness of $\boldsymbol{M}$ and $\boldsymbol{N}$, the value of $\boldsymbol{P}_0$ is also not unique. The scaling of $\boldsymbol{M}$ and $\boldsymbol{N}$ chosen here results in the following properties: $\det(\boldsymbol{P}_0) = 1$, $\boldsymbol{P}_0 = \boldsymbol{I}$ for $e = 0$, and $\boldsymbol{N}$ equals $\boldsymbol{M}$ evaluated at $e = 0$. Note that the first three rows of $\boldsymbol{M}$ differ from the first three rows of $\boldsymbol{N}$ by a single element. If the first three rows of $\boldsymbol{M}$ equaled the first three rows of $\boldsymbol{N}$, then the first three rows of $\boldsymbol{P}_0$ would equal an identity matrix and a null matrix. This would provide exact matching between the position components of $\boldsymbol{x}$ and $\boldsymbol{z}$ at periapse. The first row of Equation (5.7) shows that at periapse, the presented solution provides only approximate position matching in the radial direction.

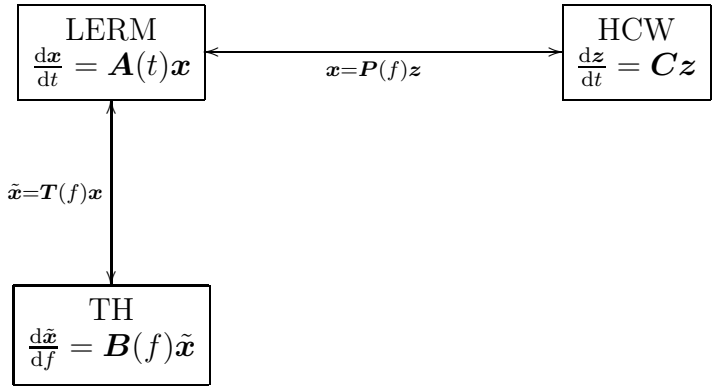

Figure 5.1: Different Representations of Relative Motion Equations

It is now possible to determine $\boldsymbol{P}(f)$ by rewriting Equation (5.1) as shown below.

$$\boldsymbol{P}(f) = \boldsymbol{\Phi}_{LERM}(f,0)\boldsymbol{P}_0 e^{-\boldsymbol{C}(t-0)} = \boldsymbol{\Phi}_{LERM}(f,0)\boldsymbol{P}_0\boldsymbol{\Phi}_{HCW}^{-1}(t,0) \tag{5.8}$$

Note that $\boldsymbol{P}_0$ equals $\boldsymbol{P}$ evaluated at periapse. The elements of $\boldsymbol{P}(f)$ are shown in Appendix A. As expected, $\boldsymbol{P}(f) = \boldsymbol{I}$ when $e = 0$. Significantly, this solution for $\boldsymbol{P}(f)$ is T-periodic, thus forming a valid LF transformation, and $\boldsymbol{\Lambda} = \boldsymbol{C}$ is indeed a valid choice for the underlying linear time-invariant system. Therefore, Figure 2.9 which depicted the different representations of relative motion equations can be updated as shown in Figure 5.1 with a periodic transformation between the LERM and the HCW equations.

5.1.2 Apoapse-Matching Transformation

Following a similar procedure, an alternative LF transformation $\bar{\boldsymbol{P}}(f)$ can be determined to provide approximate position matching at apoapse. To determine $\bar{\boldsymbol{P}}(f)$, the state-transition matrices of both the LERM and the HCW equations are evaluated over one period, beginning and ending at apoapse (i.e. choosing $t_0 = \frac{\pi}{n}$).

$$\boldsymbol{\Phi}_{LERM}(3\pi,\pi)=\begin{bmatrix} 1 & 0 & 0 & 0 & 0 & 0 \\ \frac{-6\pi(e-1)^3(e-2)}{(1-e^2)^{\frac{5}{2}}} & 1 & 0 & 0 & \frac{-6\pi p^2(e-1)^2}{h(1-e^2)^{\frac{5}{2}}} & 0 \\ 0 & 0 & 1 & 0 & 0 & 0 \\ \frac{-6\pi eh(e-1)^4(e-2)}{p^2(1-e^2)^{\frac{5}{2}}} & 0 & 0 & 1 & \frac{-6\pi e(e-1)^3}{(1-e^2)^{\frac{5}{2}}} & 0 \\ 0 & 0 & 0 & 0 & 1 & 0 \\ 0 & 0 & 0 & 0 & 0 & 1 \end{bmatrix} \tag{5.9}$$

$$\boldsymbol{\Phi}_{HCW}\left(\frac{3\pi}{n},\frac{\pi}{n}\right)=\begin{bmatrix} 1 & 0 & 0 & 0 & 0 & 0 \\ -12\pi & 1 & 0 & 0 & \frac{-6\pi}{n} & 0 \\ 0 & 0 & 1 & 0 & 0 & 0 \\ 0 & 0 & 0 & 1 & 0 & 0 \\ 0 & 0 & 0 & 0 & 1 & 0 \\ 0 & 0 & 0 & 0 & 0 & 1 \end{bmatrix} \tag{5.10}$$

Equations (5.9) and (5.10) can be written in Jordan canonical form by defining $\boldsymbol{\Phi}_{LERM}(3\pi,\pi) = \boldsymbol{MJM}^{-1}$ and $\boldsymbol{\Phi}_{HCW}\left(\frac{3\pi}{n},\frac{\pi}{n}\right) = \boldsymbol{NJN}^{-1}$.

$$\boldsymbol{M}=\begin{bmatrix} 0 & \frac{2(1-e^2)^{\frac{5}{2}}}{(e-1)^3(e-2)} & 0 & -1 & 0 & 0 \\ -12\pi & 0 & 2 & 0 & 0 & 0 \\ 0 & 0 & 0 & 0 & 1 & 0 \\ \frac{-12\pi eh(e-1)}{p^2} & 0 & \frac{2eh(e-1)}{p^2}+\frac{n(4e+1)}{2} & 0 & 0 & 0 \\ 0 & 0 & 0 & \frac{h(e-1)(e-2)}{p^2} & 0 & 0 \\ 0 & 0 & 0 & 0 & 0 & 1 \end{bmatrix} \tag{5.11}$$

$$\boldsymbol{J} = \begin{bmatrix} 1 & 1 & 0 & 0 & 0 & 0 \\ 0 & 1 & 0 & 0 & 0 & 0 \\ 0 & 0 & 1 & 0 & 0 & 0 \\ 0 & 0 & 0 & 1 & 0 & 0 \\ 0 & 0 & 0 & 0 & 1 & 0 \\ 0 & 0 & 0 & 0 & 0 & 1 \end{bmatrix} \quad ; \quad \boldsymbol{N} = \begin{bmatrix} 0 & 1 & 0 & -1 & 0 & 0 \\ -12\pi & 0 & 2 & 0 & 0 & 0 \\ 0 & 0 & 0 & 0 & 1 & 0 \\ 0 & 0 & \frac{n}{2} & 0 & 0 & 0 \\ 0 & 0 & 0 & 2n & 0 & 0 \\ 0 & 0 & 0 & 0 & 0 & 1 \end{bmatrix} \tag{5.12}$$

These matrices are used to determine $\bar{\boldsymbol{P}}_0$.

$$\bar{\boldsymbol{P}}_0 = \boldsymbol{M}\boldsymbol{N}^{-1} = \begin{bmatrix} \frac{2(1-e^2)^{\frac{5}{2}}}{(e-1)^3(e-2)} & 0 & 0 & 0 & \frac{(1-e^2)^{\frac{5}{2}}}{n(e-1)^3(e-2)} - \frac{1}{2n} & 0 \\ 0 & 1 & 0 & 0 & 0 & 0 \\ 0 & 0 & 1 & 0 & 0 & 0 \\ 0 & \frac{eh(e-1)}{p^2} & 0 & 4e+1 & 0 & 0 \\ 0 & 0 & 0 & 0 & \frac{h(e-1)(e-2)}{2np^2} & 0 \\ 0 & 0 & 0 & 0 & 0 & 1 \end{bmatrix} \tag{5.13}$$

Recall that the scaling of $\boldsymbol{M}$ and $\boldsymbol{N}$ given in Eqs. (5.11) and (5.12) is arbitrary, and note that for the scaling chosen here $\bar{\boldsymbol{P}}_0 = \boldsymbol{I}$ for $e = 0$, and $\boldsymbol{N}$ equals $\boldsymbol{M}$ evaluated at $e = 0$. Similar to the periapse-matching transformation, $\bar{\boldsymbol{P}}_0$ only provides approximate position matching in the radial direction at apoapse. It is now possible to determine $\bar{\boldsymbol{P}}(f)$ by rewriting Equation (5.1) as shown below.

$$\bar{\boldsymbol{P}}(f) = \boldsymbol{\Phi}_{LERM}(f,\pi)\bar{\boldsymbol{P}}_0 e^{-\boldsymbol{C}\left(t-\frac{\pi}{n}\right)} = \boldsymbol{\Phi}_{LERM}(f,\pi)\bar{\boldsymbol{P}}_0\boldsymbol{\Phi}_{HCW}^{-1}\left(t,\frac{\pi}{n}\right) \tag{5.14}$$

Note that $\bar{\boldsymbol{P}}_0$ equals $\bar{\boldsymbol{P}}$ evaluated at apoapse. The nonzero elements of $\bar{\boldsymbol{P}}(f)$ are shown in Appendix B. Again, $\bar{\boldsymbol{P}}(f)$ is T-periodic, providing a valid LF transformation.

Case	a_C (km)	e_C	a_D (km)	e_D	i_D (rad)	Ω_D (rad)	ω_D (rad)
1	11,000	0.3	11,000	0.30001	0	0	0
2	11,000	0.3	11,000.2	0.30001	0	0	0
3	11,000	0.3	11,000	0.30001	0	0	4×10^{-5}
4	11,000	0.6	11,000	0.60001	0	0	4×10^{-5}
5	11,000	0.3	11,000	0.30001	4×10^{-5}	0	0
6	11,000	0.3	11,000	0.30001	4×10^{-5}	$\frac{\pi}{2}$	$\frac{-\pi}{2}$

Table 5.1: Orbital elements for the chief and deputy for six different relative motion cases.

5.1.3 Relative Motion Examples

Traditionally the HCW equations are thought of as a special case of the LERM obtained by setting the chief eccentricity equal to zero. However, by applying a LF transformation, motion described by the HCW equations can be transformed at any point to motion obeying the LERM and vice versa. This section will present several cases where this transformation is demonstrated. Six cases are presented here, with the orbital elements of the chief and deputy listed in Table 5.1. Orbital elements not listed are set to zero, i.e., $i_C = \Omega_C = \omega_C = f_C = f_D = 0$. Initial conditions for the LERM were calculated using Equation (2.60), while initial conditions for the HCW equations will use the method described in Section 5.3. Figures 5.2 through 5.6 show both a LERM trajectory and an HCW trajectory. Along the HCW trajectory, nine equally spaced points in time were selected and are designated by a circle. At each point, the periapse-matching transformation was applied to transform the motion to a corresponding point along the LERM trajectory given by a diamond. Since Cases 5 and 6 include an out-of-plane component, Figures 5.8 and 5.9 show a three-dimensional representation of the trajectory geometry. The figures clearly show that the HCW equations exactly capture the LERM dynamics and that the LERM and the HCW equations can be related by periodic coordinate transformation.

In addition, the figures also show the effect of eccentricity on the relative motion. As can be seen, the equally-spaced points along the HCW trajectory are clustered near apoapse

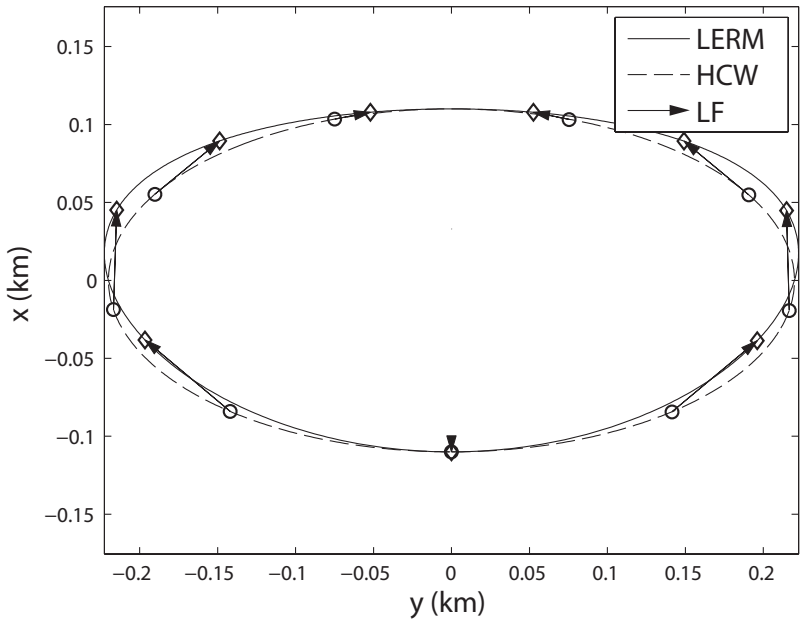

Figure 5.2: LERM, HCW, and LF transformation for case 1.

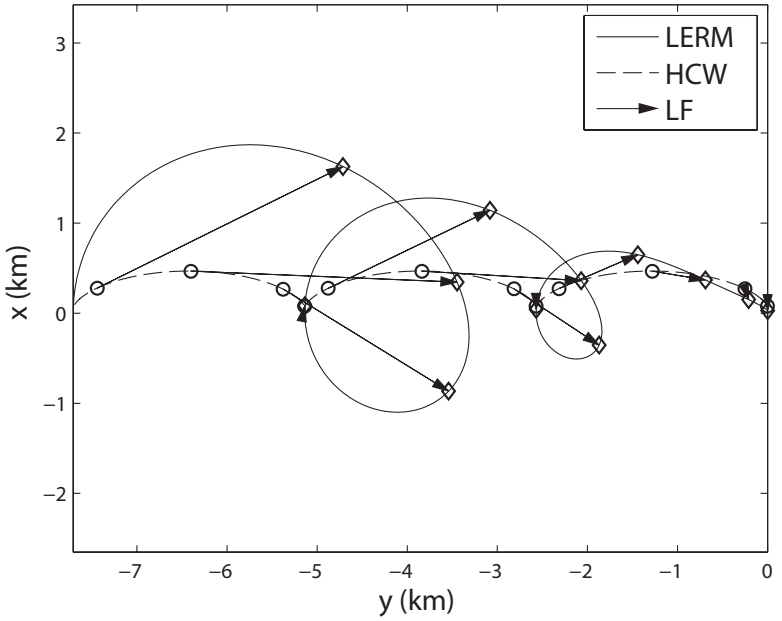

Figure 5.3: LERM, HCW, and LF transformation for case 2.

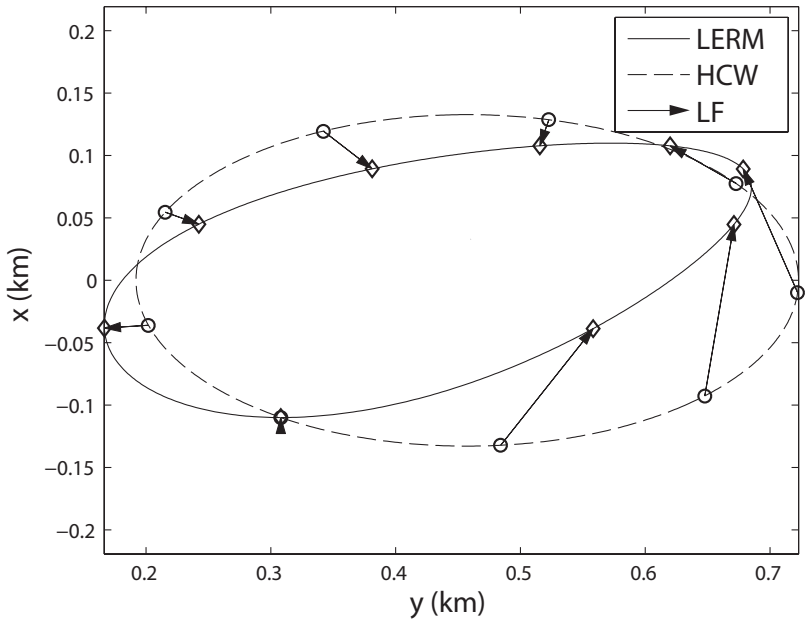

Figure 5.4: LERM, HCW, and LF transformation for case 3.

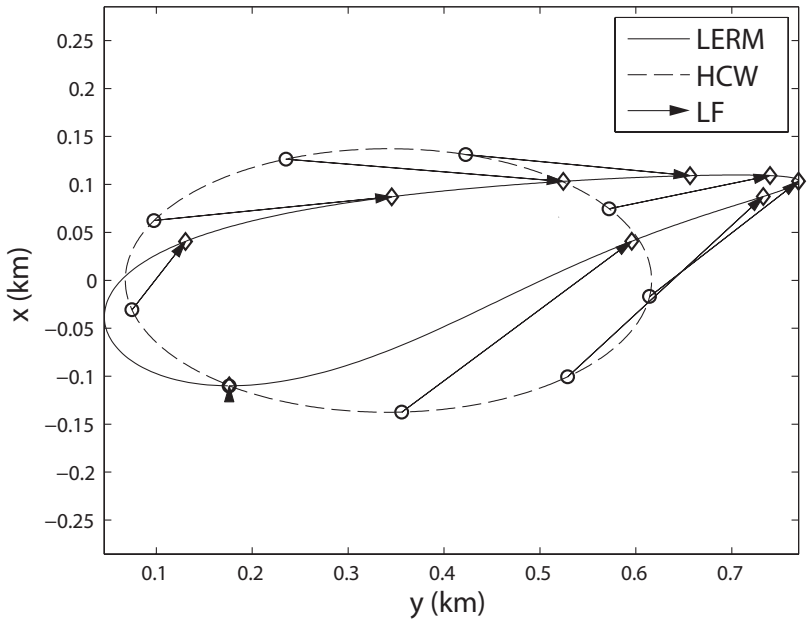

Figure 5.5: LERM, HCW, and LF transformation for case 4.

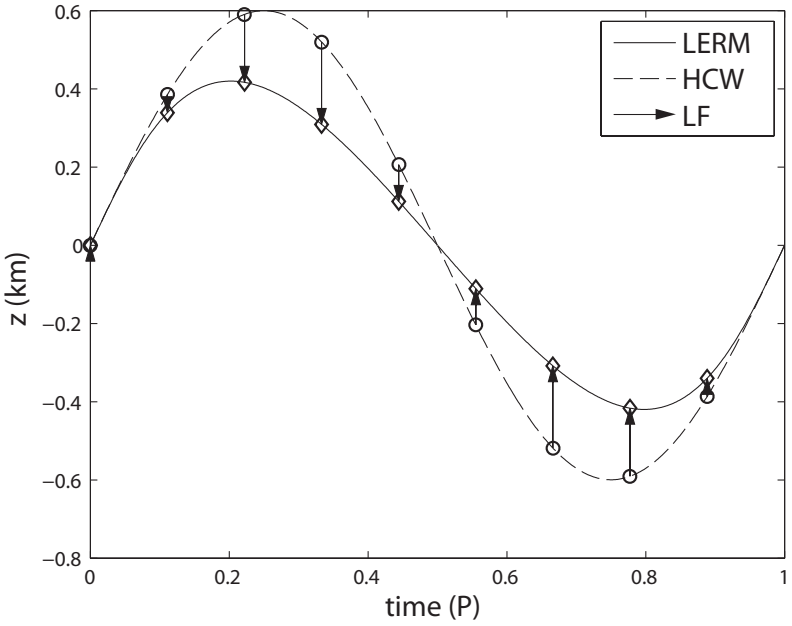

Figure 5.6: LERM, HCW, and LF transformation for case 5.

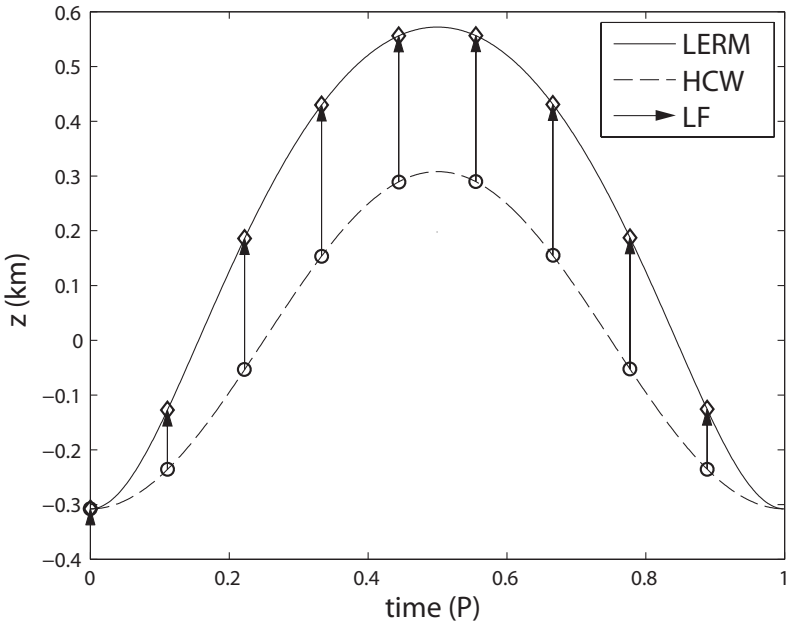

Figure 5.7: LERM, HCW, and LF transformation for case 6.

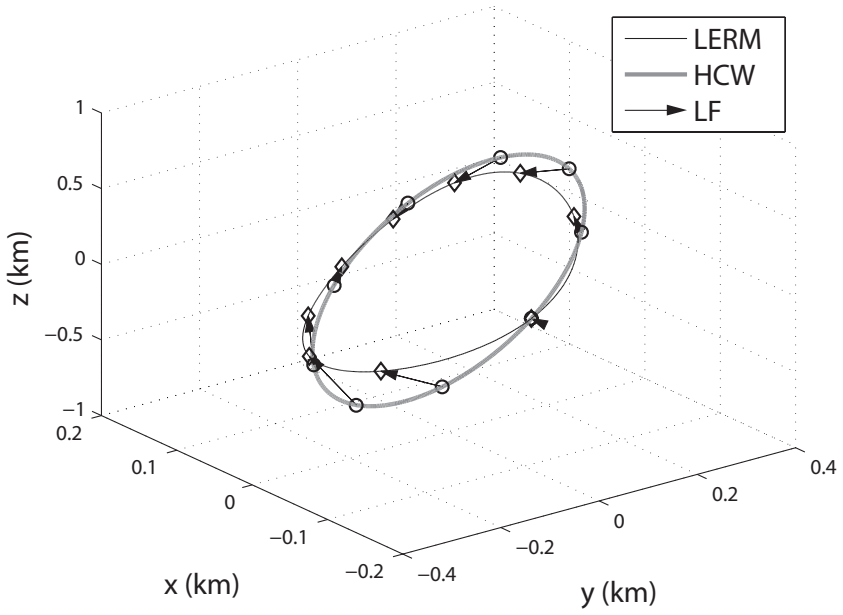

Figure 5.8: Three dimensional representation of Case 5.

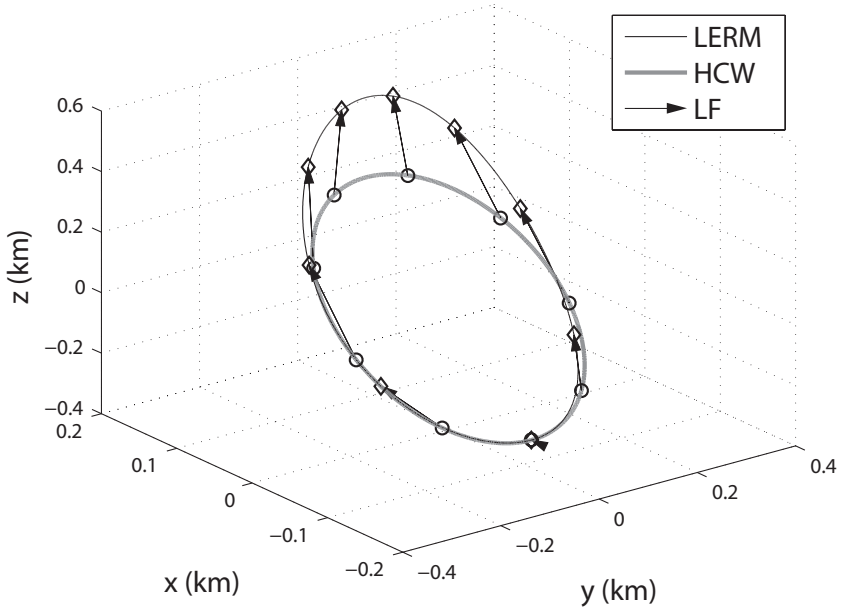

Figure 5.9: Three dimensional representation of Case 6.

on the LERM trajectory. The unequal distribution of points alludes to the motion progressing faster near periapse and slower near apoapse. The Virtual Time method described in Section 3.2 tried to emulate this natural progression of the motion by evaluating the HCW equations at a virtual time. While the VT method did significantly improve the error in directly applying the HCW equations to elliptic orbits, it was not able to capture the full time-varying dynamics.

5.2 Integral-Preserving Transformation

Besides providing approximate position matching at periapse or apoapse, another transformation choice is to match the integral values of the $\boldsymbol{x}(t)$ and $\boldsymbol{z}(t)$ solutions. Specifically, the HCW solution that shares the same values for $\boldsymbol{k}$ is chosen. Recall from Equation (2.50) that the constant $\boldsymbol{k}$ for the LERM was given by $\boldsymbol{k} = \boldsymbol{\Psi}^{-1}(f)\boldsymbol{T}(f)\boldsymbol{x}(t)$. Similarly for the HCW solution, the constant vector is given by $\boldsymbol{k} = \boldsymbol{\Psi}_{HCW}^{-1}(M)\boldsymbol{T}_{HCW}\boldsymbol{z}(t)$.

$$\boldsymbol{T}_{HCW} \equiv \boldsymbol{T}(f)|_{e=0} = \begin{bmatrix} 1 & 0 & 0 & 0 & 0 & 0 \\ 0 & 1 & 0 & 0 & 0 & 0 \\ 0 & 0 & 1 & 0 & 0 & 0 \\ 0 & 0 & 0 & \frac{1}{n} & 0 & 0 \\ 0 & 0 & 0 & 0 & \frac{1}{n} & 0 \\ 0 & 0 & 0 & 0 & 0 & \frac{1}{n} \end{bmatrix} \tag{5.15}$$

$$\boldsymbol{\Psi}_{HCW}(M) \equiv \boldsymbol{\Psi}(M)|_{e=0} = \begin{bmatrix} \sin M & \cos M & 1 & 0 & 0 & 0 \\ 2\cos M & -2\sin M & \frac{-3M}{2} & 1 & 0 & 0 \\ 0 & 0 & 0 & 0 & \sin M & \cos M \\ \cos M & -\sin M & 0 & 0 & 0 & 0 \\ -2\sin M & -2\cos M & \frac{-3}{2} & 0 & 0 & 0 \\ 0 & 0 & 0 & 0 & \cos M & \sin M \end{bmatrix} \tag{5.16}$$

Note that the $\boldsymbol{\Psi}_{HCW}$ is evaluated at the mean anomaly of the chief in the underlying circular orbit, which is equal to its true anomaly, and conveniently, also equal to the mean anomaly of the chief in the actual elliptic orbit. By equating the constants between the LERM and HCW solutions, the following transformation can be established.

$$\boldsymbol{\Psi}^{-1}(f)\boldsymbol{T}(f)\boldsymbol{x}(t) = \boldsymbol{\Psi}_{HCW}^{-1}(M)\boldsymbol{T}_{HCW}\boldsymbol{z}(t) \tag{5.17}$$

$$\boldsymbol{x}(t) = \boldsymbol{T}^{-1}(f)\boldsymbol{\Psi}(f)\boldsymbol{\Psi}_{HCW}^{-1}(M)\boldsymbol{T}_{HCW}\boldsymbol{z}(t) = \boldsymbol{\Pi}(f)\boldsymbol{z}(t) \tag{5.18}$$

By representing the LERM solution as a time-varying transformation of an HCW solution, the following integral-preserving (IP) transformation is proposed.

$$\boldsymbol{x}(t) = \boldsymbol{\Pi}(f)e^{\boldsymbol{C}(t-0)}\boldsymbol{\Pi}^{-1}(f_0)\boldsymbol{x}_0 = \boldsymbol{\Pi}(f)\boldsymbol{\Phi}_{HCW}(t,0)\boldsymbol{\Pi}^{-1}(f_0)\boldsymbol{x}_0 \tag{5.19}$$

The nonzero elements of $\boldsymbol{\Pi}(f)$ are shown in Appendix C. Note that $\boldsymbol{\Pi}(f) = \boldsymbol{I}$ when $e_c = 0$. Recall that M increases monotonically with time. Since M appears outside of the trigonometric functions in the elements of the first and fifth columns $\boldsymbol{\Pi}(f)$, this transformation is in fact aperiodic. This reveals that although $\boldsymbol{\Pi}(f)$ has a similar structure to an LF transformation, it is not an LF transformation. However, the simplicity and sparseness of $\boldsymbol{\Pi}(f)$ could make it attractive for certain relative-motion applications.

5.3 Calibration of Initial Conditions

The previous subsections introduced several transformations between the LERM solution and an HCW solution at any point in time. This subsection has a slightly different focus: using the underlying HCW solution as an approximation of the LERM solution. In this sense, the transformations are a means of calibrating initial conditions for the HCW solution.

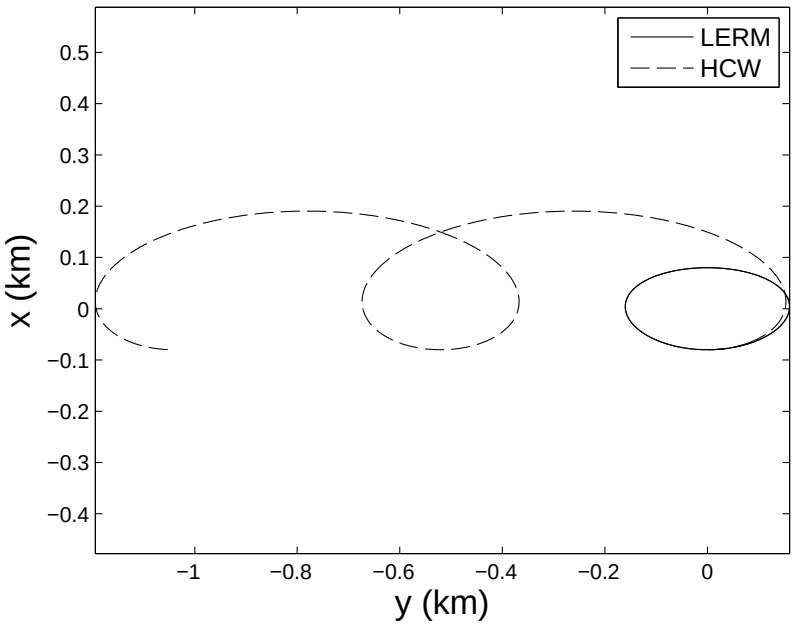

Figure 5.10: Relative-motion trajectories for LERM and HCW propagation.

5.3.1 Calculation of Initial Conditions

Section 2.2.8 gave an example of a chief and deputy satellite in close proximity. Using the initial conditions from this example the relative motion can be propagated using the LERM and HCW equations, and is presented in Fig. 5.10. Note that the instantaneous angular velocity is used in Equation (2.60), but the HCW equations assume constant angular velocity.

Figure 5.10 shows that, in this case of an elliptic chief, significant error is introduced by propagating the initial conditions using the HCW equations. The shape of the LERM trajectory, however, is similar to a nondrifting HCW trajectory. This suggests that it should be possible to select an alternative set of initial conditions, that when propagated under the HCW equations, will better match the shape of the LERM trajectory. A novel strategy for selecting initial conditions would be to transform the linear time-varying system to a linear time-invariant system that can be described by the HCW equations.

The transformations presented in this chapter relate the LERM to the HCW equations. These transformations imply that there is an underlying circular system, $\boldsymbol{z}$, which can be related to $\boldsymbol{x}$ through $\boldsymbol{x} = \boldsymbol{P}(f)\boldsymbol{z}$, $\boldsymbol{x} = \bar{\boldsymbol{P}}(f)\boldsymbol{z}$, or $\boldsymbol{x} = \boldsymbol{\Pi}(f)\boldsymbol{z}$. Since this underlying system can be described by the HCW equations, the previously-derived time-varying coordinate transformations can be used to determine a set of calibrated initial conditions. It is hoped that these calibrated initial conditions outperform the true initial conditions, given by Equation (2.60), when applied to elliptic orbits. This method can be compared to other methods in the literature which attempt to match LERM and HCW trajectories.[19]

The first HCW trajectory uses the LF transformation which approximately matches satellite position at perigee and is obtained by post-multiplying the LF transformation evaluated at the initial time, i.e., $\boldsymbol{x}_{HCW}(t) = e^{\boldsymbol{C}t}\boldsymbol{P}^{-1}(f_0)\boldsymbol{x}_0$. The second HCW trajectory uses the apogee-matching LF transformation and is similarly obtained by $\boldsymbol{x}_{HCW}(t) = e^{\boldsymbol{C}t}\bar{\boldsymbol{P}}^{-1}(f_0)\boldsymbol{x}_0$. Finally, the IP transformation is given by $\boldsymbol{x}_{HCW}(t) = e^{\boldsymbol{C}t}\boldsymbol{\Pi}^{-1}(f_0)\boldsymbol{x}_0$. The subsequent section will investigate the validity of using these transformation for several relative-motion cases.

5.3.2 Comparison of Methods

To illustrate the effectiveness of the LF and IP transformations as initial condition calibrations, consider the case where a chief and deputy satellite are in close proximity around the Earth. Six cases are considered, with the non-zero orbital elements of the chief and deputy given in Table 5.1. The initial conditions were calculated using Equation (2.60). Figures 5.11 through 5.16 show the trajectory predicted by the LERM and three different approximate HCW trajectories. Figures 5.17 and 5.18 show a three-dimensional representation of the relative motion for cases 5 and 6. These figures show that each transformation approximates elliptic motion with some HCW solution.

At each time step, k, the position error in the HCW approximations compared to the LERM solution can be computed. Let $\hat{\boldsymbol{\rho}}_k$ represent the position of the HCW approximation obtained by propagating the perigee-matching LF transformation, the apogee-matching LF

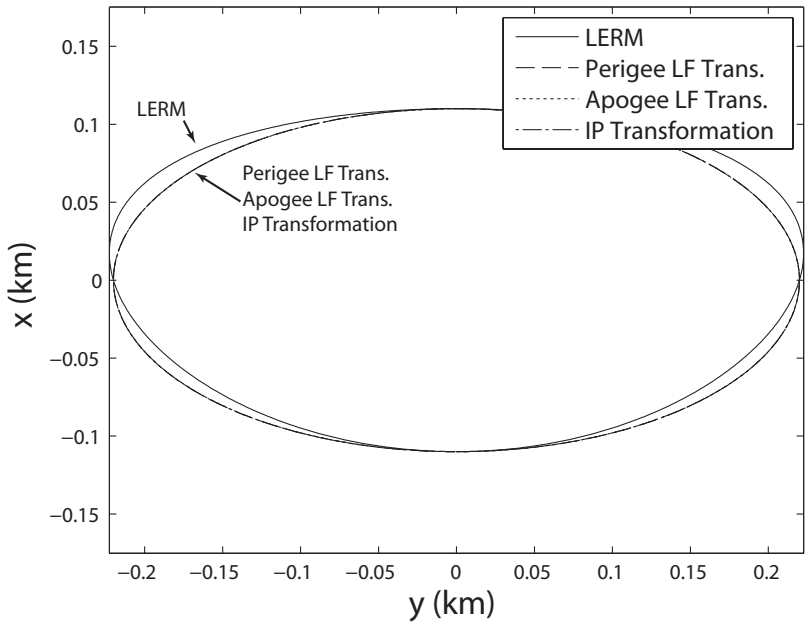

Figure 5.11: Relative-motion trajectory for the LERM and three approximate HCW solutions for case 1.

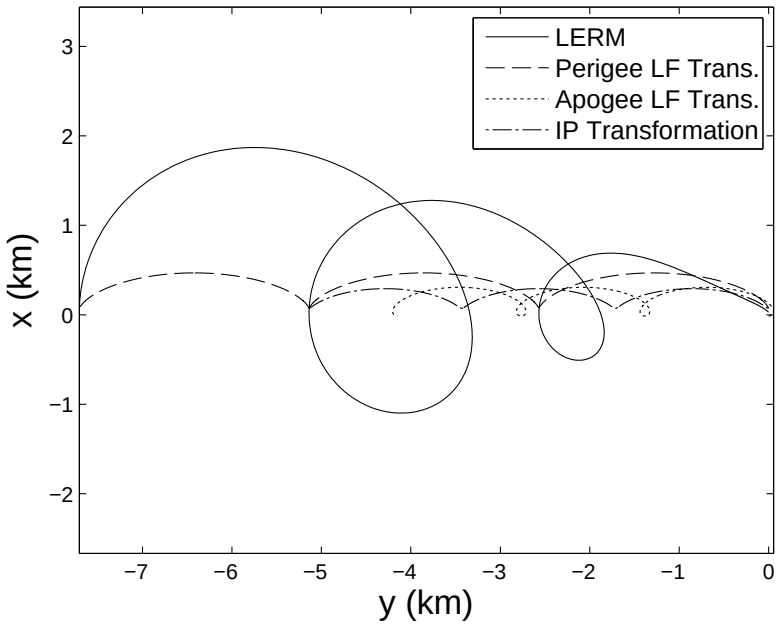

Figure 5.12: Relative-motion trajectory for the LERM and three approximate HCW solutions for case 2.

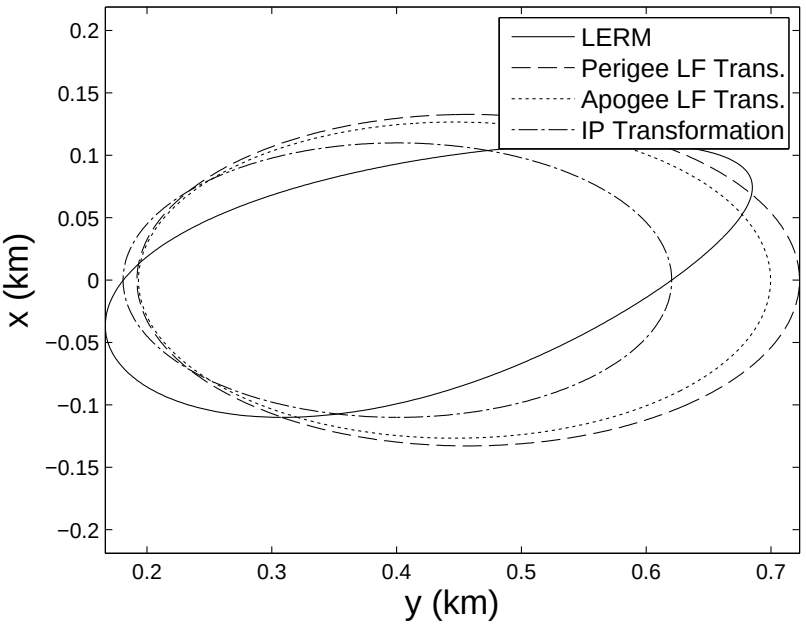

Figure 5.13: Relative-motion trajectory for the LERM and three approximate HCW solutions for case 3.

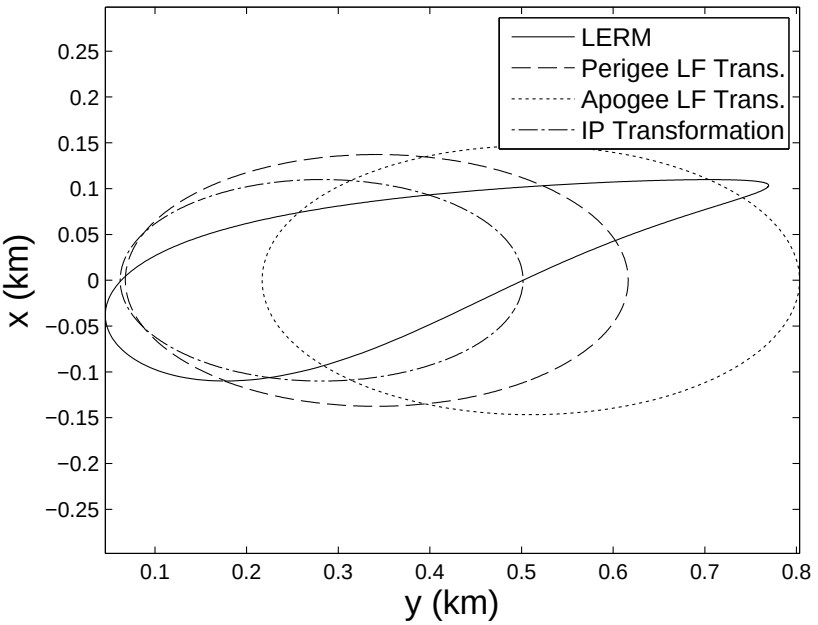

Figure 5.14: Relative-motion trajectory for the LERM and three approximate HCW solutions for case 4.

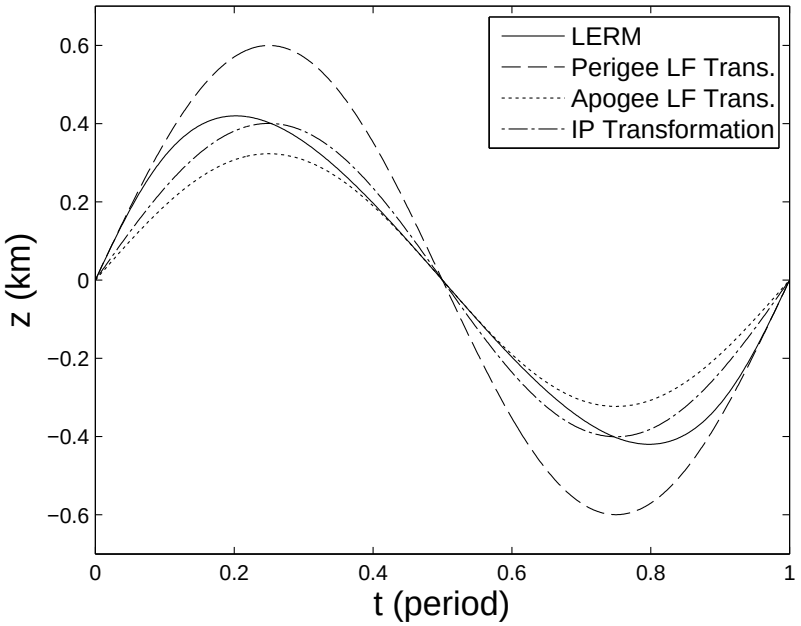

Figure 5.15: Out-of-plane trajectory for the LERM and three approximate HCW solutions for case 5.

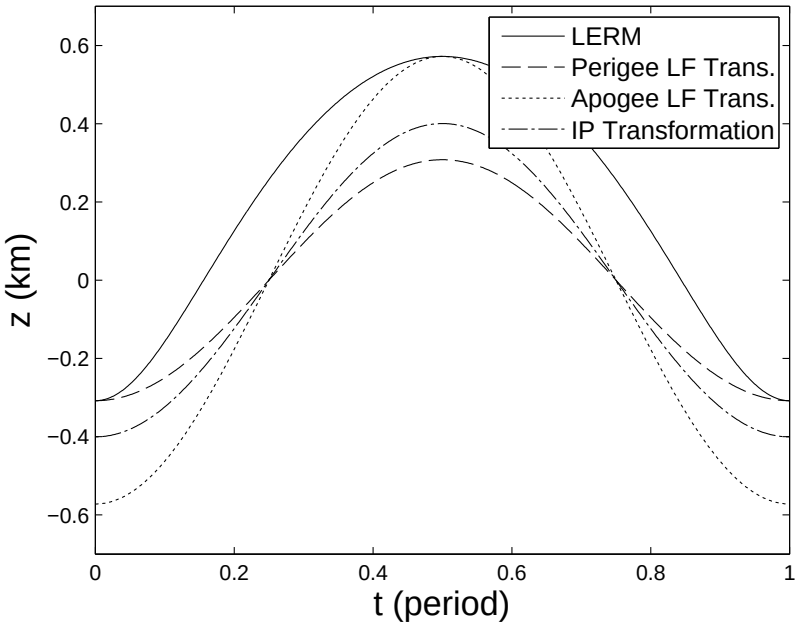

Figure 5.16: Out-of-plane trajectory for the LERM and three approximate HCW solutions for case 6.

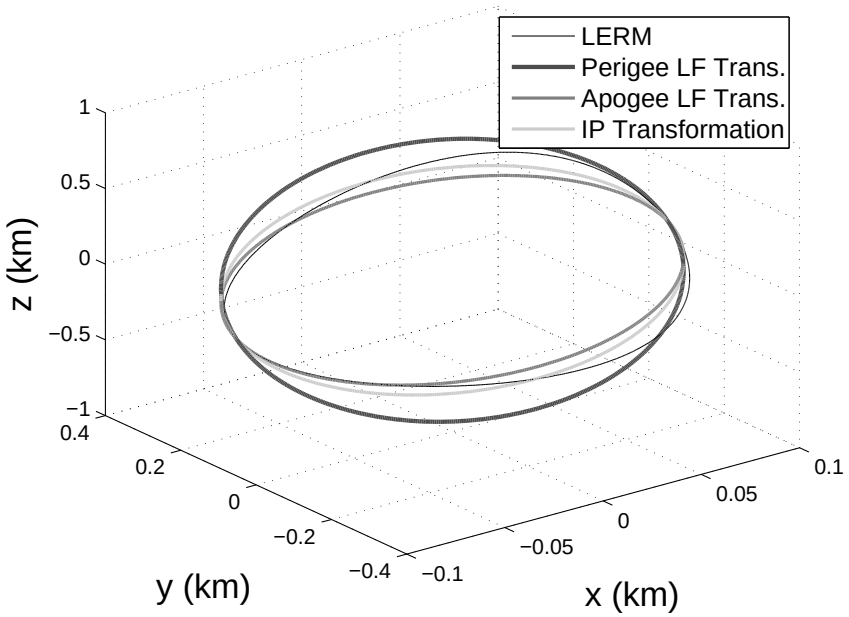

Figure 5.17: Three dimensional representation of the relative-motion trajectory for case 5.

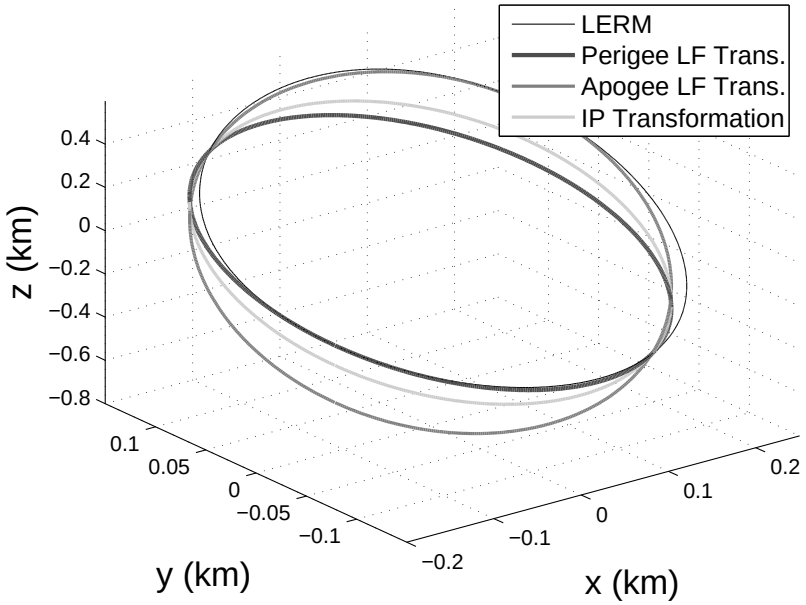

Figure 5.18: Three dimensional representation of the relative-motion trajectory for case 6.

transformation, or the IP transformation at time k. Recall that the position of the LERM solution at time k is given by $\boldsymbol{\rho}_k$. The position error at each time step is given by $\boldsymbol{e}_k = \hat{\boldsymbol{\rho}}_k - \boldsymbol{\rho}_k$. The magnitude of the error, or the error distance, is given by $d_k = \sqrt{\boldsymbol{e}_k^{\mathsf{T}} \boldsymbol{e}_k}$. Figures 5.19 through 5.24 show the error magnitude, d_k, for each case as a function of time for the perigee-matching LF transformation, the apogee-matching LF transformation, and the IP transformation.

To further investigate the error of each method, the mean error, ϵ_M, and the root-mean-square (RMS) of the error, ϵ_{RMS}, can be calculated and are given by the following.

$$\epsilon_M = \frac{1}{m} \sum_{k=1}^{m} d_k; \qquad \epsilon_{RMS} = \sqrt{\frac{1}{m} \sum_{k=1}^{m} d_k^2} \tag{5.20}$$

Here, m represents the total number of time-steps in each solution. The performance of the HCW approximation given by the perigee-matching LF transformation, the apogee-matching LF transformation, and the IP transformation can be compared to the HCW solution whose initial conditions equal the initial conditions of the LERM, i.e., $\boldsymbol{x}_0$. Table 5.2 gives the mean error for each case, while Table 5.3 gives the RMS error. As can be seen, the calibrated HCW solutions clearly outperform the nominal HCW trajectory for every case. The results also show that each transformation performed better for certain cases, but there was not a transformation which clearly outperformed the others for the cases considered. This perhaps indicates that a LF transformation can be derived for mission-specific goals instead of a general solution for all relative-motion cases.

In addition, cases where the underlying relative-motion trajectory appeared to closely match the LERM trajectory did not necessarily translate into low error. This can be best seen by examining case 2. Inspection of the relative-motion trajectory might initially indicate that the perigee-matching LF transformation might be an ideal choice to approximate the HCW trajectory. However, based on the error shown in Tables 5.2 and 5.3, the IP transformation is shown to be a better choice. This disparity is due to a satellite spending more time near

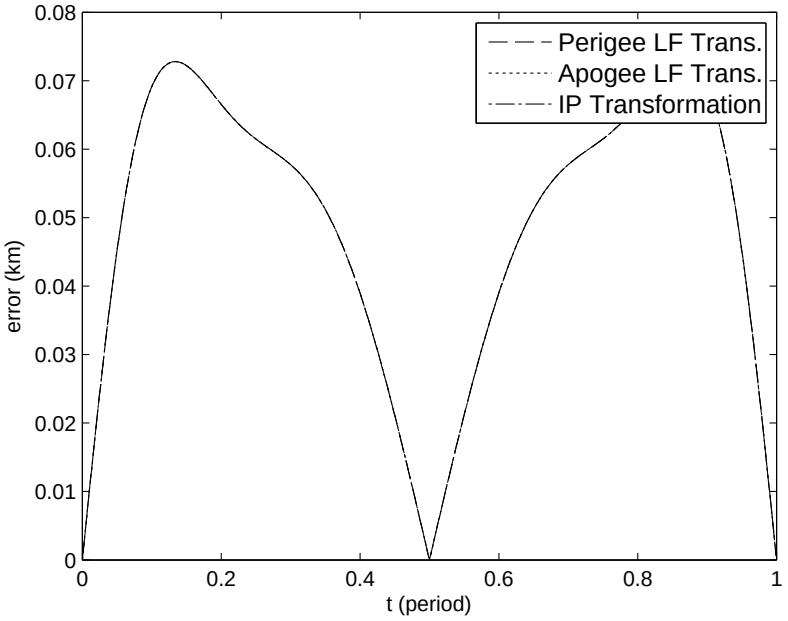

Figure 5.19: Error distance as a function of time for the three underlying HCW trajectories in case 1.

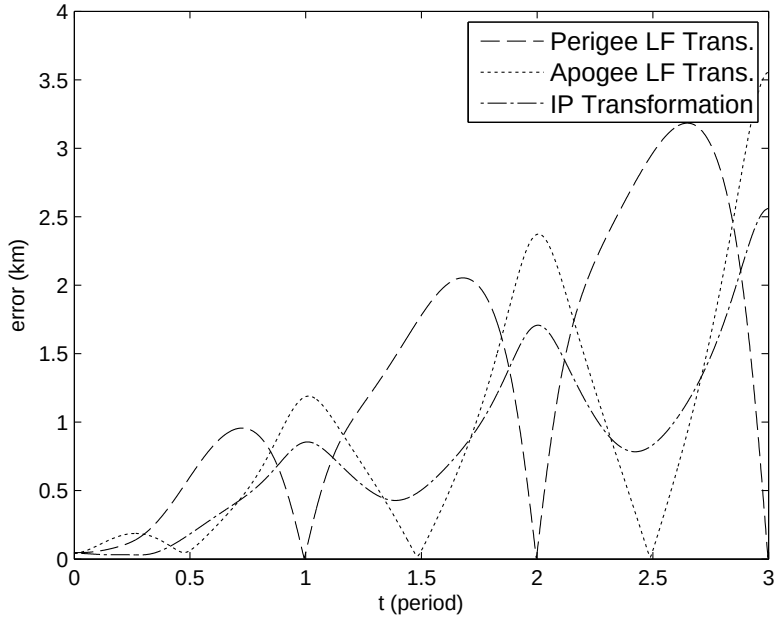

Figure 5.20: Error distance as a function of time for the three underlying HCW trajectories in case 2.

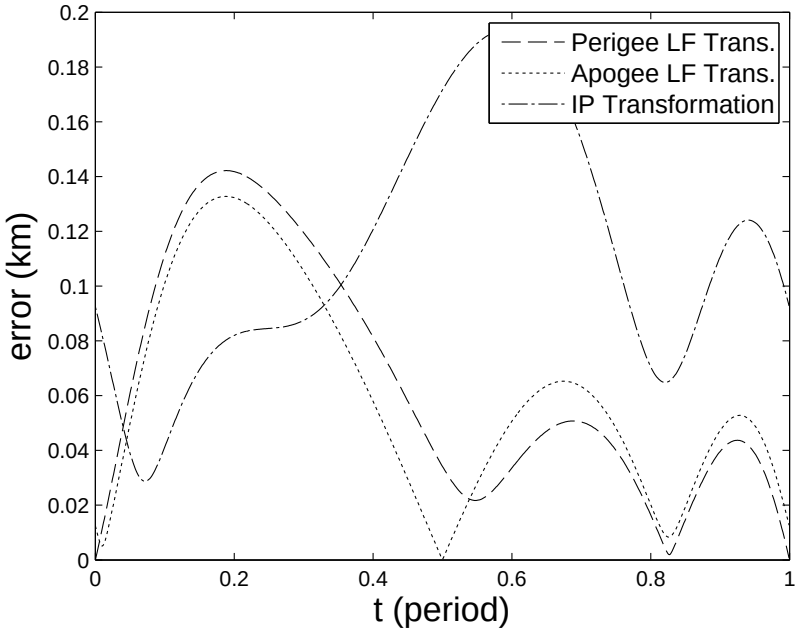

Figure 5.21: Error distance as a function of time for the three underlying HCW trajectories in case 3.

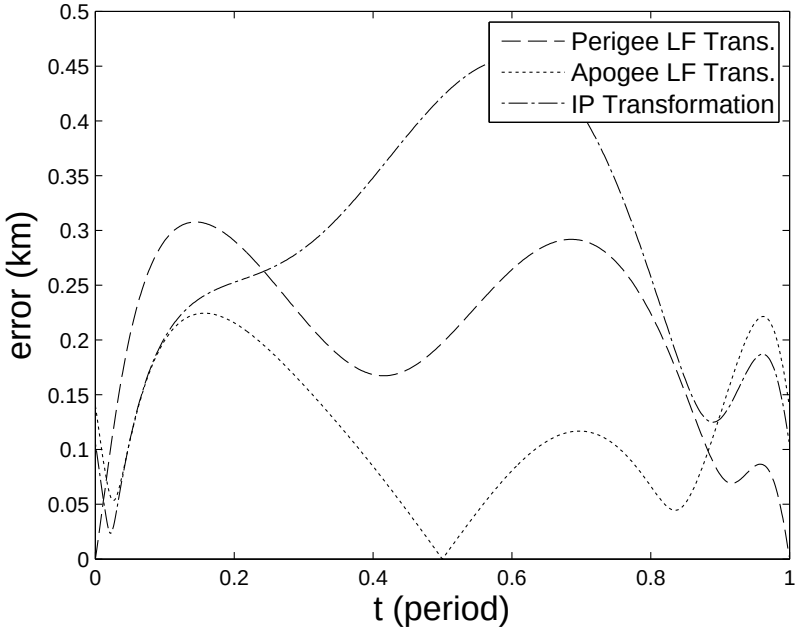

Figure 5.22: Error distance as a function of time for the three underlying HCW trajectories in case 4.

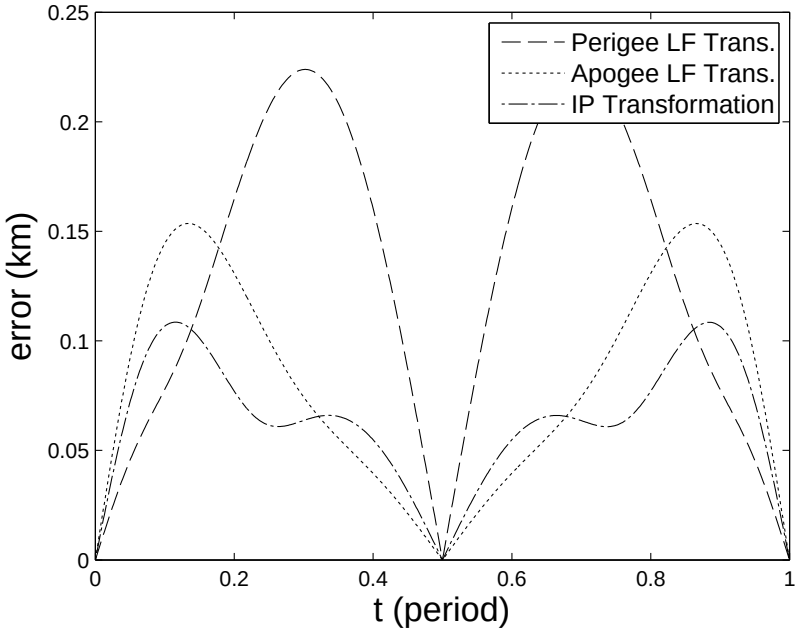

Figure 5.23: Error distance as a function of time for the three underlying HCW trajectories in case 5.

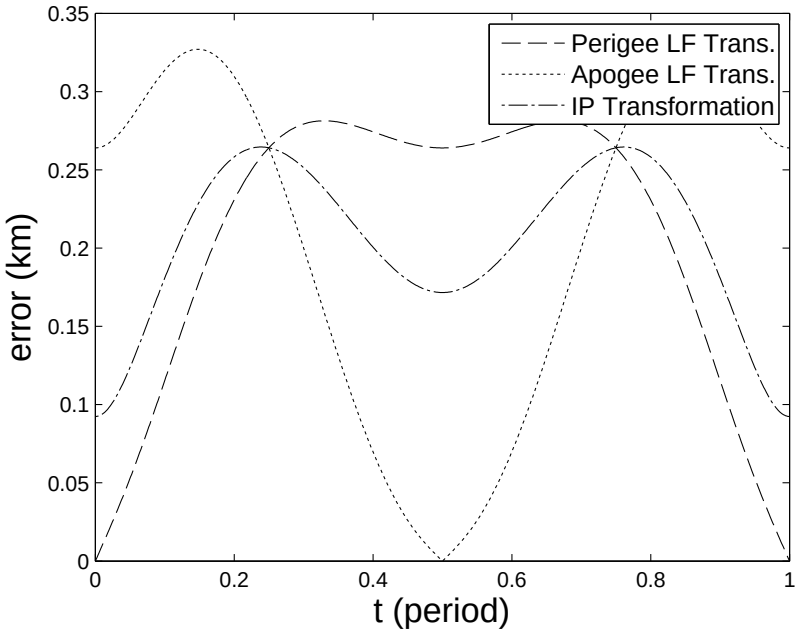

Figure 5.24: Error distance as a function of time for the three underlying HCW trajectories in case 6.

	Perigee LF Trans.	Apogee LF Trans.	IP Transformation	True IC
1	0.0489	0.0489	0.0489	1.5758
2	1.3537	0.9167	0.8183	1.9717
3	0.0644	0.0607	0.1199	1.7034
4	0.2106	0.1200	0.2869	6.9997
5	0.1300	0.0819	0.0642	1.5917
6	0.2077	0.2057	0.2046	1.6118

Table 5.2: Mean error (km) for each case over the simulation time.

	Perigee LF Trans.	Apogee LF Trans.	IP Transformation	True IC
1	0.0530	0.0530	0.0530	1.9777
2	1.6619	1.2426	1.0098	2.4002
3	0.0775	0.0718	0.1210	2.0971
4	0.2237	0.1358	0.3093	8.6714
5	0.1476	0.0949	0.0698	1.9825
6	0.2255	0.2341	0.2105	1.9900

Table 5.3: RMS error (km) for each case over the simulation time.

apogee. Since the perigee-matching LF transformation correctly matches position over a small portion of an orbit, it does not approximate the HCW trajectory over the entirety of the orbit. The apogee-matching transformation is a better choice, but trajectory lags behind the LERM causing significant error when the satellite is near perigee. The drift rate of the IP transformation is between the perigee-matching and apogee-matching LF transformations, and can better capture the motion on average over an orbit. This perhaps indicates the perigee-matching and apogee-matching transformations are upper and lower boundaries of reasonable LF transformations.

Chapter 6

Control of Relative Orbits

This chapter will develop methods to control the relative motion of satellites in elliptic orbits. The literature contains impulsive methods and continuous-thrust control of satellite formations with fixed final time.[16,57,58] This chapter will develop a method for continuous low-thrust maneuvering based on infinite-horizon optimal control. Since continuous-thrust control exists for circular orbits, it is proposed that the Lyapunov-Floquet transformations presented in the previous section be used to transform the control based on time-invariant equations to time-varying systems. This chapter will review an impulsive control method for two-burn solutions and linear quadratic regulators. Then, control of time-varying systems using Lyapunov-Floquet theory is introduced. Finally, this chapter will present four low-thrust scenarios comparing the results of different control aspects.

6.1 Impulsive Control

Because the state-transition matrix for the LERM exists in closed-form, a simple two-burn solution to the two-point boundary-value problem can be constructed. This two-burn maneuver can also referred to as pseudo-Lambert method due to the similarity to Lambert's problem for determining Keplerian transfer orbits. The first burn places the satellite on a trajectory intersecting the origin of the LVLH frame, while the second burn neutralizes any arrival velocity to keep the satellite at the origin. The state-transition matrix of the LERM, given by Equation (2.51), can be partitioned in the following manner.

$$\begin{bmatrix} \boldsymbol{r}(t) \\ \boldsymbol{v}(t) \end{bmatrix} = \begin{bmatrix} \boldsymbol{\Phi}_{rr}(t,t_0) & \boldsymbol{\Phi}_{rv}(t,t_0) \\ \boldsymbol{\Phi}_{vr}(t,t_0) & \boldsymbol{\Phi}_{vv}(t,t_0) \end{bmatrix} \begin{bmatrix} \boldsymbol{r}(t_0) \\ \boldsymbol{v}(t_0) \end{bmatrix} \tag{6.1}$$

Each partition in Equation (6.1) is a 3×3 matrix. Using the partitioned state-transition matrix, separate equations for the position and velocity at time t are given below.

$$\boldsymbol{r}(t) = \boldsymbol{\Phi}_{rr}(t, t_0)\boldsymbol{r}(t_0) + \boldsymbol{\Phi}_{rv}(t, t_0)\boldsymbol{v}(t_0) \tag{6.2}$$

$$\boldsymbol{v}(t) = \boldsymbol{\Phi}_{vr}(t, t_0)\boldsymbol{r}(t_0) + \boldsymbol{\Phi}_{vv}(t, t_0)\boldsymbol{v}(t_0) \tag{6.3}$$

Note that in this case, t is a specified time in which to complete the maneuver. Since the first burn places the satellite on a trajectory toward the origin and the goal is rendezvous at time t, $\boldsymbol{r}(t) = \boldsymbol{0}$. The velocity of this rendezvous trajectory can be determined from Equation (6.2). A superscript $(+)$ indicates velocity after the impulsive burn.

$$\boldsymbol{v}^+(t_0) = -\boldsymbol{\Phi}_{rv}^{-1}(t, t_0)\boldsymbol{\Phi}_{rr}(t, t_0)\boldsymbol{r}(t_0) \tag{6.4}$$

The change in velocity necessary to put the satellite on the rendezvous trajectory is given by the difference between the pre-burn and post-burn velocities.

$$\Delta\boldsymbol{v}_1 = \boldsymbol{v}^+(t_0) - \boldsymbol{v}(t_0) \tag{6.5}$$

The final velocity can be found from Equation (6.3) where a superscript $(-)$ indicates velocity before the impulsive burn.

$$\begin{aligned}
\boldsymbol{v}^-(t) &= \boldsymbol{\Phi}_{vr}(t, t_0)\boldsymbol{r}(t_0) + \boldsymbol{\Phi}_{vv}(t, t_0)\boldsymbol{v}^+(t_0) \\
&= \boldsymbol{\Phi}_{vr}(t, t_0)\boldsymbol{r}(t_0) - \boldsymbol{\Phi}_{vv}(t, t_0)\boldsymbol{\Phi}_{rv}^{-1}(t, t_0)\boldsymbol{\Phi}_{rr}(t, t_0)\boldsymbol{r}(t_0) &(6.6)\\
&= \left[\boldsymbol{\Phi}_{vr}(t, t_0) - \boldsymbol{\Phi}_{vv}(t, t_0)\boldsymbol{\Phi}_{rv}^{-1}(t, t_0)\boldsymbol{\Phi}_{rr}(t, t_0)\right]\boldsymbol{r}(t_0) &(6.7)
\end{aligned}$$

The second velocity change brings the final velocity to zero.

$$\Delta\boldsymbol{v}_2 = \boldsymbol{0} - \boldsymbol{v}^-(t) = -\boldsymbol{v}^-(t) \tag{6.8}$$

The total velocity magnitude is found from Equations (6.5) and (6.8).

$$v_{total} = \|\Delta \boldsymbol{v}_1\| + \|\Delta \boldsymbol{v}_2\| \tag{6.9}$$

A unique feature of the two-burn method is that the time to complete the maneuver needs to be specified. For certain initial conditions, changing the maneuver time has little effect on the deputy's trajectory. Consider the case where the chief's orbital elements are given by $a_C = 8000$ km, $e_C = 0.1$, and $i_C = \Omega_C = \omega_C = f_C = 0$. The relative position and velocity of the deputy at time t_0 is given by $x(t_0) = [0 \ -2 \ 0 \ 0 \ 0 \ 0]^\mathsf{T}$. Figure 6.1 shows the deputy's trajectory for $t = P$ with a total velocity change of 2.8872×10^{-4} km/s, while Figure 6.2 shows the deputy's trajectory for $t = 5P$ with a total velocity change of 2.1313×10^{-4} km/s. For this example of a chief and deputy satellite in a "leader-follower" configuration, the trajectory is similar for both time spans and the difference in required velocity is on the order of centimeters per second.

Consider a second case where the chief's orbital elements are the same but the relative position and velocity of the deputy at time t_0 is given by $x(t_0) = [0.1 \ 0 \ 0 \ 0 \ 0 \ 0]^\mathsf{T}$. Figure 6.3 shows the deputy's trajectory for $t = P$ with a total velocity change of 1.8051×10^{-2} km/s, while Figure 6.4 shows the deputy's trajectory for $t = 0.5P$ with a total velocity change of 2.5145×10^{-4} km/s. For this case, changing the maneuver time to a fraction of a period dramatically changes the size of the relative trajectory and lowered the required velocity change by two orders of magnitude. As was seen with the above examples, the maneuver time needs to be chosen with care when employing the two-burn method. Okasha and Newman developed a method to specify intermediate points along the relative trajectory when using the two-burn method, which forces the relative motion to be bounded.[59]

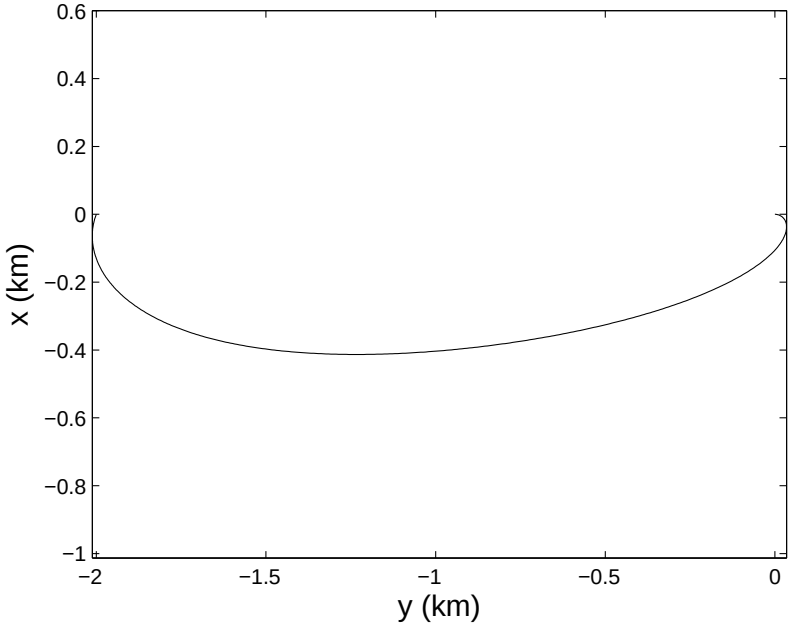

Figure 6.1: Two-burn maneuver over one period.

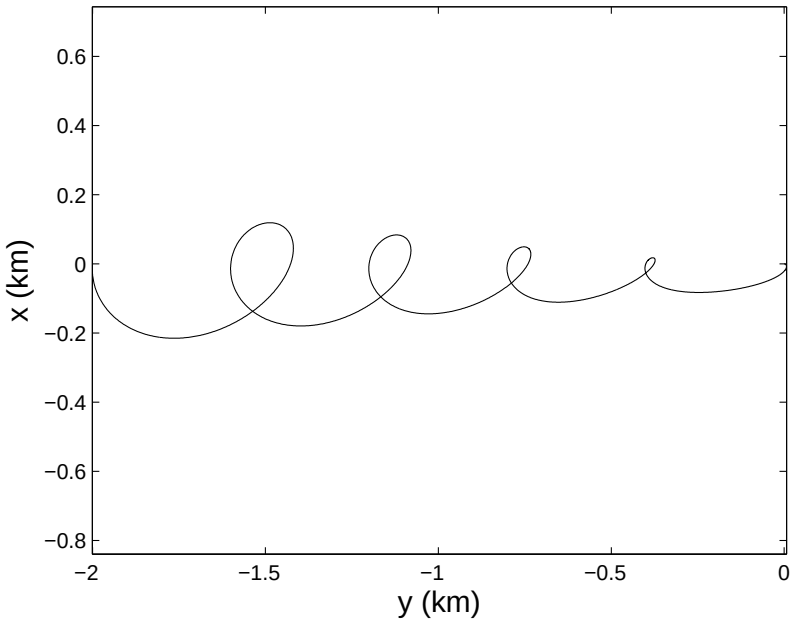

Figure 6.2: Two-burn maneuver over five periods.

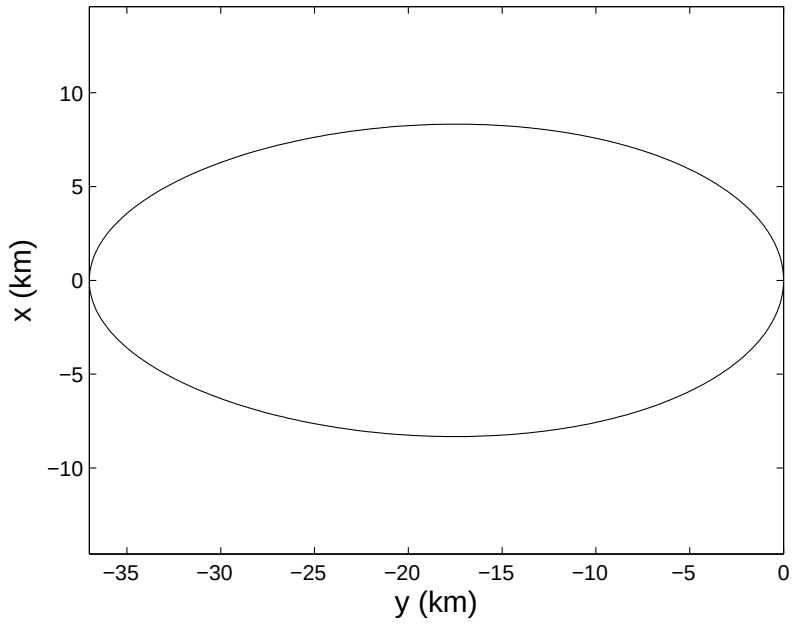

Figure 6.3: Two-burn maneuver over one period.

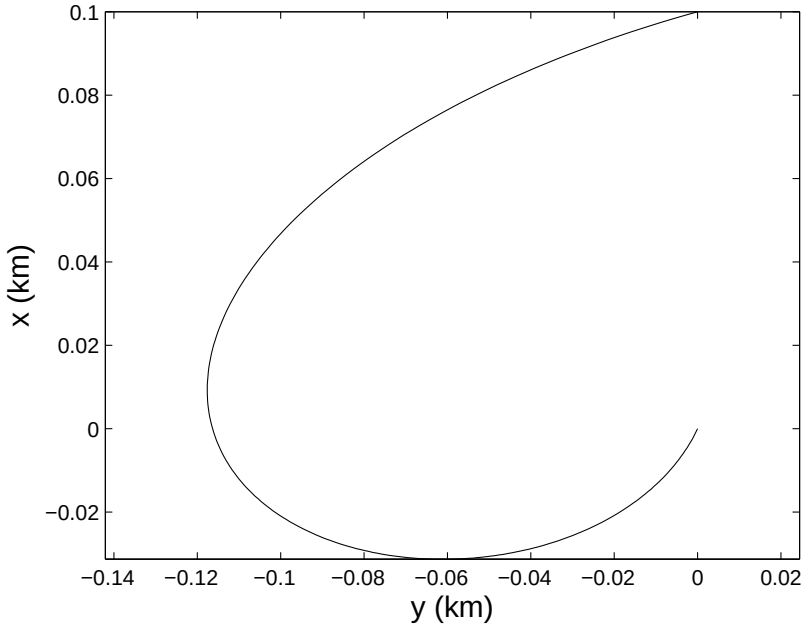

Figure 6.4: Two-burn maneuver over half a period.

6.2 Linear Quadratic Regulator

Consider the linear time-invariant system $\dot{\boldsymbol{x}} = \boldsymbol{A}\boldsymbol{x} + \boldsymbol{B}\boldsymbol{u}$ where $\boldsymbol{x}$ represents the states and $\boldsymbol{u}$ represents the control. It is desired to control the system while achieving some sort of system performance. This performance could include factors such as rise-time, overshoot, or to use a minimum control effort. To give a qualitative measure of system performance, a cost function J is introduced. By minimizing this cost function, the system can brought from an initial state at t_0 to a final state at t_f with acceptable levels of state error and using acceptable levels of control and along this trajectory.

A common choice for the performance index is to use a quadratic form of the terminal state and an integral of the quadratic form of the current state and control.

$$J = \frac{1}{2}\boldsymbol{x}^{\mathsf{T}}(t_f)\boldsymbol{S}_f\boldsymbol{x}(t_f) + \frac{1}{2}\int_{t_0}^{t_f}\left(\boldsymbol{x}^{\mathsf{T}}\boldsymbol{Q}\boldsymbol{x} + \boldsymbol{u}^{\mathsf{T}}\boldsymbol{R}\boldsymbol{u}\right)dt \tag{6.10}$$

Here, $\boldsymbol{S}_f$ and $\boldsymbol{Q}$ are symmetric positive semidefinite matrices and $\boldsymbol{R}$ is a symmetric positive definite matrix. The matrix $\boldsymbol{S}_f$ represents the weighting on the final state, $\boldsymbol{Q}$ represents the weighting on the state, and $\boldsymbol{R}$ represents the weighting on the control. The Hamiltonian, H, can be formed with the addition of Lagrange multipliers or co-states, λ. The co-states represent sensitivity of the cost to the states. The form of the Hamiltonian is shown below.

$$H = \frac{1}{2}\left(\boldsymbol{x}^{\mathsf{T}}\boldsymbol{Q}\boldsymbol{x} + \boldsymbol{u}^{\mathsf{T}}\boldsymbol{R}\boldsymbol{u}\right) + \lambda^{\mathsf{T}}\left(\boldsymbol{A}\boldsymbol{x} + \boldsymbol{B}\boldsymbol{u}\right) \tag{6.11}$$

The Hamiltonian gives the three first-order necessary conditions for optimality.

$$\dot{\boldsymbol{\lambda}} = -\frac{\partial H}{\partial \boldsymbol{x}} = -\boldsymbol{Q}\boldsymbol{x} - \boldsymbol{A}^{\mathsf{T}}\boldsymbol{\lambda} \tag{6.12}$$

$$\boldsymbol{0} = \frac{\partial H}{\partial \boldsymbol{u}} = \boldsymbol{R}\boldsymbol{u} + \boldsymbol{B}^{\mathsf{T}}\boldsymbol{\lambda} \tag{6.13}$$

$$\dot{\boldsymbol{x}} = \frac{\partial H}{\partial \boldsymbol{\lambda}} = \boldsymbol{A}\boldsymbol{x} + \boldsymbol{B}\boldsymbol{u} \tag{6.14}$$

From Equation (6.13), $\boldsymbol{u} = -\boldsymbol{R}^{-1}\boldsymbol{B}^{\mathsf{T}}\boldsymbol{\lambda}$. This allows the closed loop system to be written in the following form.

$$\dot{\boldsymbol{x}} = \boldsymbol{A}\boldsymbol{x} - \boldsymbol{B}\boldsymbol{R}^{-1}\boldsymbol{B}^{\mathsf{T}}\boldsymbol{\lambda} \tag{6.15}$$

From Equations (6.12) and (6.14), the following system can be constructed.

$$\begin{bmatrix} \dot{\boldsymbol{x}} \\ \dot{\boldsymbol{\lambda}} \end{bmatrix} = \begin{bmatrix} \boldsymbol{A} & -\boldsymbol{B}\boldsymbol{R}^{-1}\boldsymbol{B}^{\mathsf{T}} \\ -\boldsymbol{Q} & -\boldsymbol{A}^{\mathsf{T}} \end{bmatrix} \begin{bmatrix} \boldsymbol{x} \\ \boldsymbol{\lambda} \end{bmatrix} \tag{6.16}$$

Note that each entry in the state matrix in Equation (6.16) is $n \times n$. Since each system in Equation (6.16) is linear, a transformation $\boldsymbol{\lambda}(t) = \boldsymbol{S}(t)\boldsymbol{x}(t)$ is proposed. Taking one derivative and using Equation (6.12) gives the following expression.

$$\begin{gathered} \dot{\boldsymbol{\lambda}} = \dot{\boldsymbol{S}}(t)\boldsymbol{x}(t) + \boldsymbol{S}(t)\dot{\boldsymbol{x}}(t) = -\boldsymbol{Q}\boldsymbol{x}(t) - \boldsymbol{A}^{\mathsf{T}}\boldsymbol{\lambda}(t) \\ \dot{\boldsymbol{S}}(t)\boldsymbol{x}(t) + \boldsymbol{S}(t)\left(\boldsymbol{A}\boldsymbol{x}(t) - \boldsymbol{B}\boldsymbol{R}^{-1}\boldsymbol{B}^{\mathsf{T}}\boldsymbol{S}(t)\boldsymbol{x}(t)\right) = -\boldsymbol{Q}\boldsymbol{x}(t) - \boldsymbol{A}^{\mathsf{T}}\boldsymbol{S}(t)\boldsymbol{x}(t) \\ \left(\dot{\boldsymbol{S}}(t) + \boldsymbol{S}(t)\boldsymbol{A} + \boldsymbol{A}^{\mathsf{T}}\boldsymbol{S}(t) - \boldsymbol{S}(t)\boldsymbol{B}\boldsymbol{R}^{-1}\boldsymbol{B}^{\mathsf{T}}\boldsymbol{S}(t) + \boldsymbol{Q}\right)\boldsymbol{x}(t) = \boldsymbol{0} \end{gathered} \tag{6.17}$$

Since $\boldsymbol{x}(t) \neq 0$, Equation (6.17) gives the following.

$$\dot{\boldsymbol{S}}(t) + \boldsymbol{S}(t)\boldsymbol{A} + \boldsymbol{A}^{\mathsf{T}}\boldsymbol{S}(t) - \boldsymbol{S}(t)\boldsymbol{B}\boldsymbol{R}^{-1}\boldsymbol{B}^{\mathsf{T}}\boldsymbol{S}(t) + \boldsymbol{Q} = \boldsymbol{0} \tag{6.18}$$

Equation (6.18) is known as the Ricatti Equation. As $t_f \to \infty$, stead-state solutions of the Ricatti Equation give $\dot{\boldsymbol{S}} = \boldsymbol{0}$. This steady-state value is a solution to the Algebraic Ricatti Equation.

$$\boldsymbol{S}\boldsymbol{A} + \boldsymbol{A}^{\mathsf{T}}\boldsymbol{S} - \boldsymbol{S}\boldsymbol{B}\boldsymbol{R}^{-1}\boldsymbol{B}^{\mathsf{T}}\boldsymbol{S} + \boldsymbol{Q} = \boldsymbol{0} \tag{6.19}$$

Defining $\boldsymbol{K} = -\boldsymbol{R}^{-1}\boldsymbol{B}^{\mathsf{T}}\boldsymbol{S}$ and using $\boldsymbol{\lambda}(t) = \boldsymbol{S}\boldsymbol{x}(t)$, the control law can be determined from Equation (6.15) and the system can be propagated forward in time.

$$\begin{aligned} \dot{\boldsymbol{x}} &= \boldsymbol{A}\boldsymbol{x} - \boldsymbol{B}\boldsymbol{R}^{-1}\boldsymbol{B}^{\mathsf{T}}\boldsymbol{S}\boldsymbol{x} \\ \dot{\boldsymbol{x}} &= (\boldsymbol{A} - \boldsymbol{B}\boldsymbol{K})\,\boldsymbol{x} \end{aligned} \tag{6.20}$$

6.3 Control of Time-Periodic Systems using Lyapunov-Floquet Theory

6.3.1 Control Method

A control method described by Sinha and Joseph is here presented.[60,61] Consider the state equation of a controllable linear time-periodic system.

$$\dot{\boldsymbol{x}}(t) = \boldsymbol{A}(t)\boldsymbol{x}(t) + \boldsymbol{B}(t)\boldsymbol{u}(t) \tag{6.21}$$

Applying a Lyapunov-Floquet transformation of the control-free system to Equation (6.21) gives the following.

$$\dot{\boldsymbol{z}}(t) = \boldsymbol{\Lambda}\boldsymbol{z}(t) + \boldsymbol{P}^{-1}(t)\boldsymbol{B}(t)\boldsymbol{u}(t) \tag{6.22}$$

If the product $\boldsymbol{P}^{-1}(t)\boldsymbol{B}(t)$ is considered to be the control matrix, then Equation (6.22) has a constant system matrix and a time-varying control matrix. Sinha and Joseph proposed the following auxiliary system which has a more desirable form.

$$\dot{\widetilde{\boldsymbol{z}}}(t) = \boldsymbol{\Lambda}\widetilde{\boldsymbol{z}}(t) + \widetilde{\boldsymbol{B}}\boldsymbol{v}(t) \tag{6.23}$$

Here, $\widetilde{\boldsymbol{B}}$ is chosen such that $\boldsymbol{\Lambda}$ and $\widetilde{\boldsymbol{B}}$ are controllable, and a control law $\boldsymbol{v}(t) = -\widetilde{\boldsymbol{K}}\widetilde{\boldsymbol{z}}(t)$ is designed. The time-invariant gain matrix $\widetilde{\boldsymbol{K}}$ can be chosen through pole-placement or optimal control techniques such that the auxiliary system is asymptotically stable. Using this constant gain matrix, the closed-loop system is given by $\dot{\widetilde{\boldsymbol{z}}} = \left(\boldsymbol{\Lambda} - \widetilde{\boldsymbol{B}}\widetilde{\boldsymbol{K}}\right)\widetilde{\boldsymbol{z}}$, and the closed-loop state-transition matrix $\boldsymbol{\Phi}_{\widetilde{\boldsymbol{z}}}(t_2, t_1) = e^{\left(\boldsymbol{\Lambda} - \widetilde{\boldsymbol{B}}\widetilde{\boldsymbol{K}}\right)(t_2 - t_1)}$ is defined. The dynamics of the

state-transition matrix are given by $\dot{\boldsymbol{\Phi}}_{\widetilde{\boldsymbol{z}}} = \left(\boldsymbol{\Lambda} - \widetilde{\boldsymbol{B}}\widetilde{\boldsymbol{K}}\right)\boldsymbol{\Phi}_{\widetilde{\boldsymbol{z}}}$. Since $\widetilde{\boldsymbol{z}}$ is chosen to approximate $\boldsymbol{z}$, Equations (6.22) and (6.23) would be equivalent if $\boldsymbol{P}^{-1}(t)\boldsymbol{B}(t)\boldsymbol{u}(t) = -\widetilde{\boldsymbol{B}}\widetilde{\boldsymbol{K}}\boldsymbol{z}(t)$. Instead, the equality $\boldsymbol{B}(t)\boldsymbol{u}(t) = -\boldsymbol{P}(t)\widetilde{\boldsymbol{B}}\widetilde{\boldsymbol{K}}\boldsymbol{z}(t)$ is chosen because this form better approximates the true time-varying system given by Equations (6.21). In general, no exact solution for $\boldsymbol{u}(t)$ exists. The approximate solution that minimizes the error norm is given by the following expression.

$$\boldsymbol{u}(t) = -\left(\boldsymbol{B}^{\mathsf{T}}(t)\boldsymbol{B}(t)\right)^{-1}\boldsymbol{B}^{\mathsf{T}}(t)\boldsymbol{P}(t)\widetilde{\boldsymbol{B}}\widetilde{\boldsymbol{K}}\boldsymbol{z}(t) \tag{6.24}$$

Using Equations (6.24) and (6.22), the closed-loop Lyapunov-Floquet system is given by the following.

$$\begin{aligned}\dot{\boldsymbol{z}}(t) &= \boldsymbol{\Lambda}\boldsymbol{z}(t) - \boldsymbol{P}^{-1}(t)\boldsymbol{B}(t)\left(\boldsymbol{B}^{\mathsf{T}}(t)\boldsymbol{B}(t)\right)^{-1}\boldsymbol{B}^{\mathsf{T}}(t)\boldsymbol{P}(t)\widetilde{\boldsymbol{B}}\widetilde{\boldsymbol{K}}\boldsymbol{z}(t)\\ &= \left(\boldsymbol{\Lambda} - \boldsymbol{P}^{-1}(t)\boldsymbol{B}(t)\left(\boldsymbol{B}^{\mathsf{T}}(t)\boldsymbol{B}(t)\right)^{-1}\boldsymbol{B}^{\mathsf{T}}(t)\boldsymbol{P}(t)\widetilde{\boldsymbol{B}}\widetilde{\boldsymbol{K}}\right)\boldsymbol{z}(t)\end{aligned} \tag{6.25}$$

Applying the Lyapunov-Floquet transformation to Equation (6.25) results in the following.

$$\begin{aligned}\dot{\boldsymbol{x}}(t) &= \boldsymbol{A}(t)\boldsymbol{x}(t) - \boldsymbol{B}(t)\left(\boldsymbol{B}^{\mathsf{T}}(t)\boldsymbol{B}(t)\right)^{-1}\boldsymbol{B}^{\mathsf{T}}(t)\boldsymbol{P}(t)\widetilde{\boldsymbol{B}}\widetilde{\boldsymbol{K}}\boldsymbol{P}^{-1}(t)\boldsymbol{x}(t)\\ &= \left(\boldsymbol{A}(t) - \boldsymbol{B}(t)\left(\boldsymbol{B}^{\mathsf{T}}(t)\boldsymbol{B}(t)\right)^{-1}\boldsymbol{B}^{\mathsf{T}}(t)\boldsymbol{P}(t)\widetilde{\boldsymbol{B}}\widetilde{\boldsymbol{K}}\boldsymbol{P}^{-1}(t)\right)\boldsymbol{x}(t)\end{aligned} \tag{6.26}$$

Therefore, the control law for the time-varying system is given by $\boldsymbol{u}(t) = -\boldsymbol{K}(t)\boldsymbol{x}(t)$, with the following gain matrix.

$$\boldsymbol{K}(t) = \left(\boldsymbol{B}^{\mathsf{T}}(t)\boldsymbol{B}(t)\right)^{-1}\boldsymbol{B}^{\mathsf{T}}(t)\boldsymbol{P}(t)\widetilde{\boldsymbol{B}}\widetilde{\boldsymbol{K}}\boldsymbol{P}^{-1}(t) \tag{6.27}$$

This time-varying gain matrix applies the calculated time-invariant gain to the time-varying system. Equation (6.27) allows the closed-loop system given by Equation (6.26) to be written in the following form.

$$\dot{\boldsymbol{x}}(t) = \left(\boldsymbol{A}(t) - \boldsymbol{B}(t)\boldsymbol{K}(t)\right)\boldsymbol{x}(t) \tag{6.28}$$

The dynamics of the closed-loop state-transition matrix for Equation (6.28) is given by $\dot{\boldsymbol{\Phi}}_{\boldsymbol{x}} = (\boldsymbol{A}(t) - \boldsymbol{B}(t)\boldsymbol{K}(t))\,\boldsymbol{\Phi}_{\boldsymbol{x}}$. Because an approximate solution for $\boldsymbol{u}(t)$ is used, stability of $\boldsymbol{x}$ is not guaranteed. Therefore, the eigenvalues of $\boldsymbol{\Phi}_{\boldsymbol{x}}(P, 0)$ must be checked to verify stability.

To demonstrate this control method, Sinha and Joseph presented the following example of a commutative system where α is a parameter.

$$\dot{\boldsymbol{x}}(t) = 2\pi \begin{bmatrix} -1 + \alpha\cos^2(2\pi t) & 1 - \alpha\sin(2\pi t)\cos(2\pi t) \\ -1 - \alpha\sin(2\pi t)\cos(2\pi t) & -1 + \alpha\sin^2(2\pi t) \end{bmatrix} \boldsymbol{x}(t) + \begin{bmatrix} 0 \\ t \end{bmatrix} \boldsymbol{u}(t) \quad (6.29)$$

The state transition matrix of this system is given by the following.

$$\boldsymbol{\Phi}(t, t_0) = \begin{bmatrix} e^{2\pi(\alpha-1)(t-t_0)}\cos(2\pi(t-t_0)) & e^{-2\pi(t-t_0)}\sin(2\pi(t-t_0)) \\ -e^{2\pi(\alpha-1)(t-t_0)}\sin(2\pi(t-t_0)) & e^{-2\pi(t-t_0)}\cos(2\pi(t-t_0)) \end{bmatrix} \quad (6.30)$$

Equation (6.30) has a known Lyapunov-Floquet transformation where $\boldsymbol{P}(t)$ is a rotation matrix and $\boldsymbol{C}$ is a diagonal matrix.

$$\boldsymbol{P}(t) = \begin{bmatrix} \cos(2\pi t) & \sin(2\pi t) \\ -\sin(2\pi t) & \cos(2\pi t) \end{bmatrix} \quad ; \quad \boldsymbol{C} = \begin{bmatrix} 2\pi(\alpha - 1) & 0 \\ 0 & -2\pi \end{bmatrix} \quad (6.31)$$

Clearly, the system is unstable for $\alpha > 1$.

Consider the case where $\alpha = 1.2$ and $\boldsymbol{x}(0) = [0.6\ 0.3]^{\mathsf{T}}$. Figure 6.5 shows the uncontrolled response of the system. The method presented in this section will be used to stabilize the system. Here, $\widetilde{\boldsymbol{B}}$ was chosen to equal a 2×2 identity matrix, and $\widetilde{\boldsymbol{K}}$ was chosen to be a diagonal matrix. The poles, p_1 and p_2, of the closed-loop time-invariant system were selected to equal -3.5 and -5 respectively, with the gains determined through the pole-placement technique. Figure 6.6 shows the response of the closed-loop time-invariant auxiliary system

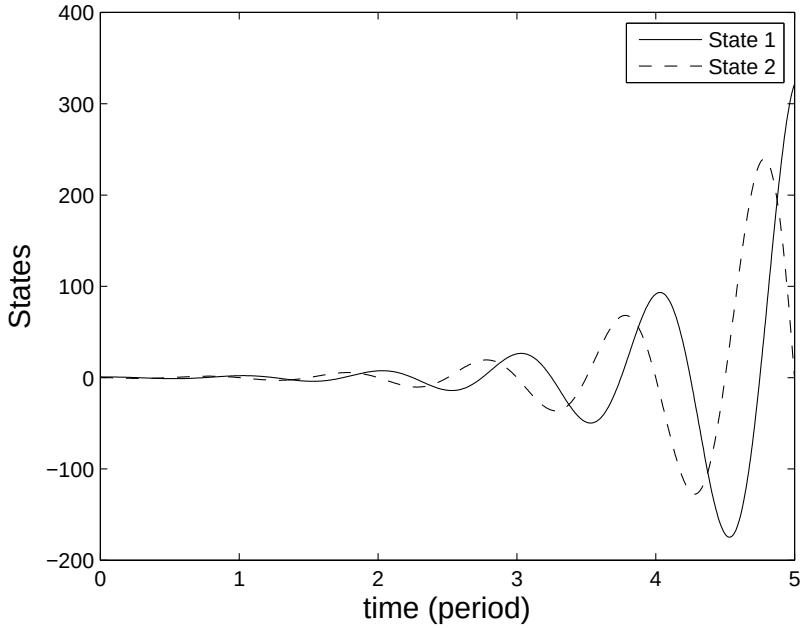

Figure 6.5: Uncontrolled states of the system.

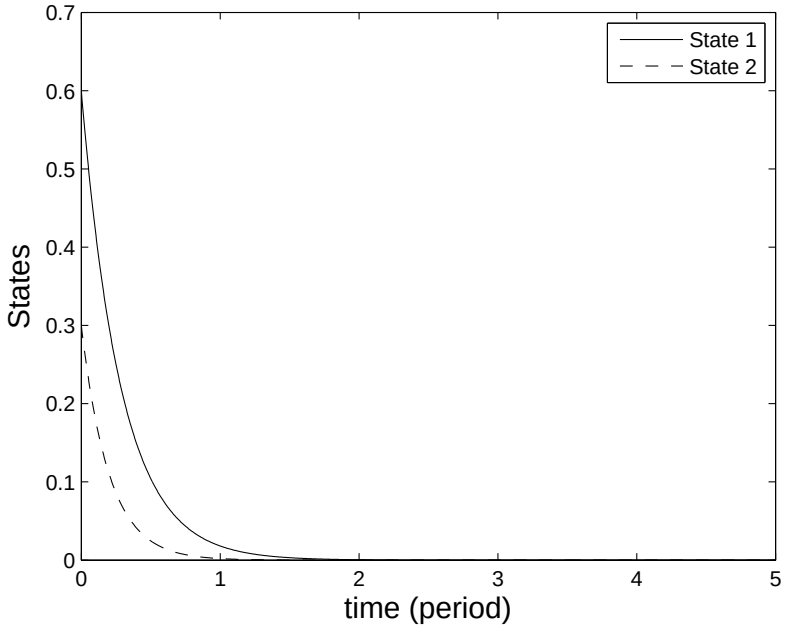

Figure 6.6: State feedback control of time-invariant auxiliary system.

given by Equation (6.23), and Figure 6.7 shows the closed-loop response to the time-varying system where the time-varying gain matrix was calculated using Equation (6.27).

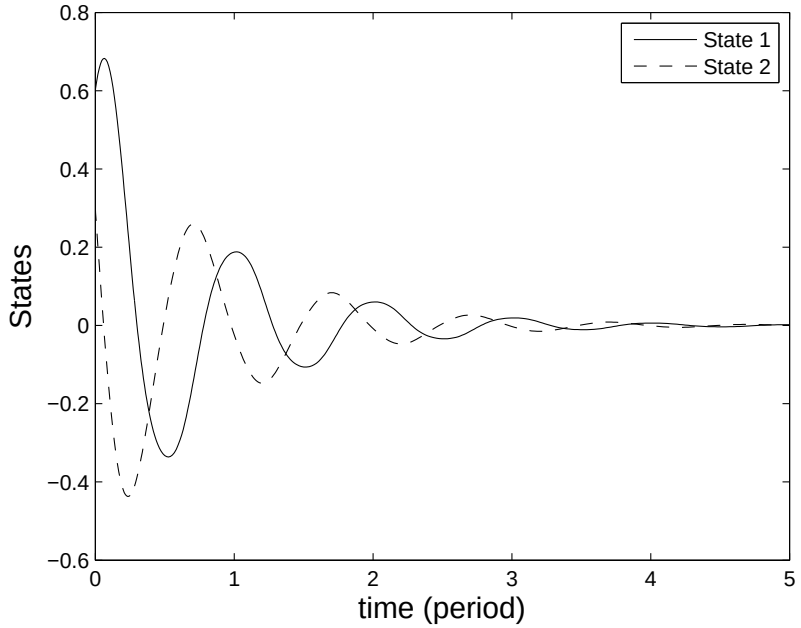

Figure 6.7: State feedback control of the time-varying system.

6.3.2 Discussion

An investigation was conducted to determine the relationship between the stability of the time-invariant auxiliary system and the time-varying system, i.e. are there pole locations that stabilize the time-invariant system but do not stabilize the time-varying system, and does the time-invariant system need to be stable for the time-varying system to be stable? Stability was determined by integrating the closed-loop state transition matrix of the time-varying system over one period. If the magnitude of all the eigenvalues are less than one, then the time-varying system is asymptotically stable.

This investigation considered both positive and negative values of p_1 and p_2. These time-invariant pole locations were varied over the range $-10 < p_1 < 10$ and $-10 < p_2 < 10$ in increments of 0.25. For each pair of pole locations, the stability of the time-varying system was determined. A dot indicates if the pole combination resulted in an unstable time-varying system. As can be seen in Figure 6.8, small negative values of p_1 which produce a stable time-invariant auxiliary system, do not produce a stable time-varying system. The values of

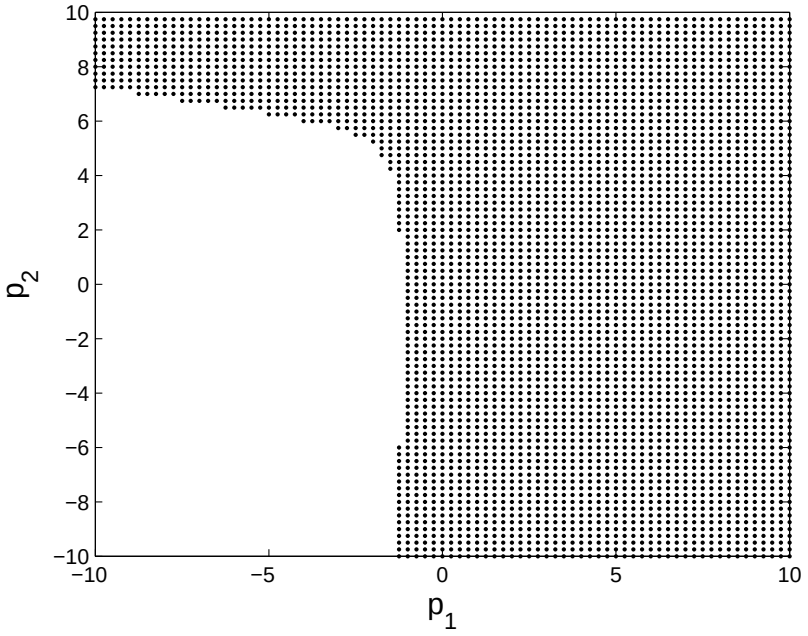

Figure 6.8: Pole locations resulting in unstable time-varying system.

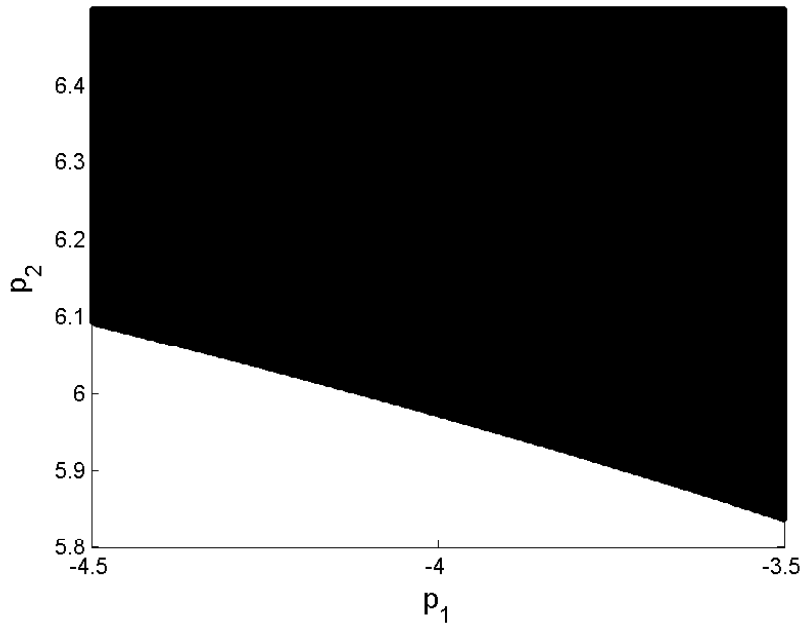

Figure 6.9: Detailed study of the stability boundary.

p_1 which do not stabilize the system have time constants greater than one. Equation (6.30) indicates that the system has a periodicity of one. This perhaps indicates that the time constant must be less than the periodicity of the system for Equation (6.27) to stabilize the time-varying system. In addition, some positive values of p_2 stabilize the time-varying system. Of course, these positive values of p_2 do not stabilize the time-invariant system. This indicates that for certain values of p_1 and p_2, stabilizing one state of the system can produce a stable time-varying system. A detailed study of the boundary between stable and unstable pole locations was also conducted using increments of 0.001. As can be seen in Figure 6.9, the boundary appears smooth and does not contain small surface features. While not shown here, pole locations were also varied over the range $-100 < p_1 < 0$ and $-100 < p_2 < 0$. The results show that even for very negative values of p_2, combined with small negative values of p_1, the closed-loop time-invariant system was unstable.

6.4 Control of Satellites in Elliptic Orbits*

Infinite-horizon continuous-thrust control of relative motion in elliptic orbits does not currently appear in the literature. The methods of Section 6.3.1 will be used with the Lyapunov-Floquet transformations from the previous chapter to several different types of elliptic orbits. Subsections 6.4.1 through 6.4.3 will use the periapse-matching transformation, whereas subsection 6.4.4 will compare the periapse-matching and apoapse-matching transformations. Here, the optimal control law will be calculated using the linear quadratic regulator discussed in Section 6.2. In addition, limited comparison to impulsive control will be presented.

6.4.1 Near-circular Orbits

The first continuous-thrust application will be for a chief satellite in a near-circular orbit. The corresponding low value of chief eccentricity represents many active satellites.

*Material in this section will be presented at the AAS/AIAA Astrodynamics Specialist Conference, Hilton Head, South Carolina, August 2013

For each initial condition, the goal is for the deputy satellite to converge to the vicinity of the chief. The motion over five orbital periods will be considered. It is assumed that the satellite can apply control in every direction. Therefore, the control matrix is given by the following.

$$\boldsymbol{B} = \begin{bmatrix} 0 & 0 & 0 \\ 0 & 0 & 0 \\ 0 & 0 & 0 \\ 1 & 0 & 0 \\ 0 & 1 & 0 \\ 0 & 0 & 1 \end{bmatrix} \tag{6.32}$$

As detailed in the previous section, an auxiliary time-invariant system is constructed and a constant gain matrix, $\widetilde{\boldsymbol{K}}$, is computed. For this auxiliary system, $\boldsymbol{\Lambda} = \boldsymbol{C}$, the state-space representation of the HCW equations, and using the same assumption that the satellite can apply control in every direction, $\widetilde{\boldsymbol{B}} = \boldsymbol{B}$. For this application, the gain matrix will be calculated using the LQR method. Similar to Reference 62, it was chosen to scale the LQR weighting matrices $\boldsymbol{Q}$ and $\boldsymbol{R}$ by the mean motion to ensure constant units. These diagonal matrices are given by the following.

$$\boldsymbol{Q} = \begin{bmatrix} 1 & 0 & 0 & 0 & 0 & 0 \\ 0 & 1 & 0 & 0 & 0 & 0 \\ 0 & 0 & 1 & 0 & 0 & 0 \\ 0 & 0 & 0 & \frac{1}{n^2} & 0 & 0 \\ 0 & 0 & 0 & 0 & \frac{1}{n^2} & 0 \\ 0 & 0 & 0 & 0 & 0 & \frac{1}{n^2} \end{bmatrix} \quad ; \quad \boldsymbol{R} = 100 \begin{bmatrix} \frac{1}{n^4} & 0 & 0 \\ 0 & \frac{1}{n^4} & 0 \\ 0 & 0 & \frac{1}{n^4} \end{bmatrix} \tag{6.33}$$

Using these values for $\boldsymbol{Q}$ and $\boldsymbol{R}$, the constant gain matrix $\widetilde{\boldsymbol{K}}$ is given by the following.

$$\widetilde{\boldsymbol{K}} = \begin{bmatrix} 2.4585 \times 10^{-7} & -2.0596 \times 10^{-8} & 0 & 1.7904 \times 10^{-4} \\ 6.1826 \times 10^{-7} & -2.1740 \times 10^{-8} & 0 & 1.9413 \times 10^{-4} \\ 0 & 0 & 1.4936 \times 10^{-9} & 0 \end{bmatrix}$$

$$\begin{bmatrix} 1.9413 \times 10^{-4} & 0 \\ 5.8887 \times 10^{-4} & 0 \\ 0 & 7.7343 \times 10^{-5} \end{bmatrix} \tag{6.34}$$

This subsection will present three different aspects of applying the control to elliptic orbits. The first aspect is the time-invariant auxiliary system, $\widetilde{\boldsymbol{z}}(t)$, given by Equation (6.23), with the control law $\boldsymbol{v} = -\widetilde{\boldsymbol{K}}\widetilde{\boldsymbol{z}}$. It is important to study the behavior of this system since it was used to compute the gain matrix $\widetilde{\boldsymbol{K}}$. For the second aspect, the time-invariant gain matrix $\widetilde{\boldsymbol{K}}$ computed from the auxiliary system is used to construct a time-varying gain matrix $\boldsymbol{K}(t)$ using Equation 6.27. This time-varying gain matrix is applied to the true time-invariant system $\boldsymbol{z}(t)$ given by Equation (6.25) with the control law $\boldsymbol{u}(t)$ given by Equation (6.24). Note that for this LF-transformed HCW system, the state matrix of the system is constant but the gain matrix is time-varying. Since both $\widetilde{\boldsymbol{z}}(t)$ and $\boldsymbol{z}(t)$ use the same state matrix, the effect of a constant gain matrix and a time-varying gain matrix can be studied. The third aspect is to apply the time-varying gain to the physical states $\boldsymbol{x}(t)$ as shown by Equation (6.26). For this system, the time-varying state matrix $\boldsymbol{A}(t)$ is controlled through a time-varying gain matrix. Note that both $\boldsymbol{z}(t)$ and $\boldsymbol{x}(t)$ use the same control, $\boldsymbol{u}(t)$. Finally, for comparison with the LF approach, a naive approach is direct application of the gain matrix from the auxiliary system to the time-varying system, i.e. $\dot{\bar{\boldsymbol{x}}}(t) = \boldsymbol{A}(t)\bar{\boldsymbol{x}}(t) + \boldsymbol{B}\bar{\boldsymbol{u}}(t)$ where $\bar{\boldsymbol{u}}(t) = -\widetilde{\boldsymbol{K}}\bar{\boldsymbol{x}}(t)$. For the direct application, the closed-loop system $\dot{\bar{\boldsymbol{x}}} = \left(\boldsymbol{A}(t) - \boldsymbol{B}\widetilde{\boldsymbol{K}}\right)\bar{\boldsymbol{x}}$ is defined, and the dynamics of the state-transition matrix

Case	a_C (km)	e_C	a_D (km)	e_D	ω_D (rad)
1	11,000	0.075	11,000	0.07501	0
2	11,000	0.075	11,000.2	0.07501	0
3	11,000	0.075	11,000	0.07501	4×10^{-5}
4	11,000	0.1125	11,000	0.11251	4×10^{-5}
5	11,000	0.1125	11,000	0.11251	0
6	11,000	0.15	11,000	0.15001	0

Table 6.1: Orbital elements for the chief and deputy for six near circular relative motion cases.

e_C	λ_1	λ_2	λ_3	λ_4	λ_5	λ_6
0.075	1.9328×10^{-3}	0.0541	0.1332	0.1871	0.6316	0.6530
0.1125	1.4651×10^{-4}	0.0692	0.1530	0.2179	0.6275	0.6593
0.15	1.2371×10^{-5}	0.0777	0.1796	0.2480	0.6240	0.6660

Table 6.2: Eigenvalues of $\boldsymbol{\Phi}_{\boldsymbol{x}}(P,0)$.

e_C	λ_1	λ_2	λ_3, λ_4	λ_5, λ_6
0.075	-0.0212	-0.2554	$0.1213 \pm 0.1121i$	$0.6414 \pm 1.2636 \times 10^{-5}i$
0.1125	-8.9514×10^{-3}	-0.6572	$0.1158 \pm 0.1085i$	$0.6414 \pm 1.2788 \times 10^{-5}i$
0.15	-5.1441×10^{-3}	-1.2245	$0.1161 \pm 0.1002i$	$0.6414 \pm 1.3003 \times 10^{-5}i$

Table 6.3: Eigenvalues of $\boldsymbol{\Phi}_{\bar{\boldsymbol{x}}}(P,0)$.

are given by $\dot{\boldsymbol{\Phi}}_{\bar{\boldsymbol{x}}} = \left(\boldsymbol{A}(t) - \boldsymbol{B}\widetilde{\boldsymbol{K}}\right)\boldsymbol{\Phi}_{\bar{\boldsymbol{x}}}$. Since LF transformations are not used, the system consists of a time-varying state matrix and a time-invariant gain matrix.

The two different control approaches described above were applied to six in-plane near circular test cases with nonzero elements listed in Table 6.1. Since the closed-loop system $\dot{\widetilde{\boldsymbol{z}}} = \left(\boldsymbol{\Lambda} - \widetilde{\boldsymbol{B}}\widetilde{\boldsymbol{K}}\right)\widetilde{\boldsymbol{z}}$ is time-invariant, the eigenvalues of $\boldsymbol{\Phi}_{\widetilde{\boldsymbol{z}}}(P,0)$ were $\lambda_1, \lambda_2 = -6.7343 \times 10^{-4} \pm 0.0724i$, $\lambda_3, \lambda_4 = 0.1434 \pm 0.0874i$, and $\lambda_5, \lambda_6 = 0.6414 \pm 1.2532 \times 10^{-5}i$ for every case considered. Tables 6.2 and 6.3 list the eigenvalues of $\boldsymbol{\Phi}_{\boldsymbol{x}}(P,0)$ and $\boldsymbol{\Phi}_{\bar{\boldsymbol{x}}}(P,0)$ respectively for each value of chief eccentricity. After five complete periods of the chief, Table 6.4 gives the final position $\widetilde{\boldsymbol{z}}(5P)$ and total control effort v for the auxiliary system, Table 6.5 gives the final position $\boldsymbol{z}(5P)$ and total control effort u for the LF transformed HCW system, Table 6.6 gives the final position $\boldsymbol{x}(5P)$ and total control effort u for the LF transformed

Case	$x(5P)$ (km)	$y(5P)$ (km)	Total v (km/s)
1	9.9481×10^{-6}	2.3293×10^{-5}	6.8887×10^{-7}
2	1.2895×10^{-5}	-1.7511×10^{-5}	1.6482×10^{-6}
3	1.0287×10^{-5}	4.6877×10^{-5}	1.1511×10^{-6}
4	9.2856×10^{-6}	4.9141×10^{-5}	1.1967×10^{-6}
5	9.9482×10^{-6}	2.3293×10^{-5}	6.8887×10^{-7}
6	9.9482×10^{-6}	2.3293×10^{-5}	6.8887×10^{-7}

Table 6.4: Final position and total control effort for the auxiliary system $\widetilde{\boldsymbol{z}}(t)$.

Case	$x(5P)$ (km)	$y(5P)$ (km)	Total u (km/s)
1	-1.6306×10^{-5}	-9.9882×10^{-7}	4.3485×10^{-6}
2	-1.4614×10^{-5}	8.8547×10^{-6}	9.7845×10^{-6}
3	-1.6381×10^{-4}	6.4188×10^{-6}	8.3630×10^{-6}
4	1.6893×10^{-5}	-1.8269×10^{-5}	9.6316×10^{-6}
5	-1.4808×10^{-5}	-1.2156×10^{-5}	4.6696×10^{-6}
6	-2.9857×10^{-6}	-2.3592×10^{-5}	5.0711×10^{-6}

Table 6.5: Final position and total control effort for the LF transformed HCW system $\boldsymbol{z}(t)$.

Case	$x(5P)$ (km)	$y(5P)$ (km)	Total u (km/s)
1	1.5914×10^{-5}	9.9881×10^{-7}	4.3485×10^{-6}
2	-1.3728×10^{-5}	8.8547×10^{-6}	9.7845×10^{-6}
3	-1.6297×10^{-5}	6.4187×10^{-6}	8.3630×10^{-6}
4	1.4610×10^{-5}	-1.8269×10^{-5}	9.6316×10^{-6}
5	1.4732×10^{-5}	-1.2156×10^{-5}	4.6696×10^{-6}
6	-4.3034×10^{-6}	-2.3592×10^{-5}	5.0711×10^{-6}

Table 6.6: Final position and total control effort for the LF transformed LERM system $\boldsymbol{x}(t)$.

Case	$x(5P)$ (km)	$y(5P)$ (km)	Total $\bar{u}$ (km/s)
1	7.7854×10^{-5}	2.7937×10^{-5}	5.2068×10^{-6}
2	-3.3263×10^{-4}	-2.5757×10^{-4}	1.2854×10^{-5}
3	3.6112×10^{-4}	1.9564×10^{-4}	1.1513×10^{-5}
4	2.8078×10^{-2}	6.7727×10^{-4}	3.4486×10^{-5}
5	8.4896×10^{-3}	1.9962×10^{-4}	1.1458×10^{-5}
6	0.1825	-7.6089×10^{-2}	5.9142×10^{-5}

Table 6.7: Final position and total control effort for the direct application of the gain matrix to the LERM $\bar{\boldsymbol{x}}(t)$.

LERM system, and Table 6.7 gives the final position $\bar{\boldsymbol{x}}(5P)$ and total control effort $\bar{u}$ for the direct application of the LQR gain to the LERM. The tables show that the systems $\widetilde{\boldsymbol{z}}(t)$, $\boldsymbol{z}(t)$, and $\boldsymbol{x}(t)$ were able to drive the deputy's position toward rendezvous with the chief within five orbits with comparable control effort. As the chief's eccentricity increased, $\bar{\boldsymbol{x}}(t)$ performed worse than the LF approach. In fact for case 6, $\bar{\boldsymbol{x}}(t)$ was unstable, showing the importance of transforming the gain to control a time-varying system.

Plots of the inplane components of $\dot{\boldsymbol{x}}(t)$ for each case are shown in Figures 6.10 through 6.15. For each case, the deputy converges toward rendezvous. Figures 6.16 through 6.21 show the x and y position error over five orbits for each case. Since rendezvous is desired, the position error is the current position of the satellite. For each case, $\widetilde{\boldsymbol{z}}(t)$ has been driven to near zero after about three orbits. Both $\boldsymbol{z}(t)$ and $\boldsymbol{x}(t)$ take slightly longer but also converge to zero on the order of three orbits. Since the cases considered are near circular, the HCW equations are a good approximation of the time-varying LERM, which explains the similarity of these two systems. The figures show the degraded performance of $\bar{\boldsymbol{x}}(t)$ for every case considered, and recall that $\bar{\boldsymbol{x}}(t)$ does not stabilize the system for case 6. Figures 6.22 through 6.27 show the control effort $\boldsymbol{v}(t)$, $\boldsymbol{u}(t)$, and $\bar{\boldsymbol{u}}(t)$ as a function of time for each case.

The impulsive control method described in Section 6.1 can be compared to the results of the continuous-thrust methods described above. The impulsive control method will only be applied to case 6. The total control effort was calculated for four choices of the transfer time: $0.5P$; P; $2P$; and $5P$ where P is the period of the chief's orbit. The control effort was 7.7450×10^{-5} km/s for a transfer time of $0.5P$, 3.3661×10^{-2} km/s for a transfer time of P, 1.6830×10^{-2} km/s for a transfer time of $2P$, and 8.2151×10^{-2} km/s for a transfer time of $5P$. These results show that for all cases, the impulsive control method had greater control effort than $\boldsymbol{v}(t)$, $\boldsymbol{u}(t)$, and $\bar{\boldsymbol{u}}(t)$, but for a transfer time of half an orbit, the impulsive method was within one order of magnitude.

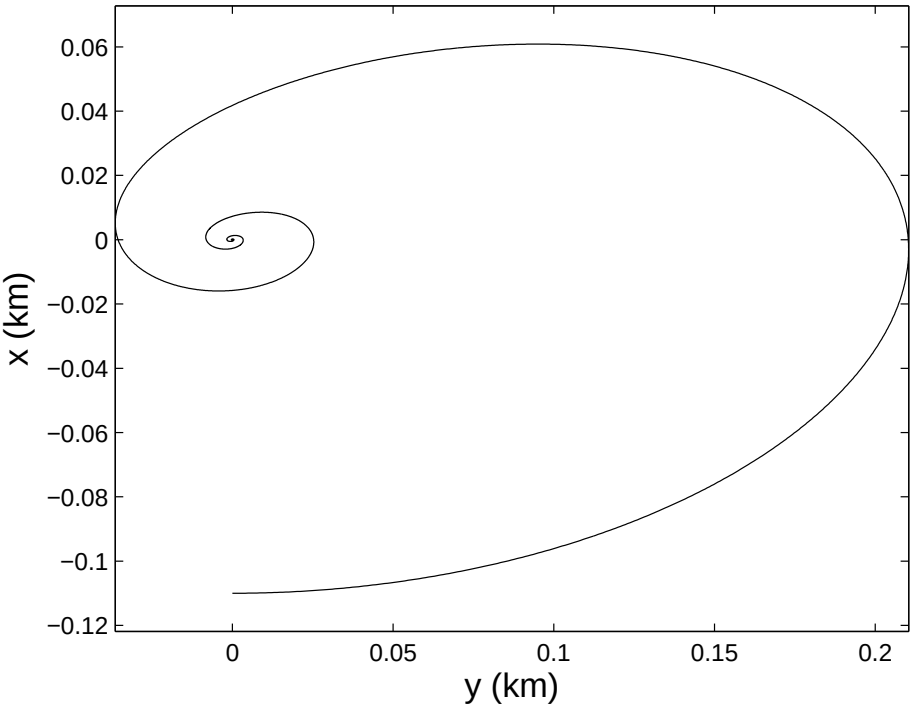

Figure 6.10: Deputy trajectory case 1.

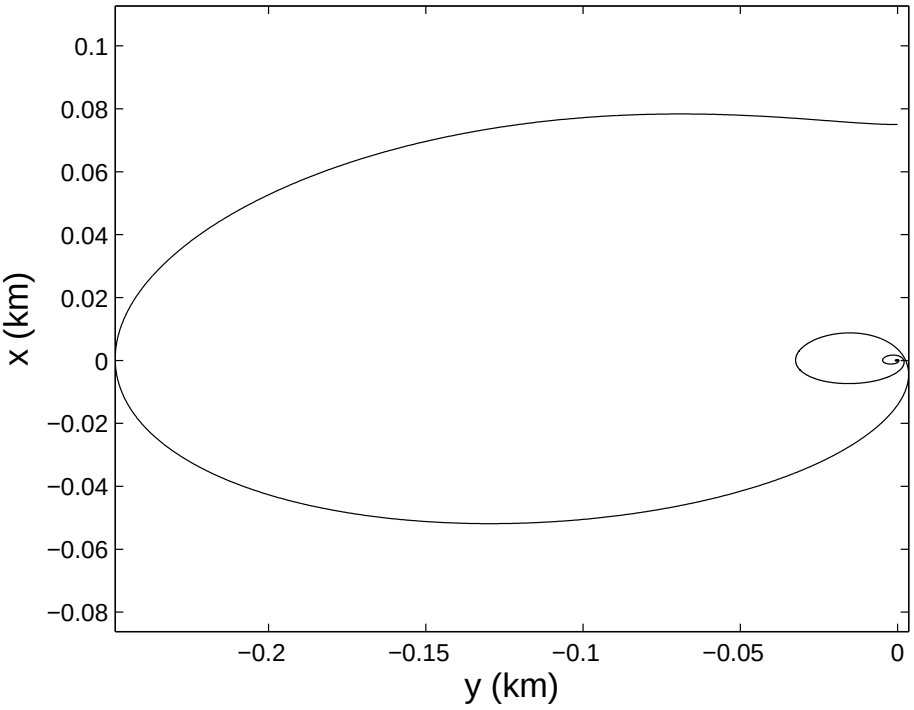

Figure 6.11: Deputy trajectory case 2.

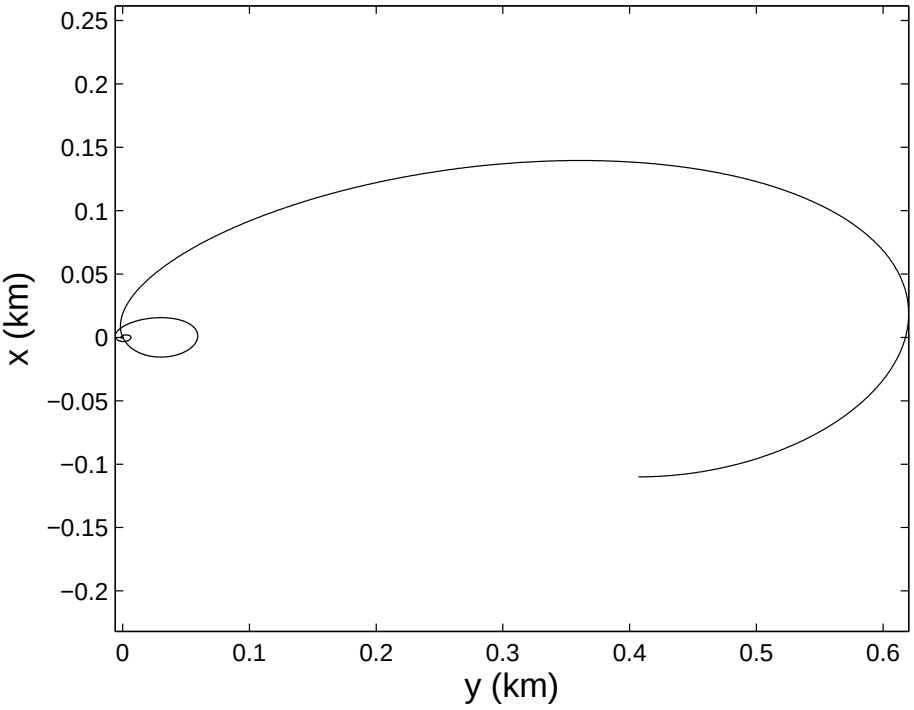

Figure 6.12: Deputy trajectory case 3.

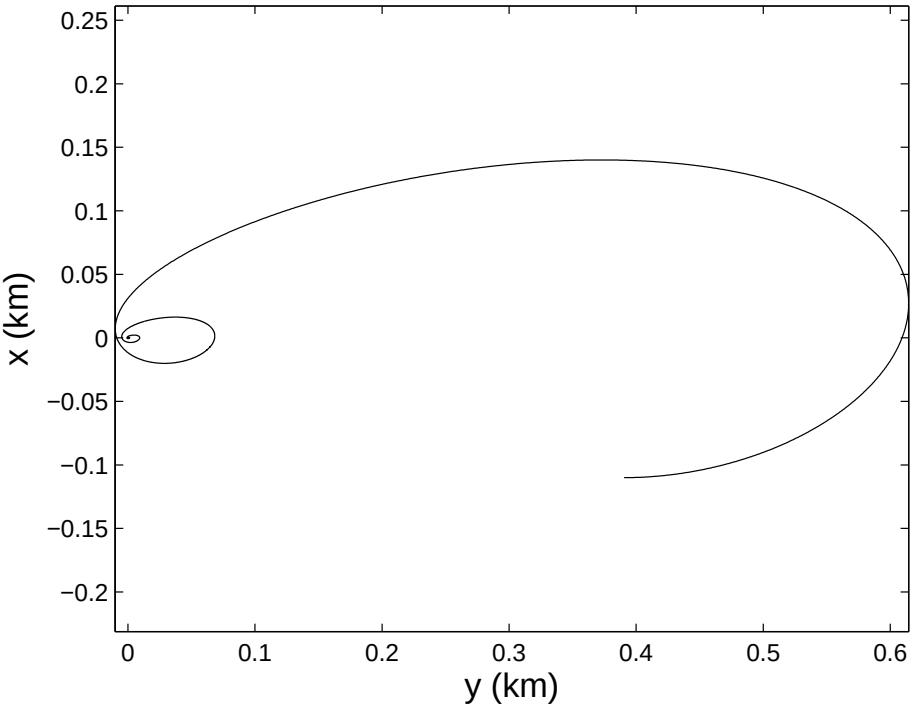

Figure 6.13: Deputy trajectory case 4.

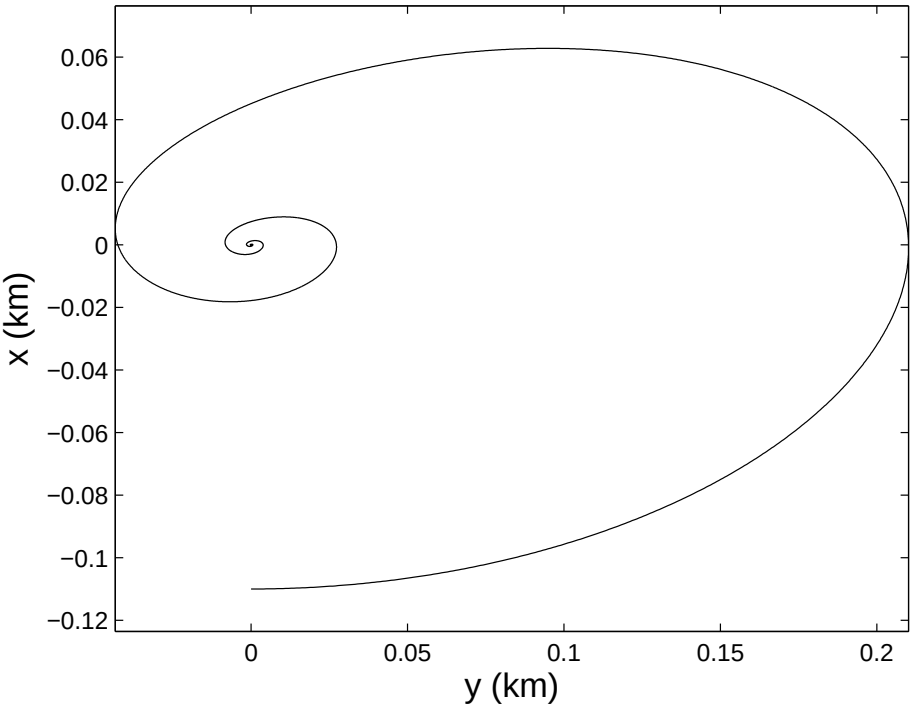

Figure 6.14: Deputy trajectory case 5.

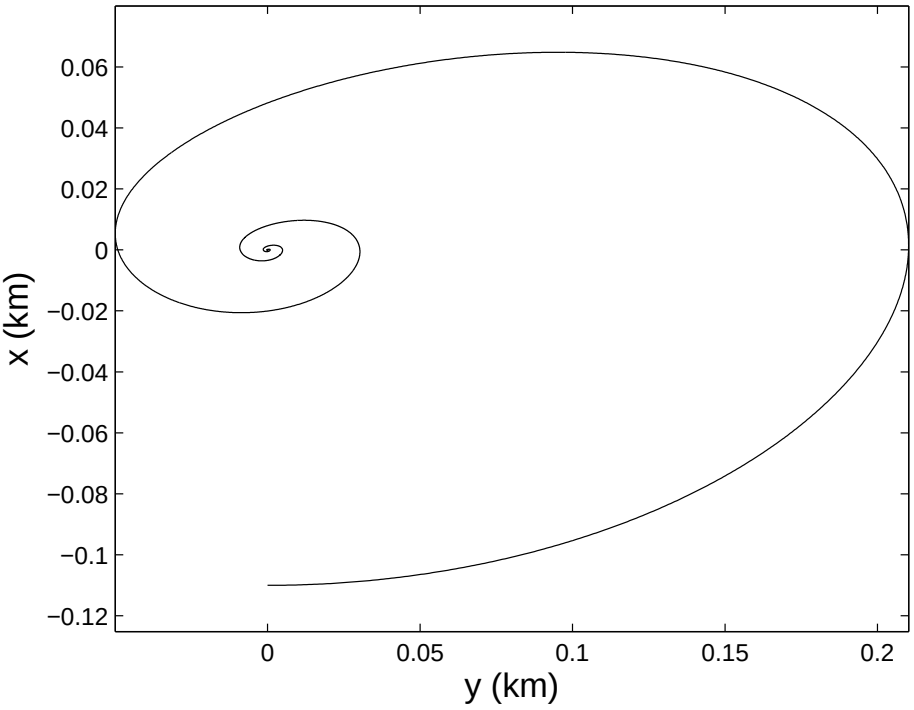

Figure 6.15: Deputy trajectory case 6.

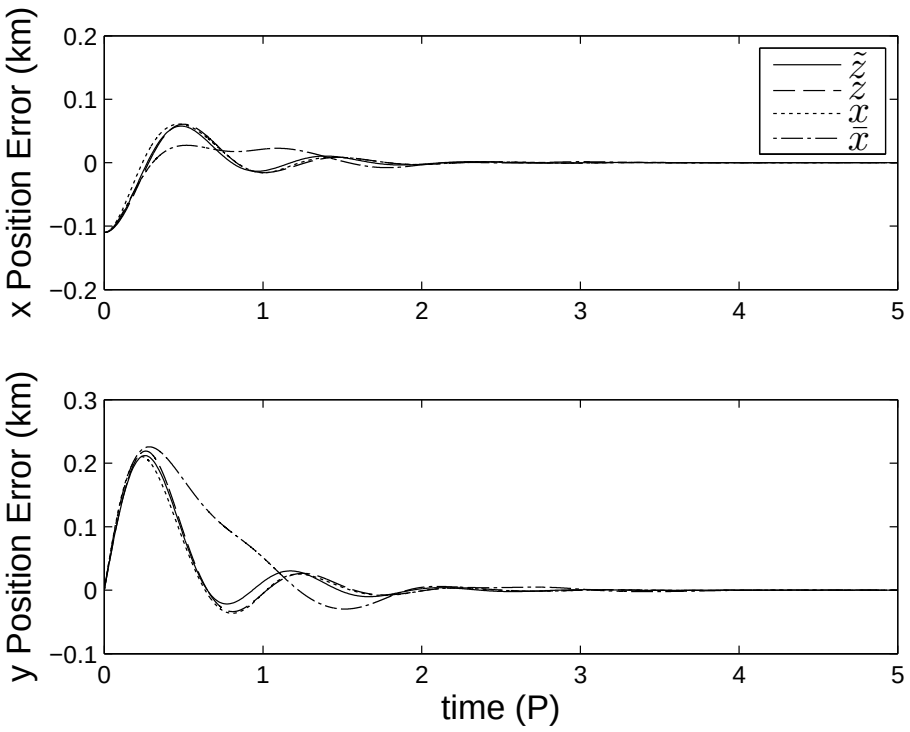

Figure 6.16: Position error for case 1.

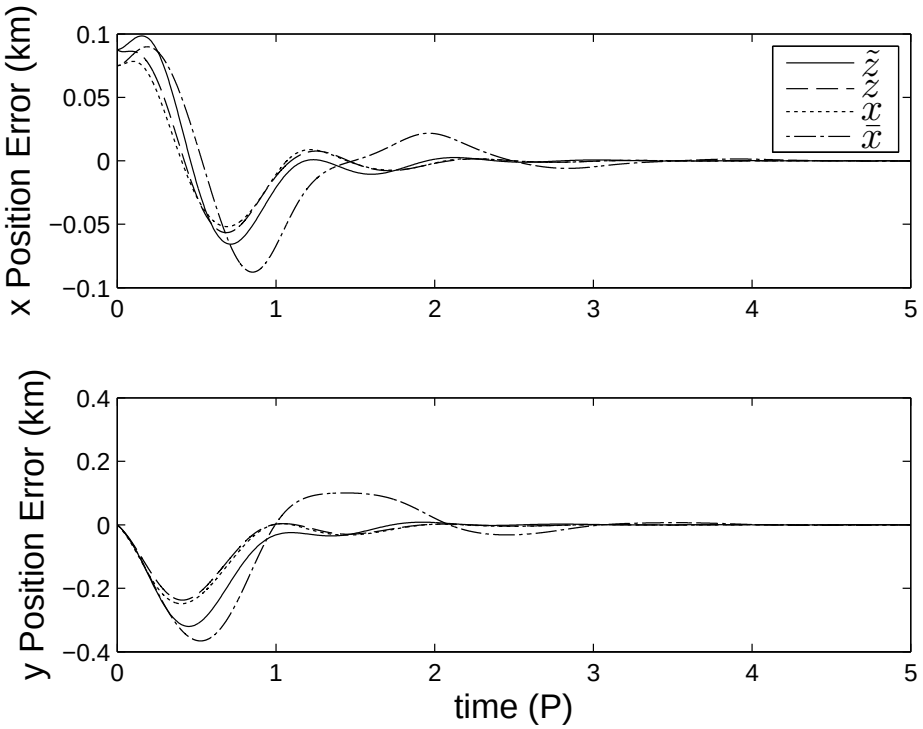

Figure 6.17: Position error for case 2.

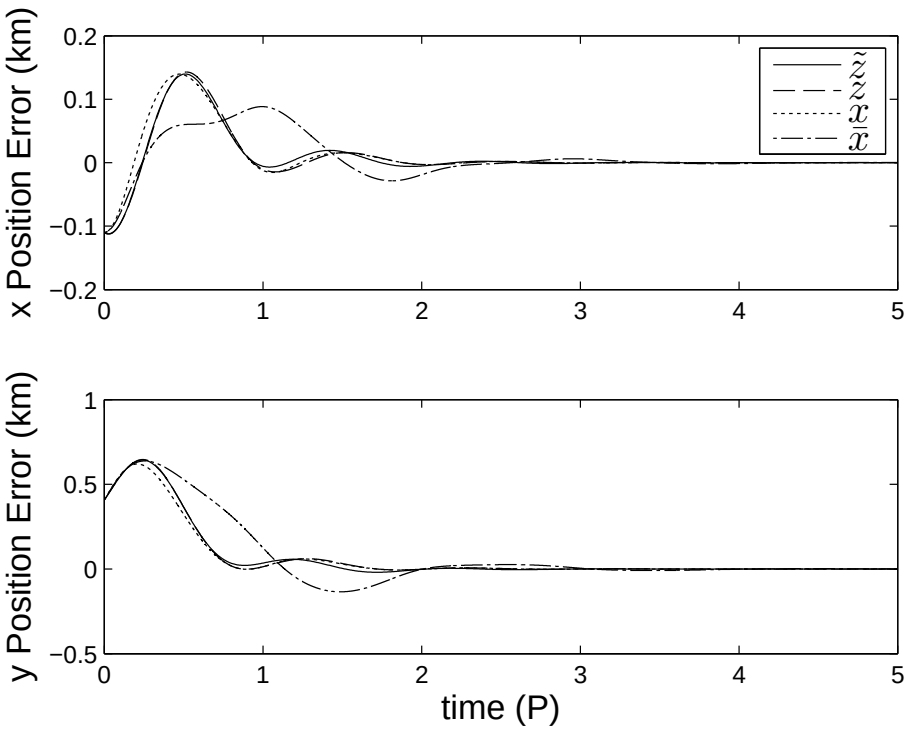

Figure 6.18: Position error for case 3.

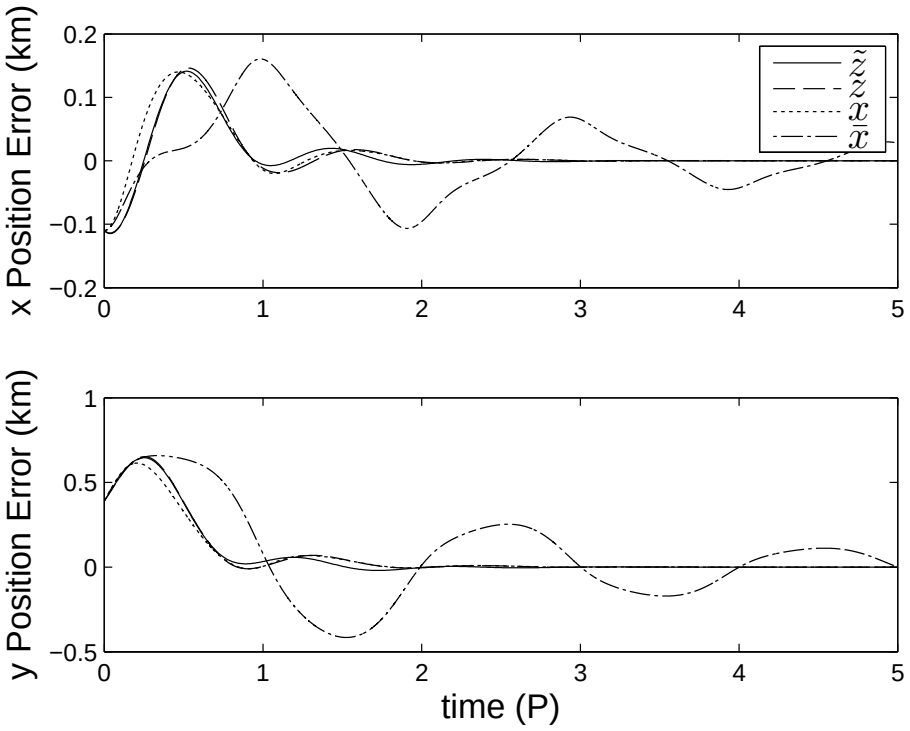

Figure 6.19: Position error for case 4.

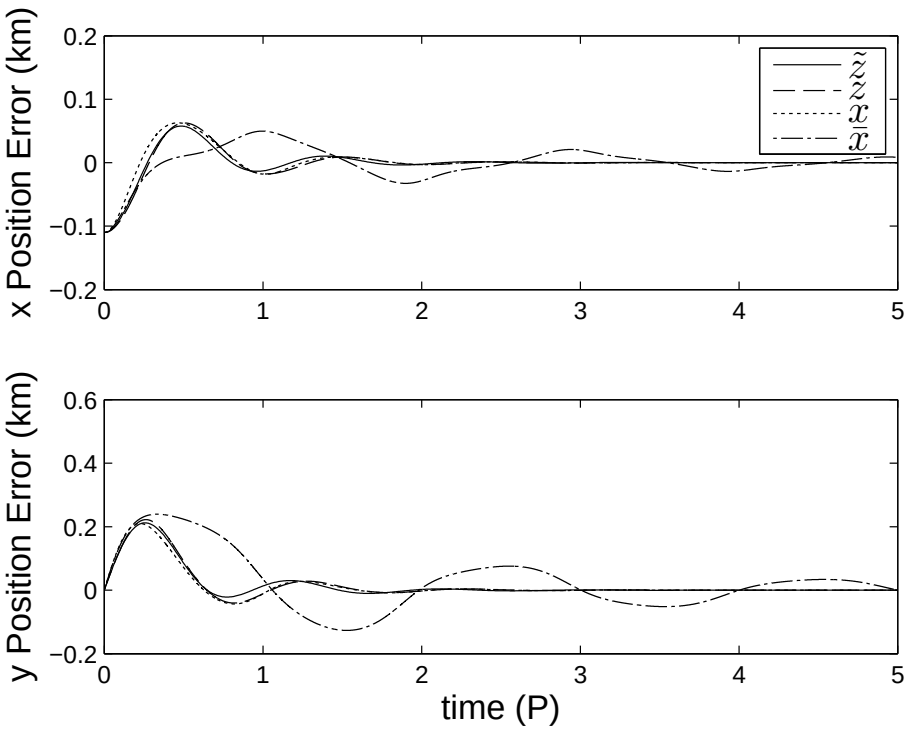

Figure 6.20: Position error for case 5.

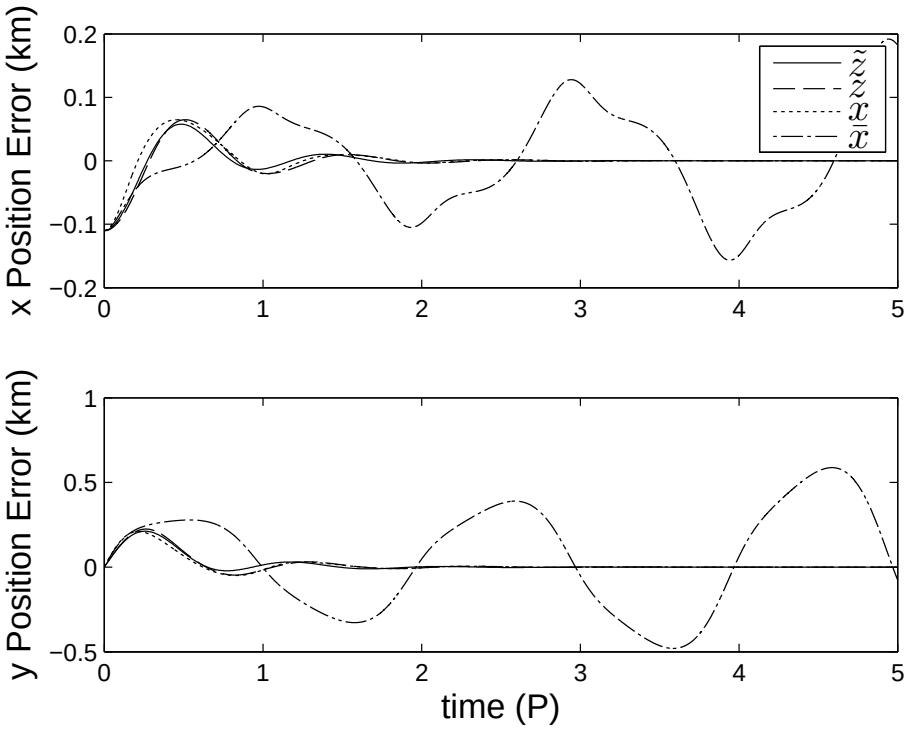

Figure 6.21: Position error for case 6.

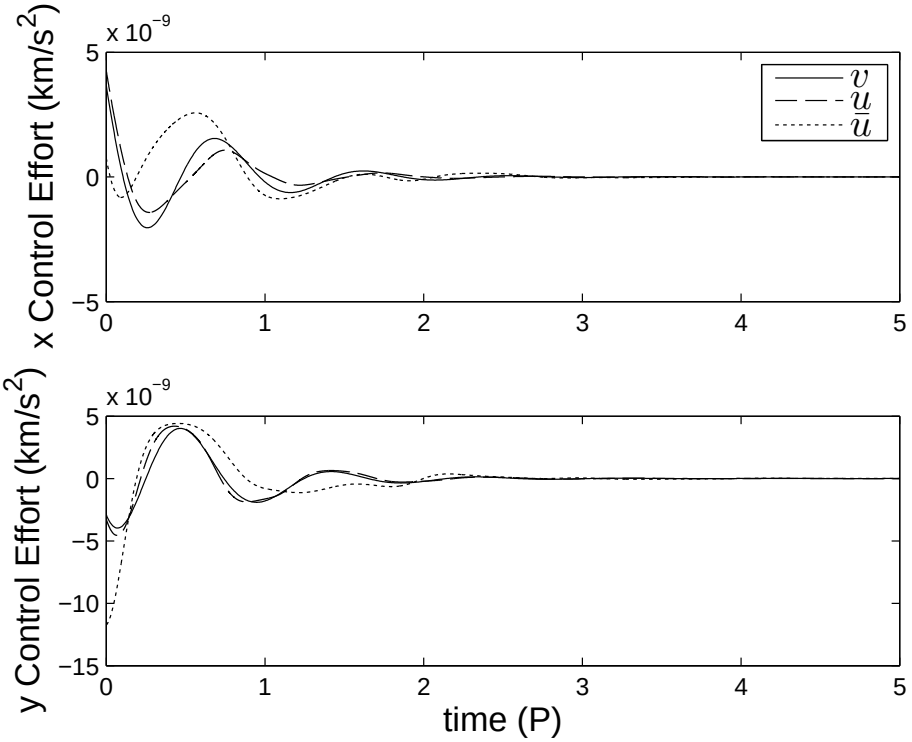

Figure 6.22: Control effort for case 1.

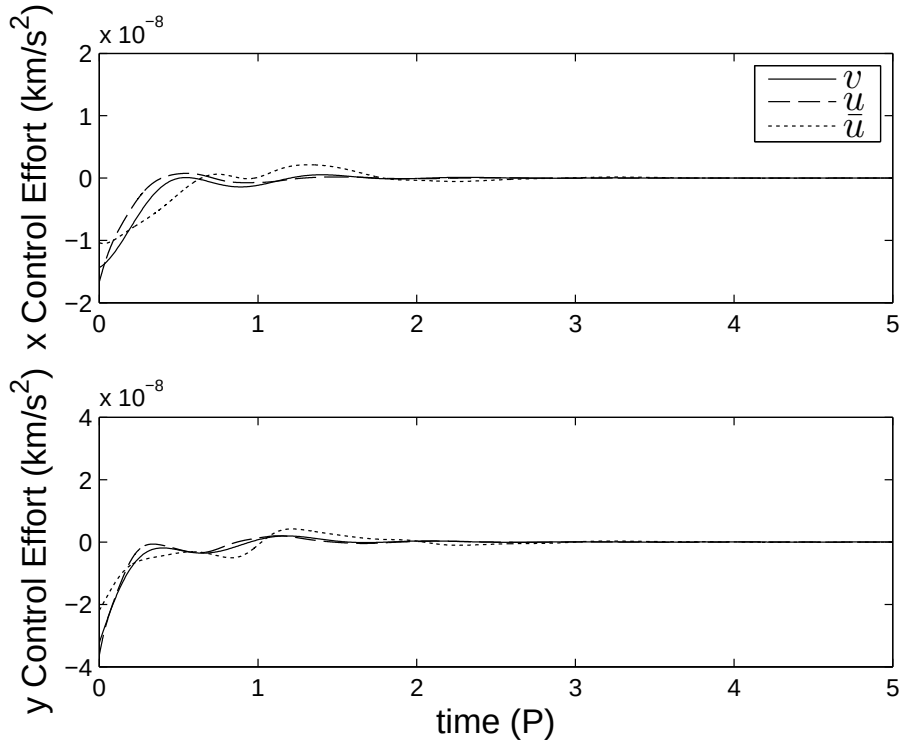

Figure 6.23: Control effort for case 2.

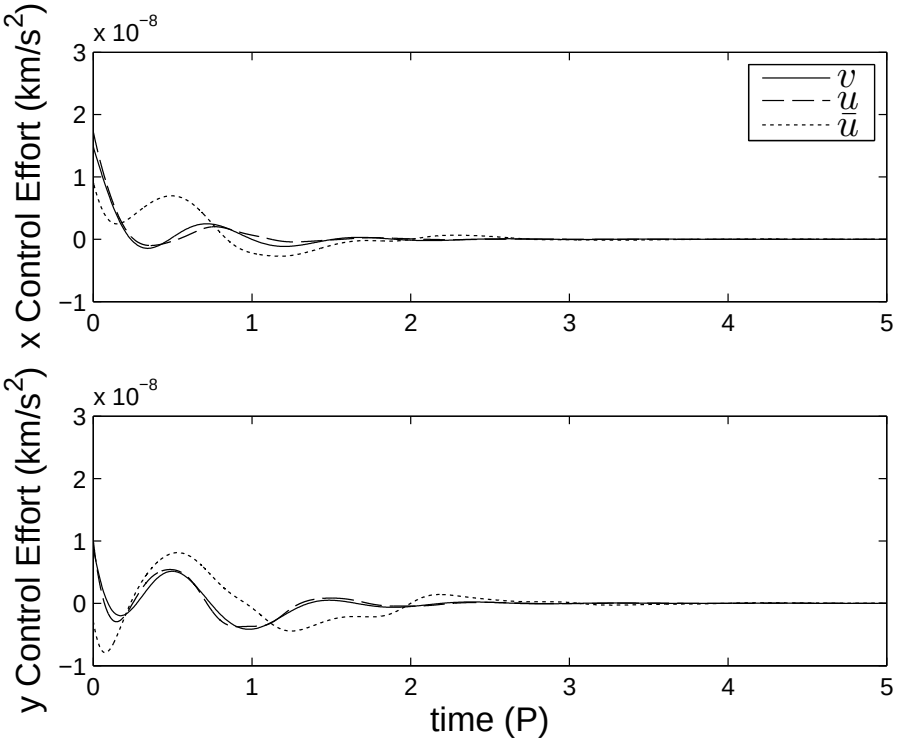

Figure 6.24: Control effort for case 3.

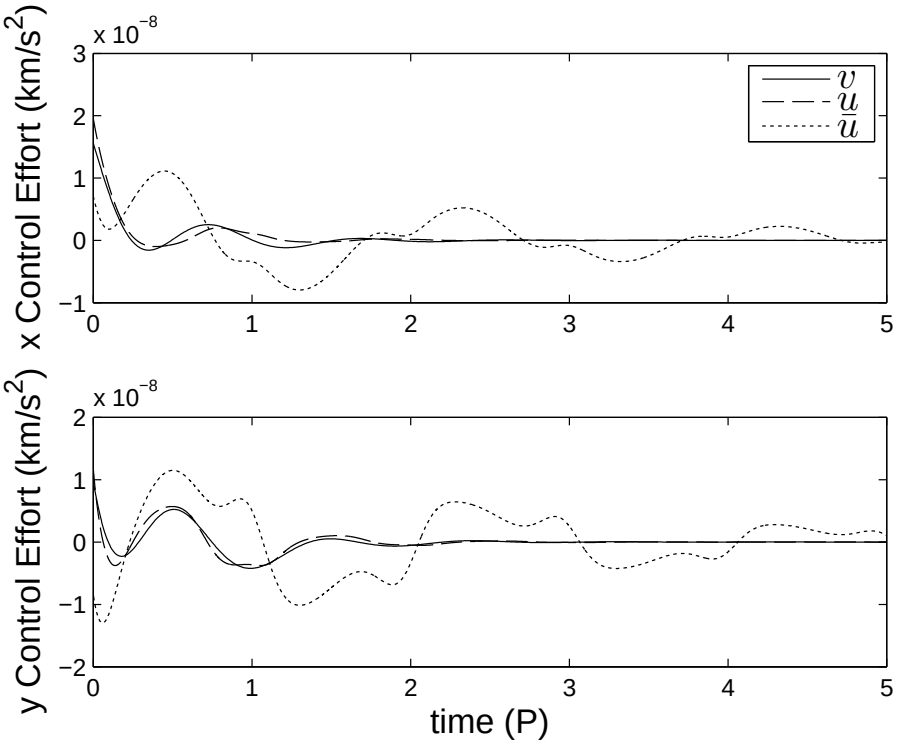

Figure 6.25: Control effort for case 4.

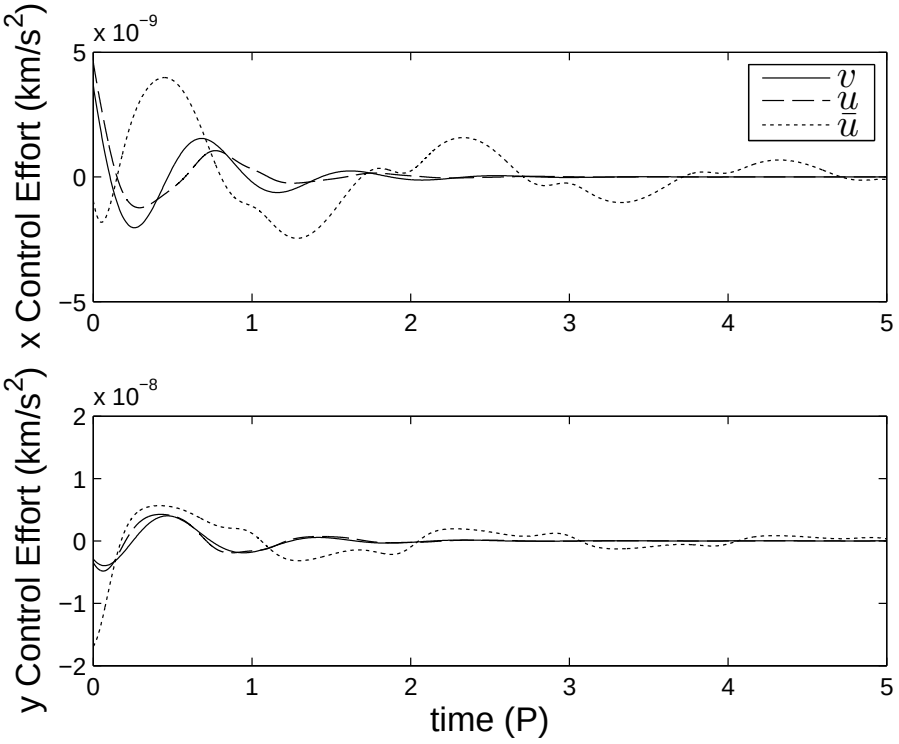

Figure 6.26: Control effort for case 5.

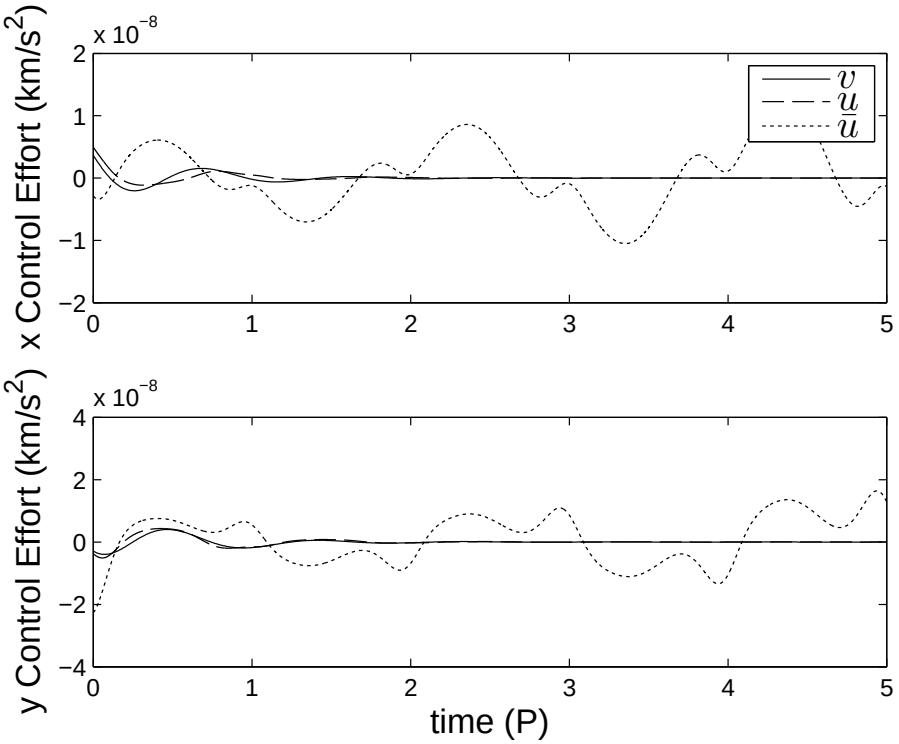

Figure 6.27: Control effort for case 6.

Case	a_C (km)	e_C	a_D (km)	e_D	i_D (rad)	Ω_D (rad)	ω_D (rad)
1	11,000	0.3	11,000	0.30001	0	0	0
2	11,000	0.3	11,000.2	0.30001	0	0	0
3	11,000	0.3	11,000	0.30001	0	0	4×10^{-5}
4	11,000	0.6	11,000	0.60001	0	0	4×10^{-5}
5	11,000	0.3	11,000	0.30001	4×10^{-5}	0	0
6	11,000	0.3	11,000	0.30001	4×10^{-5}	$\frac{\pi}{2}$	$\frac{-\pi}{2}$

Table 6.8: Orbital elements for the chief and deputy for six different relative motion cases.

e_C	λ_1	λ_2	λ_3	λ_4	λ_5	λ_6
0.3	7.6726×10^{-10}	0.0921	0.2511	0.4095	0.6175	0.6956
0.6	-1.0206×10^{-4}	0.1000	0.3910	0.6926	0.6989	0.7845

Table 6.9: Eigenvalues of $\mathbf{\Phi}_{\boldsymbol{x}}(P,0)$.

6.4.2 Highly Elliptic Orbits

The previous subsection focused on six cases where the chief was nearly circular, while this subsection considers the case of a highly elliptic chief. Six cases are considered with the orbital elements given in Table 5.1 reproduced here in Table 6.8. Here, only the LF approach will be presented as $\bar{\boldsymbol{x}}(t)$ was unstable for all the cases considered.

Table 6.9 gives the eigenvalues of $\mathbf{\Phi}_{\boldsymbol{x}}(P,0)$ for chief eccentricities of 0.3 and 0.6. After five complete periods of the chief, Table 6.10 gives the final position $\widetilde{\boldsymbol{z}}(5P)$ and total control effort v for the auxiliary system, Table 6.11 gives the final position $\boldsymbol{z}(5P)$ and total control effort u for the LF transformed HCW system, and Table 6.12 gives the final position $\boldsymbol{x}(5P)$ and total control effort u for the LF transformed LERM system. For higher eccentricities $\boldsymbol{u}$ less accurately approximates $\boldsymbol{v}$. The final position after five orbits for both $\boldsymbol{z}(t)$, and $\boldsymbol{x}(t)$ were one to two orders of magnitude worse than $\widetilde{\boldsymbol{z}}(t)$ for the cases considered. These two systems performed particulary poor in case 4 for both position error after five orbits and total control effort.

Plots of the in-plane trajectory of $\boldsymbol{x}(t)$ for each case are shown in Figures 6.28 through 6.33. The figures show that the deputy converges toward rendezvous. Figures 6.34 through 6.39

Case	$x(5P)$ (km)	$y(5P)$ (km)	$z(5P)$ (km)	Total u (km/s)
1	9.9484×10^{-6}	2.3293×10^{-5}	–	6.8889×10^{-7}
2	1.9374×10^{-5}	-1.4939×10^{-5}	–	2.0737×10^{-6}
3	5.9913×10^{-6}	5.4871×10^{-5}	–	1.3249×10^{-6}
4	4.5027×10^{-6}	5.1694×10^{-5}	–	1.2378×10^{-6}
5	9.9448×10^{-6}	2.3294×10^{-5}	-6.3614×10^{-6}	6.5747×10^{-6}
6	9.9462×10^{-6}	2.3295×10^{-5}	3.3448×10^{-2}	3.5302×10^{-6}

Table 6.10: Final position and total control effort for the auxiliary system $\widetilde{\boldsymbol{z}}(t)$.

Case	$x(5P)$ (km)	$y(5P)$ (km)	$z(5P)$ (km)	Total u (km/s)
1	1.3246×10^{-4}	-1.7181×10^{-4}	–	7.6300×10^{-6}
2	-4.2660×10^{-4}	3.8406×10^{-5}	–	1.3822×10^{-5}
3	1.4761×10^{-3}	-2.8224×10^{-3}	–	1.9680×10^{-5}
4	1.0527×10^{-2}	1.1389×10^{-2}	–	6.9638×10^{-5}
5	1.3252×10^{-4}	-1.7181×10^{-4}	3.1137×10^{-3}	5.2771×10^{-5}
6	1.3252×10^{-4}	-1.7182×10^{-4}	4.9825×10^{-2}	3.7197×10^{-5}

Table 6.11: Final position and total control effort for the LF transformed HCW system $\boldsymbol{z}(t)$.

Case	$x(5P)$ (km)	$y(5P)$ (km)	$z(5P)$ (km)	Total u (km/s)
1	1.0429×10^{-4}	-1.7181×10^{-4}	–	7.6300×10^{-5}
2	-3.7013×10^{-4}	3.8407×10^{-5}	–	1.3822×10^{-5}
3	1.2706×10^{-3}	-2.8224×10^{-4}	–	1.9680×10^{-5}
4	8.2016×10^{-3}	-1.1390×10^{-2}	–	6.9638×10^{-5}
5	1.0435×10^{-4}	-1.7181×10^{-4}	3.1137×10^{-3}	5.2771×10^{-5}
6	1.0434×10^{-4}	-1.7182×10^{-4}	4.9825×10^{-2}	3.7197×10^{-5}

Table 6.12: Final position and total control effort for the LF transformed LERM system $\boldsymbol{x}(t)$.

show the position error over five orbits for each case. As in the near circular case, the system $\widetilde{\boldsymbol{z}}(t)$ has driven the position error to near zero after about three orbits. The other two systems take slightly longer, most significantly in the y direction for case four and in the z direction for cases 5 and 6. Figures 6.40 through 6.45 show the control effort $\boldsymbol{v}(t)$ and $\boldsymbol{u}(t)$ as a function of time for each case.

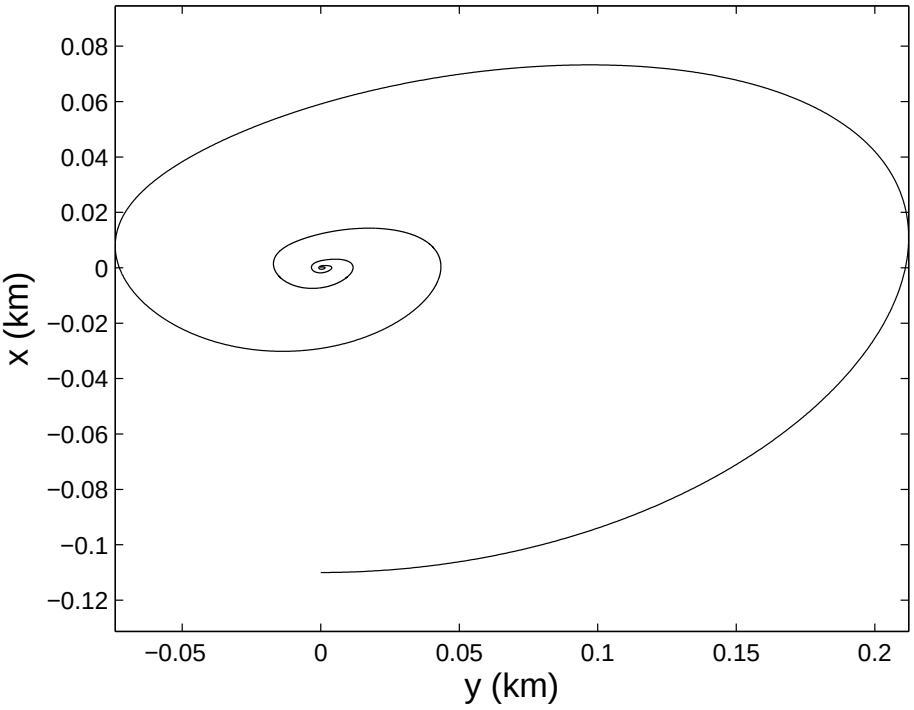

Figure 6.28: Deputy trajectory for case 1.

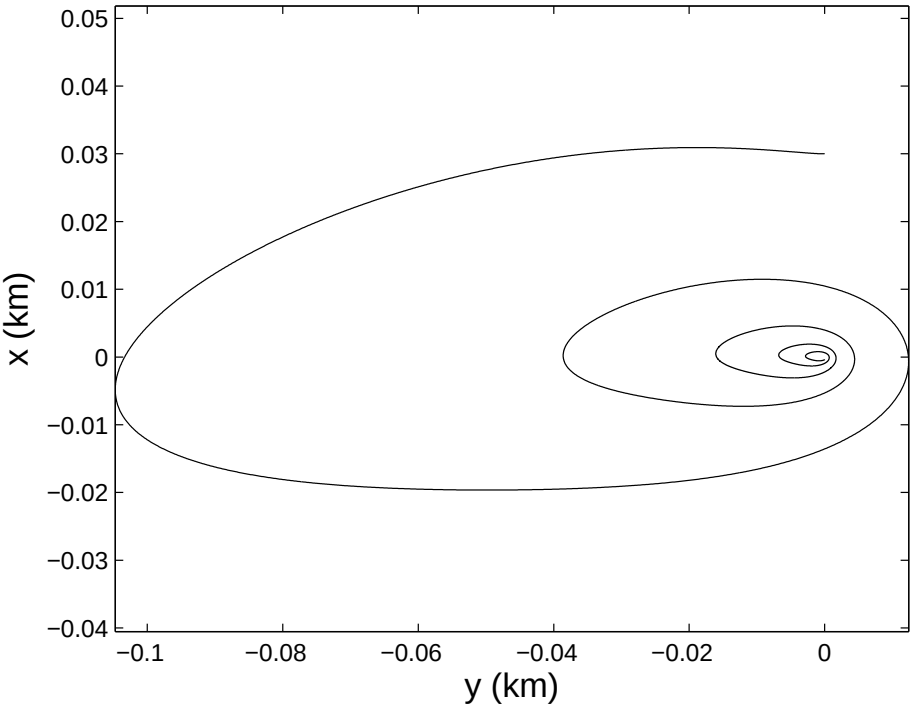

Figure 6.29: Deputy trajectory for case 2.

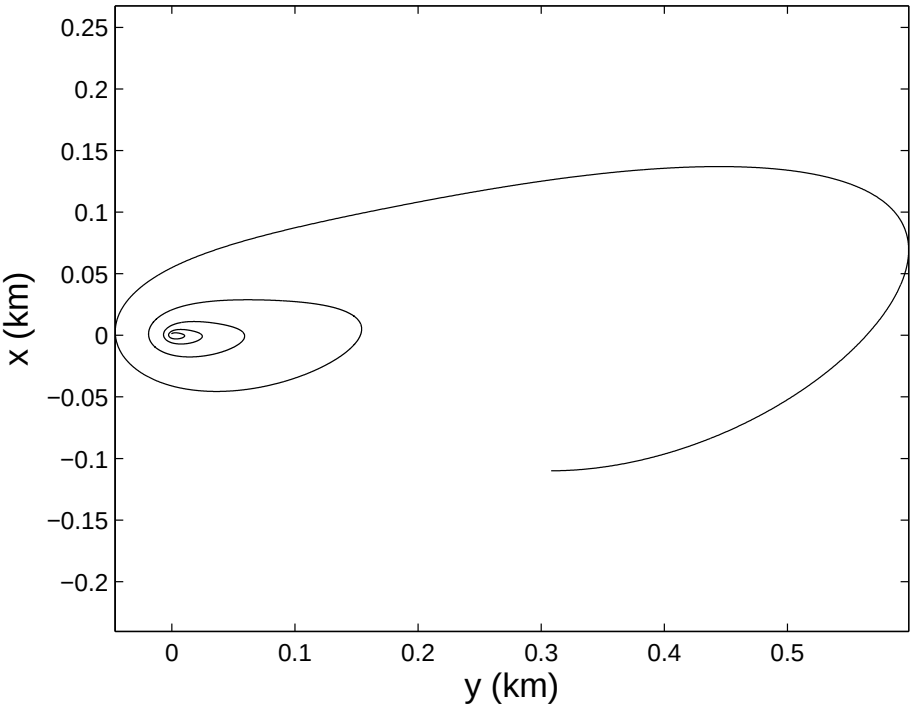

Figure 6.30: Deputy trajectory for case 3.

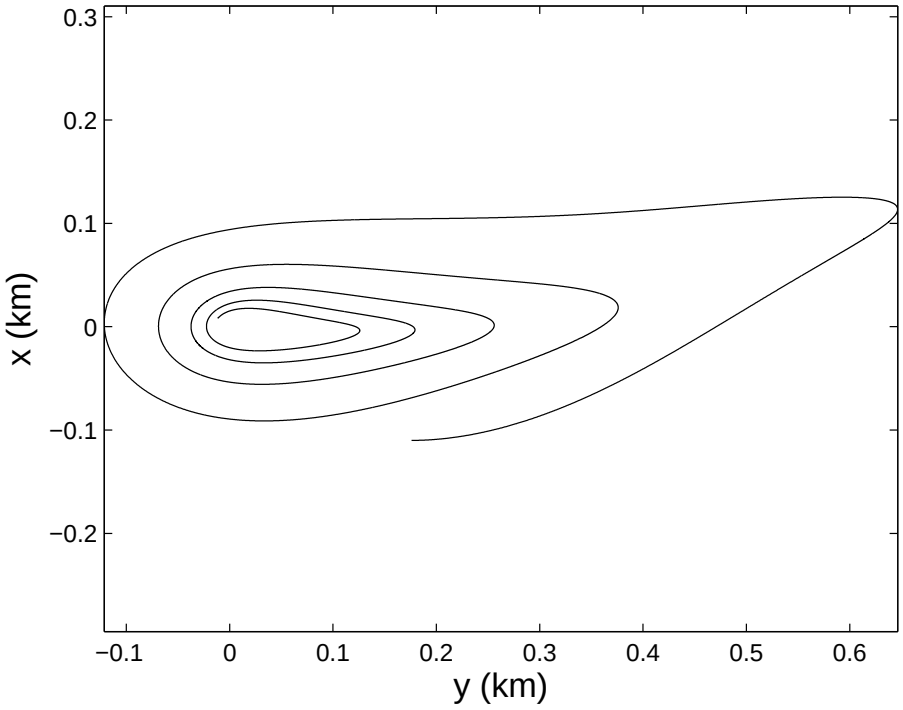

Figure 6.31: Deputy trajectory for case 4.

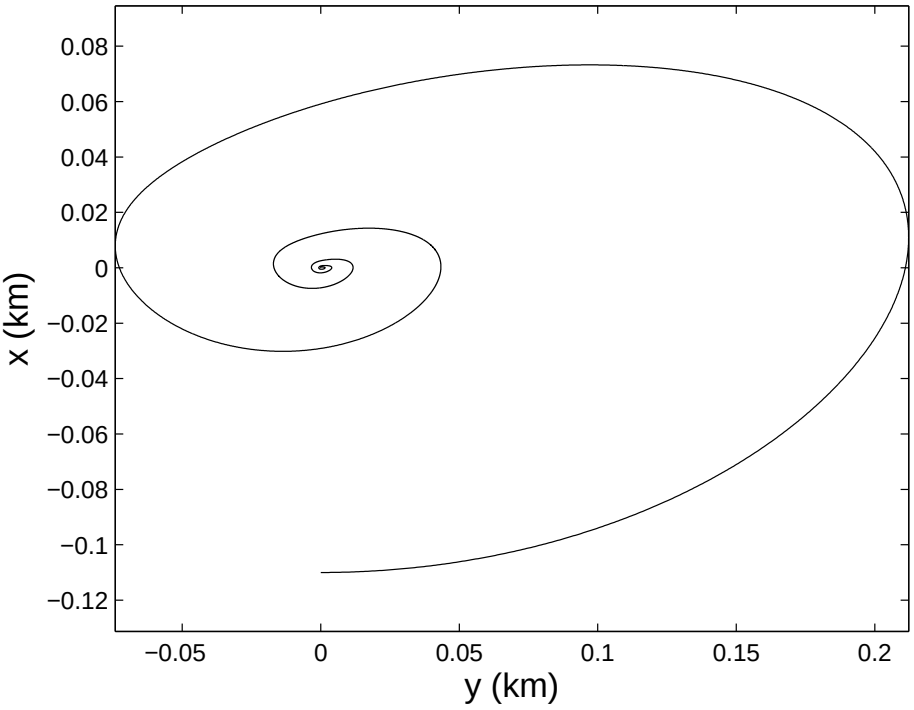

Figure 6.32: Deputy trajectory for case 5.

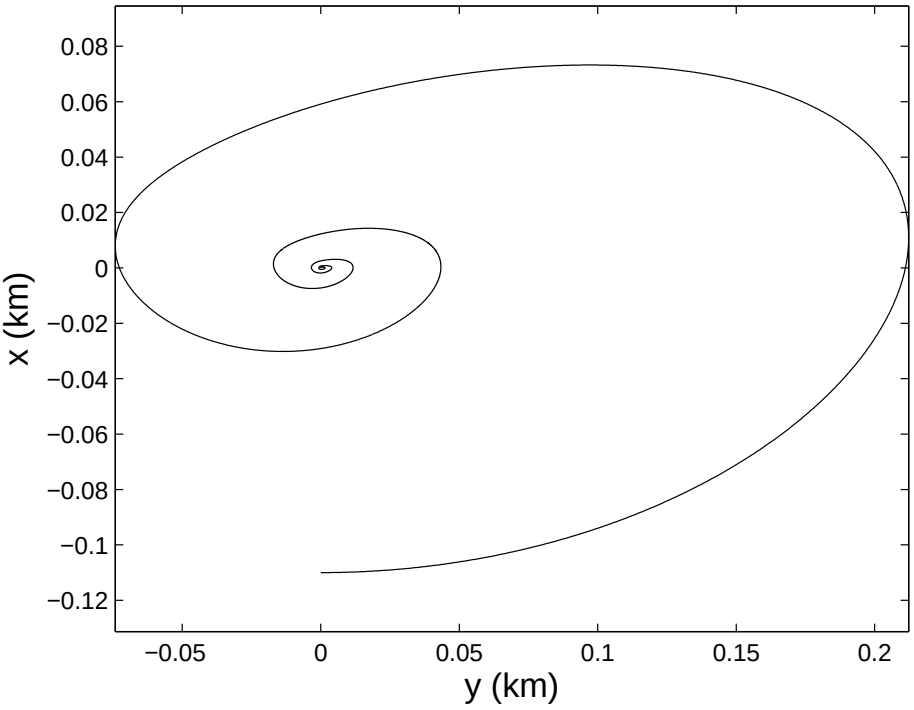

Figure 6.33: Deputy trajectory for case 6.

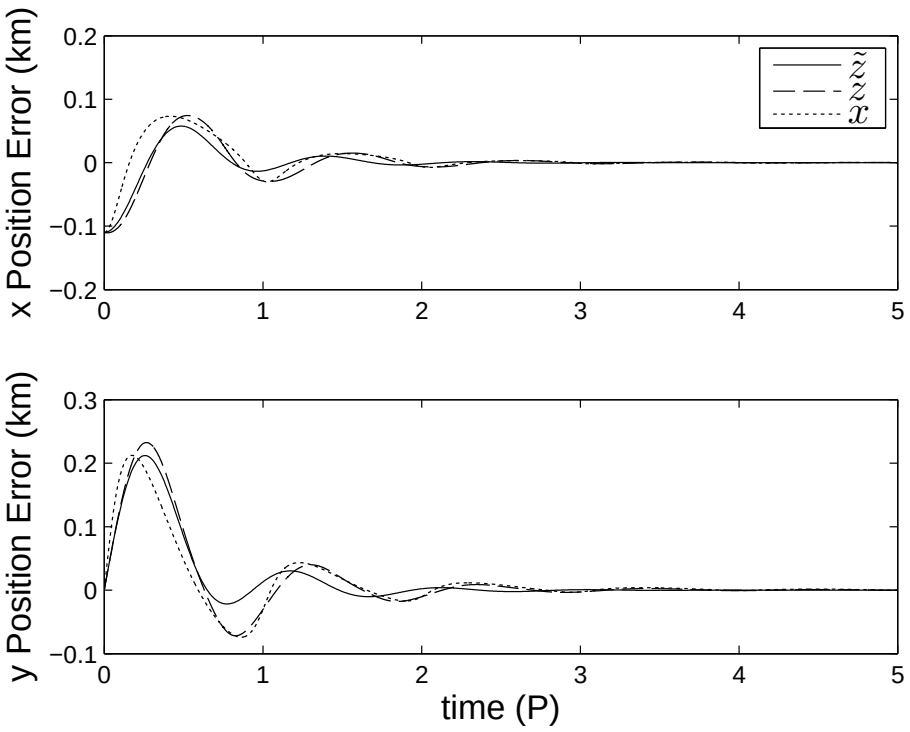

Figure 6.34: Position error for case 1.

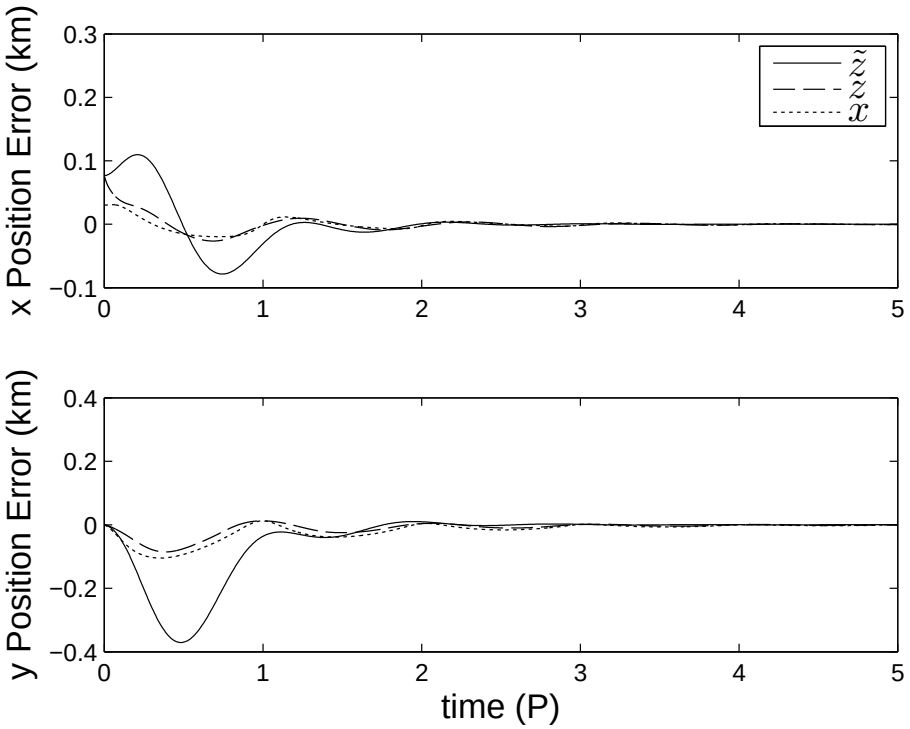

Figure 6.35: Position error for case 2.

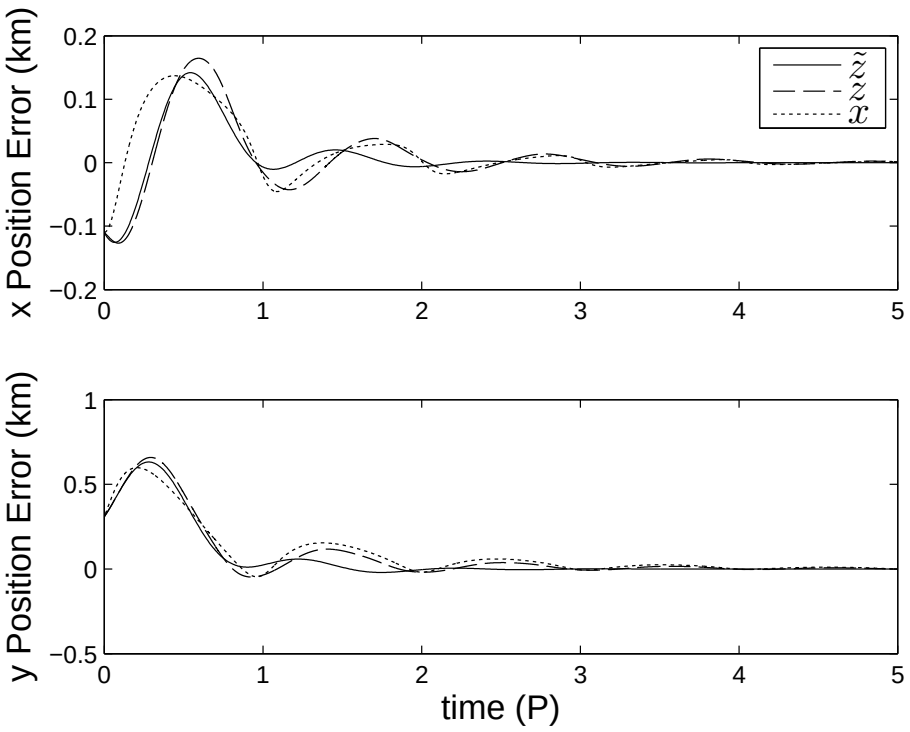

Figure 6.36: Position error for case 3.

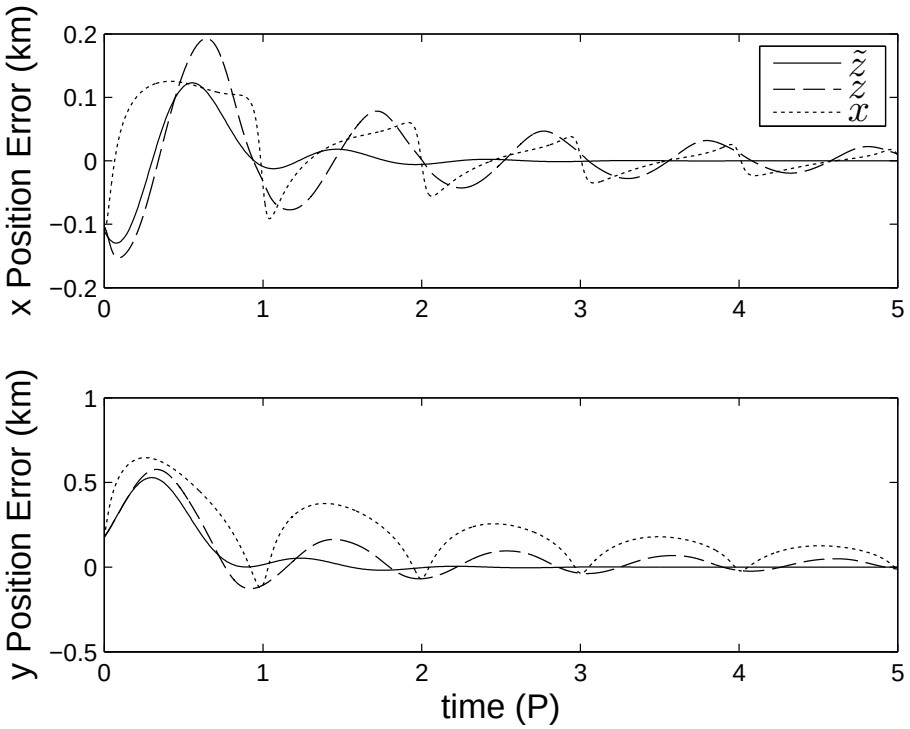

Figure 6.37: Position error for case 4.

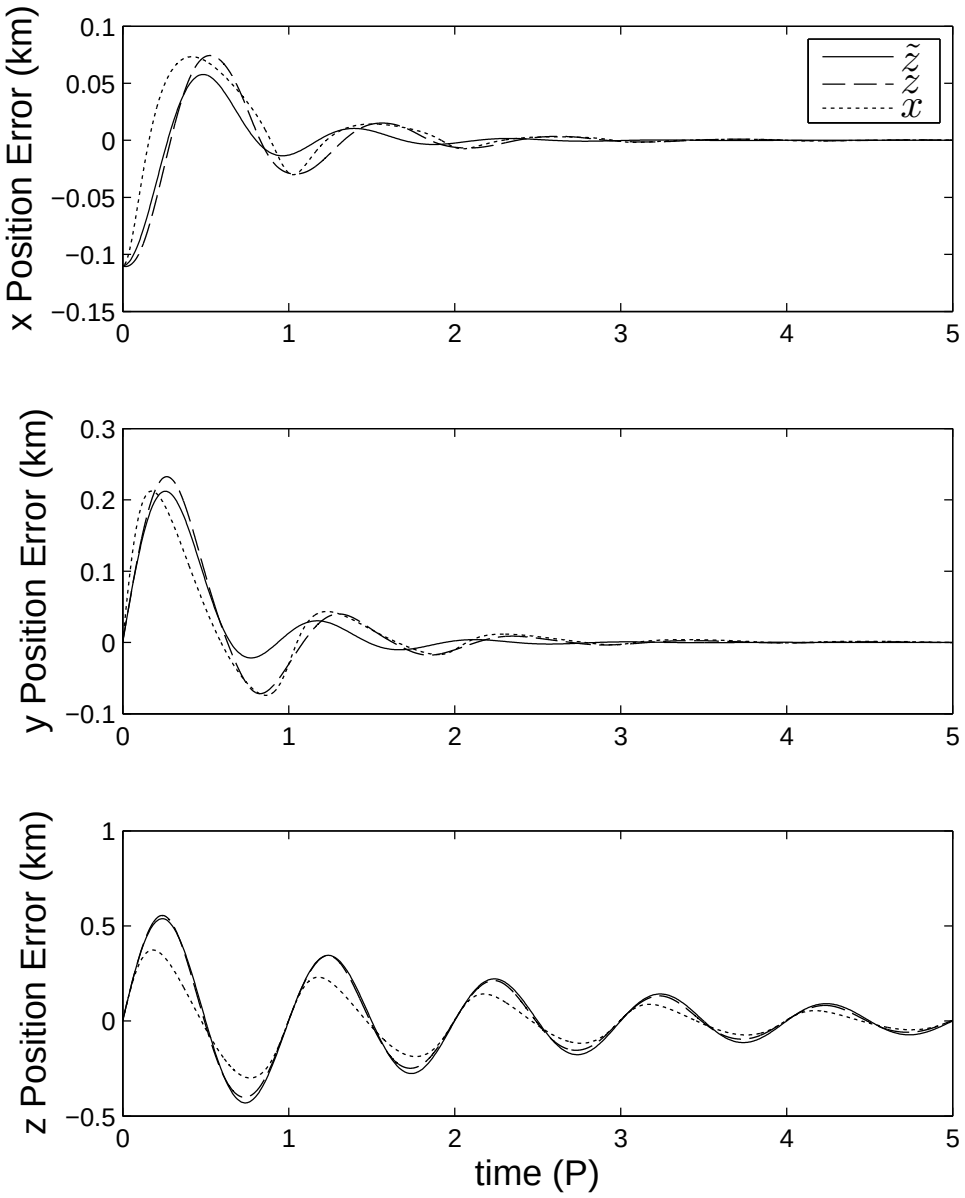

Figure 6.38: Position error for case 5.

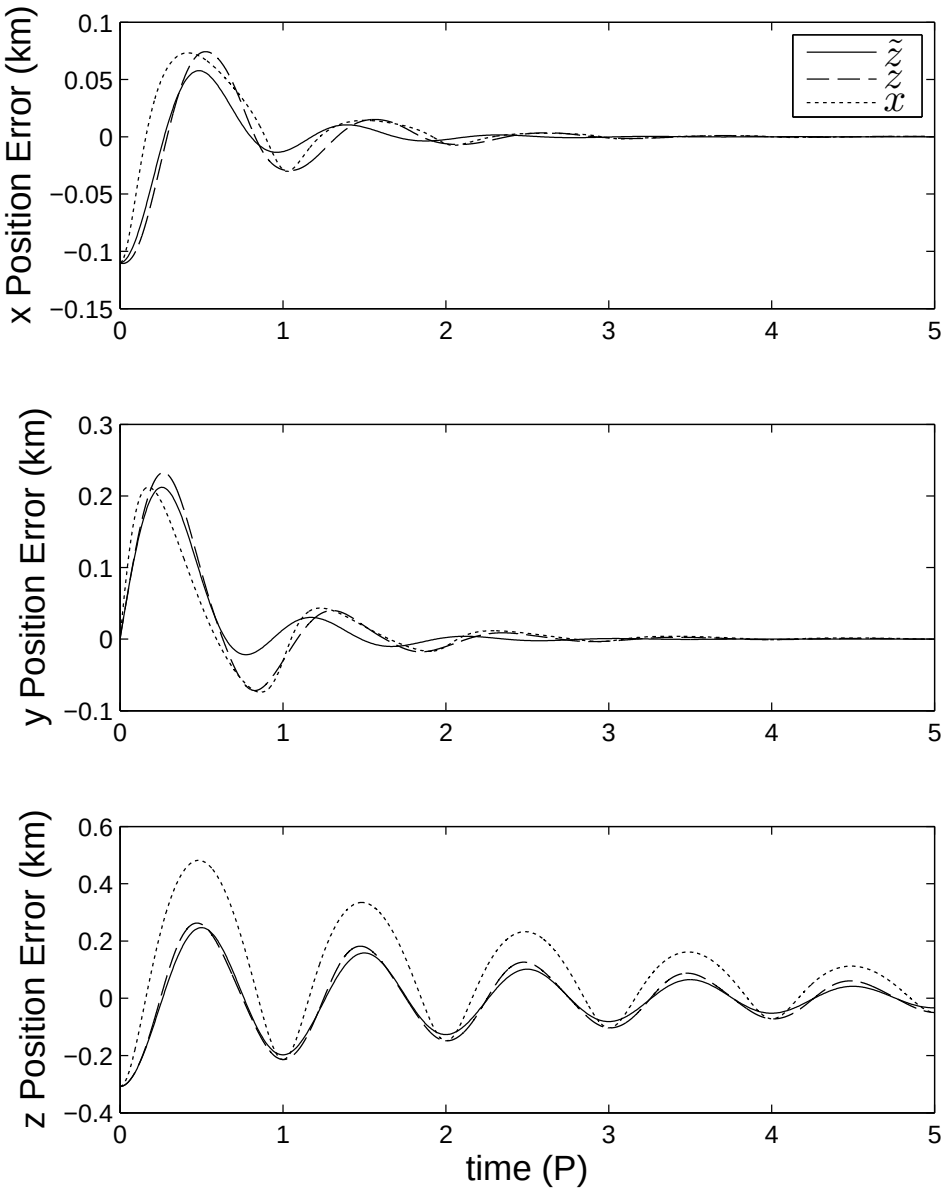

Figure 6.39: Position error for case 6.

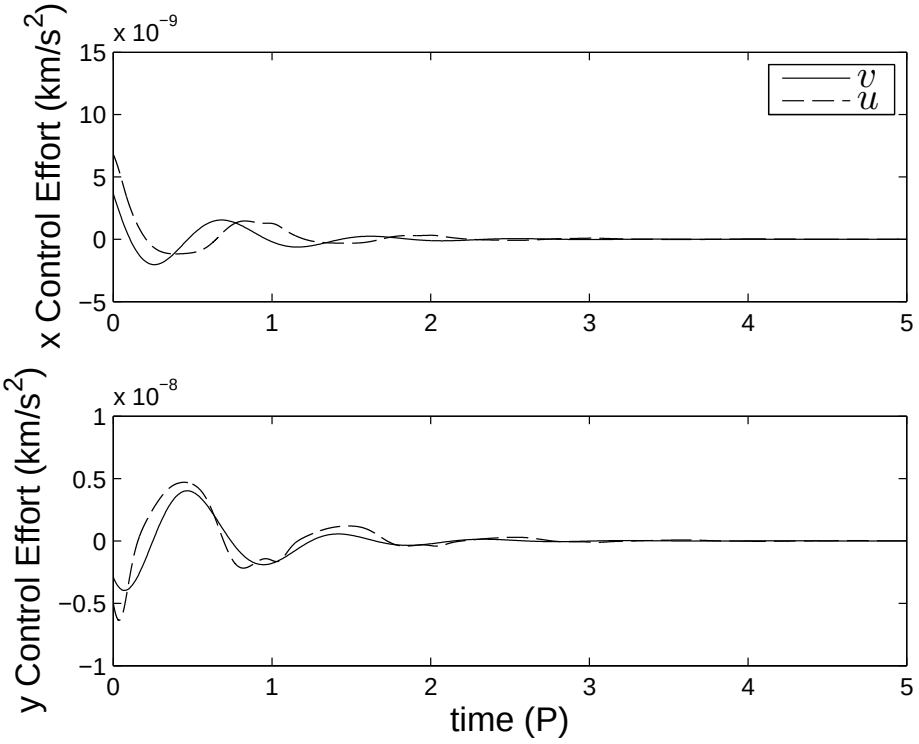

Figure 6.40: Control effort for case 1.

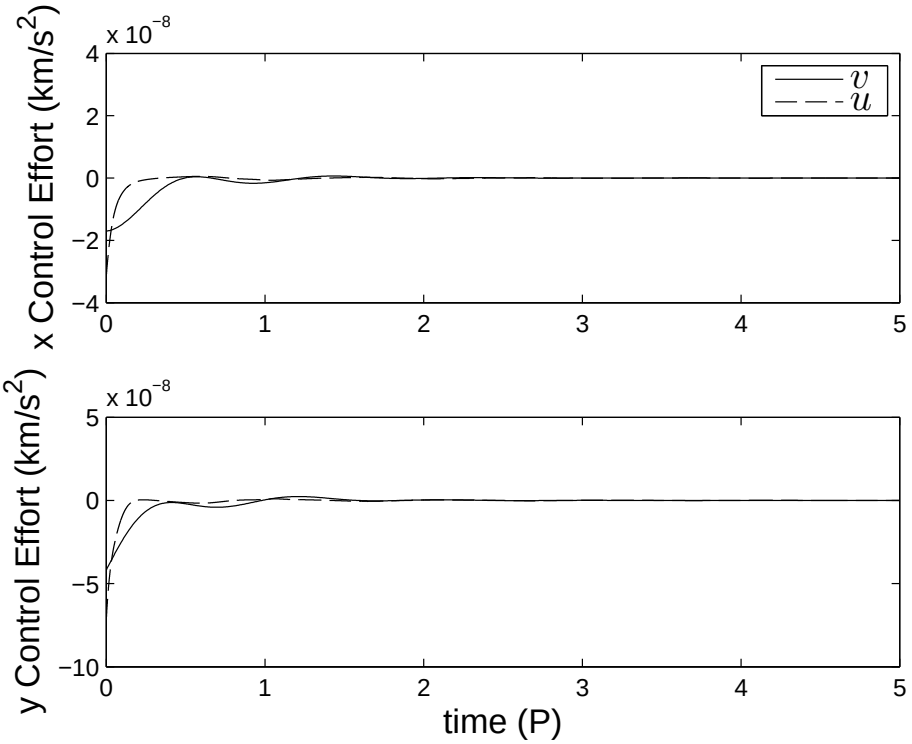

Figure 6.41: Control effort for case 2.

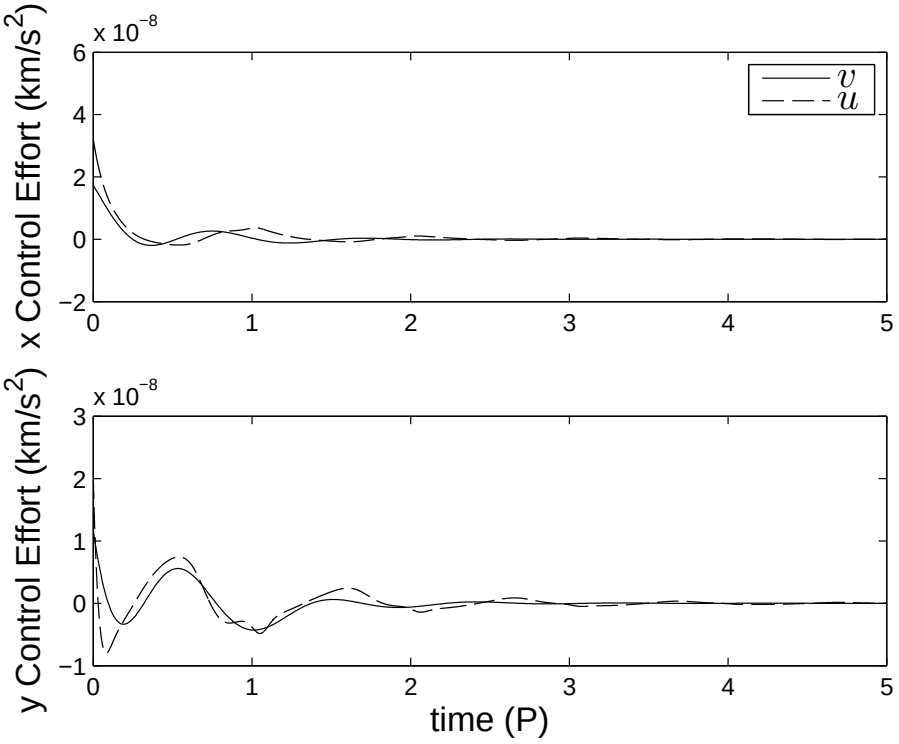

Figure 6.42: Control effort for case 3.

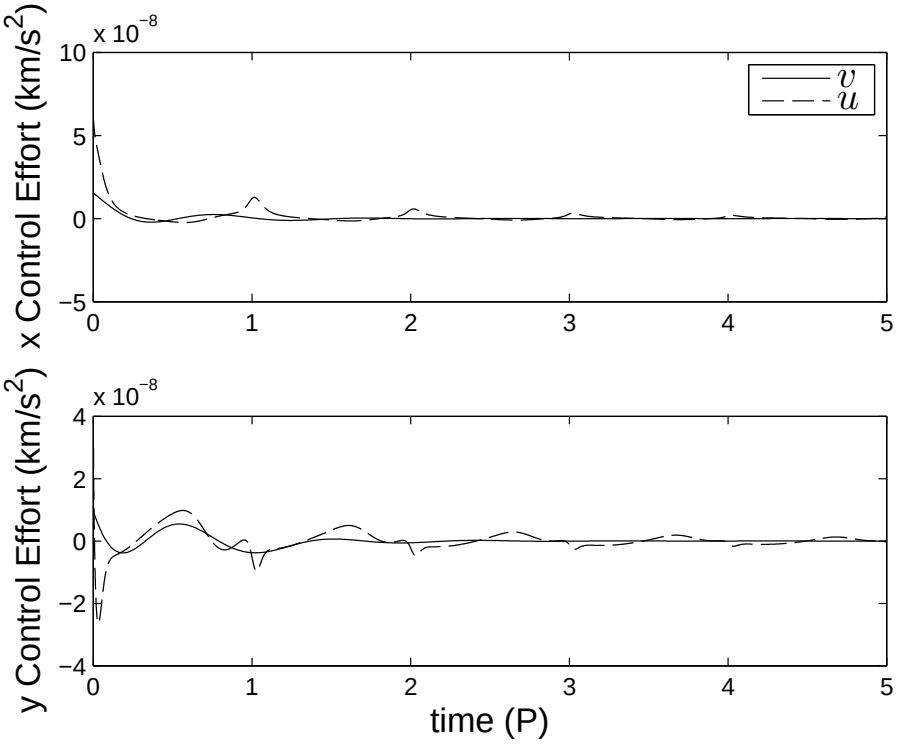

Figure 6.43: Control effort for case 4.

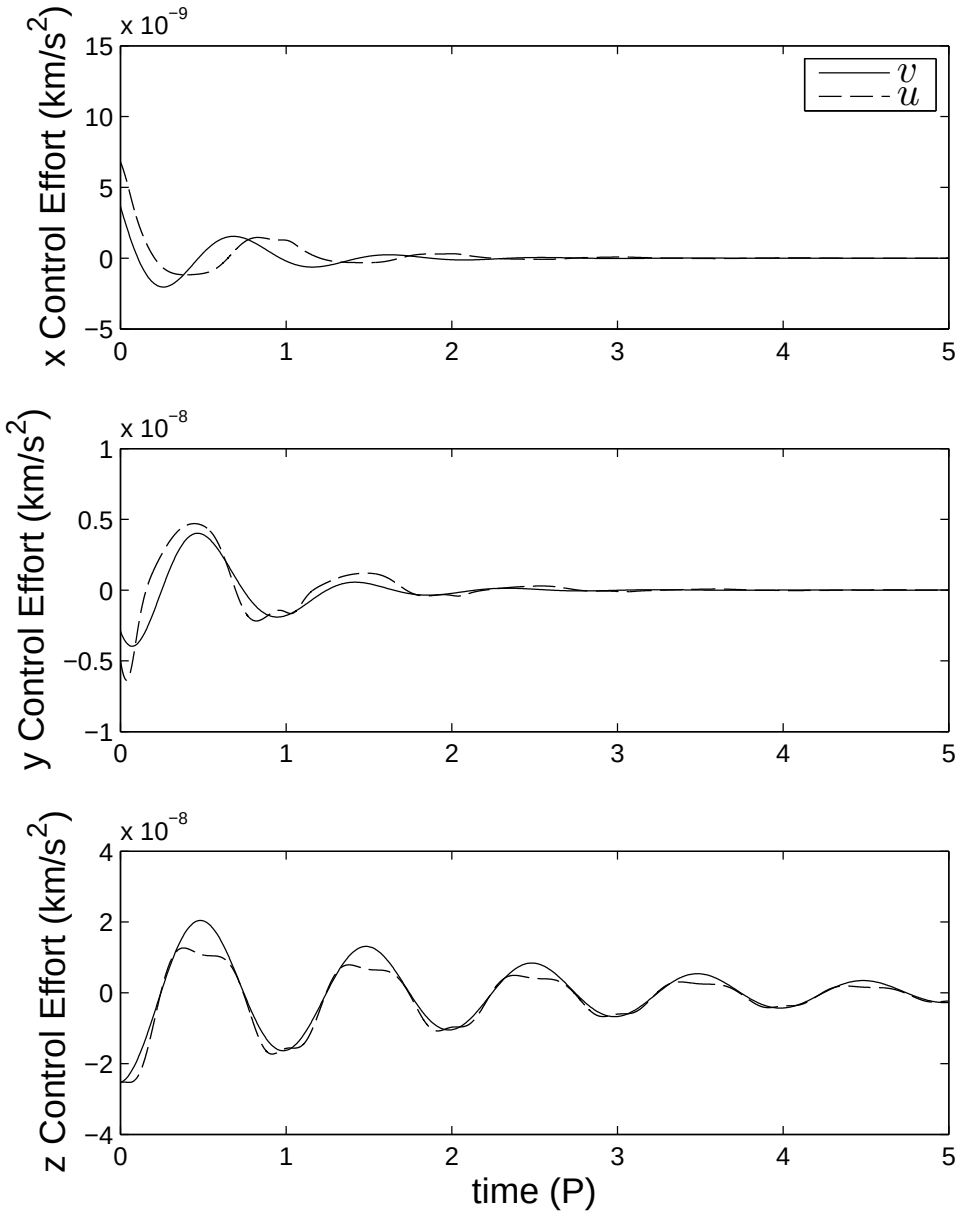

Figure 6.44: Control effort for case 5.

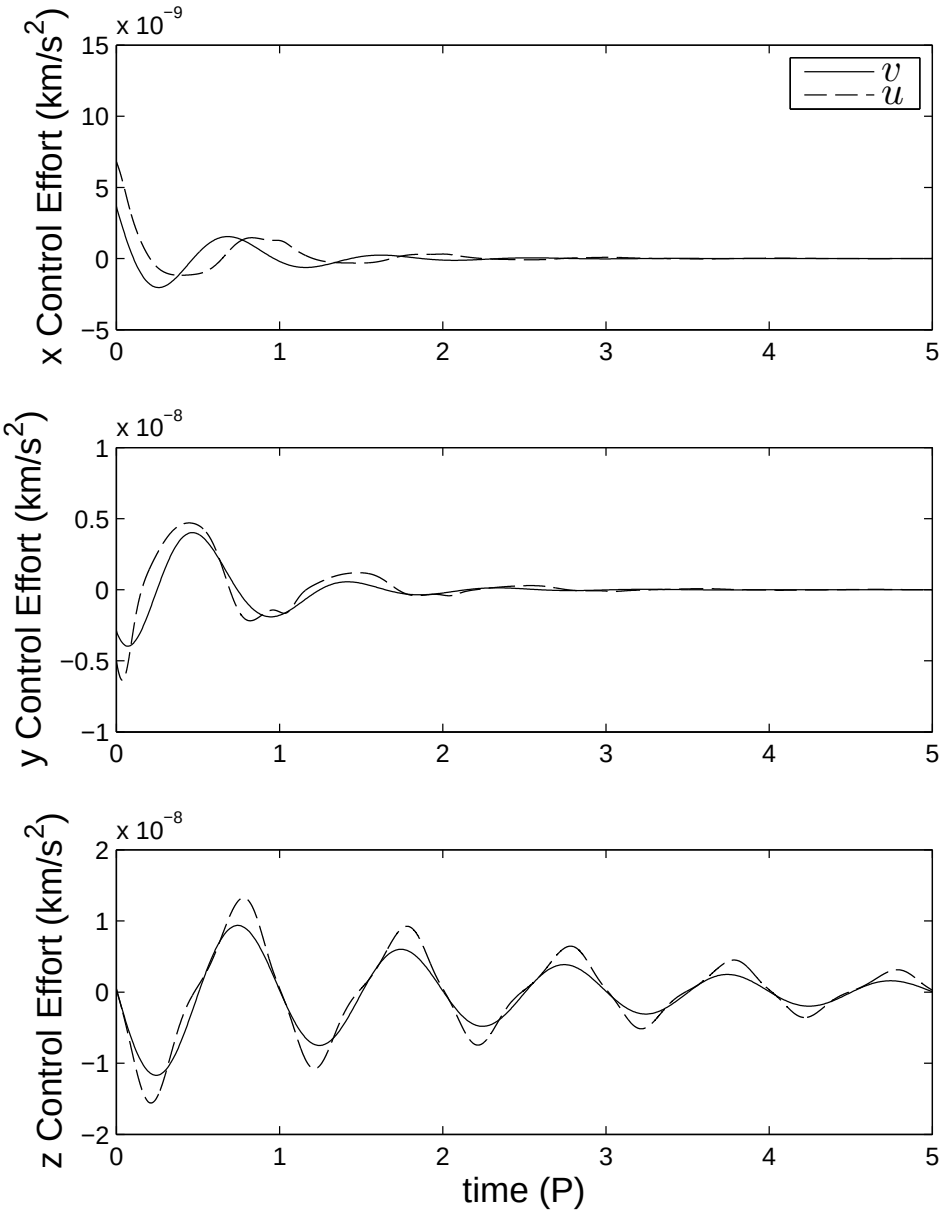

Figure 6.45: Control effort for case 6.

For case four, the worse performing case, the results of the continuous-thrust methods are here compared to the impulsive control method. The same four choices of the transfer time from the previous section were selected, and the total control effort was calculated. The control effort was 2.8477×10^{-4} km/s for a transfer time of $0.5P$, 3.3482×10^{-2} km/s for a transfer time of P, 1.6650×10^{-2} km/s for a transfer time of $2P$, and 8.1973×10^{-2} km/s for a transfer time of $5P$. These results show that for a transfer time of half a period, the two-burn method had one magnitude greater control effort than $\boldsymbol{u}(t)$. For other choices of the transfer time, the two-burn method performed significantly worse.

6.4.3 Effects of Eccentricity on Control Effort

This section will study the effect of eccentricity on the time-varying control, $\boldsymbol{K}(t)$. For this study, the orbital elements of the chief at the initial time are given by $a_C = 17000$ km, and $i_C = \Omega_C = \omega_C = f_C = 0$. The chief's eccentricity will be swept through three values: $e_C = 0.2$, $e_C = 0.4$, and $e_C = 0.6$. Corresponding to these chief orbital elements, the deputy's semi-major axis is given by $a_D = 17000.2$ km, $a_D = 17000.2666$ km, and $a_D = 17000.4$ km. The remaining orbital elements of the deputy at the initial time are given by $e_D = e_C$, and $i_D = \Omega_D = \omega_D = f_D = 0$. Note that these initial conditions give a constant initial relative position of $\boldsymbol{\rho}(0) = [0.1600\ 0\ 0]^\mathsf{T}$ km, but the initial relative velocity $\dot{\boldsymbol{\rho}}(0)$ varies for each case.

Similar to the previous section, only the LF approach will be studied: $\widetilde{\boldsymbol{z}}(t)$, $\boldsymbol{z}(t)$, and $\boldsymbol{x}(t)$. After five complete periods of the chief, Table 6.13 gives the final position $\widetilde{\boldsymbol{z}}(5P)$ and total control effort v for the auxiliary system, Table 6.14 gives the final position $\boldsymbol{z}(5P)$ and total control effort u for the LF transformed HCW system, and Table 6.15 gives the final position $\boldsymbol{x}(5P)$ and total control effort u for the LF transformed LERM system. Figures 6.46 through 6.48 show the position error over five orbits for each case. Figures 6.49 through 6.51 show the control effort $\boldsymbol{v}(t)$ and $\boldsymbol{u}(t)$, as a function of time for each case. As in the previous subsection, the auxiliary system $\widetilde{\boldsymbol{z}}$ performed better that both $\boldsymbol{z}(t)$, and $\boldsymbol{x}(t)$ in driving the deputy's position to zero, while utilizing less control effort. The ratio of the increase in v

Case	$x(5P)$ (km)	$y(5P)$ (km)	Total v (km/s)
1	6.2805×10^{-6}	-3.9492×10^{-5}	5.4257×10^{-7}
2	1.7467×10^{-5}	-4.9210×10^{-5}	8.6499×10^{-7}
3	4.5824×10^{-5}	-6.9724×10^{-5}	1.6611×10^{-6}

Table 6.13: Final position and total control effort for the auxiliary system $\widetilde{\boldsymbol{z}}(t)$.

Case	$x(5P)$ (km)	$y(5P)$ (km)	Total u (km/s)
1	-2.3135×10^{-4}	3.0330×10^{-5}	4.0620×10^{-6}
2	-9.0791×10^{-4}	8.3720×10^{-4}	9.1127×10^{-6}
3	1.1727×10^{-3}	2.9579×10^{-3}	3.1454×10^{-5}

Table 6.14: Final position and total control effort for the LF transformed HCW system $\boldsymbol{z}(t)$.

Case	$x(5P)$ (km)	$y(5P)$ (km)	Total u (km/s)
1	-2.0636×10^{-4}	3.0330×10^{-5}	4.0620×10^{-6}
2	-7.2241×10^{-4}	8.3720×10^{-4}	9.1127×10^{-6}
3	1.1639×10^{-3}	2.9579×10^{-3}	3.1454×10^{-5}

Table 6.15: Final position and total control effort for the LF transformed LERM system $\boldsymbol{x}(t)$.

and u from $e_C = 0.2$ to $e_C = 0.4$ was comparable to the increase from $e_C = 0.4$ to $e_C = 0.6$. The largest closed-loop eigenvalues of $\boldsymbol{x}(t)$ were 0.6754 for case one, 0.7173 for case two, and 0.7845 for case three.

An additional observation can be made since the chief and deputy differ only in semi-major axis. For this type of configuration, it is more efficient to apply thrust at perigee. As can be seen in Figure 6.51, $\boldsymbol{u}$ peaks slightly at periapse, but remains fairly constant for the rest of the orbit. This indicates that even though the LQR optimization uses the HCW equations, the LF transformations makes sure that the control corresponds with the natural dynamics of elliptic orbits.

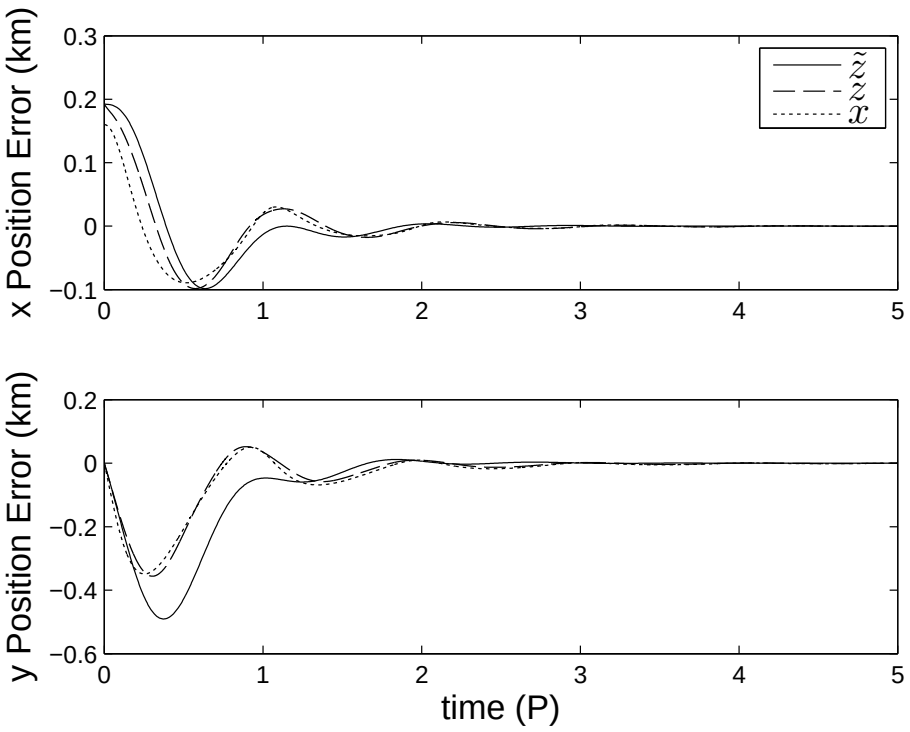

Figure 6.46: Position error for case 1.

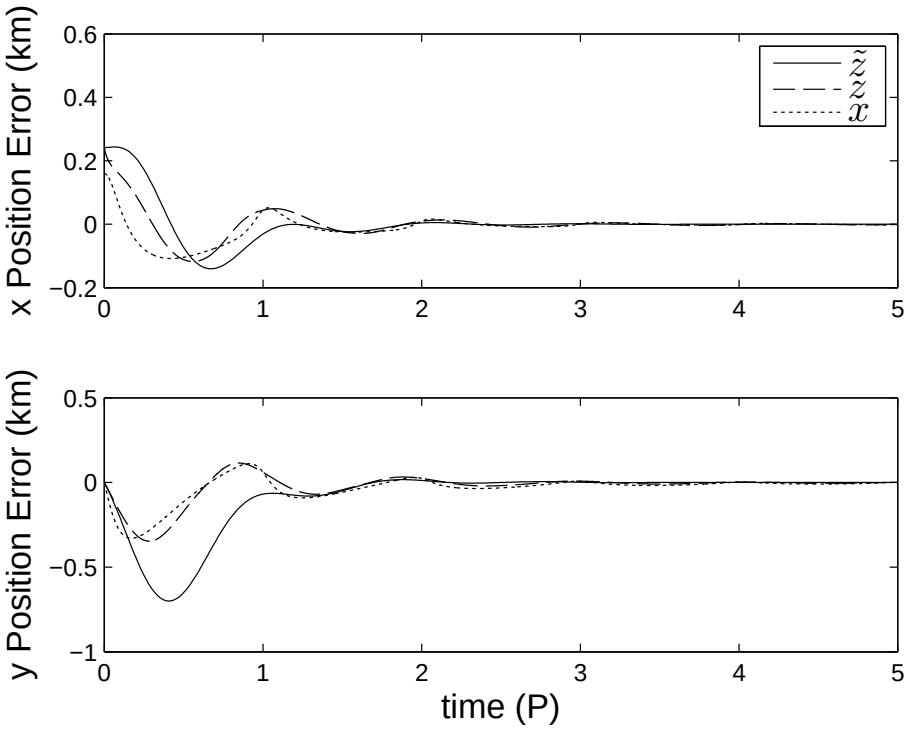

Figure 6.47: Position error for case 2.

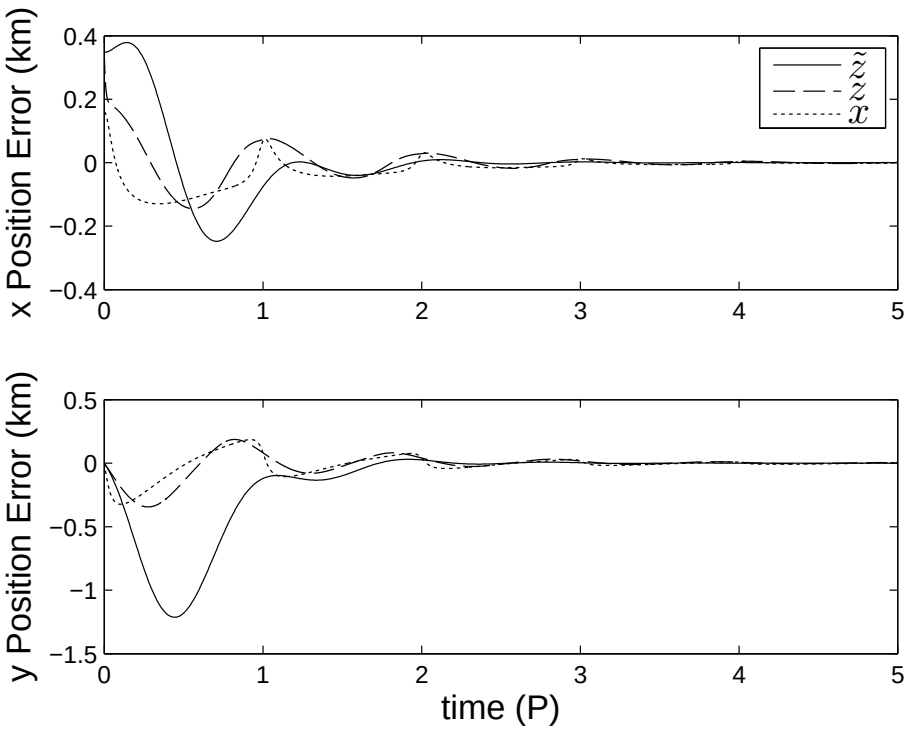

Figure 6.48: Position error for case 3.

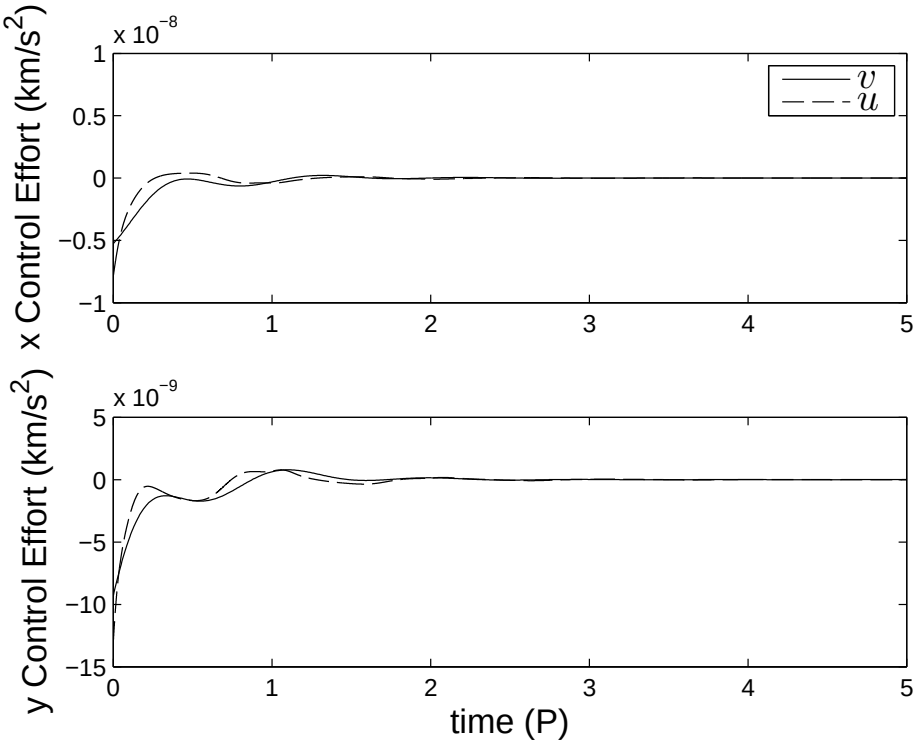

Figure 6.49: Control effort for case 1.

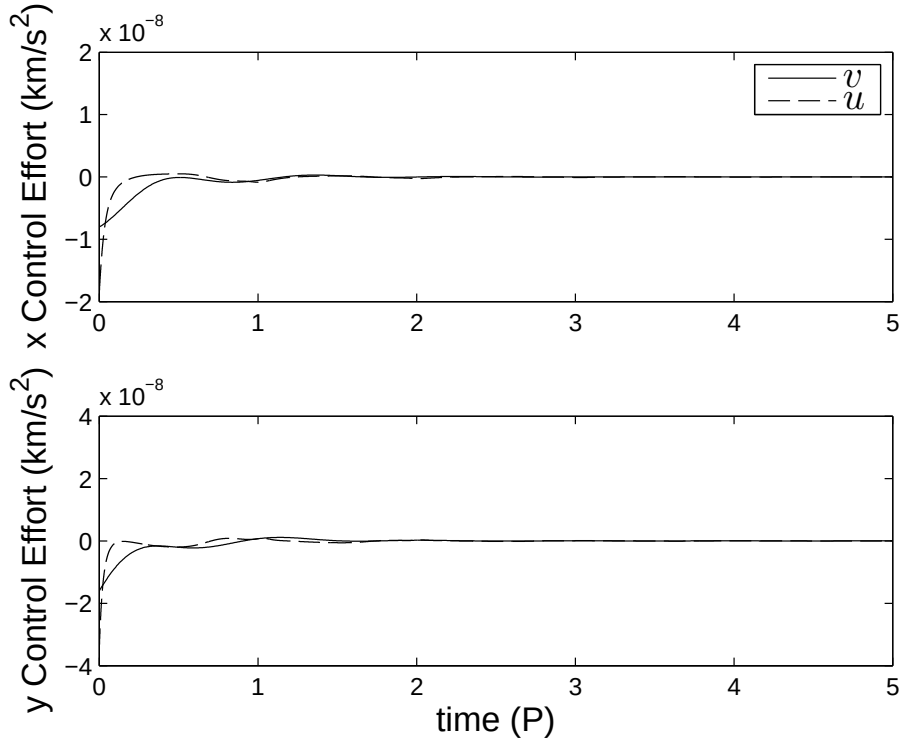

Figure 6.50: Control effort for case 2.

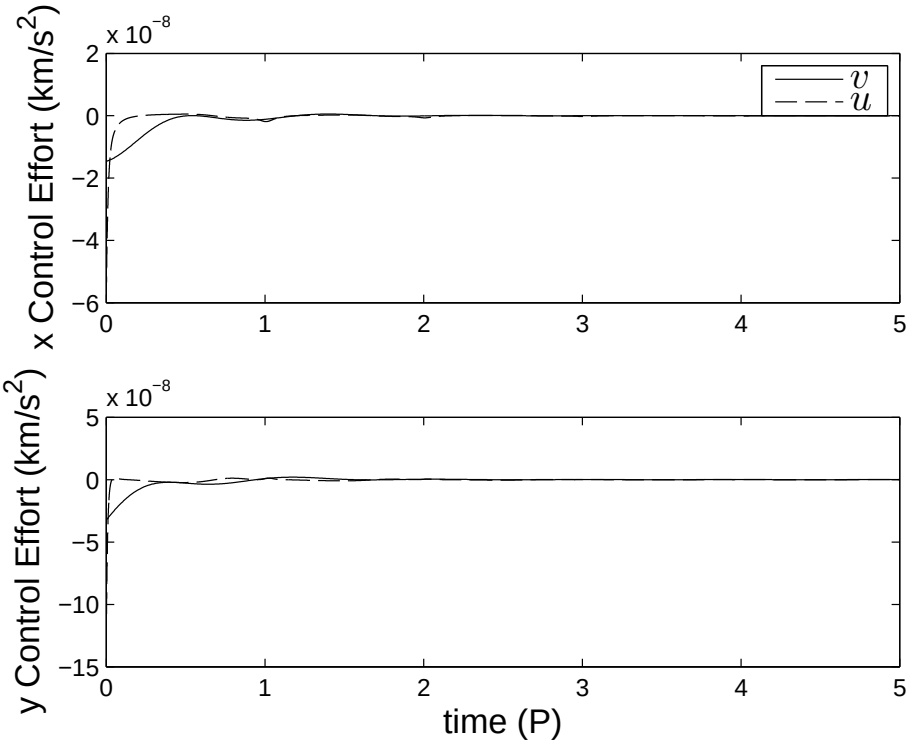

Figure 6.51: Control effort for case 3.

Case	$x(5P)$ (km)	$y(5P)$ (km)	$z(5P)$ (km)	Total u (km/s)
1	2.9620×10^{-4}	-3.7259×10^{-3}	–	-6.5349×10^{-6}
2	5.8495×10^{-5}	-4.9883×10^{-3}	–	-4.4681×10^{-5}
3	1.3629×10^{-3}	-2.5851×10^{-3}	–	-1.4862×10^{-5}
4	-6.0484×10^{-4}	8.3863×10^{-1}	–	-1.0848×10^{-3}
5	2.9620×10^{-4}	-3.7250×10^{-3}	4.3636×10^{-3}	-4.0046×10^{-6}
6	2.9622×10^{-4}	-3.7254×10^{-3}	-2.2571×10^{-2}	-1.0979×10^{-5}

Table 6.16: Difference in final position and control effort between the periapse-matching transformation and the apoapse-matching transformation

6.4.4 Choice of Periapse-Matching or Apoapse-Matching Transformation

The previous subsections have all used the periapse-matching LF transformation to compute the time-varying control matrix $\boldsymbol{K}(t)$. However, a highly elliptic satellite spends more time near apoapse than periapse. This subsection will compare using periapse-matching LF transformation to the apoapse-matching LF transformation when computing $\boldsymbol{K}(t)$. Six cases will be considered, with the nonzero orbital elements at the initial time for the chief and deputy given in Table 6.8. Here, only the physical states $\boldsymbol{x}(t)$ will be considered.

Recall that for the physical states, the final position and total control effort after five complete orbits of the chief using the periapse-matching transformation was given in Table 6.12. Table 6.16 gives the difference between using the periapse-matching LF transformation and the apoapse-matching transformation after five periods. Figures 6.52 through 6.57 show the position error of $\boldsymbol{x}(t)$ using both LF transformations over five orbits and Figures 6.58 through 6.63 show the control effort $\boldsymbol{u}(t)$, as a function of time for each case. The results indicate that the apoapse-matching transformation performed worse than the perigee-matching transformation for every case considered, but was able to drive the deputy toward rendezvous with the chief.

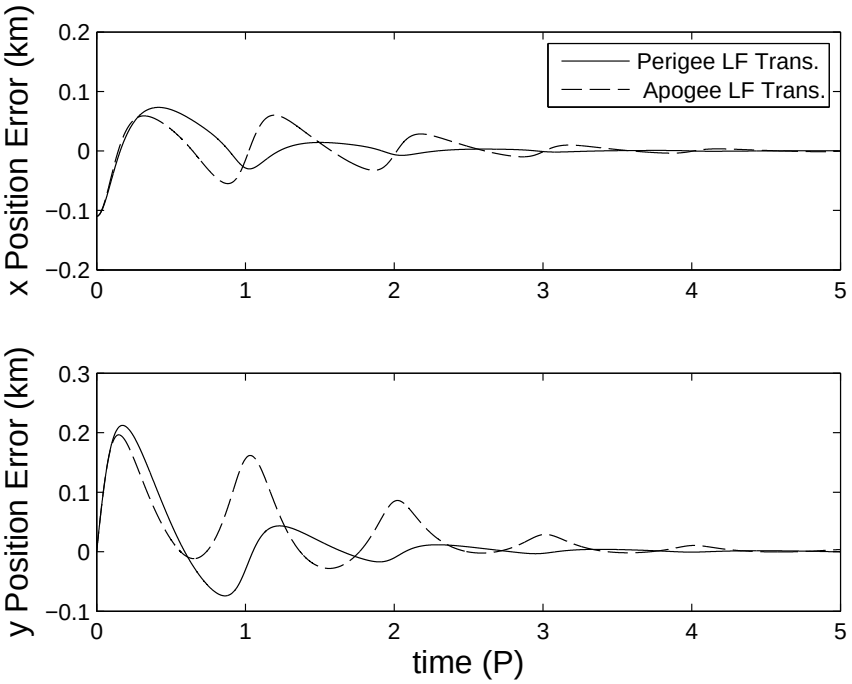

Figure 6.52: Position error for periapse-matching transformation and apoapse-matching transformation for case 1.

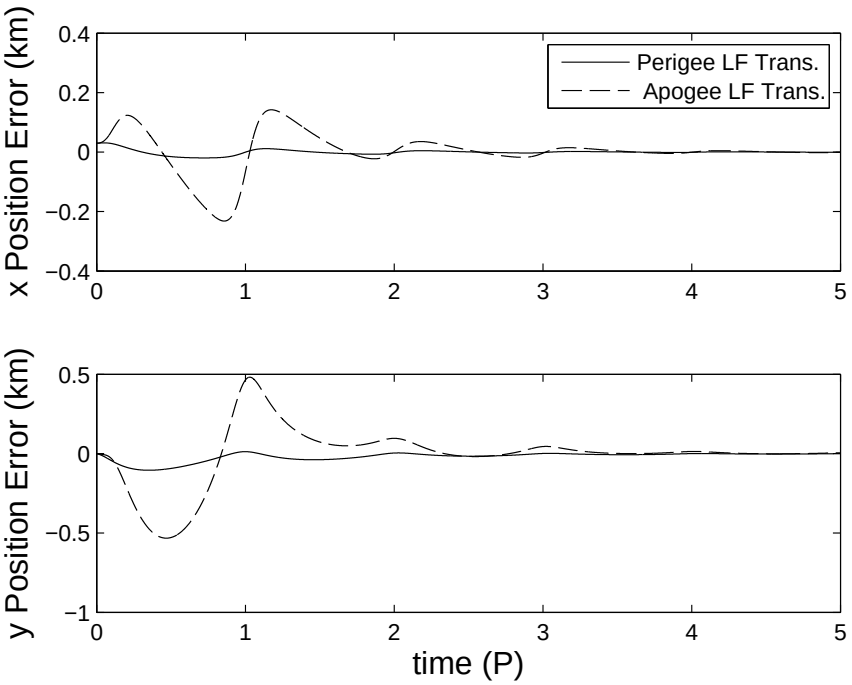

Figure 6.53: Position error for periapse-matching transformation and apoapse-matching transformation for case 2.

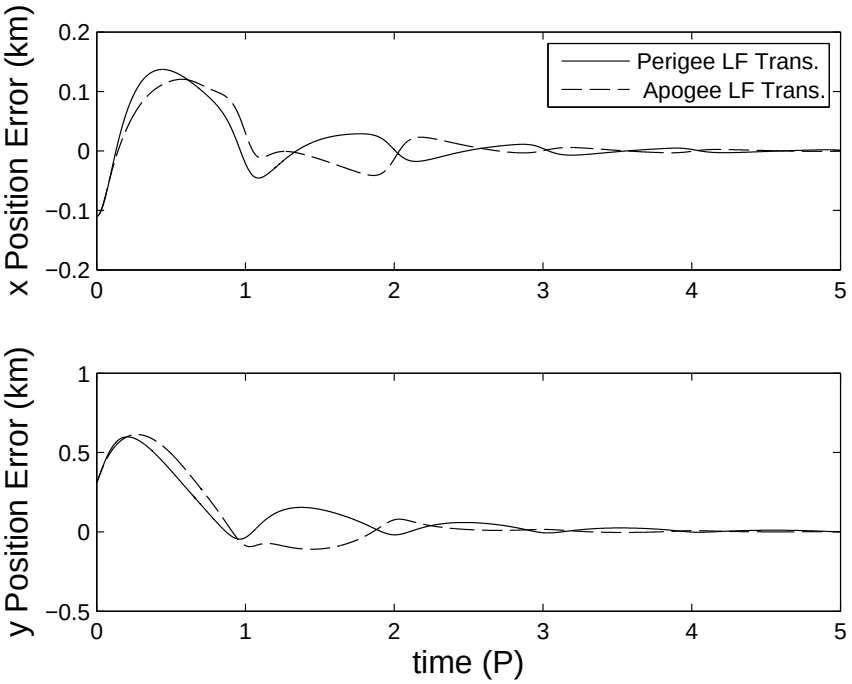

Figure 6.54: Position error for periapse-matching transformation and apoapse-matching transformation for case 3.

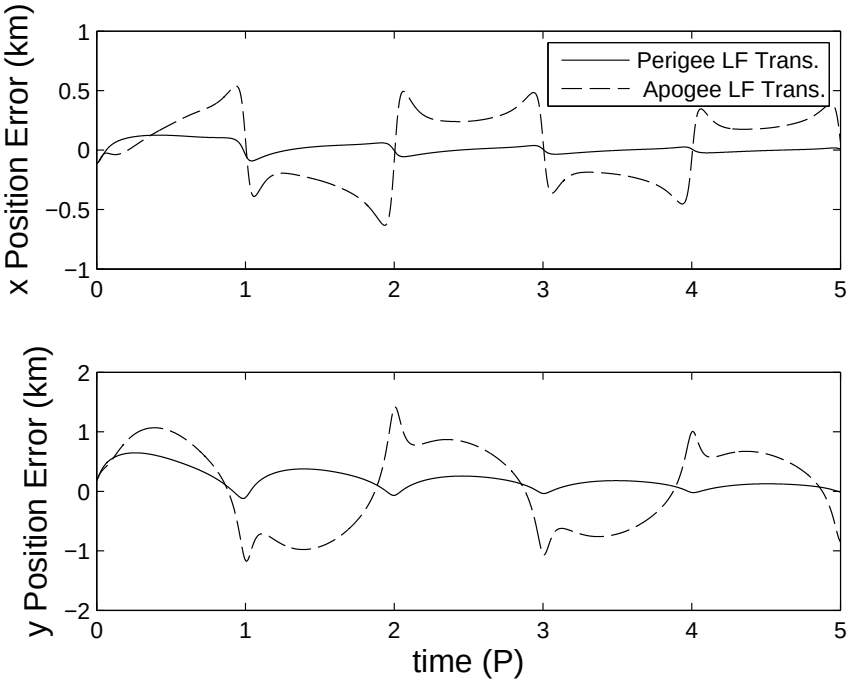

Figure 6.55: Position error for periapse-matching transformation and apoapse-matching transformation for case 4.

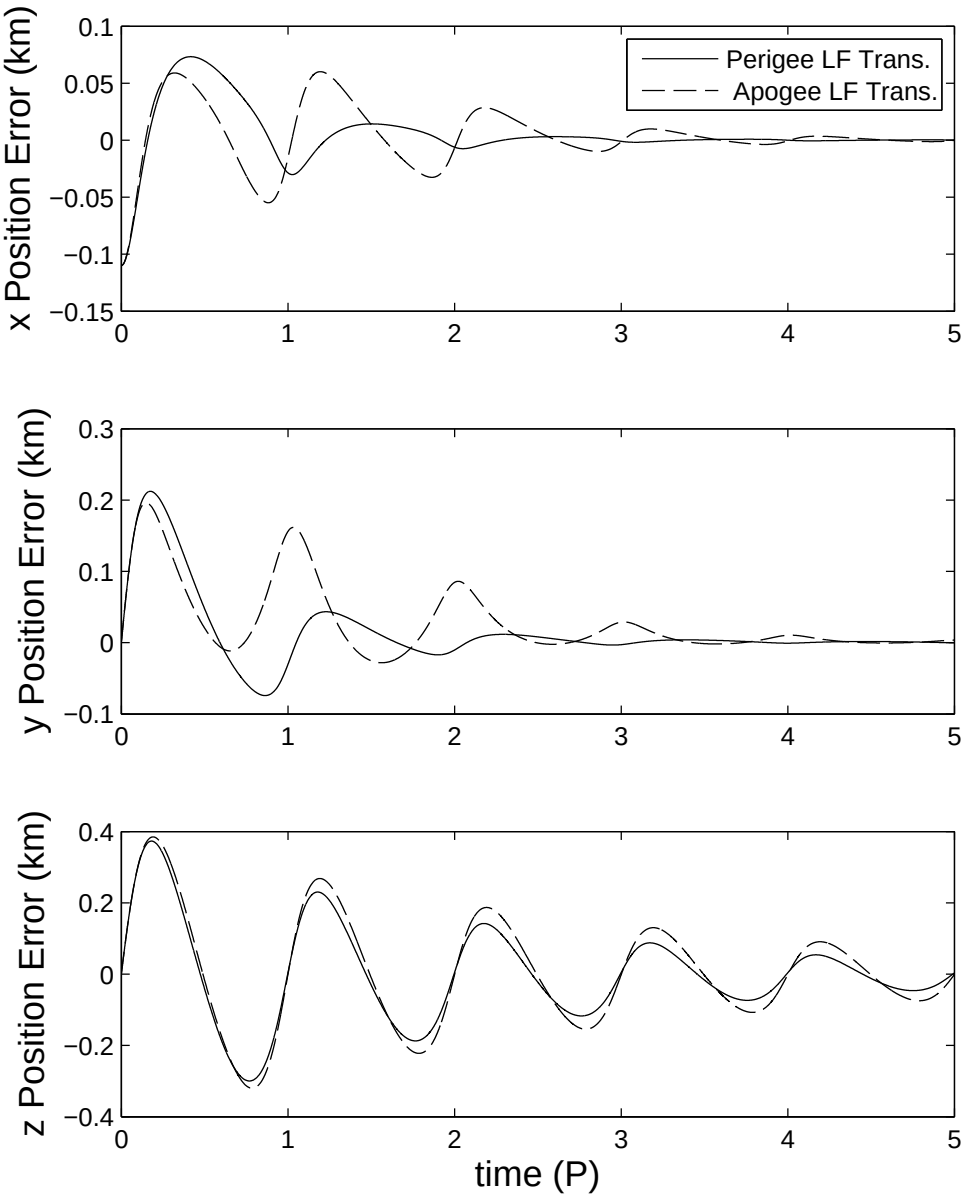

Figure 6.56: Position error for periapse-matching transformation and apoapse-matching transformation for case 5.

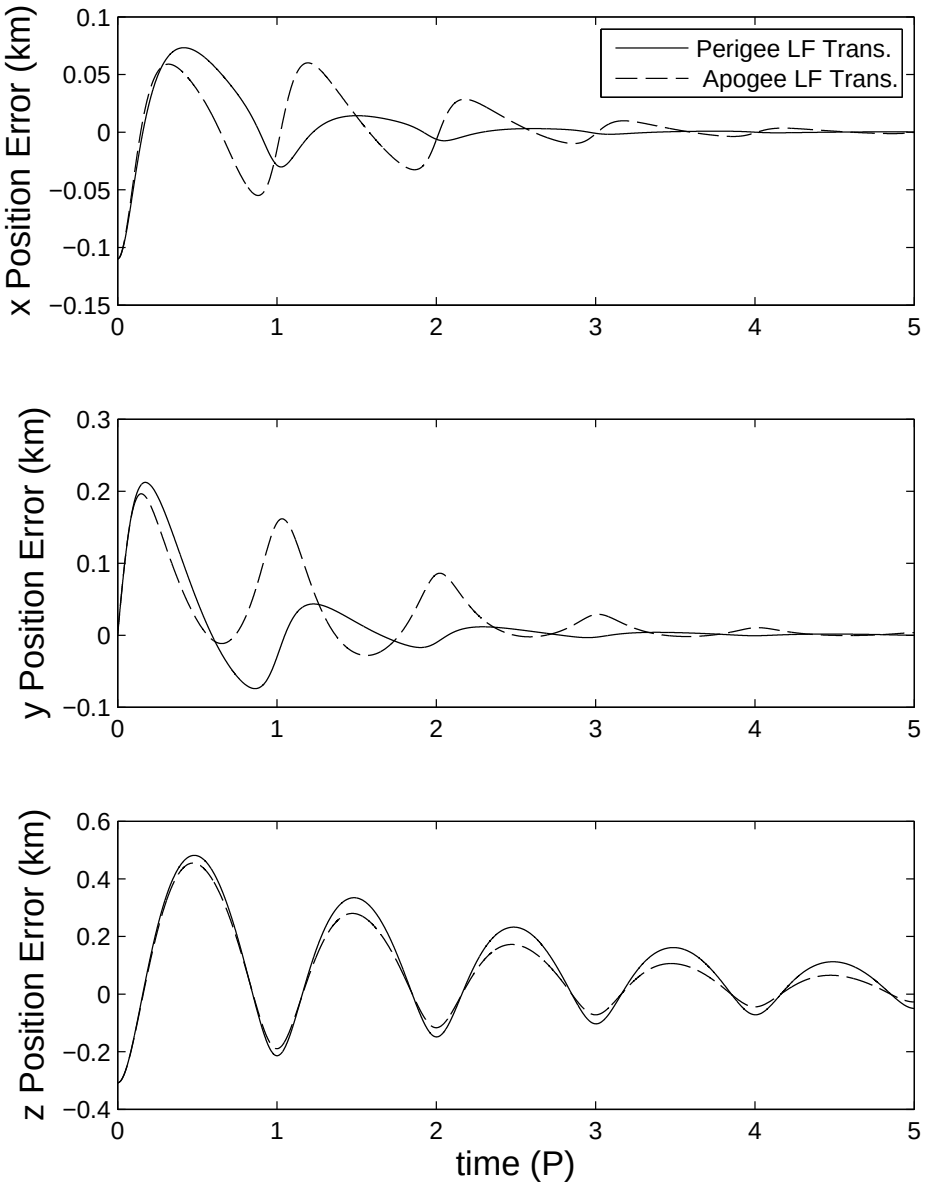

Figure 6.57: Position error for periapse-matching transformation and apoapse-matching transformation for case 6.

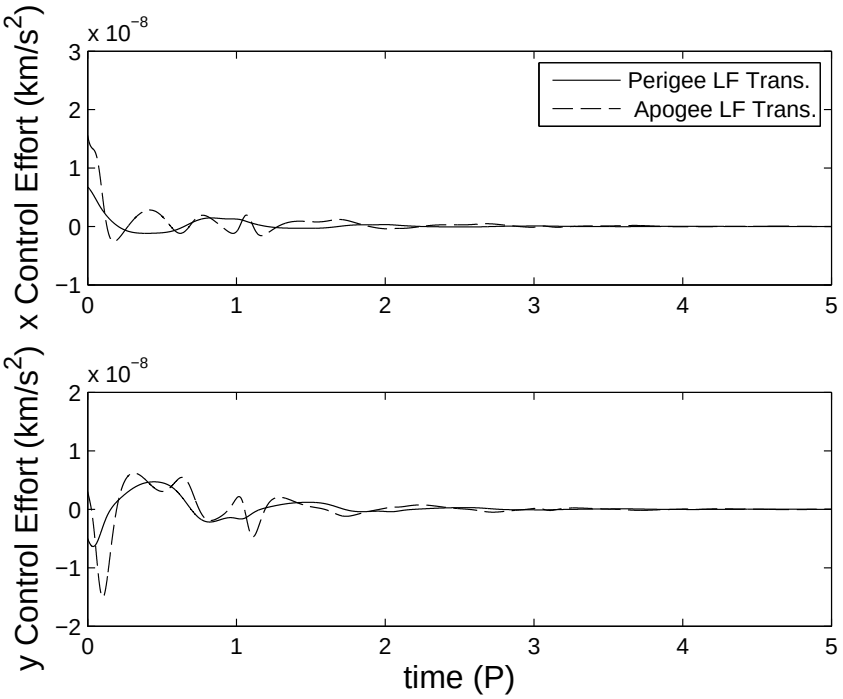

Figure 6.58: Control effort for periapse-matching transformation and apoapse-matching transformation for case 1.

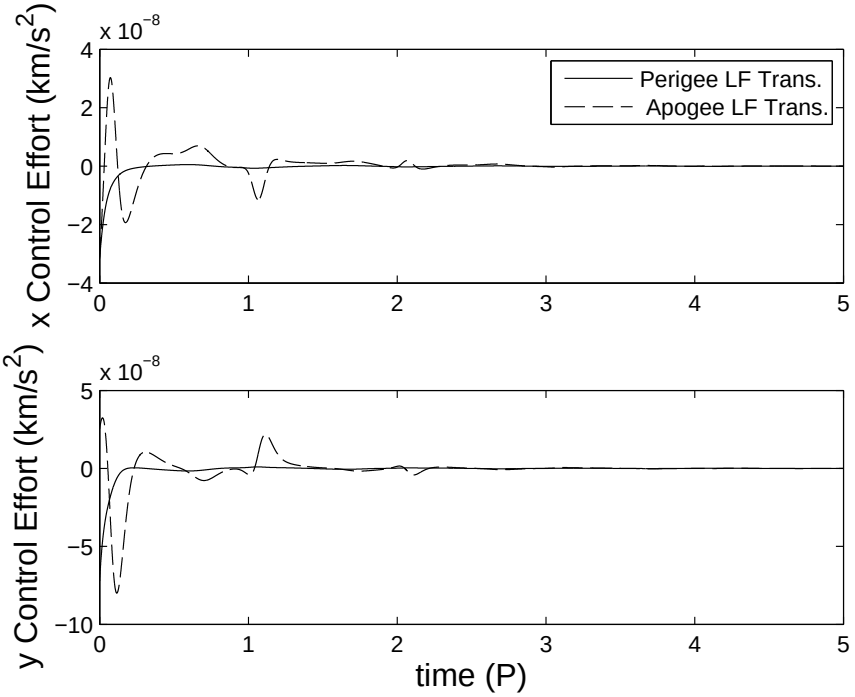

Figure 6.59: Control effort for periapse-matching transformation and apoapse-matching transformation for case 2.

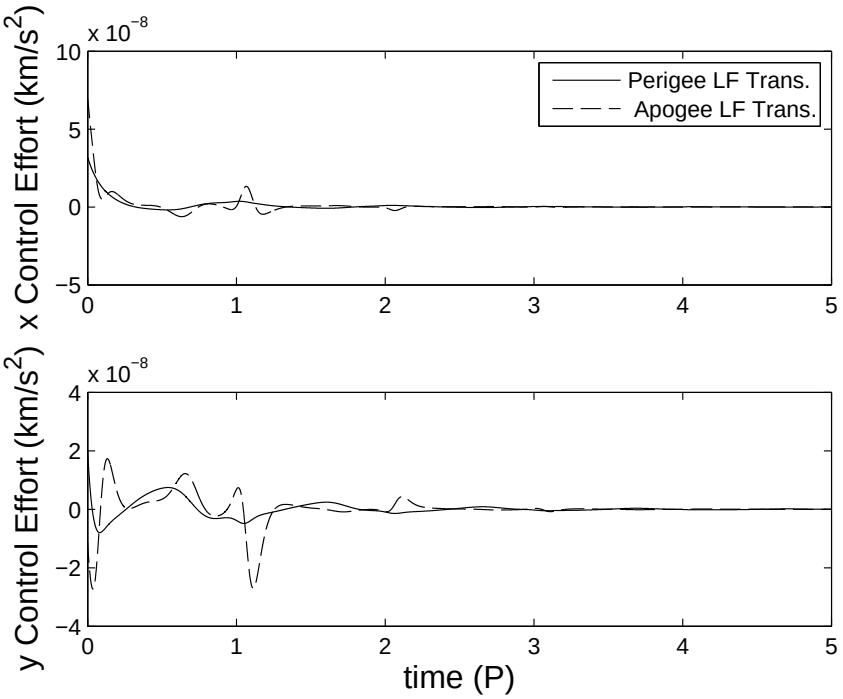

Figure 6.60: Control effort for periapse-matching transformation and apoapse-matching transformation for case 3.

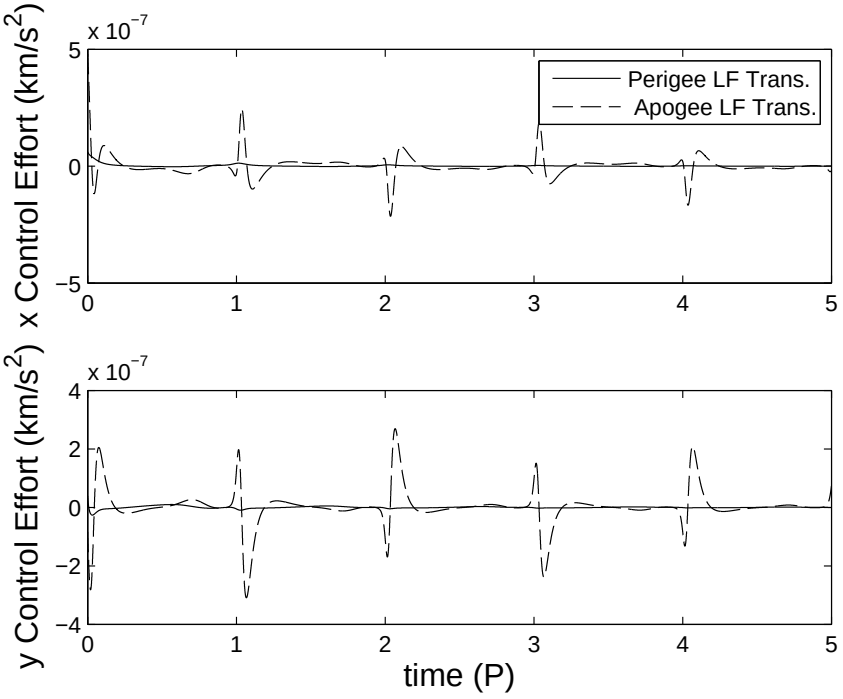

Figure 6.61: Control effort for periapse-matching transformation and apoapse-matching transformation for case 4.

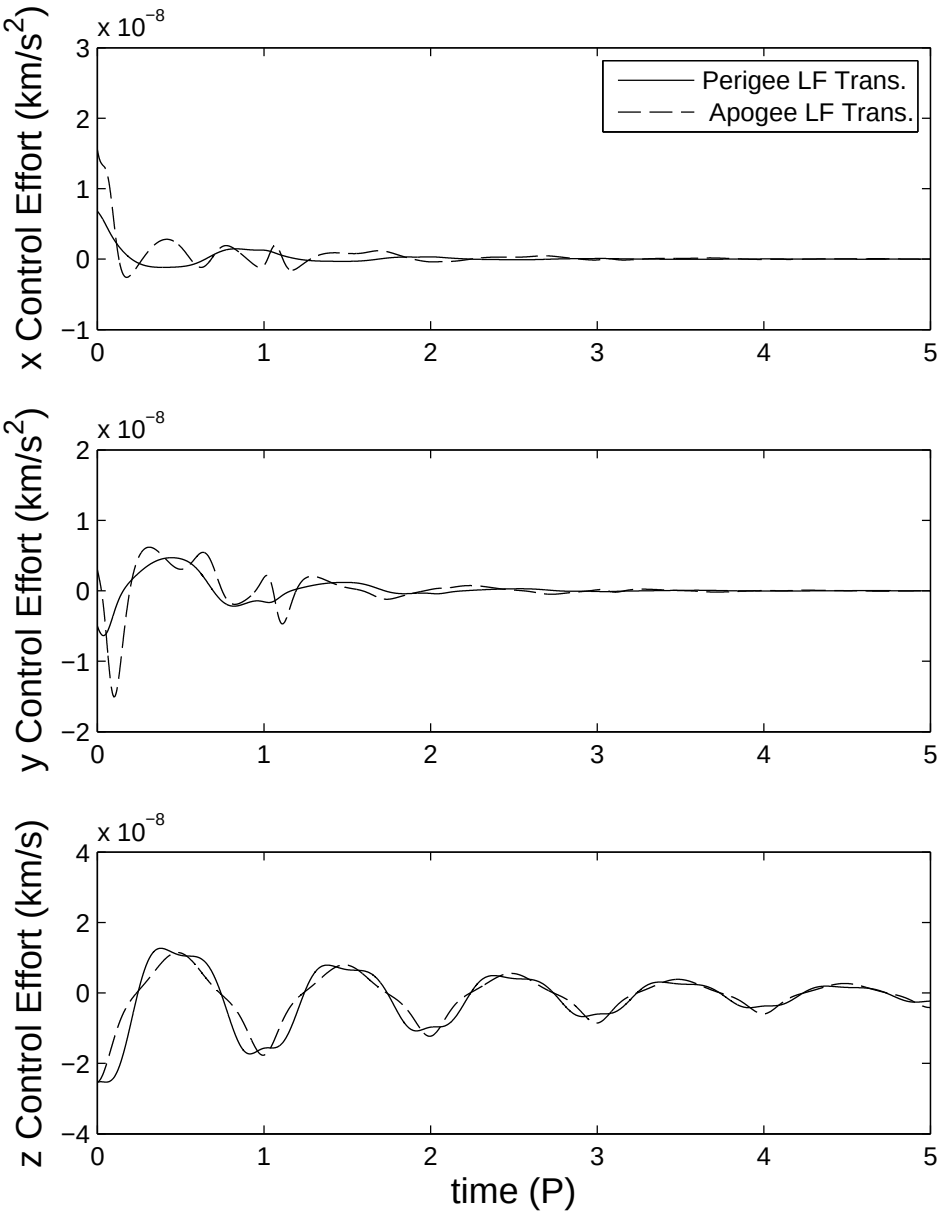

Figure 6.62: Control effort for periapse-matching transformation and apoapse-matching transformation for case 5.

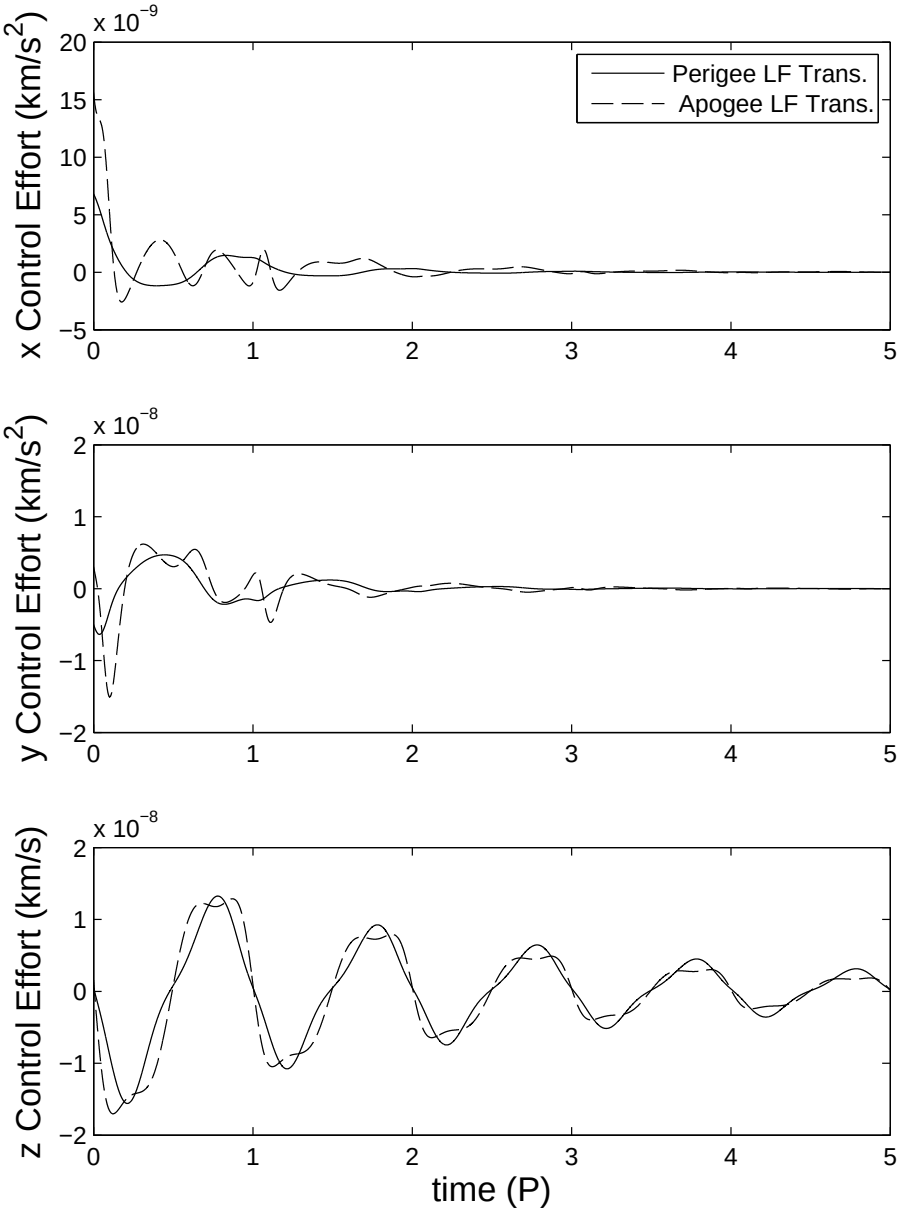

Figure 6.63: Control effort for periapse-matching transformation and apoapse-matching transformation for case 6.

Chapter 7

Conclusion

In satellite proximity operations, it is desirable to express the motion of a deputy satellite with respect to a chief satellite. One choice to describe this motion is the linear time-invariant Hill-Clohessy-Wiltshire equations, which were derived by assuming a circular chief orbit. An advantage of the Hill-Clohessy-Wiltshire equations are that the relative motion can by easily understood and visualized. Linearized equations derived without assuming a circular chief results in time-varying differential equations. These solutions are more accurate in describing relative motion in elliptic orbits, but can be difficult to intuitively visualize.

Due to the abundance of algorithms in the literature based on the Hill-Clohessy-Wiltshire equations, this dissertation explored the relationship between the Hill-Clohessy-Wiltshire equations and relative motion in elliptic orbits. Preliminary investigation lead to the development of the Virtual-Chief and Virtual-Time methods. These methods showed improvement in accuracy when applying the Hill-Clohessy-Wiltshire equations to elliptic orbits, but also showed a lower fidelity than the Linearized Equations of Relative Motion.

Instead of selecting a time-varying transformation for the Hill-Clohessy-Wiltshire equations, a direct transformation was calculated using Lyapunov-Floquet theory. It was shown in this dissertation that the Hill-Clohessy-Wiltshire equations capture the exact time-varying dynamics for chief satellites of arbitrary eccentricity through time-periodic coordinate transformations. Two transformations were presented here, a periapse-matching transformation and an apoapse-matching transformation. In addition to the Lyapunov-Floquet transformations, a time-varying transformation derived by matching integrals of the motion was also presented. These three transformations show that the Hill-Clohessy-Wiltshire equations can be generalized to describe relative motion in elliptic orbits. Using these transformations

to calibrate initial conditions for applying the Hill-Clohessy-Wiltshire equations to elliptic orbits was also investigated.

The literature does not currently contain infinite-horizon continuous-thrust control of satellites in elliptic orbits. Using a linear quadratic regulator and a control method from the literature, the Lyapunov-Floquet transformations calculated previously were used to compute a time-varying gain matrix. Results were presented using both the periapse-matching transformation and the apoapse-matching Lyapunov-Floquet transformation. These results show that this control was able to drive the deputy's position toward rendezvous with the chief for both near-circular and highly elliptic chief satellites. Results were also compared to solutions using two-burn impulsive control.

Future work could include further investigation of Lyapunov-Floquet transformations of the Linearized Equations of Relative Motion. Two members of a family of Lyapunov-Floquet transformations have been determined. For certain applications, a transformation based on other criteria not considered in this dissertation may be needed. An algorithm to quickly calculate these transformations would greatly assist future researchers. The time-varying control law used in this dissertation could not guarantee stability. Further improvement to this work could involve an alternative approach by Sinha et al. which allows symbolic placement of the poles of the time-varying system, see References 63 and 64. In addition, further study into the effect of different values of the LQR weighting matrices $\boldsymbol{Q}$ and $\boldsymbol{R}$ could provide a decrease in position error and control effort. Investigation into continuous-thrust control using the integral-preserving transformation is also warranted.

Bibliography

[1] G. J. Toomer, "The Size of the Lunar Epicycle According to Hipparchus," *Centaurus*, Vol. 12, No. 3, 1967, pp. 145–150.

[2] G. J. Toomer, *Ptolemy's Almagest*. Springer Verlag, 1984.

[3] O. Gingerich, *The Book Nobody Read: Chasing the Revolutions of Nicolaus Copernicus*. Walker, 2004.

[4] J. Prussing and B. Conway, *Orbital Mechanics*. Oxford University Press, 1993.

[5] D. Zwillinger, *Standard Mathematical Tables and Formulae, 31st Edition*. Chapman & Hall/CRC, 2003.

[6] O. Montenbruck and E. Gill, *Satellite Orbits: Models, Methods, and Applications*. Springer, 2005.

[7] J. Tschauner and P. Hempel, "Rendezvous zu einem in elliptischer Bahn unlaufenden Ziel," *Astronautica Acta*, Vol. 11, No. 2, 1965, pp. 104–109.

[8] J. P. DeVries, "Elliptic Elements in Terms of Small Increments of Position and Velocity Components," *AIAA Journal*, Vol. 1, No. 11, 1963, pp. 2626–2629.

[9] D. Lawden, "Fundamentals of Space Navigation," *British Interplanetary Science Journal*, Vol. 13, 1954, pp. 87–101.

[10] K. Yamanaka and F. Ankersen, "New State Transition Matrix for Relative Motion on an Arbitrary Elliptical Orbit," *Journal of Guidance, Control and Dynamics*, Vol. 25, No. 1, 2002.

[11] T. Carter, "State Transition Matricies for Terminal Rendezvous Studies: Brief Survey and New Example," *Journal of Guidance, Control and Dynamics*, Vol. 21, No. 1, 1998.

[12] A. J. Sinclair, R. E. Sherrill, and T. A. Lovell, "Review of the Solutions to the Tschauner-Hempel Equations for Satellite Relative Motion," *AAS 12-149*, presented at the 22nd AAS/AIAA Space Flight Mechanics Meeting, Charleston, South Carolina, 2012.

[13] R. E. Sherrill, A. J. Sinclair, and T. A. Lovell, "Fundamental-Solution Guidance for Satellite Relative Motion in Elliptic Orbits," *IAA-AAS-DyCoSS1-06-09*, presented at the IAA Conference on Dynamics & Control of Space Systems, Porto, Portugal, 2012.

[14] W. H. Clohessy and R. S. Wiltshire, "Terminal Guidance System for Satellite Rendezvous," *Journal of Guidance, Control, and Dynamics*, Vol. 27, No. 9, 1960, pp. 653–658.

[15] G. W. Hill, "Researches in the Lunar Theory," *American Journal of Mathematics*, Vol. 23, No. 1, 1878, pp. 5–26.

[16] H. Curtis, *Orbital Mechanics for Engineering Students*. Elsevier, 2005.

[17] D. Jezewski and J. Donaldson, "An Analytic Approach to Optimal Rendezvous Using Clohessy-Wiltshire Equations," *Journal of the Astronautical Sciences*, Vol. 27, No. 3, 1979, pp. 293–310.

[18] T. A. Lovell and S. Tragesser, "Guidance for Relative Motion of Low Earth Orbit Spacecraft Based on Relative Orbit Elements," *AIAA Paper 2004-4988*, presented at the AAS/AIAA Astrodynamics Specialist Conference, Providence, RI, 2004.

[19] D. Vallado, *Fundamentals of Astrodynamics and Applications*. Microcosm Press and Kluwer Academic Publishers, 2001.

[20] V. Chobotov, *Orbital Mechanics, 3rd Ed.* AIAA Education Series, 2002.

[21] K. Alfriend, S. Vadali, P. Gurfil, J. How, and L. Breger, *Spacecraft Formation Flying*. Elsevier, 2010.

[22] H. London, "Second Approximation to the Solution of the Rendezvous Equations," *AIAA Journal*, Vol. 1, No. 7, 1963, pp. 1691–1693.

[23] K. Johnson, "Relative Orbit Elements for Satellites in Elliptical Orbits," MS Thesis, Air Force Institute of Technology, 2010.

[24] J. Hess, "Osculating Relative Orbit Elements Resulting from Chief Eccentrity and J2 Perturbing Forces," MS Thesis, Air Force Institute of Technology, 2011.

[25] R. Bevilacqua and T. A. Lovell, "Analytical Guidance for Spacecraft Relative Motion Under Constant Thrust Using Relative Orbit Elements," *AAS 13-471*, presented at the 23nd AAS/AIAA Space Flight Mechanics Meeting, Kauai, Hawaii, 2013.

[26] V. A. Brumberg, "Perturbation Theory in Rectangular Coordinates," *Celestial Mechanics*, Vol. 18, 1978, pp. 319–336.

[27] T. Kelly, "An Analytical Approach to the Two-Impulse Optimal Rendezvous Problem," *AAS 94-156*, 1994.

[28] E. M. Soop, *Handbook of Geostationary Orbits*. European Space Agency, 1994.

[29] J. B. Jones, "Optimal Rendezvous in the Neighborhood of a Circular Orbit," *Journal of the Astronautical Sciences*, Vol. 24, No. 1, 1976, pp. 55–90.

[30] S. D'Amico and O. Montenbruck, "Proximity Operations of Formation-Flying Spacecraft Using an Eccentricity/Inclination Vector Separation," *Journal of Guidance, Control, and Dynamics*, Vol. 29, No. 3, 2006, pp. 554–563.

[31] H. Schaub and J. L. Junkins, *Analytical Mechanics of Space Systems, 2nd Edition*. AIAA, 2009.

[32] H. Schaub, "Relative Orbit Geometry Through Classical Orbit Element Differences," *Journal of Guidance, Control, and Dynamics*, Vol. 27, 2004.

[33] R. E. Sherrill, A. J. Sinclair, T. A. Lovell, K. W. Johnson, and D. D. Decker, "The Virtual-Chief Method for Modeling Relative Motion of Noncircular Satellites," *AAS 11-214*, presented at the 21st AAS/AIAA Space Flight Mechanics Meeting, New Orleans, Louisiana, 2011.

[34] R. E. Sherrill, A. J. Sinclair, and T. A. Lovell, "A Virtual-Time Method for Modeling Relative Motion of Noncircular Satellites," *AAS 11-208*, presented at the 21st AAS/AIAA Space Flight Mechanics Meeting, New Orleans, Louisiana, 2011.

[35] R. Grimshaw, *Nonlinear Ordinary Differential Equations*. CRC Press, 1993.

[36] J. A. Richards, *Analysis of Periodically Time-Varying Systems*. Springer-Verlag, 1983.

[37] R. Battin, *An Introduction to the Mathematics and Methods of Astrodynamics, Revised Edition*. AIAA, 1999.

[38] R. G. Melton, "Time-Explicit Representation of Relative Motion Between Elliptical Orbits," *Journal of Guidance, Control and Dynamics*, Vol. 23, No. 4, 2000.

[39] M. G. Floquet, "Sur Les Equations Differentielles Lineaires A Coefficients Periodiques," *Annales Scientifiques de l'Ecole Normale Superieure*, Vol. 12, No. 2, 1883.

[40] E. Coddington and N. Levinson, *Theory of Ordinary Differential Equations*. McGraw-Hill, 1955.

[41] L. Perko, *Differential Equations and Dynamical Systems*. Springer, 2001.

[42] J. Bibb, "Computation of Lyapunov-Floquet Transformation Matrices for General Periodic Systems," Master's thesis, 1992.

[43] S. C. Sinha and E. A. Butcher, "Solution and Stability of a Set of pth Order Linear Differential Equations with Periodic Coefficients via Chebyshev Polynomials," *Mathematical Problems in Engineering*, Vol. 2, 1996, pp. 165–190.

[44] S. C. Sinha and E. A. Butcher, "Symbolic Computation of Fundamental Solution Matrices for Time-Periodic Dynamical Systems," *Journal of Sound and Vibration*, Vol. 206, No. 1, 1997, pp. 61–85.

[45] E. A. Butcher and S. C. Sinha, "Symbolic Computation of Local Stability and Bifurcation Surfaces of Time-Periodic Nonlinear Systems," *Nonlinear Dynamics*, Vol. 17, 1998, pp. 1–21.

[46] S. M. Wooden and S. C. Sinha, "Analysis of Periodic-Quasiperiodic Nonlinear Systems via Lyapunov-Floquet Transformation and Normal Forms," *Nonlinear Dynamics*, Vol. 47, 2007, pp. 263–273.

[47] A. P. Gabale and S. C. Sinha, "Construction of Reduced Order Controllers for Nonlinear Systems with Periodic Coefficients," *Journal of Vibration and Control*, Vol. 17, No. 3, 2011, pp. 391–406.

[48] A. P. Gabale and S. C. Sinha, "Model Reduction of Nonlinear Systems with External Periodic Excitations via Construction of Invariant Manifolds," *Journal of Sound and Vibration*, Vol. 330, No. 11, 2011, pp. 2596–2607.

[49] F. Verhulst, *Nonlinear Differential Equations and Dynamical Systems*. Springer, 2000.

[50] D. L. Lukes, *Differential Equations: Classical to Controlled*. Academic Press, 1982.

[51] S. C. Sinha, R. Pandiyan, and J. S. Bibb, "Liapunov-Floquet Transformation: Computation and Applications to Periodic Systems," *Journal of Vibration and Acoustics*, Vol. 118, 1996, pp. 209–219.

[52] B. Lange and R. Smith, "The Application of Floquet Theory to the Computation of Small Orbital Perturbations Over Long Time Intervals Using the Tschauner-Hempel Equations," *International Astronautical Federation*, 1966, pp. 61–93.

[53] K. T. Alfriend and Y. Kashiwagil, "Minimum-Time Orbital Rendezvous Between Neighboring Elliptic Orbits," *Journal of Optimization Theory and Applications*, Vol. 4, No. 4, 1969.

[54] R. E. Sherrill, A. J. Sinclair, and T. A. Lovell, "A Lyapunov-Floquet Generalization of the Hill-Clohessy-Wiltshire Equations," *AAS 12-103*, presented at the 22nd AAS/AIAA Space Flight Mechanics Meeting, Charleston, SC, 2012.

[55] R. E. Sherrill, A. J. Sinclair, S. C. Sinha, and T. A. Lovell, "Lyapunov-Floquet Transformation of Satellite Relative Motion in Elliptic Orbits," *AAS 13-466*, presented at the 23nd AAS/AIAA Space Flight Mechanics Meeting, Kauai, Hawaii, 2013.

[56] R. E. Sherrill, A. J. Sinclair, S. C. Sinha, and T. A. Lovell, "Calibration of Hill-Clohessy-Wiltshire Initial Conditions for Elliptic Relative Motion," submitted to AAS/AIAA Astrodynamics Specialist Conference, Hilton Head, South Carolina, 2013.

[57] P. Sengupta and S. R. Vadali, "Analytical Solutions for Power-Limited Optimal Rendezvous near an Elliptic Orbit," *Journal of Optimization Theory and Applications*, Vol. 138, 2008, pp. 115–137.

[58] H. Cho, S. Y. Park, S. M. Yoo, and K. H. Choi, "Analytical Solution to Optimal Relocation of Satellite Formation Flying in Arbitrary Elliptic Orbits," *Journal of Aerospace Science and Technology*, 2012.

[59] M. Okasha and B. Newman, "Relative Motion Modeling and Control in a Perturbed Orbit," *AAS 11-211*, presented at the 21st AAS/AIAA Space Flight Mechanics Meeting, New Orleans, Louisiana, 2011.

[60] P. Joseph, *New Strategies in the Control of Linear Dynamic Systems with Periodically Varying Coefficients*. PhD thesis, 1993.

[61] P. Joseph and S. C. Sinha, "Control of General Dynamic Systems with Periodically Varying Parameters via Liapunov-Floquet Transformation," *Journal of Dynamic Systems, Measurements, and Control*, Vol. 116, 1994, pp. 650–658.

[62] S. S. Vaddi and S. R. Vadali, "Linear and Nonlinear Control Laws for Formation Flying," *AAS 03-109*, presented at the AAS/AIAA Space Flight Mechanics Meeting, Ponce, Puerto Rico, 2003.

[63] S. C. Sinha, E. Gourdon, and Y. Zhang, "Control of Time-Periodic System via Symbolic Computation with Application to Chaos Control," *Communications in Nonlinear Science and Numerical Simulation*, Vol. 10, 2005, pp. 835–854.

[64] Y. Zhang and S. C. Sinha, "Control of Nonlinear Systems with Periodic Coefficients via Feedback Linearization," *Journal of Computational and Nonlinear Dynamics*, Vol. 2, 2007, pp. 124–131.

Appendices

Appendix A

Elements of $\boldsymbol{P}(f)$

Equations (A.1) through (A.36) give the elements of $\boldsymbol{P}(f)$. Additionally, Figures A.1 through A.6 plot these element for two periods.

$$P_{11} = 6\,n\,(\cos(n\,t)-1)\left[\frac{(\cos(f)-1)\,(e+2)\,(e+e\,\cos(f)+1)}{n\,(e-1)\,(e\,\cos(f)+1)} + \frac{(-3\,e\,\cos^2(f)-3\,\cos(f)+2\,e+4)\,p_3}{2\,n\,(e-1)\,(e+1)^2\,(e+2)\,(e\,\cos(f)+1)}\right] - \frac{3\,n^2\,p^4\,\sin(n\,t)\,\sin(f)}{h^2\,(1-e^2)^{\frac{5}{2}}} - \frac{6\,e\,\sin(n\,t)\,\sin(f)}{e+1} + \frac{2\,(1-e^2)^{\frac{5}{2}}\,(3\,\cos(n\,t)-4)\,(-3\,e\,\cos^2(f)-3\,\cos(f)+2\,e+4)}{(e-1)\,(e+1)^2\,(e+2)\,(e\,\cos(f)+1)} \tag{A.1}$$

$$P_{12} = \frac{e\,\sin(f)}{e+1} \tag{A.2}$$

$$P_{13} = 0 \tag{A.3}$$

$$P_{14} = -\frac{1}{h^2\,n\,(1-e^2)^{\frac{5}{2}}}\left[(e+1)\,2\,e\,h^2\,\sin(f)\,\left(1-e^2\right)^{\frac{5}{2}} - n^2\,p^4\,\cos(n\,t)\,\sin(f) + h^2\,\sin(n\,t)\,\cos(f)\,\left(1-e^2\right)^{\frac{5}{2}} - e\,n^2\,p^4\,\cos(n\,t)\,\sin(f) - 2\,e\,h^2\,\cos(n\,t)\,\sin(f)\,\left(1-e^2\right)^{\frac{5}{2}} + e\,h^2\,\sin(n\,t)\,\cos(f)\,\left(1-e^2\right)^{\frac{5}{2}}\right] \tag{A.4}$$

$$P_{15} = (4\,\cos(n\,t) - 3)\,\left[\frac{(\cos(f) - 1)\,(e + 2)\,(e + e\,\cos(f) + 1)}{n\,(e - 1)\,(e\,\cos(f) + 1)} + \frac{(-3\,e\,\cos^2(f) - 3\,\cos(f) + 2\,e + 4)\,p_3}{2\,n\,(e - 1)\,(e + 1)^2\,(e + 2)\,(e\,\cos(f) + 1)}\right] - \frac{2\,n\,p^4\,\sin(n\,t)\,\sin(f)}{h^2\,(1 - e^2)^{\frac{5}{2}}} - \frac{4\,e\,\sin(n\,t)\,\sin(f)}{n\,(e + 1)} + \frac{2\,(1 - e^2)^{\frac{5}{2}}\,(2\,\cos(n\,t) - 2)\,(-3\,e\,\cos^2(f) - 3\,\cos(f) + 2\,e + 4)}{n\,(e - 1)\,(e + 1)^2\,(e + 2)\,(e\,\cos(f) + 1)} \tag{A.5}$$

$$P_{16} = 0 \tag{A.6}$$

$$P_{21} = \frac{6\,(1 - e^2)^{\frac{5}{2}}\,(3\,\cos(n\,t) - 4)\,\left(2\,\sin(f) + \frac{e\,\sin(2\,f)}{2}\right)}{(e - 1)\,(e + 1)^2\,(e + 2)\,(e\,\cos(f) + 1)} - \frac{3\,(\cos(n\,t) - 1)\,(4\,\sin(f) + e\,\sin(2\,f))\,\left(3\,e - e^2 - 3\,e^3 - e^4 + 6\,(1 - e^2)^{\frac{5}{2}} + 2\right)}{2\,(e + 1)^2\,(e\,\cos(f) + 1)\,(e^2 + e - 2)} - \frac{6\,\sin(n\,t)\,(e\,\cos(f) + 1)}{e + 1} - \frac{3\,n^2\,p^4\,\sin(n\,t)\,(\cos(f) - 1)\,(e + e\,\cos(f) + 2)}{h^2\,(1 - e^2)^{\frac{5}{2}}\,(e\,\cos(f) + 1)} \tag{A.7}$$

$$P_{22} = \frac{e\,\cos(f) + 1}{e + 1} \tag{A.8}$$

$$P_{23} = 0 \tag{A.9}$$

$$P_{24} = \frac{(2\,\cos(n\,t) - 2)\,(e\,\cos(f) + 1)}{n\,(e + 1)} + \frac{6\,\sin(n\,t)\,(1 - e^2)^{\frac{5}{2}}\,\left(2\,\sin(f) + \frac{e\,\sin(2\,f)}{2}\right)}{n\,(e - 1)\,(e + 1)^2\,(e + 2)\,(e\,\cos(f) + 1)} - \frac{\sin(n\,t)\,(4\,\sin(f) + e\,\sin(2\,f))\,\left(3\,e - e^2 - 3\,e^3 - e^4 + 6\,(1 - e^2)^{\frac{5}{2}} + 2\right)}{2\,n\,(e + 1)^2\,(e\,\cos(f) + 1)\,(e^2 + e - 2)} + \frac{n\,p^4\,\cos(n\,t)\,(\cos(f) - 1)\,(e + e\,\cos(f) + 2)}{h^2\,(1 - e^2)^{\frac{5}{2}}\,(e\,\cos(f) + 1)} \tag{A.10}$$

$$P_{25} = \frac{6\,(1-e^2)^{\frac{5}{2}}\;(2\,\cos(n\,t)-2)\;\left(2\,\sin(f)+\frac{e\,\sin(2\,f)}{2}\right)}{n\;(e-1)\;(e+1)^2\;(e+2)\;(e\,\cos(f)+1)}$$
$$-\frac{(4\,\cos(n\,t)-3)\;(4\,\sin(f)+e\,\sin(2\,f))\;\left(3\,e-e^2-3\,e^3-e^4+6\,(1-e^2)^{\frac{5}{2}}+2\right)}{4\,n\,(e+1)^2\;(e\,\cos(f)+1)\;(e^2+e-2)}$$
$$-\frac{4\,\sin(n\,t)\;(e\,\cos(f)+1)}{n\;(e+1)}-\frac{2\,n\,p^4\,\sin(n\,t)\;(\cos(f)-1)\;(e+e\,\cos(f)+2)}{h^2\,(1-e^2)^{\frac{5}{2}}\;(e\,\cos(f)+1)} \tag{A.11}$$

$$P_{26} = 0 \tag{A.12}$$

$$P_{31} = 0 \tag{A.13}$$

$$P_{32} = 0 \tag{A.14}$$

$$P_{33} = \frac{\cos(n\,t)\;\cos(f)\;(e+1)}{e\,\cos(f)+1}+\frac{n\,p^2\,\sin(n\,t)\;\sin(f)}{h\;(e+1)\;(e\,\cos(f)+1)} \tag{A.15}$$

$$P_{34} = 0 \tag{A.16}$$

$$P_{35} = 0 \tag{A.17}$$

$$P_{36} = \frac{p^2\,\cos(n\,t)\;\sin(f)}{h\;(e+1)\;(e\,\cos(f)+1)}-\frac{\sin(n\,t)\;\cos(f)\;(e+1)}{n\;(e\,\cos(f)+1)} \tag{A.18}$$

$$P_{41} = \frac{2\,h\,\sin(f)\;(1-e^2)^{\frac{5}{2}}\;(3\,\cos(n\,t)-4)\;(3\,e^2\,\cos^2(f)-e^2+6\,e\,\cos(f)-2\,e+3)}{p^2\;(e-1)\;(e+1)^2\;(e+2)}$$
$$-\frac{6\,e\,h\,\sin(n\,t)\;(e^2\,\cos^3(f)+2\,e\,\cos^2(f)+\cos(f))}{p^2\;(e+1)}$$
$$-\frac{3\,n^2\,p^2\,\sin(n\,t)\;(e^2\,\cos^3(f)+2\,e\,\cos^2(f)+\cos(f))}{h\,(1-e^2)^{\frac{5}{2}}}$$
$$-6\,n\;(\cos(n\,t)-1)\left[\frac{h\,\sin(f)\;(e+2)\;(2\,e^2\,\cos^2(f)-e^2+4\,e\,\cos(f)-e+2)}{2\,n\,p^2\;(e-1)}\right.$$
$$\left.-\frac{h\,\sin(f)\;(3\,e^2\,\cos^2(f)-e^2+6\,e\,\cos(f)-2\,e+3)\;\left((e+1)^3\,(e+2)-2\,(1-e^2)^{\frac{5}{2}}\right)}{2\,n\,p^2\;(e-1)\;(e+1)^2\;(e+2)}\right] \tag{A.19}$$

$$P_{42} = \frac{e\,h\,\left(e^2\,\cos^3(f) + 2\,e\,\cos^2(f) + \cos(f)\right)}{p^2\,\left(e+1\right)} \tag{A.20}$$

$$P_{43} = 0 \tag{A.21}$$

$$\begin{aligned} P_{44} = \frac{\left(e\,\cos(f)+1\right)^2}{h\,n\,p^2\,\left(1-e^2\right)^{\frac{5}{2}}\,\left(e+1\right)}\,\Big[& n^2\,p^4\,\cos(n\,t)\,\cos(f) - 2\,e\,h^2\,\cos(f)\,\left(1-e^2\right)^{\frac{5}{2}} \\ & + h^2\,\sin(n\,t)\,\sin(f)\,\left(1-e^2\right)^{\frac{5}{2}} + e\,n^2\,p^4\,\cos(n\,t)\,\cos(f) \\ & + 2\,e\,h^2\,\cos(n\,t)\,\cos(f)\,\left(1-e^2\right)^{\frac{5}{2}} + e\,h^2\,\sin(n\,t)\,\sin(f)\,\left(1-e^2\right)^{\frac{5}{2}}\Big] \end{aligned} \tag{A.22}$$

$$\begin{aligned} P_{45} = & \frac{2\,h\,\sin(f)\,\left(1-e^2\right)^{\frac{5}{2}}\,\left(2\,\cos(n\,t)-2\right)\,\left(3\,e^2\,\cos^2(f) - e^2 + 6\,e\,\cos(f) - 2\,e + 3\right)}{n\,p^2\,\left(e-1\right)\,\left(e+1\right)^2\,\left(e+2\right)} \\ & - \frac{2\,n\,p^2\,\sin(n\,t)\,\left(e^2\,\cos^3(f) + 2\,e\,\cos^2(f) + \cos(f)\right)}{h\,\left(1-e^2\right)^{\frac{5}{2}}} \\ & - \frac{4\,e\,h\,\sin(n\,t)\,\left(e^2\,\cos^3(f) + 2\,e\,\cos^2(f) + \cos(f)\right)}{n\,p^2\,\left(e+1\right)} \\ & - \left(4\,\cos(n\,t)-3\right)\,\Bigg[\frac{h\,\sin(f)\,\left(e+2\right)\,\left(2\,e^2\,\cos^2(f) - e^2 + 4\,e\,\cos(f) - e + 2\right)}{2\,n\,p^2\,\left(e-1\right)} \\ & - \frac{h\,\sin(f)\,\left(3\,e^2\,\cos^2(f) - e^2 + 6\,e\,\cos(f) - 2\,e + 3\right)\,\left(\left(e+1\right)^3\,\left(e+2\right) - 2\,\left(1-e^2\right)^{\frac{5}{2}}\right)}{2\,n\,p^2\,\left(e-1\right)\,\left(e+1\right)^2\,\left(e+2\right)}\Bigg] \end{aligned} \tag{A.23}$$

$$P_{46} = 0 \tag{A.24}$$

$$P_{51} = \frac{6\,n\,\left(\cos(n\,t)-1\right)\,\left(h\,\left(e+1\right)^2\left(e+2\right)^2\,p_1+3\,h\,\left(\cos(f)-1\right)\,p_2\,p_3\right)}{2\,n\,p^2\,\left(e-1\right)} + \frac{3\,n^2\,p^2\,\sin(n\,t)\,\left(2\,\sin(f)+\frac{e^2\,\sin(3\,f)}{4}+2\,e\,\sin(f)+e\,\sin(2\,f)+\frac{5\,e^2\,\sin(f)}{4}\right)}{h\,\left(1-e^2\right)^{\frac{5}{2}}} + \frac{6\,e\,h\,\sin(n\,t)\,\sin(f)\,\left(e\,\cos(f)+1\right)^2}{p^2\,\left(e+1\right)} + \frac{6\,h\,\left(1-e^2\right)^{\frac{5}{2}}\,\left(\cos(f)-1\right)\,\left(3\,\cos(n\,t)-4\right)\,p_2}{p^2\,\left(e-1\right)\,\left(e+1\right)^2\,\left(e+2\right)} \tag{A.25}$$

$$P_{52} = -\frac{e\,h\,\sin(f)\,\left(e\,\cos(f)+1\right)^2}{p^2\,\left(e+1\right)} \tag{A.26}$$

$$P_{53} = 0 \tag{A.27}$$

$$P_{54} = 2\,\sin(n\,t)\,\left(\frac{h\,\left(e+2\right)\,p_1}{2\,n\,p^2\,\left(e-1\right)}+\frac{3\,h\,\left(\cos(f)-1\right)\,p_2\,p_3}{2\,n\,p^2\,\left(e-1\right)\,\left(e+1\right)^2\,\left(e+2\right)}\right) - \frac{n\,p^2\,\cos(n\,t)\,\left(2\,\sin(f)+\frac{e^2\,\sin(3\,f)}{4}+2\,e\,\sin(f)+e\,\sin(2\,f)+\frac{5\,e^2\,\sin(f)}{4}\right)}{h\,\left(1-e^2\right)^{\frac{5}{2}}} - \frac{e\,h\,\sin(f)\,\left(2\,\cos(n\,t)-2\right)\,\left(e\,\cos(f)+1\right)^2}{n\,p^2\,\left(e+1\right)} + \frac{6\,h\,\sin(n\,t)\,\left(1-e^2\right)^{\frac{5}{2}}\,\left(\cos(f)-1\right)\,p_2}{n\,p^2\,\left(e-1\right)\,\left(e+1\right)^2\,\left(e+2\right)} \tag{A.28}$$

$$P_{55} = \left(4\,\cos(n\,t)-3\right)\,\left[\frac{h\,\left(e+2\right)\,p_1}{2\,n\,p^2\,\left(e-1\right)}+\frac{3\,h\,\left(\cos(f)-1\right)\,p_2\,p_3}{2\,n\,p^2\,\left(e-1\right)\,\left(e+1\right)^2\,\left(e+2\right)}\right] + \frac{2\,n\,p^2\,\sin(n\,t)\,\left(2\,\sin(f)+\frac{e^2\,\sin(3\,f)}{4}+2\,e\,\sin(f)+e\,\sin(2\,f)+\frac{5\,e^2\,\sin(f)}{4}\right)}{h\,\left(1-e^2\right)^{\frac{5}{2}}} + \frac{4\,e\,h\,\sin(n\,t)\,\sin(f)\,\left(e\,\cos(f)+1\right)^2}{n\,p^2\,\left(e+1\right)} + \frac{6\,h\,\left(1-e^2\right)^{\frac{5}{2}}\,\left(\cos(f)-1\right)\,\left(2\,\cos(n\,t)-2\right)\,p_2}{n\,p^2\,\left(e-1\right)\,\left(e+1\right)^2\,\left(e+2\right)} \tag{A.29}$$

$$P_{56} = 0 \tag{A.30}$$

$$P_{61} = 0 \tag{A.31}$$

$$P_{62} = 0 \tag{A.32}$$

$$P_{63} = \frac{n\,\sin(n\,t)\,\left(e + \cos(f)\right)}{e+1} - \frac{h\,\cos(n\,t)\,\sin(f)\,\left(e+1\right)}{p^2} \tag{A.33}$$

$$P_{64} = 0 \tag{A.34}$$

$$P_{65} = 0 \tag{A.35}$$

$$P_{66} = \frac{\cos(n\,t)\,\left(e + \cos(f)\right)}{e+1} + \frac{h\,\sin(n\,t)\,\sin(f)\,\left(e+1\right)}{n\,p^2} \tag{A.36}$$

The variables p_1, p_2, and p_3 are given by the following.

$p_1 = -2\,e^2\,\cos^3(f) + 3\,e^2\,\cos(f) - 4\,e\,\cos^2(f) + 3\,e\,\cos(f) + e - 4\,\cos(f) + 3$

$p_2 = e^2\,\cos^2(f) + e^2\,\cos(f) + 2\,e\,\cos(f) + 2$

$p_3 = 7\,e + 9\,e^2 + 5\,e^3 + e^4 - 2\,(1 - e^2)^{\frac{5}{2}} + 2$

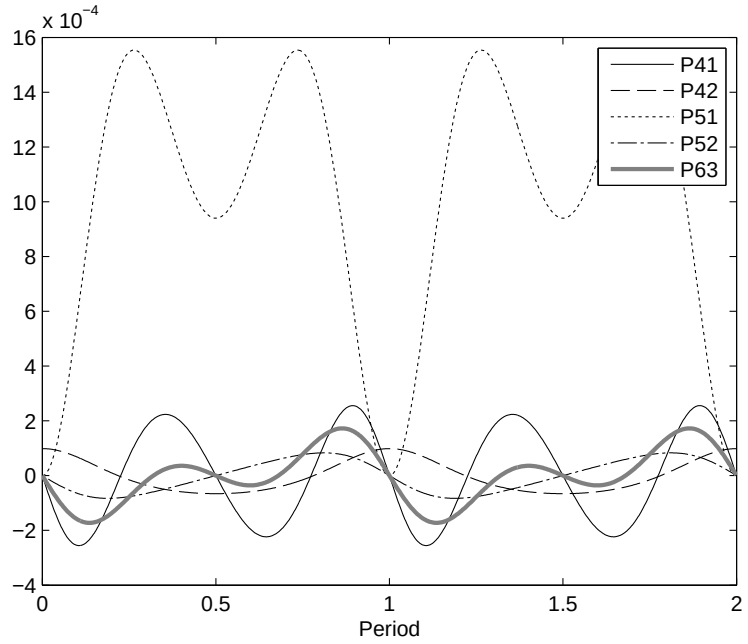

Figure A.1: Elements of $\boldsymbol{P}(f)$ (1 of 6).

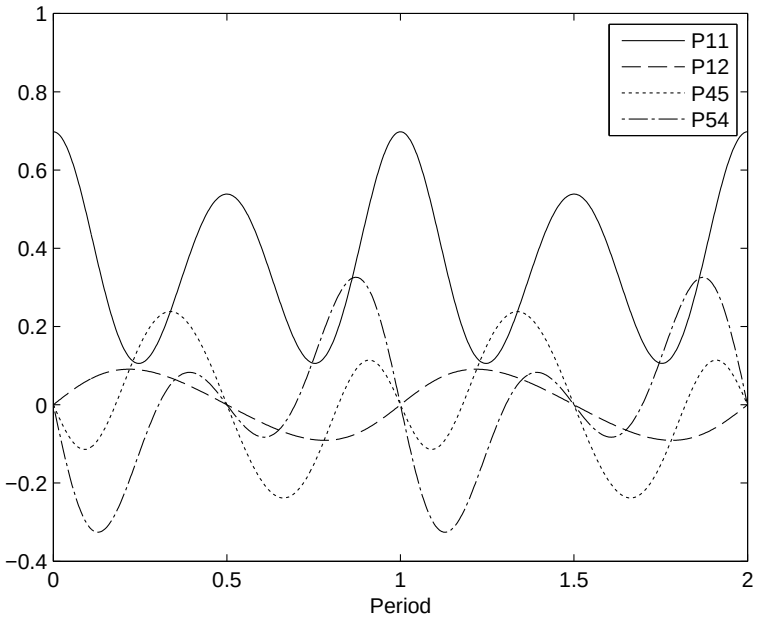

Figure A.2: Elements of $\boldsymbol{P}(f)$ (2 of 6).

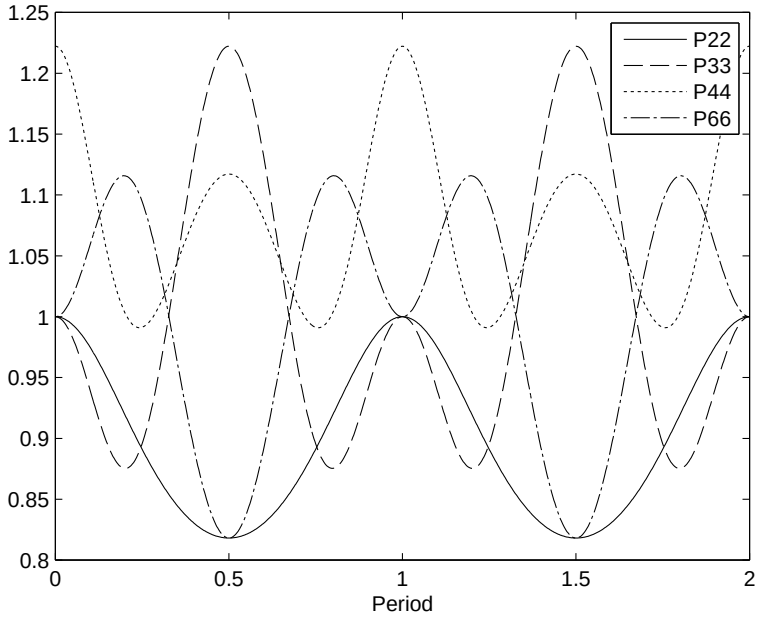

Figure A.3: Elements of $\boldsymbol{P}(f)$ (3 of 6).

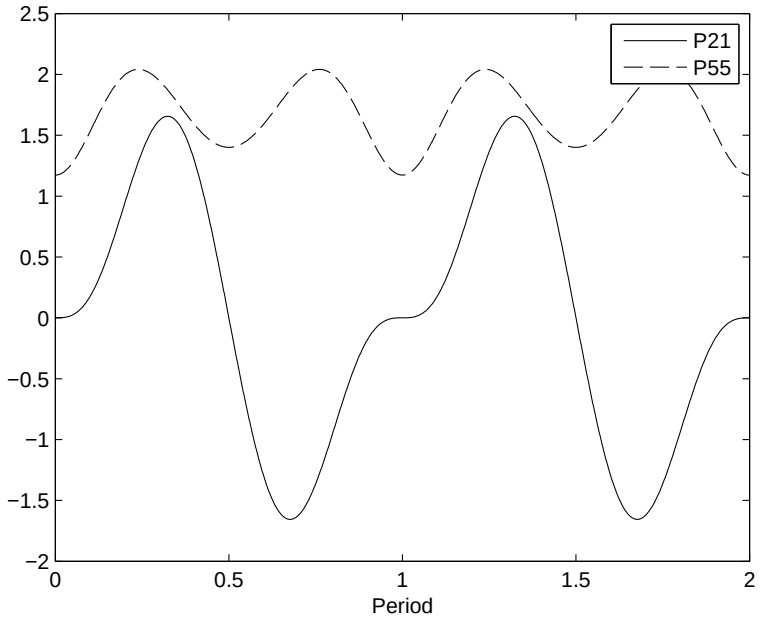

Figure A.4: Elements of $\boldsymbol{P}(f)$ (4 of 6).

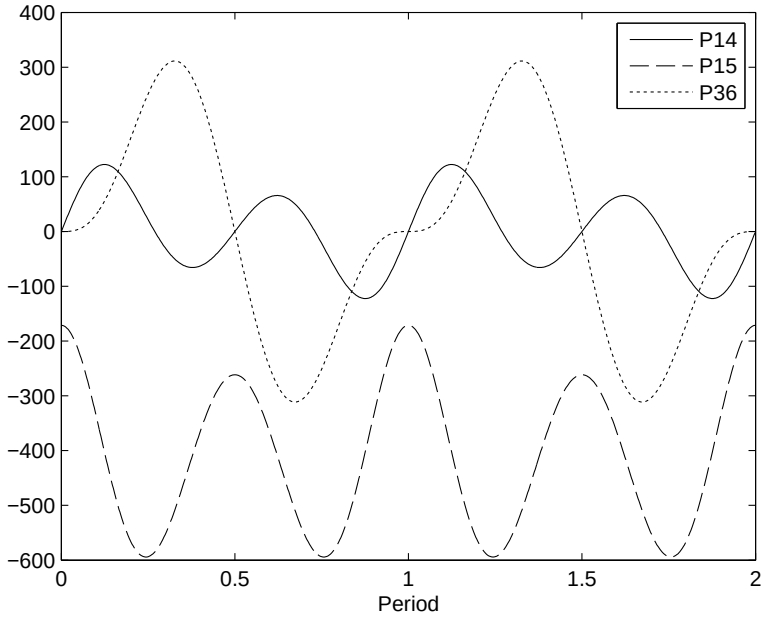

Figure A.5: Elements of $\boldsymbol{P}(f)$ (5 of 6).

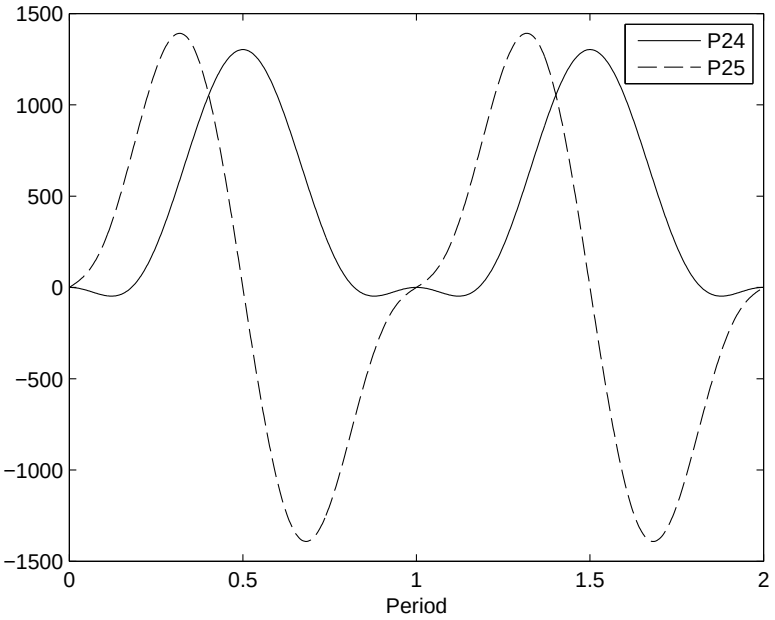

Figure A.6: Elements of $\boldsymbol{P}(f)$ (6 of 6).

Appendix B

Elements of $\bar{\boldsymbol{P}}(f)$

Equations (B.1) through (B.36) give the elements of $\bar{\boldsymbol{P}}(f)$. Additionally, Figures B.1 through B.6 plot these element for two periods.

$$\begin{aligned}\bar{P}_{11} = -\frac{1}{h\,(e-1)^2\,(e-2)\,(e\,\cos(f)+1)}\Big[3\,\cos(f)\,\Big(h\,\cos(n\,t)\,(e-1)^2\,(e-2)\\ +h\,(e-1)^2\,\Big(e-2+2\,e\,\sqrt{1-e^2}+2\,\sqrt{1-e^2}\Big)-e\,\sin(n\,t)\,\sin(f)\,\Big(-2\,h\,e^3+7\,n\,e\,p^2+2\,n\,p^2\Big)\Big)\\ +8\,h\,\sqrt{1-e^2}-12\,e\,h\,\sqrt{1-e^2}-4\,e^2\,h\,\sqrt{1-e^2}+12\,e^3\,h\,\sqrt{1-e^2}-4\,e^4\,h\,\sqrt{1-e^2}\\ +6\,e^2\,h\,\sin(2\,f)\,\sin(n\,t)-9\,e^3\,h\,\sin(2\,f)\,\sin(n\,t)+6\,e^3\,n\,p^2\,\sin(2\,f)\,\sin(n\,t)\\ +\sin(n\,t)\,\sin(f)\,(3\,e-6)\,\Big(2\,h\,e^2+4\,n\,e\,p^2-2\,h\,e+n\,p^2\Big)\\ +3\,e\,h\cos^2(f)\,(e-1)^2\,\Big(e+2\,e\,\sqrt{1-e^2}+\cos(n\,t)\,(e-2)+2\,\sqrt{1-e^2}-2\Big)\end{aligned} \tag{B.1}$$

$$\bar{P}_{12} = \frac{-e\,\sin(f)}{(e-1)} \tag{B.2}$$

$$\bar{P}_{13} = 0 \tag{B.3}$$

$$\begin{aligned}\bar{P}_{14} = \frac{1}{h\,n\,(e-1)^2}\Big[\sin(f)\,\Big(\cos(n\,t)\,\Big(2\,h\,e^2+4\,n\,e\,p^2-2\,h\,e+n\,p^2\Big)+e\,h\,(2\,e-2)\Big)\\ -h\,\sin(n\,t)\,\cos(f)\,(e-1)^2\Big]\end{aligned} \tag{B.4}$$

$$\bar{P}_{15} = \frac{-1}{h\,n\,(2\,e-4)\,(e-1)^2\,(e\,\cos(f)+1)}\Big[\cos(f)\,\Big(h\,\cos(n\,t)\,(4\,e-8)\,(e-1)^2 + 3\,h\,(e-1)^2\,\Big(e+2\,e\,\sqrt{1-e^2}+2\,\sqrt{1-e^2}-2\Big) - 4\,e\,\sin(n\,t)\,\sin(f)\,\Big(-2\,h\,e^3+6\,h\,e^2+7\,n\,e\,p^2+2\,n\,p^2\Big)\Big) + 4\,\sin(n\,t)\,\sin(f)\,(e-2)\,\Big(2\,h\,e^2+4\,n\,e\,p^2-2\,h\,e+n\,p^2\Big) + 4\,h\,\sqrt{1-e^2}\,(e-1)^2\,\Big(-e^2+e+2\Big)+8\,e^2\,\sin(2\,f)\,\sin(n\,t)\,\Big(e\,n\,p^2+h\Big) + e\,h\cos^2(f)\,(e-1)^2\,\Big(3\,e+\cos(n\,t)\,(4\,e-8)+6\,e\,\sqrt{1-e^2}+6\,\sqrt{1-e^2}-6\Big)\Big] \quad \text{(B.5)}$$

$$\bar{P}_{16} = 0 \quad \text{(B.6)}$$

$$\bar{P}_{21} = \frac{-1}{h\,(e-1)^2\,(e-2)\,(e\,\cos(f)+1)}\Big[3\,\sin(n\,t)\,\Big(\frac{e}{2}-1\Big)\,\Big(4\,e\,h-4\,h-2\,e^2\,h + 2\,e^3\,h+4\,n\,p^2+\cos(f)\,\Big(8\,h\,e^2+16\,n\,e\,p^2-8\,h\,e+4\,n\,p^2\Big)+15\,e\,n\,p^2-4\,e^2\,n\,p^2 + e\,\cos(2\,f)\,\Big(2\,h\,e^2+4\,n\,e\,p^2-2\,h\,e+n\,p^2\Big)\Big) - 3\,h\,\sin(f)\,\Big(2\,(e-1)^2\,\Big(e+2\,e\,\sqrt{1-e^2}+\cos(n\,t)\,(e-2)+2\,\sqrt{1-e^2}-2\Big) + e\,\cos(f)\,\Big(e\,\Big(e^2+5\Big)+\cos(n\,t)\,(e-1)^2\,(e-2)\Big)\Big) + 3\,e\,h\,\sin(2\,f)\,\Big(e^2\,\Big(\sqrt{1-e^2}+2\Big)-e^3\,\sqrt{1-e^2}+e\,\sqrt{1-e^2}-\sqrt{1-e^2}+1\Big)\Big] \quad \text{(B.7)}$$

$$\bar{P}_{22} = \frac{-\,(e\,\cos(f)+1)}{(e-1)} \quad \text{(B.8)}$$

$$\bar{P}_{23} = 0 \quad \text{(B.9)}$$

$$\bar{P}_{24} = \frac{1}{h\,n\,(e-1)^2\,(e\,\cos(f)+1)}\left[e\,\left(\cos(n\,t)\,\left(2\,h\,e^2+4\,n\,e\,p^2-2\,h\,e+n\,p^2\right)\right.\right.$$
$$+e\,h\,(2\,e-2))\,\cos^2(f)+\left(\cos(n\,t)\,\left(4\,h\,e^2+8\,n\,e\,p^2-4\,h\,e+2\,n\,p^2\right)\right.$$
$$\left.+e\,h\,(\sin(n\,t)\,\sin(f)\,(e-1)+4)\,(e-1)\right)\cos(f)$$
$$\left.+\cos(n\,t)\,\left(n\,\left(-4\,e^2+7\,e+2\right)\,p^2+h\,(2\,e-2)\right)+h\,(\sin(n\,t)\,\sin(f)\,(e-1)+1)\,(2\,e-2)\right] \tag{B.10}$$

$$\bar{P}_{25} = \frac{-1}{h\,n\,(4\,e-8)\,(e-1)^2\,(e\,\cos(f)+1)}\left[\sin(n\,t)\,(4\,e-8)\,\left(4\,e\,h-4\,h-2\,e^2\,h\right.\right.$$
$$+2\,e^3\,h+4\,n\,p^2+\cos(f)\,\left(8\,h\,e^2+16\,n\,e\,p^2-8\,h\,e+4\,n\,p^2\right)+15\,e\,n\,p^2-4\,e^2\,n\,p^2$$
$$\left.+e\,\cos(2\,f)\,\left(2\,h\,e^2+4\,n\,e\,p^2-2\,h\,e+n\,p^2\right)\right)$$
$$-4\,h\,\sin(f)\,\left(3\,(e-1)^2\,\left(e+2\,e\,\sqrt{1-e^2}+2\,\sqrt{1-e^2}-2\right)\right.$$
$$+\cos(n\,t)\,\left(2\,(2\,e-4)\,(e-1)^2+2\,e^2\,\cos(f)\,\left(e^2-4\,e+5\right)\right)\Big)$$
$$\left.+e\,h\,\sin(2\,f)\,\left(8\,\cos(n\,t)-3\,(e-1)^2\,\left(e+2\,e\,\sqrt{1-e^2}+2\,\sqrt{1-e^2}-2\right)\right)\right] \tag{B.11}$$

$$\bar{P}_{26} = 0 \tag{B.12}$$

$$\bar{P}_{31} = 0 \tag{B.13}$$

$$\bar{P}_{32} = 0 \tag{B.14}$$

$$\bar{P}_{33} = \frac{-\left(h\,\cos(n\,t)\,\cos(f)\,e^2-2\,h\,\cos(n\,t)\,\cos(f)\,e+n\,\sin(n\,t)\,\sin(f)\,p^2+h\,\cos(n\,t)\,\cos(f)\right)}{h\,(e-1)\,(e\,\cos(f)+1)} \tag{B.15}$$

$$\bar{P}_{34} = 0 \tag{B.16}$$

$$\bar{P}_{35} = 0 \tag{B.17}$$

$$\bar{P}_{36} = \frac{\left(h\,\sin(n\,t)\,\cos(f)\,e^2-2\,h\,\sin(n\,t)\,\cos(f)\,e-n\,\cos(n\,t)\,\sin(f)\,p^2+h\,\sin(n\,t)\,\cos(f)\right)}{hn\,(e-1)\,(e\,\cos(f)+1)} \tag{B.18}$$

$$\bar{P}_{41} = \frac{-1}{p^2\,(e-1)^2\,(e-2)}\left[6\,e^2\,\cos(n\,t)\,\cos(f)\,\left(e^2-4\,e+5\right)+3\,e\,h\,\sin(2\,f)\,\left(2\,\cos(n\,t)\right.\right.$$
$$-(e-1)^2\,\left(e+2\,e\,\sqrt{1-e^2}+2\,\sqrt{1-e^2}-2\right)\Big)-h\,\sin(f)\,\Big((e-1)^2\,(\cos(n\,t)\,(3\,e-6)$$
$$+e\,\left(10\,\sqrt{1-e^2}+3\right)+2\,e^2\,\left(\sqrt{1-e^2}-3\right)-e^3\,\left(2\,\sqrt{1-e^2}-3\right)+6\,\sqrt{1-e^2}-6\Big)$$
$$+3\,e^2\cos^2(f)\,\left((2\,e+2)\,\sqrt{1-e^2}+\cos(n\,t)\,(e-2)\right)\,(e-1)^2\Big)$$
$$+\,e^2\,h\sin^3(f)\,(3\,e-6)\,(e-1)^2$$
$$\left.+3\,\sin(n\,t)\,\cos(f)\,(e-2)\,(e\,\cos(f)+1)^2\,\left(2\,h\,e^2+4\,n\,e\,p^2-2\,h\,e+n\,p^2\right)\right] \quad \text{(B.19)}$$

$$\bar{P}_{42} = \frac{-eh\cos(f)\,(e\,\cos(f)+1)^2}{p^2\,(e-1)} \quad \text{(B.20)}$$

$$\bar{P}_{43} = 0 \quad \text{(B.21)}$$

$$\bar{P}_{44} = \frac{1}{n\,p^2\,(e-1)^2}\left[\left(\cos(f)\,\left(\cos(n\,t)\,\left(2\,h\,e^2+4\,n\,e\,p^2-2\,h\,e+n\,p^2\right)+e\,h\,\left(2\,e-2\right)\right)\right.$$
$$\left.+h\,\sin(n\,t)\,\sin(f)\,(e-1)^2\right)\,(e\,\cos(f)+1)^2\Big] \quad \text{(B.22)}$$

$$\bar{P}_{45} = \frac{-1}{n\,p^2\,(2\,e-4)\,(e-1)^2}\left[e\,h\,\sin(2\,f)\,\left(8\,\cos(n\,t)-3\,(e-1)^2\,\left(e+2\,e\,\sqrt{1-e^2}\right.\right.\right.$$
$$\left.\left.+2\,\sqrt{1-e^2}-2\right)\right)-h\,\sin(f)\,\left((e-1)^2\,(\cos(n\,t)\,(4\,e-8)\right.$$
$$+e\,\left(10\,\sqrt{1-e^2}+3\right)+2\,e^2\,\left(\sqrt{1-e^2}-3\right)-e^3\,\left(2\,\sqrt{1-e^2}-3\right)+6\,\sqrt{1-e^2}-6\Big)$$
$$+\,2\,e^2\cos^2(f)\,(e-1)^2\,\left(\cos(n\,t)\,(2\,e-4)+(3\,e+3)\,\sqrt{1-e^2}\right)$$
$$+8\,e^2\,\cos(n\,t)\,\cos(f)\,\left(e^2-4\,e+5\right)\Big)$$
$$+\sin(n\,t)\,\cos(f)\,(4\,e-8)\,(e\,\cos(f)+1)^2\,\left(2\,h\,e^2+4\,n\,e\,p^2-2\,h\,e+n\,p^2\right)$$
$$\left.+e^2\,h\sin^3(f)\,(3\,e-6)\,(e-1)^2\right] \quad \text{(B.23)}$$

$$\bar{P}_{46} = 0 \quad \text{(B.24)}$$

$$\bar{P}_{51} = \frac{-1}{p^2\,(e-1)^2\,(e-2)}\Big[15\,e^2\,h - 6\,e\,h - 12\,e^3\,h + 3\,e^4\,h + 12\,h\,\sqrt{1-e^2}$$
$$+ 6\,\cos(f)\,\Big(h\,(e-1)^2\,\Big(e + e^2\,\sqrt{1-e^2} - e^3\,\sqrt{1-e^2} + 4\,e\,\sqrt{1-e^2} + 2\,\sqrt{1-e^2} - 2\Big)$$
$$+h\,\cos(n\,t)\,(e-1)^2\,(e-2) + 2\,e\,\sin(n\,t)\,\sin(f)\,\left(h\,e^3 + 2\,n\,e^2\,p^2 + 2\,h\,e - n\,p^2\right)\Big)$$
$$- 12\,e\,h\,\sqrt{1-e^2} + 3\,e\cos^2(f)\,\Big(2\,h\,(e-1)^2\,\Big(e + 2\,e\,\sqrt{1-e^2} + 2\,\sqrt{1-e^2} - 2\Big)$$
$$+h\,\cos(n\,t)\,(2\,e-4)\,(e-1)^2 + e\,\sin(n\,t)\,\sin(f)\,(e-2)\,\left(2\,h\,e^2 + 4\,n\,e\,p^2 - 2\,h\,e + n\,p^2\right)\Big)$$
$$- 12\,e^2\,h\,\sqrt{1-e^2} + 12\,e^3\,h\,\sqrt{1-e^2} - 18\,e^2\,h\,\sin(n\,t)\,\sin(f) + 6\,e^3\,h\,\sin(n\,t)\,\sin(f)$$
$$- 12\,n\,p^2\,\sin(n\,t)\,\sin(f) - 18\,e^3\,h\,\sin(2\,f)\,\sin(n\,t) + 12\,e\,h\,\sin(n\,t)\,\sin(f)$$
$$- 21\,e^2\,n\,p^2\,\sin(2\,f)\,\sin(n\,t)$$
$$+ 3\,e^2\,h\cos^3(f)\,(e-1)^2\,\Big(e + 2\,e\,\sqrt{1-e^2} + \cos(n\,t)\,(e-2) + 2\,\sqrt{1-e^2} - 2\Big)$$
$$- 30\,e\,n\,p^2\,\sin(n\,t)\,\sin(f) + 3\,e\,h\,\cos(n\,t)\,(e-1)^2\,(e-2) + 60\,e^2\,n\,p^2\,\sin(n\,t)\,\sin(f)$$
$$-45\,e^3\,n\,p^2\,\sin(n\,t)\,\sin(f) + 12\,e^4\,n\,p^2\,\sin(n\,t)\,\sin(f)\Big] \quad \text{(B.25)}$$

$$\bar{P}_{52} = \frac{e h \sin(f)\,(e\,\cos(f)+1)^2}{p^2\,(e-1)} \quad \text{(B.26)}$$

$$\bar{P}_{53} = 0 \quad \text{(B.27)}$$

$$\bar{P}_{54} = \frac{-1}{n\,p^2\,(e-1)^2}\Big[\sin(f)\,\Big(\cos(n\,t)\,\Big(2\,e^2\,h - 2\,e\,h + 2\,n\,p^2 + 6\,e\,n\,p^2$$
$$+e^2\cos^2(f)\,\left(2\,h\,e^2 + 4\,n\,e\,p^2 - 2\,h\,e + n\,p^2\right) + 2\,e\,\cos(f)\,\left(2\,h\,e^2 + 4\,n\,e\,p^2 - 2\,h\,e + n\,p^2\right)$$
$$-7\,e^2\,n\,p^2 + 4\,e^3\,n\,p^2\Big) + 2\,e\,h\,\left(e^3 - e^2 + e - 1\right)\Big) - e^3\,h\sin^3(f)\,(2\,e-2)$$
$$+h\,\Big(2\,e^2\,\sin(2\,f) - \sin(n\,t)\,(e-1)\,\Big(e^2\cos^3(f) + 2\,e\cos^2(f) + e + 2\,\cos(f)\Big)\Big)\,(e-1)\Big] \quad \text{(B.28)}$$

$$\bar{P}_{55} = \frac{1}{n\,p^2\,(2\,e-4)\,(e-1)^2}\Big[15\,e^2\,h - 6\,e\,h - 12\,e^3\,h + 3\,e^4\,h + 12\,h\,\sqrt{1-e^2}$$
$$+ 2\,\cos(f)\,\left(3\,h\,(e-1)^2\,\left(e^2\,\sqrt{1-e^2} - e^3\,\sqrt{1-e^2} + e\,\left(4\,\sqrt{1-e^2}+1\right) + 2\,\sqrt{1-e^2} - 2\right)\right.$$
$$\left. + h\,\cos(n\,t)\,(4\,e-8)\,(e-1)^2 - 4\,e^2\,\sin(n\,t)\,\sin(f)\,\left(h\,(6\,e-4) - n\,p^2\,(4\,e-7)\right)\right)$$
$$- 12\,e\,h\,\sqrt{1-e^2} - 12\,e^2\,h\,\sqrt{1-e^2} + 12\,e^3\,h\,\sqrt{1-e^2}$$
$$+ 2\,e\cos^2(f)\,\left(3\,h\,(e-1)^2\,\left(e + 2\,e\,\sqrt{1-e^2} + 2\,\sqrt{1-e^2} - 2\right) + h\,\cos(n\,t)\,(4\,e-8)\,(e-1)^2\right.$$
$$\left. + e\,\sin(n\,t)\,\sin(f)\,(2\,e-4)\,\left(2\,h\,e^2 + 4\,n\,e\,p^2 - 2\,h\,e + n\,p^2\right)\right)$$
$$- 24\,e^2\,h\,\sin(n\,t)\,\sin(f) + 8\,e^3\,h\,\sin(n\,t)\,\sin(f) - 16\,n\,p^2\,\sin(n\,t)\,\sin(f)$$
$$+ 8\,e^4\,h\,\sin(2\,f)\,\sin(n\,t) + 16\,e\,h\,\sin(n\,t)\,\sin(f)$$
$$+ e^2\,h\cos^3(f)\,(e-1)^2\,\left(3\,e + \cos(n\,t)\,(4\,e-8) + 6\,e\,\sqrt{1-e^2} + 6\,\sqrt{1-e^2} - 6\right)$$
$$+ e\,h\,\cos(n\,t)\,(4\,e-8)\,(e-1)^2 - 40\,e\,n\,p^2\,\sin(n\,t)\,\sin(f) - 8\,e\,n\,p^2\,\sin(2\,f)\,\sin(n\,t)$$
$$+ 80\,e^2\,n\,p^2\,\sin(n\,t)\,\sin(f) - 60\,e^3\,n\,p^2\,\sin(n\,t)\,\sin(f) + 16\,e^4\,n\,p^2\,\sin(n\,t)\,\sin(f)\Big] \quad \text{(B.29)}$$

$$\bar{P}_{56} = 0 \quad \text{(B.30)}$$

$$\bar{P}_{61} = 0 \quad \text{(B.31)}$$

$$\bar{P}_{62} = 0 \quad \text{(B.32)}$$

$$\bar{P}_{63} = \frac{1}{p^2\,(e-1)}\Big[h\,\cos(n\,t)\,\sin(f)\,e^2 - n\,\sin(n\,t)\,e\,p^2 - 2\,h\,\cos(n\,t)\,\sin(f)\,e$$
$$- n\,\sin(n\,t)\,\cos(f)\,p^2 + h\,\cos(n\,t)\,\sin(f)\Big] \quad \text{(B.33)}$$

$$\bar{P}_{64} = 0 \quad \text{(B.34)}$$

$$\bar{P}_{65} = 0 \quad \text{(B.35)}$$

$$\bar{P}_{66} = \frac{-1}{np^2\,(e-1)} \big[h\,\sin(n\,t)\,\sin(f)\,e^2 + n\,\cos(n\,t)\,e\,p^2 - 2\,h\,\sin(n\,t)\,\sin(f)\,e$$
$$+n\,\cos(n\,t)\,\cos(f)\,p^2 + h\,\sin(n\,t)\,\sin(f)\big] \quad \text{(B.36)}$$

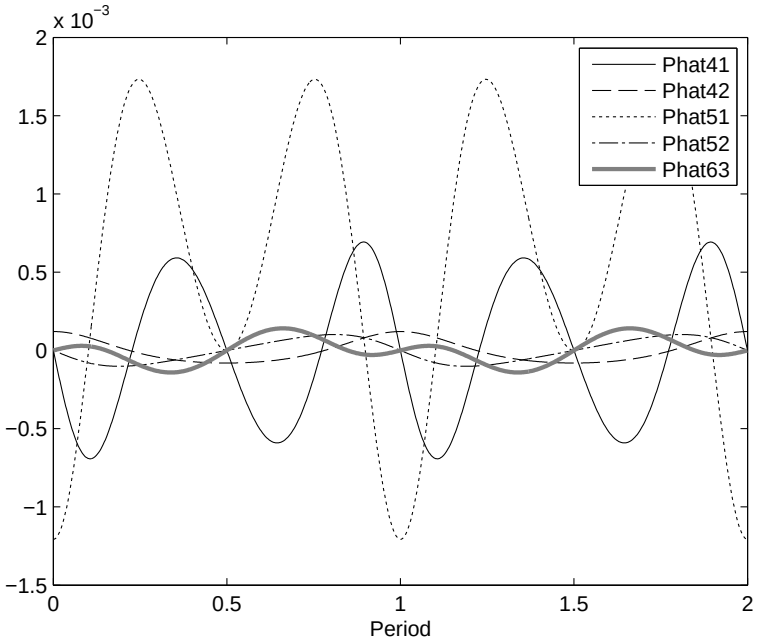

Figure B.1: Elements of $\bar{\boldsymbol{P}}(f)$ (1 of 6).

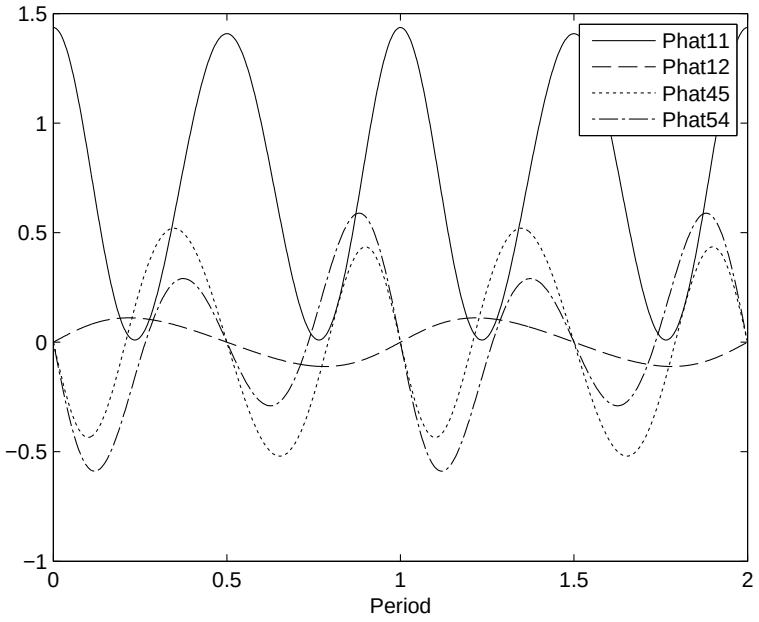

Figure B.2: Elements of $\bar{\boldsymbol{P}}(f)$ (2 of 6).

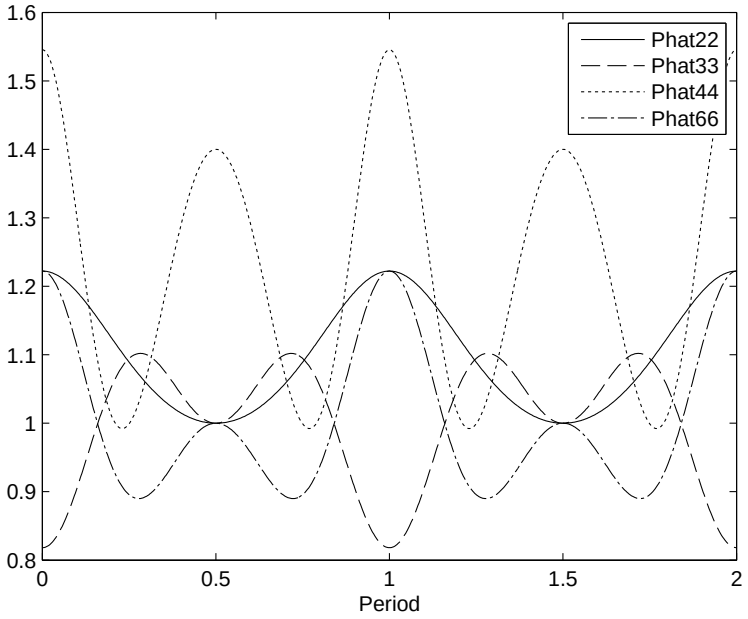

Figure B.3: Elements of $\bar{\boldsymbol{P}}(f)$ (3 of 6).

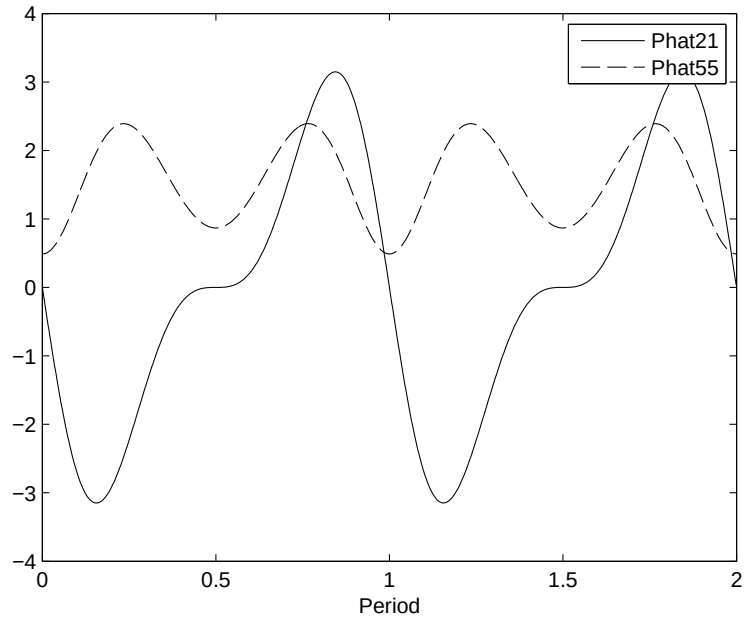

Figure B.4: Elements of $\bar{\boldsymbol{P}}(f)$ (4 of 6).

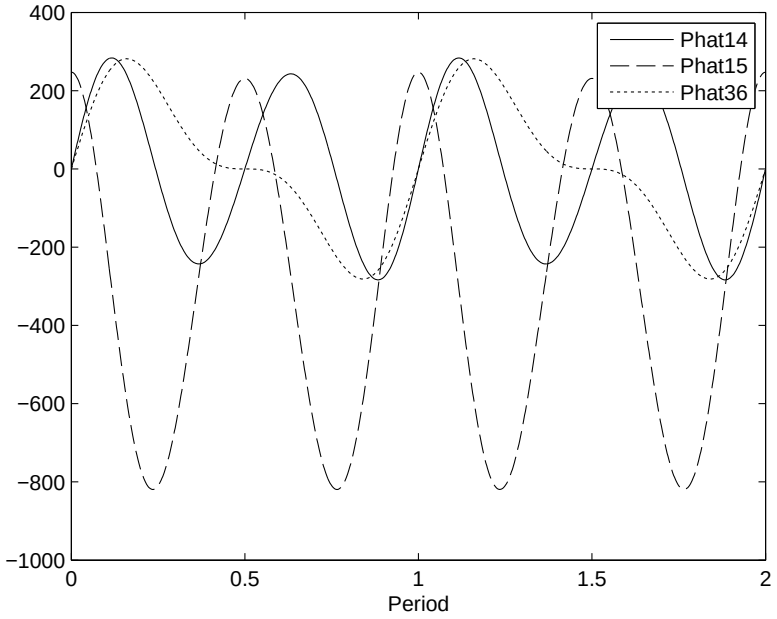

Figure B.5: Elements of $\bar{\boldsymbol{P}}(f)$ (5 of 6).

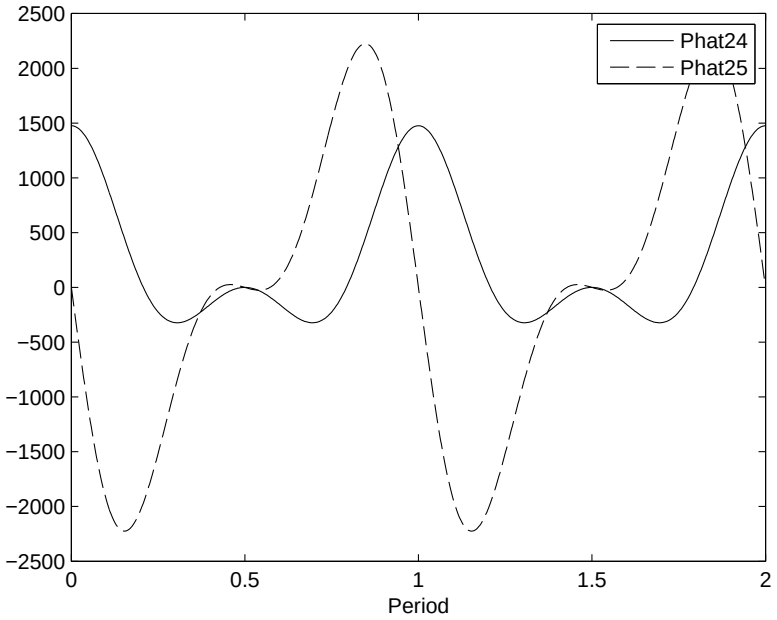

Figure B.6: Elements of $\bar{\boldsymbol{P}}(f)$ (6 of 6).

Appendix C

Elements of $\mathbf{\Pi}(f)$

Equations (C.1) through (C.36) give the elements of $\mathbf{\Pi}(f)$. Additionally, Figures C.1 through C.6 plot these element for two periods.

$$\Pi_{11} = -\frac{6\,\cos(M-f) + 3\,e\,\cos(M) + 3\,e\,\cos(M-2\,f) - 8}{2\,(e\,\cos(f)+1)} - \frac{6\,M\,e\,\sin(f)}{(1-e^2)^{\frac{3}{2}}} \tag{C.1}$$

$$\Pi_{12} = 0 \tag{C.2}$$

$$\Pi_{13} = 0 \tag{C.3}$$

$$\Pi_{14} = -\frac{\sin(M-f)}{n} \tag{C.4}$$

$$\Pi_{15} = -\frac{2\,\cos(M-f) + e\,\cos(M) + e\,\cos(M-2\,f) - 2}{n\,(e\,\cos(f)\,+1)} - \frac{3\,M\,e\,\sin(f)}{n\,(1-e^2)^{\frac{3}{2}}} \tag{C.5}$$

$$\Pi_{16} = 0 \tag{C.6}$$

$$\Pi_{21} = \frac{12\,M - 12\,\sin(M-f) + 3\,e\,\sin(M) - 3\,e\,\sin(M-2\,f)}{2\,(e\,\cos(f)+1)} - \frac{6\,M}{(1-e^2)^{\frac{3}{2}}} - \frac{6\,M\,e\,\cos(f)}{(1-e^2)^{\frac{3}{2}}} \tag{C.7}$$

$$\Pi_{22} = \frac{1}{e\,\cos(f)+1} \tag{C.8}$$

$$\Pi_{23} = 0 \tag{C.9}$$

$$\Pi_{24} = \frac{4\,\cos(M-f) - e\,\cos(M) + e\,\cos(M-2\,f) - 4}{2\,n\,(e\,\cos(f)+1)} \tag{C.10}$$

$$\Pi_{25} = \frac{3\,M - 4\,\sin(M-f) + e\,\sin(M) - e\,\sin(M-2\,f)}{n\,(e\,\cos(f)+1)} - \frac{3\,M}{n\,(1-e^2)^{\frac{3}{2}}} - \frac{3\,M\,e\,\cos(f)}{n\,(1-e^2)^{\frac{3}{2}}} \tag{C.11}$$

$$\Pi_{26} = 0 \tag{C.12}$$

$$\Pi_{31} = 0 \tag{C.13}$$

$$\Pi_{32} = 0 \tag{C.14}$$

$$\Pi_{33} = \frac{\cos(M-f)}{e\,\cos(f)+1} \tag{C.15}$$

$$\Pi_{34} = 0 \tag{C.16}$$

$$\Pi_{35} = 0 \tag{C.17}$$

$$\Pi_{36} = -\frac{\sin(M-f)}{n\,(e\,\cos(f)+1)} \tag{C.18}$$

$$\begin{aligned}\Pi_{41} = -\frac{h}{p^2}\,\Big(&2\,e\,\sin(f) - 3\,\cos(M)\,\sin(f) + 3\,\sin(M)\,\cos(f) + 3\,e^2\,\sin(M)\,\cos^3(f)\\ &+ 6\,e\,\sin(M)\,\cos^2(f) + \frac{12\,M\,e^2\cos^2(f)}{(1-e^2)^{\frac{3}{2}}} + \frac{6\,M\,e^3\cos^3(f)}{(1-e^2)^{\frac{3}{2}}} + \frac{6\,M\,e\,\cos(f)}{(1-e^2)^{\frac{3}{2}}}\\ &-6\,e\,\cos(M)\,\cos(f)\,\sin(f) - 3\,e^2\,\cos(M)\,\cos^2(f)\,\sin(f)\Big)\end{aligned} \tag{C.19}$$

$$\Pi_{42} = 0 \tag{C.20}$$

$$\Pi_{43} = 0 \tag{C.21}$$

$$\Pi_{44} = \frac{h\,\cos(M-f)\,(e\,\cos(f)+1)^2}{n\,p^2} \tag{C.22}$$

$$\begin{aligned}\Pi_{45} = -\frac{h}{n\,p^2}\,\Big(&e\,\sin(f) - 2\,\cos(M)\,\sin(f) + 2\,\sin(M)\,\cos(f) + 2\,e^2\,\sin(M)\,\cos^3(f)\\ &+ 4\,e\,\sin(M)\,\cos^2(f) + \frac{6\,M\,e^2\cos^2(f)}{(1-e^2)^{\frac{3}{2}}} + \frac{3\,M\,e^3\cos^3(f)}{(1-e^2)^{\frac{3}{2}}} + \frac{3\,M\,e\,\cos(f)}{(1-e^2)^{\frac{3}{2}}}\\ &-2\,e^2\,\cos(M)\,\cos^2(f)\,\sin(f) - 4\,e\,\cos(M)\,\cos(f)\,\sin(f)\Big)\end{aligned} \tag{C.23}$$

$$\Pi_{46} = 0 \tag{C.24}$$

$$\Pi_{51} = \frac{3\,h}{4\,p^2}\,\left(8\,\cos(M-f) + 8\,e\,\cos(M) - 8\,e\,\cos(f) + 4\,e\,\cos(M-2\,f)\right.$$
$$+ \frac{8\,M\,e\,\sin(f)}{(1-e^2)^{\frac{3}{2}}} + \frac{8\,M\,e^3\cos^2(f)\,\sin(f)}{(1-e^2)^{\frac{3}{2}}} + \frac{16\,M\,e^2\,\cos(f)\,\sin(f)}{(1-e^2)^{\frac{3}{2}}}$$
$$\left. -e^2\,\cos(M+f) + 4\,e^2\,\cos(M-f) + e^2\,\cos(M-3\,f) + 8\,M\,e\,\sin(f) - 8\right) \quad \text{(C.25)}$$

$$\Pi_{52} = \frac{e\,h\,\sin(f)}{p^2} \quad \text{(C.26)}$$

$$\Pi_{53} = 0 \quad \text{(C.27)}$$

$$\Pi_{54} = \frac{h}{4\,n\,p^2}\,\left(8\,\sin(M-f) + 4\,e^2\,\sin(M-f) + e^2\,\sin(M-3\,f) + 8\,e\,\sin(M)\right.$$
$$\left. -8\,e\,\sin(f) + 4\,e\,\sin(M-2\,f) - e^2\,\sin(M+f)\right) \quad \text{(C.28)}$$

$$\Pi_{55} = \frac{h}{2\,n\,p^2}\,\left(8\,\cos(M-f) + 8\,e\,\cos(M) - 6\,e\,\cos(f) + 4\,e\,\cos(M-2\,f)\right.$$
$$+ \frac{6\,M\,e\,\sin(f)}{(1-e^2)^{\frac{3}{2}}} + \frac{6\,M\,e^3\cos^2(f)\,\sin(f)}{(1-e^2)^{\frac{3}{2}}} + \frac{12\,M\,e^2\,\cos(f)\,\sin(f)}{(1-e^2)^{\frac{3}{2}}}$$
$$\left. -e^2\,\cos(M+f) + 4\,e^2\,\cos(M-f) + e^2\,\cos(M-3\,f) + 6\,M\,e\,\sin(f) - 6\right) \quad \text{(C.29)}$$

$$\Pi_{56} = 0 \quad \text{(C.30)}$$

$$\Pi_{61} = 0 \quad \text{(C.31)}$$

$$\Pi_{62} = 0 \quad \text{(C.32)}$$

$$\Pi_{63} = \frac{h\,\left(\sin(M-f) + e\,\sin(M)\right)}{p^2} \quad \text{(C.33)}$$

$$\Pi_{64} = 0 \quad \text{(C.34)}$$

$$\Pi_{65} = 0 \quad \text{(C.35)}$$

$$\Pi_{66} = \frac{h\,\left(\cos(M-f) + e\,\cos(M)\right)}{n\,p^2} \quad \text{(C.36)}$$

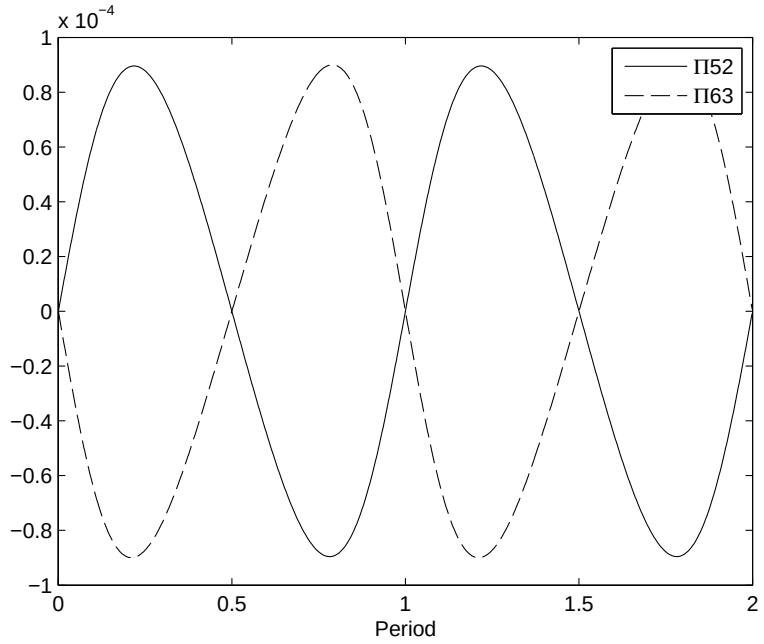

Figure C.1: Elements of $\mathbf{\Pi}(f)$ (1 of 6).

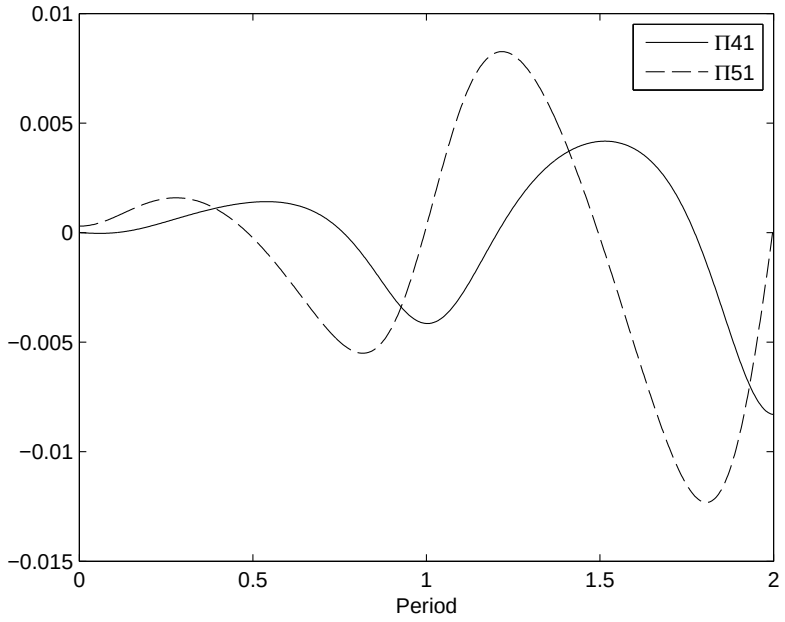

Figure C.2: Elements of $\mathbf{\Pi}(f)$ (2 of 6).

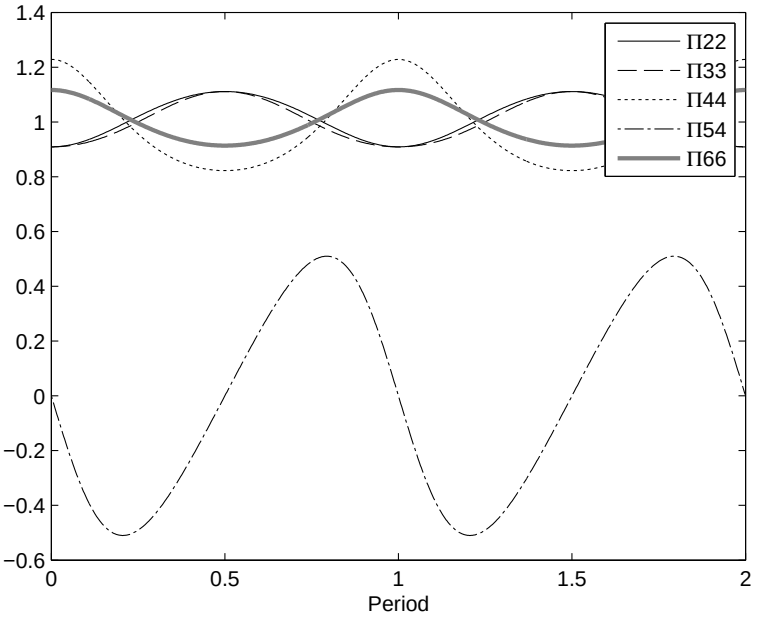

Figure C.3: Elements of $\mathbf{\Pi}(f)$ (3 of 6).

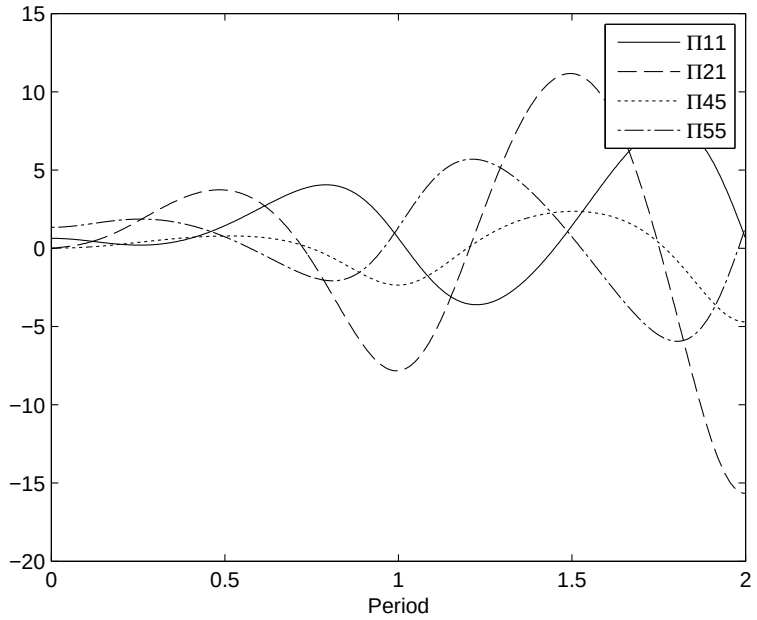

Figure C.4: Elements of $\mathbf{\Pi}(f)$ (4 of 6).

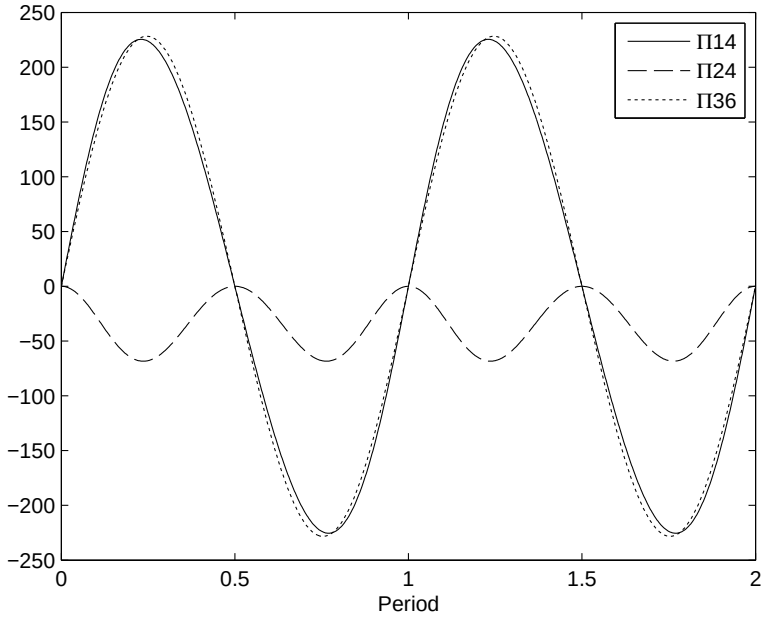

Figure C.5: Elements of $\mathbf{\Pi}(f)$ (5 of 6).

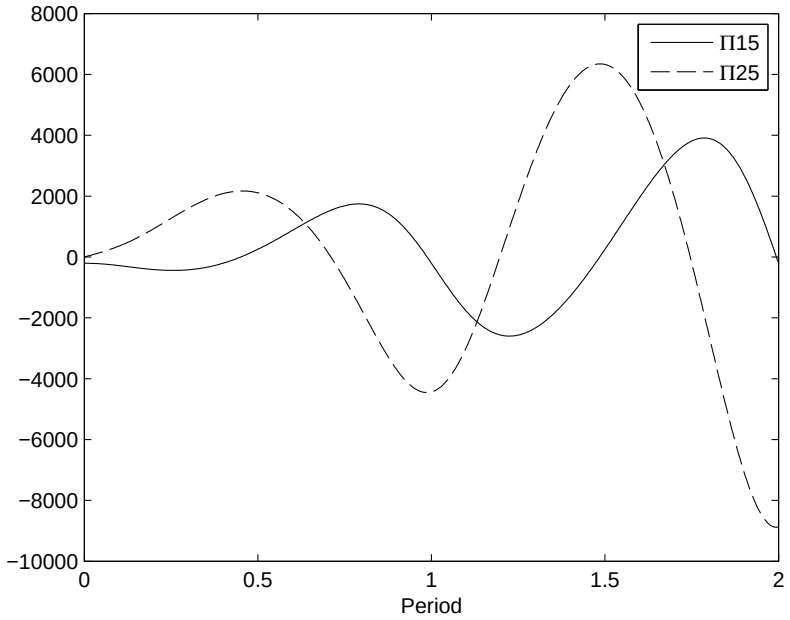

Figure C.6: Elements of $\mathbf{\Pi}(f)$ (6 of 6).